TECHNISCHE UNIVERSITÄT MÜNCHEN

Fakultät für Elektrotechnik und Informationstechnik

Lehrstuhl für Biologische Bildgebung

Multispectral Optoacoustic Dermoscopy: Methods and Applications

Mathias Schwarz

Vollständiger Abdruck der von der Fakultät für Elektrotechnik und Informationstechnik der Technischen Universität München zur Erlangung des akademischen Grades eines Doktors der Naturwissenschaften (Dr. rer. nat.) genehmigten Dissertation.

Vorsitzender:	Prof. Dr. Werner Hemmert
Prüfer:	1. Prof. Dr. Vasilis Ntziachristos
	2. Prof. Dr. Friedrich Simmel
	3. Prof. Dr. Norbert Hanik

Die Dissertation wurde am 24.11.2016 bei der Technischen Universität München eingereicht und durch die Fakultät für Elektrotechnik und Informationstechnik am 27.04.2017 angenommen.

Multispectral Optoacoustic Dermoscopy: Methods and Applications

Mathias Schwarz

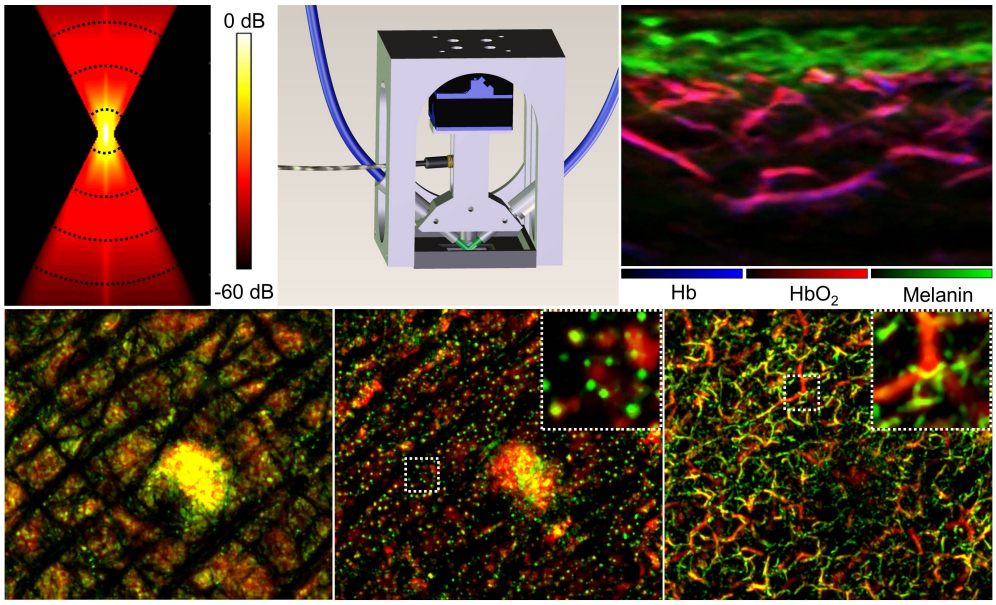

Dissertation an der Fakultät für Elektrotechnik und Informationstechnik der Technischen Universität München
vorgelegt von
Mathias Schwarz

Abstract

The skin is the largest organ in humans, constitutes the boundary to our environment, and plays an important role in human immune defense. Skin disorders, e.g. skin cancer, inflammatory diseases, and autoimmune diseases, impair skin functionality, and recent statistics show that the incidence rates are rising. Typical assessment of skin disease in dermatology includes the visual examination, which in some cases does not provide sufficient information for precise diagnosis. Complementary histological diagnosis of biopsies is time-consuming and burdens the health care system with excessive costs. Alternative imaging techniques are required, however, current biomedical imaging techniques lack in imaging depth and/or identifying angiogenic vessels.

Herein, a new imaging method, termed multispectral optoacoustic dermoscopy (MOD), was developed and explored in the context of clinical translation. MOD offers optical contrast at ultrasound diffraction-limited resolution, rendering resolution and imaging depth highly scalable. By exploiting the spectral information on absorbing moieties, functional and metabolic information, e.g. blood oxygenation, is provided. Major developments presented herein comprise the analysis of detection bandwidth and imaging depth in order to concurrently image all human skin layers, optimized and accelerated reconstruction algorithms, robust motion compensation algorithms, the design of a miniaturized and portable imaging device for the clinic, and an elaborate acquisition and data processing protocol established for multispectral imaging. These developments lead to a wide range of applications, culminating in the definition of objective disease biomarkers that could extend the state-of-the-art severity index classifications based on the unaided eye in the clinic.

Simulations show that due to the broadband optoacoustic signal generated by human skin (from a few to hundreds of MHz) - owing largely to the wide variability of the size of dermal vessels ($3.5\,\mu$m to $100\,\mu$m) - none of the current optoacoustic dermoscopy setups allow for concurrent imaging of all human skin layers. This work is dedicated to the development and applications of MOD, aiming to overcome the limitations of state-of-the-art optoacoustic dermoscopy setups. To this end, raster-scan optoacoustic mesoscopy (RSOM) is introduced, which was developed in our group. RSOM is based on a spherically focused ultrasound detector, which is raster-scanned over a two-dimensional surface. Four different RSOM implementations are developed and evaluated: high-frequency RSOM100 ($20 - 180\,$MHz), fast and sensitive RSOM50 ($10 - 90\,$MHz), a miniaturized and portable RSOM55 ($14 - 126\,$MHz) developed for clinical applications, and a multispectral raster-scan optoacoustic mesoscopy (MSOM) system providing functional information. Technical detail on improved pre-processing of the raw data and optimal sampling of both acquisition and reconstruction is presented and evaluated. A custom-designed three-dimensional reconstruction algorithm was implemented on a GPU to allow for parallel and fast reconstruction of three-dimensional images.

The first quantitative account is given on the relation between the excitation energy, detection bandwidth, and imaging depth achieved with MOD. Computer modeling is combined

with phantom measurements and *in vivo* imaging of human skin to specify optimal and marginal energy ranges required for concurrent visualization of all skin layers. A powerful motion correction algorithm is presented, which was designed to overcome deterioration of image quality and resolution due to patient/volunteer motion during the acquisition process. The improvement in image quality after motion correction is demonstrated for RSOM100, clinical RSOM55, and MSOM. Due to motion correction, unprecedented imaging performance is obtained with RSOM100, visualizing the epidermal-dermal junction as well as the superficial horizontal plexus. In clinical data the algorithm is able to reliably correct for strong breathing motion in patients. Analysis of blood oxygenation in single vessels shows that motion correction is indispensable in MSOM.

MOD provides a wide range of application in dermatology. First, melanoma tumor growth and angiogenesis in the vicinity of the tumor is visualized in longitudinal tumor growth studies in mice. Correct visualization of the tumor mass is confirmed by cryo-slices. Second, based on a newly-conceived acquisition and processing protocol, the unique spectral ability of optoacoustic dermoscopy is shown in humans. No other imaging modality enables high resolution quantification of intrinsic chromophores of a volume. Previously undisclosed broadband ($460 - 650\,\mathrm{nm}$) optoacoustic absorption spectra of skin compartments *in vivo* are recorded. For the first time, three-dimensional non-invasive imaging of blood-oxygenation in human skin *in vivo* is demonstrated. Third, the first account on non-invasive *in vivo* clinical optoacoustic imaging of the dermal human vascular is presented. The strength of optoacoustic dermoscopy in visualizing vascular features and changes due to disease is shown, and a set of objective disease biomarkers is established for both inflammatory and autoimmune diseases. Time course measurements reveal the progression of psoriasis through the entire skin.

The developments in hardware, software algorithms, and experimental protocols presented in this work pave the way for effective applications of MOD in basic and translational dermatology and dermoscopy. The classification of inflammatory diseases by objective disease biomarkers through optoacoustic dermoscopy could establish a new age of diagnostics and monitoring, extending the state-of-the-art severity index classifications by the unaided eye. Clinical MOD, implemented in a fast and easy to use format, opens up new possibilities for the structured evaluation for a large set of skin disorders in the clinic. The non-invasive monitoring of disease progression or therapy monitoring provides new opportunities inaccessible to traditional diagnostic methods.

Zusammenfassung

Die Haut ist das größte Organ des Menschen, bildet die Grenze zu unserer Umwelt und spielt eine wichtige Rolle in der Immunabwehr. Erkrankungen der Haut, z.B. Hautkrebs, entzündliche Erkrankungen und Autoimmunerkrankungen, beeinträchtigen die Funktionalität der Haut. Jüngste Statistiken zeigen, dass die Inzidenzraten von Hautkrankheiten steigen. Typischerweise werden in der Klinik Hautkrankheiten mit Hilfe eines Dermatoskops untersucht. Unzureichende Tiefeninformation verhindert in einigen Fällen jedoch eine präzise Diagnose. Ergänzende histologische Untersuchungen von Biopsien sind zeitraubend und belasten das Gesundheitssystem mit hohen Kosten. Alternative Bildgebungstechniken sind erforderlich, aber aktuellen biomedizinischen Bildgebungsverfahren fehlt die Eindringtiefe und/oder die Möglichkeit angiogene Gefäße zu identifizieren.

In dieser Arbeit wird ein neues Bildgebungsverfahren, die sogenannte Multispektrale Optoakustische Dermatoskopie (MOD), entwickelt und erforscht. MOD bietet optischen Kontrast bei Ultraschall-beugungsbegrenzter Auflösung. Eindringtiefe und Auflösung sind skalierbar. Durch die spektrale Information können funktionelle und metabolische Informationen gewonnen werden, z.B. der Blutsauerstoffgehalt in einzelnen Blutgefäßen. Die wichtigsten Entwicklungen, die in dieser Arbeit vorgestellt werden, umfassen eine detaillierte Analyse von Detektionsbandbreite und Eindringtiefe für die gleichzeitige Darstellung aller menschlichen Hautschichten, optimierte und beschleunigte Rekonstruktionsalgorithmen, robuste Bewegungskompensationsalgorithmen, die Konstruktion eines miniaturisierten und tragbaren Hautscanners für die Klinik und ein aufwendiges Aufnahme- und Rekonstruktionsprotokoll für multispektrale Bildgebung. Diese Entwicklungen ermöglichen eine Reihe von Anwendungen, die ihren Höhepunkt in der Definition von objektiven Krankheitsmarkern findet, welche die derzeitige Klassifikationsschemata in der Klinik ersetzen könnten.

Diese Arbeit befasst sich mit der Entwicklung und Anwendung von MOD und zeigt, wie die Einschränkungen aktueller optoakustischer Systeme überwunden werden. Zu diesem Zweck wird Raster-Scan Optoakustische Mesoskopie (RSOM) eingeführt, die in unserer Gruppe entwickelt wurde. RSOM basiert auf einem sphärisch fokussierten Piezodetektor, der in einem Schachbrettmuster über eine zweidimensionale Oberfläche gescannt wird. Vier verschiedene RSOM Implementierungen werden entwickelt und evaluiert: Hochfrequenz-RSOM100 ($20-180\,\mathrm{MHz}$), schnelle und sensitive RSOM50 ($10-90\,\mathrm{MHz}$), miniaturisierte und tragbare RSOM55 ($14-126\,\mathrm{MHz}$) für klinische Anwendungen, und Multispektrale Raster-Scan Optoakustische Mesoskopie (MSOM) zur Gewinnung funktioneller Informationen. Technische Details zur Verarbeitung und Rekonstruktion der Rohdaten werden präsentiert. Ein speziell angefertigter Rekonstruktionsalgorithmus wurde auf einer GPU implementiert um die parallele und schnelle Rekonstruktion von dreidimensionalen Bildern zu ermöglichen.

Zum ersten Mal wird die Beziehung zwischen Anregungsenergie, Eindringtiefe und Detektionsbandbreite in MOD ermittelt. Durch die Kombination aus Computersimulationen, Phantommessungen und *in vivo* Messungen der menschlichen Haut wird die minimale Anregungsenergie ermittelt, die für die gleichzeitige Visualisierung aller Hautschichten erforderlich ist.

Ein leistungsfähiger Bewegungskorrektur-Algorithmus wird vorgestellt, der entwickelt wurde um Bewegungsartifakte zu verbessern. Die Verbesserung der Bildqualität nach Bewegungskorrektur wird für RSOM100, klinische RSOM55 und MSOM demonstriert. Bewegungskorrektur ermöglicht noch nie dagewesene Bildqualität mit RSOM100, welche die Darstellung einzelner Kapillare und kleiner Blutgefäße erlaubt. Bei klinischen Daten ist der Algorithmus in der Lage zuverlässig starke Atembewegung zu korrigieren. Die Analyse der Sauerstoffsättigung des Blutes in einzelnen Gefäßen zeigt, dass Bewegungskorrektur in MSOM unverzichtbar ist.

Mit MOD wird ein breites Spektrum an dermatologischen Anwendungen gezeigt. Zunächst wird Melanomtumorwachstum in Mäusen und die Angiogenese in der Nähe des Tumors in einer Zeitverlaufsstudie visualisiert. Die korrekte Darstellung der Tumormasse wird durch Kryo-Elektronen-Tomografie bestätigt. Zweitens wird die einzigartige spektrale Fähigkeit von optoakustischer Dermatoskopie im Menschen gezeigt. Keine anderes Bildgebungsverfahren ermöglicht die Quantifizierung intrinsischer Chromophore eines Volumens bei hoher räumlicher Auflösung. Bisher nicht bekannte breitbandige Absorptionsspektren ($460 - 650\,\mathrm{nm}$) von Hautkompartimenten werden *in vivo* aufgezeichnet. Zum ersten Mal wird die Blutsauerstoffsättigung in der menschlichen Haut *in vivo* in einem Volumen demonstriert. Drittens werden zum ersten Mal mit MOD klinische Studien zu Gefäßveränderungen in der Dermis vorgestellt. Eine Reihe von objektiven und quantifizierbaren Krankheitsmarkern wird vorgestellt. In einer Teststudie werden vaskuläre Veränderungen von Psoriasis in einer Zeitverlaufsmessung erfasst.

Die in dieser Arbeit vorgestellten Entwicklungen in Hardware, Algorithmen und experimentellen Protokollen bereiten den Weg für eine effektive Anwendung von MOD in der Grundlagenforschung und klinischen Dermatologie. Die Klassifizierung von entzündlichen Erkrankungen durch objektive Krankheitsmarker mit Hilfe von optoakustischer Dermatoskopie könnte ein neues Zeitalter der Diagnose und Überwachung einleiten, die herkömmlichen Methoden stark überlegen ist. Klinische MOD eröffnet die Möglichkeit eine Reihe von Hauterkrankungen neu zu klassifizieren und zu diagnostizieren. Die nicht-invasive Überwachung des Krankheitsverlaufs oder die Therapieüberwachung bieten neue Möglichkeiten, die weit über die Möglichkeiten herkömmlichen Diagnosemethoden hinausreichen.

Glossary

1D	One-dimensional
2D	Two-dimensional
3D	Three-dimensional
AD	Atopic dermatitis
ANSI	American National Standards Institute
AVF	Absorber volume fraction
BCC	Basal cell carcinoma
BOLD	Blood oxygenation level dependent
CARS	Coherent anti-Stokes Raman scattering
CDS	Color Doppler sonography
cmOCT	Correlation mapping OCT
CMUT	Capacitive micromachined ultrasonic transducer
CNR	Contrast-to-noise ratio
DAQ	Data acquisition
DOCT	Doppler-OCT
DPSS	Diode-pumped solid state
EPR	Enhanced permeability and retention
FFT	Fast Fourier transform
fs-axis	Fast-scanning axis
FWHM	Full width at half maximum
GPU	Graphical processing unit
HGb	Hemoglobin
Hb	Oxyhemoglobin
HbO_2	Deoxyhemoglobin
IU	Interface unit
IPPS	Imaged pixels per second
MAP	Maximum amplitude projection
MM	Malignant melanoma
MOD	Multispectral optoacoustic dermoscopy
MPE	Maximum permissible exposure
MPM	Multiphoton microscopy
MRI	Magnetic resonance imaging
MSOM	Multispectral raster-scan optoacoustic mesoscopy
NEP	Noise-equivalent pressure
NIRS	Near-infrared spectroscopy
OAI	Optoacoustic imaging
OCT	Optical coherence tomography
OD	Optical density
OMAG	Optical microangiography
OPO	Optical parametric oscillator

ORS	Optical reflectance spectroscopy
PASI	Psoriasis area severity index
PC	Personal computer
PLA	Polylactide
PRR	Pulse repetition rate
RCM	Reflectance confocal microscopy
ROI	Region of interest
RSOM	Raster-scan optoacoustic mesoscopy
RSOM100	Raster-scan optoacoustic mesoscopy employing a 100 MHz detector
RSOM55	Raster-scan optoacoustic mesoscopy employing a 55 MHz detector
RSOM50	Raster-scan optoacoustic mesoscopy employing a 50 MHz detector
SAFT	Synthetic aperture focusing technique
SCC	Squamous cell carcinoma
SF	Sensitivity field
SHG	Second harmonic generation
SIR	Spatial impulse response
SNBI	Sequential narrow band inversion
SNR	Signal-to-noise ratio
SRS	Stimulated Raman scattering
ss-axis	Slow-scanning axis
TPEF	Two-photon excitation fluorescence
TUM	Technical university of Munich
UK	United Kingdom
UB-RSOM	Ultra-wideband raster-scan optoacoustic mesoscopy
US	Ultrasound
USA	United States of America
YAG	Yttrium aluminium garnet

List of Figures

List of Tables

Contents

1. Introduction

1.1. Motivation

In the journal of Nature Medicine, Donald M. McDonald and Peter L. Choyke have concisely summarized the current limitations of biomedical imaging techniques in the scope of visualizing angiogenesis in cancer, chronic inflammatory diseases, and other diseases: "An ongoing dilemma is, however, that [optical] microscopic methods provide their highest resolution on preserved tissue specimens, whereas clinical methods give images of living tissues deep within the body but at much lower resolution and specificity and generally cannot resolve vessels of the microcirculation. Future challenges include developing new imaging methods that can bridge this resolution gap and specifically identify angiogenic vessels." [2].

The ambitious goal of this thesis is to develop and explore a new imaging method that bridges the resolution gap, identifies microvessels, and in addition provides functional information of the vasculature. This new imaging method is termed multispectral optoacoustic dermoscopy (MOD) offering a unique imaging window termed the mesoscopic range, which is characterized by high resolution imaging at depths up to 5 mm [3, 4]. The main diagnostic focus will be put on the human skin, which constitutes a well-suited target for visualizing microvasculature in the mesoscopic range.

This chapter will motivate the clinical relevance of improved non-invasive diagnostics in dermatology. A detailed literature survey will show the limitations of current skin imaging techniques, according to the above-mentioned statement of Donald M. McDonald and Peter L. Choyke. Hence, MOD will be introduced as a comprehensive approach to overcome the limitations of modern skin imaging techniques. A literature on state-of-the-art optoacoustic dermoscopes will summarize the present development status of optoacoustic dermoscopy, opening up a wide space for improvement in terms of hardware, software algorithms, and experimental protocols. Finally, a brief synopsis of the thesis will be given, which outlines the main developments and applications presented in the following chapters.

1.2. Clinical relevance of improved diagnostics

The skin is the largest organ in humans, constitutes the boundary between our inner organs and the environment, and plays an important role in human immune defense [5]. The function of the skin to protect the body from the environment is impaired by skin disorders. Recent

statistics show that the incidence rate of skin diseases, especially skin cancer, are rising in Western societies [6–10]. According to cancer statistics in the USA, approximately 20% of the population will develop skin cancer in the course of a lifetime [11]. The most common form of skin cancer is basal cell carcinoma (BCC), followed by squamous cell carcinoma (SCC), and malignant melanoma (MM). Although MM is the least frequent form of skin cancer, it is responsible for the vast majority of skin cancer deaths [7, 12]. Since 1980 the incidence rate of MM has increased by more than 3-fold in Germany, and the current lifetime risk of developing melanoma is 1 in 50 [10]. Early detection of melanomas is crucial since the overall 5-year survival rate drops from approximately 98 percent (early detection), to 62 percent (disease has reached the lymph nodes), and 15 percent (disease has metastasized to distant organs) [7].

Apart from skin cancer, a large number of people are affected by skin conditions that can be classified into inflammatory diseases and autoimmune diseases. In the case of the inflammatory skin diseases psoriasis and atopic eczema, differential diagnosis can be difficult in some cases [13, 14]. At the same time, modern, cost-intensive, and specific therapies respond only to one of the two diseases. That is why it would be very helpful to have a reliable and preferably non-invasive method that improves the differential diagnosis. Enhanced non-invasive diagnosis is desirable in autoimmune diseases as well. In collagenosis, for instance, a circular disorder is manifest [15], which is currently recommended to be diagnosed by the subjective method of capillary microscopy [16]. Differential diagnosis of the autoimmune disease alopecia areata, the circular hair loss, from other forms of hair loss, such as androgenetic alopecia or posttraumatic, may be difficult but is of therapeutic relevance [17]. Currently, the standard diagnostic procedure is the trichogram, which is complex and requires the exhaustion of a lot of hair.

As of today, typical assessment of skin disease in dermatology includes the visual examination of the skin under magnification with a dermatoscope, complemented by photographic imaging with a video dermatoscope. Based on the two-dimensional (2D) appearance of the lesion, *i.e.* architectural features and color features, the physician decides if the lesion should be removed/biopsied and histologically diagnosed. Whole body lesion photography is also exercised in order to follow up lesion feature changes, which helps in detecting critical lesions. This procedure, while widely exercised, comes with several limitations.

Overall, visual inspection and photographic imaging only allows for the 2D visualization of a three-dimensional (3D) disease. Nonetheless, depth information is an important factor in skin disease. The total thickness of the skin depends on the dermal layer and varies between $1.5 - 4\,\mathrm{mm}$ [18]. The dermis contains an extensive system of blood vessels. In many instances, it would be ideal to determine the depth of the lesion and to monitor the vascular changes of the disease as it can better outline an optimal therapeutic strategy. Melanoma thickness, for instance, is an important factor in the prognosis of recurrence and metastasis [19, 20]. The treatment of melanoma is chosen according to the stage of the melanoma, which correlates to tumor depth. If melanoma thickness is less than 2 mm, it should be excised with a 1-cm margin. If the tumor measures more than 2 mm in depth, it should be resected with a 2-cm margin, and an additional biopsy of the sentinel node should be performed [21]. Incomplete removal of tumors can have more significant adverse effects as it can lead to cancer recurrence. Often the physician is confronted with decision making based on incomplete information. While this is a common practice in medicine, it may lead to missed lesions or more commonly to over-prescription for lesion biopsy, which is a burden on the patient and on the health care system in cost and time.

The National Cancer Institute estimated the cost of melanoma treatment in 2010 to $2.36 billion in the USA [22]. The cost of non-melanoma skin cancer in 2004 in the USA was $1.4 billion [23]. There is a need to reduce health care costs and patient suffering, which can be achieved by reducing the number of unnecessary biopsies. Besides cost, there are several limitations due to the visual or photographic inspection. Screening significantly benefits from the quality of information leading to increased sensitivity and specificity. Conversely, decision making based on incomplete information makes health care subjective, *i.e.* the screening results of an individual depend on his access to well-trained physicians or expert centers. A non-invasive monitoring device giving specific diagnostic information on various skin diseases could direct the appropriate treatment and help to decrease the cost.

1.3. Current biomedical imaging portfolio applied in dermatology

Resulting from the demand of improved diagnosis and treatment monitoring, multiple biomedical imaging techniques have emerged in the field of dermatology, which play an important role in biomedical research. Most of the applied techniques are based on optical imaging and provide anatomical, functional, and molecular information. In the following, several imaging techniques that have been applied to dermatology will be discussed in the light of contrast mechanism, resolution, imaging depth, and clinical application.

Sonography/Ultrasound (US)

Ultrasonography is a well-established technique in the current medical practice, enabling the visualization of cross-sectional slices in real-time, blood flow of larger vessels by Doppler sonography, and 3D sweep images. Ultrasound (US) imaging offers optimal balance between penetration depth and resolution without the need for contrast agents, penetrating several millimeters into human tissue. For skin imaging US probes of 15 MHz or higher are recommended. US contrast in skin is generated by changes in acoustic impedance, thus, visualizing keratin in the epidermis, collagen in the dermis, and the amount of fat globules in the subcutaneous layer [24, 25]. Super-resolution ultrasound enables the visualization of entire vessel systems but requires infusion of gas-filled microbubbles into the blood vessels [26].

US imaging has been widely used for melanoma thickness measurements, showing up as hypoechoic structures with a well-defined boundary [27]. Sonography at frequencies of $20 - 100$ MHz offers assessment of MM thickness with good correlation to histological measurements [28–31]. Sonography at frequencies up to 15 MHz shows lower correlation to histology but profits from deeper penetration [32–35]. Apart from melanoma skin cancer, sonography has been used for imaging the boundaries of BCC [36], SCC [24], and a number of inflammatory and autoimmune diseases [24, 25, 32, 37].

Sonography of human skin is faced with several limitations. First, US is not capable of differentiating MM from benign nevi or lymphocytic infiltrates, resulting in overestimation of melanoma thickness [27, 38, 39]. Second, boundary detection of BCC correlates only fairly with histology [32, 36, 40]. Third, color Doppler sonography (CDS) is usually operated at frequencies below 18 MHz [32], hence, blood flow readings of the fine microvasculature is not offered by current devices. Fourth, thickness measurements of inflammatory diseases are not very specific [32].

Reflectance confocal microscopy (RCM)

Reflectance confocal microscopy (RCM) is a non-invasive imaging tool that allows for the detection of back-scattered light from a focal spot through conjugated focal location of the light spot and the detection aperture [41]. Contrast in RCM is generated by back-scattered photons due to changes in refractive index [42]. RCM provides lateral resolution of $0.5 - 1.0\,\mu$m and axial resolution of $3 - 5\,\mu$m [43]. The maximal penetration depth in human skin for RCM systems operating in the near-infrared ($800 - 850\,$nm) is $200 - 250\,\mu$m [44].

Confocal imaging has been applied to imaging the epidermis, papillary dermis, and superficial reticular dermis of healthy skin [43]. RCM reached a sensitivity of approximately 90% in melanoma screening, comparable to dermoscopy. [45, 46]. RCM has shown morphological changes in the capillaries of the dermal papillae in psoriatic skin [47] and has been applied to other inflammatory skin conditions, such as contact dermatitis, rosacea, pyogenic granuloma, onychomycosis, bacterial folliculitis, warts, and herpes [41].

The main limitation of confocal imaging is its small penetration depth, especially in highly scattering skin tissue. Furthermore, confocal microscopy is limited in its capability to distinguish Langerhans cells from melanocytes, which is crucial for the identification of melanoma cells. While MM cells are identified by melanocytes migrating from dermis to more superficial layers (epithelium), the presence of Langerhans cells in the epithelium is a benign condition. The VivaScope from MAVIG (VivaScope Systems, MAVIG GmbH, Munich, Germany) is an implementation of confocal microscopy for dermatology. In practice, the VivaScope shows high resolution images but only in superficial skin layers and requires long acquisition times (several minutes).

Raman scattering (CARS/SRS)

Raman scattering describes the inelastic scattering of photons with atoms or molecules. Raman scattering occurs with a probability orders of magnitudes lower than the elastic Rayleigh scattering. To overcome the low generation of spontaneous Raman events, stimulated Raman scattering has been developed, namely coherent anti-Stokes Raman scattering (CARS) and stimulated Raman scattering (SRS). CARS utilizes a pump beam at frequency f_p and a Stokes beam at frequency f_s. If $(f_p - f_s)$ oscillates with a Raman active molecular vibration, there is a resonance in the anti-Stokes signal [48]. Signal is only generated at the laser focus because CARS is a nonlinear process [48]. Since CH_2 exhibits a vibrational resonance at $2.845\,\text{cm}^{-2}$, CARS is typically performed in the spectral range of this resonance, yielding lipid contrast [48]. Consequently, contrast is observed in the lamellar lipid intercellular space of the *stratum corneum*, sebaceous glands, and adipocytes [48]. Very similar to CARS is SRS, where the Stokes scattering process is stimulated. A real-time SRS system has been developed, producing 30 images per second [49]. Very often Raman scattering techniques are combined with multiphoton tomography, which provides additional contrast [50, 51].

Raman scattering techniques in human skin are limited in contrast and imaging depth. Since SRS/CARS is a nonlinear process, which depends on tight focusing within the tissue, the maximum penetration depth is $125 - 150\,\mu$m at a resolution of $1 - 5\,\mu$m [44, 48].

Multiphoton microscopy (MPM)

Multiphoton microscopy (MPM) takes advantage of two different nonlinear physical processes, where multiple photons are converted within the tissue into one photon of higher energy. Photon conversion happens either through multiphoton fluorescence or by higher harmonic generation. In skin imaging two-photon excitation fluorescence (TPEF) and second harmonic generation (SHG) are of importance because they provide contrast in backward mode, *i.e.* achievable through epi-illumination. TPEF provides contrast of endogenous fluorescent biomolecules: flavines, elastin, collagen, melanin, nicotinamide adenine dinucleotide phosphate, and protoporphyrin IX [52]. SHG in skin gives mainly contrast of collagen [52,53]. MPM provides spatial resolution around $1-2\,\mu$m [44] and reveals abnormal tissue architecture in melanoma [54]. Recently, a clinical study on 83 melanoma patients has shown a sensitivity and a specificity of $\sim 75\%$ [55].

The main limitation of MPM is its penetration depth, which is typically less than $300\,\mu$m [56], since signal generation of MPM relies on tight focusing of light in highly scattering tissue.

Magnetic resonance imaging (MRI)

Magnetic resonance imaging (MRI) is a noninvasive imaging technique that is not limited in depth and provides *in vivo* images of the whole body, yet, the spatial resolution in humans is limited to approximately $500\,\mu$m [57]. A specific implementation of MRI, named blood oxygenation level dependent (BOLD) MRI is capable of quantifying blood oxygenation levels [58], the microcirculation is, however, not resolved [2].

Optical reflectance spectroscopy (ORS) and near-infrared spectroscopy (NIRS)

Optical reflectance spectroscopy (ORS) and near-infrared spectroscopy (NIRS) have been used in clinical practice to determine the blood oxygenation level. ORS enables the measurement of bulk blood oxygen saturation or the oxygenation levels of macroscopic vessels. The penetration depth in tissue can be adapted by using light in the visible [59–61] or in the near-infrared spectral range [62,63]. In a clinical context bulk tissue oxygenation is measured by transmissive pulse oximetry at very specific locations, e.g. the fingertip or the earlobes.

Reflectance spectroscopy lacks spatial resolution, thus, pinpointing individual small vessels at a specific depth and calculating its oxygenation level is not possible.

Optical Coherence tomography (OCT)

Optical coherence tomography (OCT) is a non-invasive imaging tool that is based on the interferometry of back-scattered coherent light. Contrast in OCT is generated by the backscattering potential, which is proportional to the first and second order derivative of the refractive index [64]. OCT imaging systems of human skin are typically designed to provide slightly more than 1 mm penetration depth at axial resolution of $15\,\mu$m [65, 66].

Since particle movement modulates the recorded OCT signal, blood vessels can be used as a source of contrast. Doppler-OCT (DOCT) measures the phase shift in the OCT signal

Modality	Imaging depth	Resolution	Contrast
Dermatoscopy	$0\,\mu$m	depends on lens	complementary absorption
Raman scattering (CARS, SRS)	$< 150\,\mu$m $\approx$ 0.3 TMFP	$1-5\,\mu$m	inelastic scattering
Reflectance confocal microscopy (RCM)	$< 250\,\mu$m $\approx$ 0.5 TMFP	$0.5-5\,\mu$m	scattering, fluorescence
Multiphoton microscopy (MPM)	$< 300\,\mu$m $\approx$ 0.6 TMFP	$1-2\,\mu$m	fluorescence, second harmonic generation
Optical coherence tomography (OCT)	< 1 mm $\approx$ 2 TMFP	$2-15\,\mu$m	scattering
Ultrasound (US)	$0.8-70$ mm	$16-210\,\mu$m	change in refractive index
Magnetic resonance imaging (MRI)	no limit	$500\,\mu$m	nuclear magnetic resonance
Multispectral optoacoustic dermoscopy (MOD)	$1-5$ mm $\approx$ $2-10$ TMFP	$5-40\,\mu$m	absorption

Table 1.1.: Imaging depth, resolution, and source of contrast of current skin imaging techniques.

and detects moving particles relative to the scanning beam [67–72], but not perpendicular to it [73]. To detect particle motion perpendicular to the scanning beam, correlation mapping OCT (cmOCT) is employed, which is sensitive to changes in the magnitude of the OCT signal [73,74]. Optical microangiography (OMAG) takes advantage of both changes in phase and amplitude of the recorded OCT signal [74–76], providing enough sensitivity to detect blood flow in capillaries [77].

Since OCT contrast is based on changes in the refractive index and not on optical absorption, OCT has been shown to offer only poor spectral information in imaging oxygenation of blood vessels through a skin window in mice [78, 79]. To our knowledge, OCT has not been able to provide *in vivo* readings of oxygen levels in humans.

OCT provides valuable information in non-pigmented lesions [80] and melanocytic tumors [81]. OMAG has been applied to diseased skin [82], showing elongated capillary loops in psoriasis [83] and higher blood volume percentage in scar tissue [84].

OCT is limited to an imaging depth of approximately 1 mm in skin, which is a limitation when extracting melanoma thickness or tumor invasion depth [72]. A general disadvantage of OMAG is its sensitivity to sample motion, its dramatic loss of axial resolution below vessels due to decorrelation [82], and its relatively low imaging depth. Additionally, it is difficult to use OCT to obtain spectral information [78, 79].

1.3.1. Limitations of current skin imaging techniques

Table 1.1 summarizes the resolution, imaging depth, and contrast achieved by the skin imaging techniques presented above. All optical imaging techniques provide good resolution but are limited in penetration depth, resulting from the strong optical scattering in cutaneous

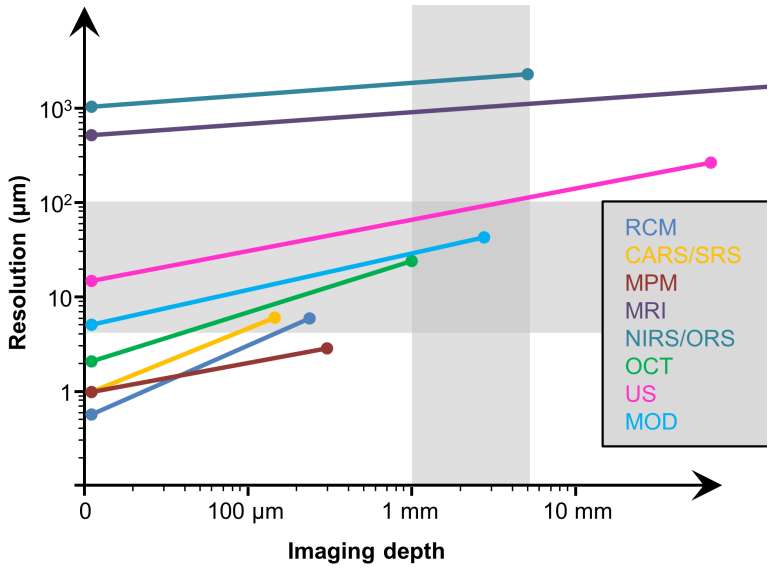

Figure 1.1.: Resolution and imaging depth achieved by current skin imaging techniques. The colored bars mark the lower and upper resolution and imaging depth achieved by each technique, as summarized in section 1.3. The gray shaded area indicates the resolution and imaging depth required for concurrent imaging of relevant anatomical features of human skin (see section 2.5).

tissue (see section 2.3). MRI allows for deep penetration but the resolution is not sufficient to resolve the dermal vessels. US imaging allows for scalable resolution and penetration depth but suffers from poor contrast. None of the presented techniques provide absorption contrast and, thus, are not able to directly measure blood vessels and their oxygenation state.

Figure 1.1 illustrates the resolution and imaging depth achieved by current skin imaging techniques. The gray shaded area indicates the resolution and imaging depth required for concurrent imaging of relevant anatomical features of human skin (see section 2.5).

Donald M. McDonald and Peter L. Choyke have concisely summarized the current limitations of biomedical imaging techniques in the scope of visualizing angiogenesis in cancer, chronic inflammatory diseases, and other diseases: “An ongoing dilemma is, however, that [optical] microscopic methods provide their highest resolution on preserved tissue specimens, whereas clinical methods give images of living tissues deep within the body but at much lower resolution and specificity and generally cannot resolve vessels of the microcirculation. Future challenges include developing new imaging methods that can bridge this resolution gap and specifically identify angiogenic vessels.” [2].

1.4. A comprehensive approach: multispectral optoacoustic dermoscopy (MOD)

In this context, MOD presents a comprehensive approach to imaging in dermatology. Optoacoustic (photoacoustic) imaging (OAI) is based on the photoacoustic effect discovered by Alexander Graham Bell in 1880 [85]. The photoacoustic effect describes the process of sound generation upon excitation of tissue with modulated light, mediated by thermoelastic expansion of the tissue. The first application of optoacoustic imaging was spectroscopy of gases,

which was shown in 1938 [86]. It was, however, only in the 1990's with new developments in laser and detector technology that the generation of sound by light has been utilized for biomedical imaging [87]. By measuring the pattern of acoustic waves outside of the biological tissue, the 3D distribution of optical absorption within the tissue can be reconstructed *in vivo*.

MOD offers three major advantages not available in other methods. First, OAI offers optical contrast at ultrasound diffraction-limited resolution, rendering resolution and imaging depth highly scalable [88, 89]. While other optical imaging techniques such as RCM, MPM, and OCT are limited to visualize superficial skin layers due to high optical scattering in the skin, it is possible to penetrate several millimeters into biological tissue with optoacoustics [90]. More specifically, a resolution of 200 μm is achieved for structures located several centimeters deep in tissue, whereas optical absorbers located at a depth smaller than a millimeter may be imaged with a resolution of several micrometers [89]. Due to its scalability of depth and resolution, MOD offers a unique imaging window termed the mesoscopic range, which is characterized by high resolution imaging at depths up to 5 mm [3, 4]. In the case of human skin, MOD offers imaging through the whole skin depth, which could offer improved delineation of ulcer or BCC among many other skin conditions. Second, the contrast in OAI is generated on absorption. Consequently, the natural chromophores melanin and hemoglobin yield direct and strong contrast [91]. Direct contrast of hemoglobin in MOD enables unique visualization of the rich vascular network in human skin, which is affected in wound healing and disease, e.g. systemic sclerosis [92, 92, 93], collagenoses [15], and psoriasis [47, 94]. Third, the absorption spectra of melanin, deoxyhemoglobin, oxyhemoglobin, and other chromophores show clearly distinct patterns in the visible and near-infrared electromagnetic spectrum. Multispectral excitation can be used to distinguish deoxyhemoglobin from oxyhemoglobin, melanin, and other chromophores. Spectral information of MOD could help discriminate benign nevi from MM and help identifying early stages of actinic keratosis or early stage carcinoma. Extrinsically administered fluorescent dyes that bind specifically to tumor cells could help to locate non-superficial malignant tissue *in vivo* and monitor drug distribution.

1.4.1. State of the art in optoacoustic dermoscopy

Optoacoustic tomography has found applications in dermatology since the late '90s. Several groups have developed optoacoustic imaging devices that allow for the visualization of human skin to a depth of several millimeters. Most of the developed imaging platforms share a common design, which consists of a light delivery system and a single piezoelectric transducer that is raster-scanned over the skin surface. Alternative approaches that are reported on are based on a transparent Fabry-Pérot detector as well as a linear transducer array for parallel acquisition of many channels.

In 1999, the first optoacoustic imaging device applied to human skin achieved in-depth resolution of $10 - 15\,\mu$m and light penetration of up to 4 mm, but suffered from a low lateral resolution of 200 μm [95]. To improve upon the lateral resolution of the first optoacoustic systems, a focused ultrasound transducer with central frequency of 50 MHz and darkfield illumination has been introduced in 2006, providing lateral resolution of $\sim 45\,\mu$m in the focal region [96]. With this setup volumetric images of human cutaneous vasculature have been imaged [97].

The first optoacoustic imaging systems in human skin showed the strong potential of optoacoustics in dermatology, providing direct contrast of the human vascular network. However, the development status of laser sources and ultrasound sensors had so far prevented optoacoustics to find application in dermatology. The main limiting components were: first, low pulse repetition rate (PRR) of single-wavelength lasers; second, the bulkiness of the optoacoustic systems; and, third, the moderate lateral resolution. All of the above mentioned setups employed laser sources with a PRR of 10 Hz. Thus, the acquisition time of a region of interest (ROI) measuring 8 mm × 8 mm took approximately 50 minutes [98]. Long acquisition times lead involuntarily to motion artifacts when imaging live samples and made imaging in the clinical context cumbersome. The bulky and fixed systems rendered certain skin areas on certain body sites inaccessible for imaging. The lateral resolution of $\sim 45\,\mu$m was sufficient for imaging the large vessels of the lower dermis and hypodermis, but insufficient for imaging the microvessels of the epidermal-dermal junction. Nevertheless, within the last decade, technological advancements have pushed the limits of optoacoustic imaging in dermatology.

More advanced laser sources, operating at PRRs of up to 3 kHz, have reduced acquisition times dramatically [99]. With faster excitation sources, the maximal PRR and, thus, acquisition times are mainly limited by the maximum permissible laser power on the skin surface, as specified for example by the ANSI laser safety standards [100].

Miniaturization of optoacoustic systems into handheld devices has also progressed in the last years, although no handheld device has reached a resolution better than 90 μm. Two transportable skin imaging systems have been recently developed/described [101, 102]. The first system was based on a transducer with a central frequency of 25 MHz, designed for detection of melanoma depth that was used to visualize the boundaries of B16 melanoma tumors in mice [101]. The second system was based on a PZT transducer with a central frequency of 35 MHz and was capable of imaging the large vessels of the lower dermis and hypodermis in humans [102].

Transparent interferometric Fabry-Pérot detector was employed to visualize the large vessels of the reticular dermis and hypodermis [103], providing in-depth resolution of 20 μm and in-plane resolution of $< 100\,\mu$m. The transparency of the Fabry-Pérot detector enabled an integration into a multimodal opoacoustic and OCT scanner [104, 105].

In the context of clinical translation, the presented state-of-the-art optoacoustic dermoscopes are faced by several challenges that need to be addressed:

1. Concurrent imaging of all human skin layers. None of the above presented devices is able to image all layers at once. So far, the requirements of optoacoustic dermoscopy in terms of imaging depth, detection bandwidth, and resolution have not been defined.

2. Motion compensation methods. To enable high resolution imaging in a clinical context, a robust motion compensation method is necessary.

3. Extraction of functional information from the skin. So far, only anatomical features of the skin have been visualized with MOD. Yet, multispectral illumination enables functional information, e.g. the quantification of blood oxygenation levels.

4. Miniaturization of the optoacoustic device without loss of resolution and sensitivity. Translation into the clinics requires robust, easy-to-use, and portable optoacoustic devices.

5. Optimized reconstruction methods. Improved reconstruction methods may improve image quality, accelerate imaging speed, and enhance the extraction of disease biomarkers.

1.5. Outline of the thesis

Overall, optoacoustic dermoscopy has the ability to impact screening in dermatology beyond the abilities of current optical or other imaging techniques. To establish MOD as a valuable diagnostic imaging technique in dermatology, the aforementioned challenges have to be addressed in optoacoustic dermoscopy. The following seven chapters will guide the reader through essential improvements of hardware, software algorithms, and experimental protocols, up to the stage where MOD will offer the possibility to extract biomarkers of skin diseases in a clinical study.

Chapter 2 presents the conceptual background of optoacoustic dermoscopy. First, the anatomy and optical properties of the human skin will be presented, summarizing the major anatomical structures and chromophores in skin. Second, the reader will be introduced to the theoretical background of the photoacoustic effect, explaining the basic principles of optoacoustic imaging. Third, the background information of optoacoustic signal generation, the anatomy of human skin, and the optical properties of human skin will be merged to formulate the requirements of optoacoustic dermoscopy in terms of imaging depth and detection bandwidth. An optoacoustic atlas of human skin will be created, mapping skin anatomy to the ultrasonic frequencies produced as a function of depth.

Chapters 3-8 are dedicated to the development and applications of MOD, aiming to overcome the limitations of state-of-the-art optoacoustic dermoscopy setups. Chapter 3 will introduce the experimental setups, acquisition protocols, and reconstruction algorithms of raster-scan optoacoustic mesoscopy (RSOM), a specific imaging platform for optoacoustic dermoscopy that will be used throughout the thesis. Specific implementations of RSOM technology will be presented, namely high-frequency RSOM100, fast and sensitive RSOM50, a miniaturized clinical RSOM55 setup, and a multispectral RSOM (MSOM) system. Thereafter, the concept of sequential narrow band inversion (SNBI) and an optimized reconstruction algorithm will be presented, enabling fast reconstruction of 3D images. Finally, optimal parameters for spatial and temporal sampling of acquisition as well as reconstruction grid will be evaluated experimentally.

In chapter 4, the relation between the excitation energy, frequency response, and the imaging depth achieved by RSOM will by investigated in simulations, phantom measurements, and *in vivo* measurements of the human skin. The experimental results on depth-dependent detection bandwidth will be related to the emitted frequency response of skin (see chapter 2), confirming that RSOM is well-suited to detect vessels of various sizes through all skin layers. Optimal detection bandwidth and excitation energy for fast and high contrast optoacoustic dermoscopy will be evaluated, taking into account laser safety regulations.

In chapter 5, a powerful motion correction algorithm will be presented, which was developed for RSOM. Impressive performance of the motion correction algorithm will be shown for high resolution RSOM100 images, clinical data recorded by RSOM55, and MSOM *in vivo*.

Starting with chapter 6, applications of RSOM to dermatology will be presented. In chapter 6, the rich potential of RSOM100 and RSOM50 in imaging angiogenesis of microvessels

around melanoma tumors in a preclinical model will be shown. Special attention will be paid to the usage of broadband piezoelectric detectors, leading to new and previously not reported performance in resolving tumor vasculature.

In chapter 7, the strength of MOD in extracting functional information will be shown. An elaborate multispectral acquisition protocol and data processing scheme will be presented, enabling for the first time three-dimensional spectral mesoscopy of human skin *in vivo*.

Finally, in chapter 8, the strength of optoacoustic dermoscopy in visualizing vascular features and changes due to disease will be shown, aiming for the establishment of an objective set of disease biomarkers. A broad range of interesting results of various skin diseases will be reported on.

2. Optoacoustic imaging in dermatology

Section 2.5 contains adapted text passages and figures from a manuscript submitted for publication by Schwarz *et al.* [106]. More information on the permission to reproduce textual material, illustrations, and tables is found in appendix B.

2.1. Introduction

In this chapter, the anatomy of human skin as well as its optical properties will be presented as far as it lies within the scope of optoacoustic imaging. Thereafter, the theoretical details of optoacoustic signal generation will be developed. The background information given in the first three sections will, then, be merged to demonstrate how optical contrast in human skin is generated in optoacoustics. Furthermore, the requirements of optoacoustic dermoscopy for concurrently imaging all human skin layers will be defined in terms of imaging depth and detection bandwidth.

2.2. Anatomy of the human skin

The skin is the largest organ in humans; it has a surface of approximately $1.2 - 2.3\,\mathrm{m}^2$ and weighs $3.5 - 10\,\mathrm{kg}$ [5, 18]. Its main function is to protect humans from the environment. Skin plays an important role in the human immune defense [5], it contains a large blood reservoir, and it helps to maintain thermal balance. Multiple appendages and receptors help in retaining skin function, e.g. hair, nails, sebaceous glands, and sweat glands [18], as well as receptors for temperature, pressure, and touch [107]. Skin consists of three different layers: the epidermis, the dermis, and the subcutis/hypodermis [5]. The thickness of the skin (epidermis plus dermis) depends mostly on the thickness of the dermis and measures $1 - 4\,\mathrm{mm}$ [18, 108].

The epidermis is a multilayered stratified squamous epithelium, consisting to more than 90% of keratinocytes. Other cell types include melanocytes, Langerhans cells, Merkel cells, and lymphocytes [5, 108]. The epidermis is a proliferation tissue and is renewed approximately every 28 days. Its thickness is in the range of $30 - 150\,\mu\mathrm{m}$ [5,18] for hair-bearing skin and up to $600\,\mu\mathrm{m}$ for hairless skin [18]. Most of the body is covered by $40 - 50\,\mu\mathrm{m}$ thick epidermis, increasing to $80\,\mu\mathrm{m}$ on the wrists and back of hands, reaching $400\,\mu\mathrm{m}$ on the front of the fingers [109]. *In vivo* measurements carried out with OCT have reported slightly larger values for the thickness of the epidermis [110]. The epidermis can be subdivided into five layers: the *stratum corneum*, the *stratum lucidum*, the *stratum granulosum*, the *stratum spinosum*, and the *stratum basale* (also called *stratum germinativum*) [5, 108]. The most important layers in optoacoustic imaging are the *stratum corneum* consisting of dry dead cells, and the *stratum basale*, containing melanin. The thickness of the *stratum corneum* ranges between

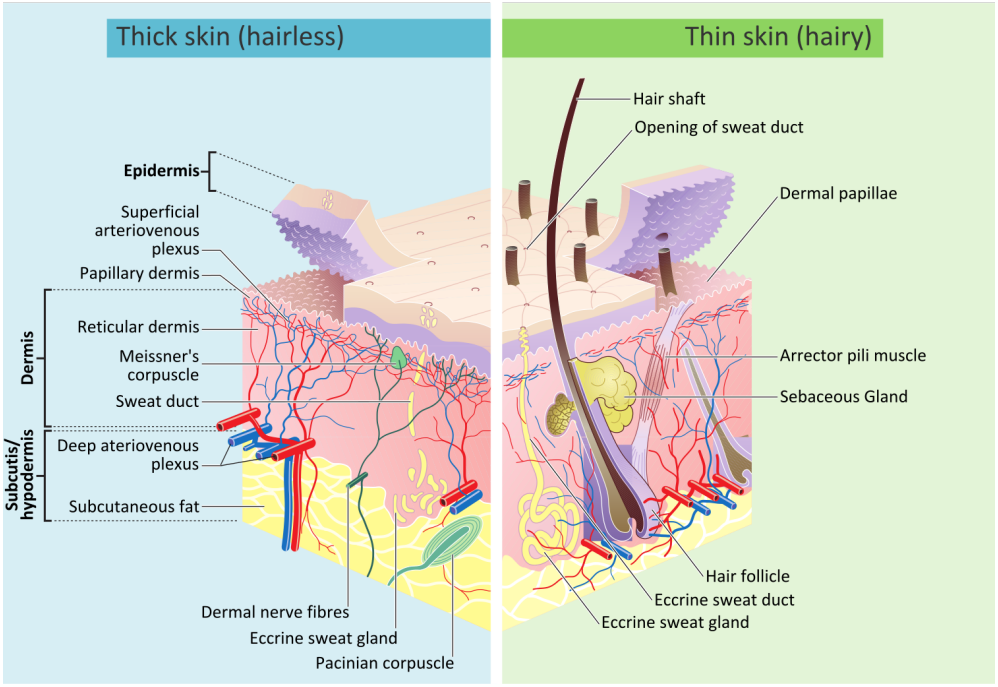

Figure 2.1.: Anatomy of the human skin by Madhero88 and M.Komorniczak (https://en.wikipedia.org/wiki/File:Skin_layers.png) [Creative Commons BY-SA 3.0 (http://creativecommons.org/licenses/by-sa/3.0)], via Wikimedia Commons.

2 μm at the scalp and 70 μm at the back of the knee [111], measuring $8-13\,\mu$m on average [5]. Melanin is produced within melanocytes, which are located in the *stratum basale*. Melanin, then, migrates to neighboring keratinocytes and accumulates in vesicles above the nucleus, protecting them from UV sun light [18]. In the keratynocytes the melanin granules fuse with lysosomes that dispose of melanin. That is why in the upper layers of the epidermis less melanin remains [18]. There are two different types of melanin: the brownish eumelanin and the yellow-reddish pheomelanin. The ratio between pheomelanin and eumelanin shows strong variations between individuals [108]. Another important cell type is Langerhans cells, which constitute $2-8\%$ of epidermal cells and play an important role in the immunologic reaction of the skin [18].

The dermis and epidermis are separated by a basement membrane, a thin lamella ($30-150$ nm), that regulates the exchange of molecules between the two layers [5]. The basement membrane plays an important role in wound healing and tumor invasion. The upper part of the dermis contains papillae that interconnect with the pins of the epidermis and allow for the exchange of vital molecules.

The dermis gives the skin its mechanical strength [18], consisting mainly of connective tissue (fascia), fibroblasts, and collagen fibrils [18]. Hair follicles, sebaceous glands, and sweat glands are located in the dermis [5, 18]. The dermis can be divided into two different layers: $\sim 250\,\mu$m papillary dermis, including superficial horizontal plexus, and $1-4$ mm reticular dermis, including the deep horizontal plexus [112]. A vast network of blood and lymph vessels runs through the dermis [18]. The arteries and veins are arranged in two plexuses parallel to the skin surface [5]. One plexus is located between the papillary and reticular dermis (subpapillary plexus/superficial arteriovenous plexus). The second plexus is located between the dermis and the hypodermis (deep arteriovenous plexus). Additional veins are located

in an intermediate plexus, between superficial and deep plexus [18]. Ascending arterioles and descending venules occur in pairs and connect the plexuses [113]. Capillaries run from the subpapillary plexus into the papillae, providing nutrition to the epidermis. The vessel size tends to increase with depth. The endothelial tube diameter of the capillaries in the dermal papillae measures $3.5 - 10\,\mu$m, increasing to $4 - 15\,\mu$m in the microvessels of the papillary dermis [113,114]. In the mid- and deep dermis microvascular diameters increase to $40 - 50\,\mu$m with wall thickness of $10 - 16\,\mu$m. The largest vessels of the lower dermis are as large as $100\,\mu$m [113, 115]. From the deep dermis; vessels in the range of $70 - 120\,\mu$m pass into the superficial layer of the fat. Post-capillary venules, measuring $25 - 50\,\mu$m, join these larger vessels from all directions [113, 116].

The subcutis/hypodermis consists of loose connective tissue, made up by adipocytes. In normal humans the fat is stored in small droplets within the adipocytes, in obese people the droplets are larger. The diameter of adipocytes ranges from $15 - 250\,\mu$m. Between the cells of the subcutnaeous tissue, there is a network of vessels, nerves, and reticular fibrils. The subcutaneous layer measures $1 - 6\,$mm [108].

2.3. Optical properties of the human skin

In this chapter, the optical properties of the human skin are summarized. There are several works and reviews on this matter; however, there are large variations between different studies. Here, an overview of optical properties, *i.e.* refractive index, anisotropy, absorption, and scattering, will be reported and discussed. Note that there are significant variations in optical properties between different persons and body sites [117].

2.3.1. Refractive index

The refractive index has a strong influence on light propagation within tissue, defining the speed of light and the propagation of photons. A mismatch in the refractive index between cell components leads to light scattering. The refractive indices of most tissues are reported to lie in the range of $n = 1.335 - 1.620$ for light in the visible range. Since the refractive index strongly depends on the water content, *in vitro* measurements may differ significantly from *in vivo* measurements [108].

The upper and lower boundary for the refractive index ranges between the refractive index of water ($n_{\text{water}} \approx 1.33$) and dry tissue mass ($n_{\text{dry}} = 1.514$) [117]. The value of the refractive index is underestimated by simply modeling skin as a mixture of water (70%) and protein (30%) [108], resulting in a refractive index lower than water (see Figure 2.2).

Ding *et al.* performed measurements on *in vitro* skin samples from $325 - 1550\,$nm [122]. The experimental values of the refractive index for the epidermis and dermis were fitted by the Cauchy dispersion relation:

$$n_{\text{epidermis}}(\lambda) = 1.4114 + \frac{8.73974e3}{\lambda^2} - \frac{7.9394e7}{\lambda^4} \tag{2.1}$$

$$n_{\text{dermis}}(\lambda) = 1.3696 + \frac{3.9168e3}{\lambda^2} + \frac{2.5588e3}{\lambda^4} \tag{2.2}$$

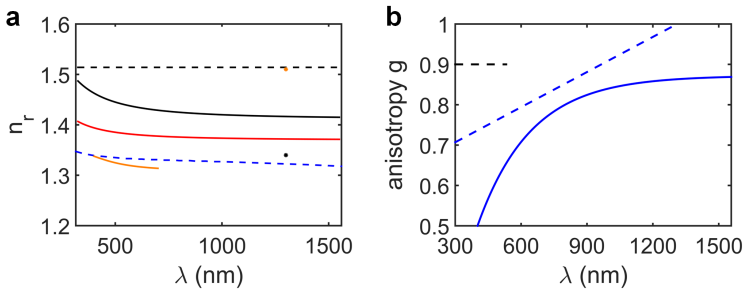

Figure 2.2.: Refractive index and anisotropy of human skin. **a)** Refractive index. Blue dashed: water [118], black dashed: dry tissue [117], orange: water-protein-mixture [108], black: epidermis (see equation (2.1)), red: dermis (see equation (2.2)), orange dot: *stratum corneum* [119], black dot: living epidermis [119]. **b)** Anisotropy of cutaneous tissue. Black dashed: *stratum corneum* [120], blue dashed: epidermis and dermis [120], blue: porcine dermis [121].

Figure 2.2a shows that the measurements performed by Ding *et al.* nicely fit into the upper and lower boundary given by water and tissue dry mass. The epidermis, which contains less water and more melanin, is expected to have a higher refractive index [108], as shown in Figure 2.2a. *In vivo* measurements performed by Tearney *et al.* [119] indicate that the refractive index of the *stratum corneum* is even higher ($n = 1.52$ at 1300 nm) due to its low water content.

Figure 2.2a summarizes the reported values for the refractive index. From all the reported values and models, the experimental values of Ding *et al.* seem to be the most accurate.

2.3.2. Anisotropy

Large variations are found in the literature reporting on measurements of the anisotropy g, however, the values of g are rather high [108, 117]. Experiments indicate that the anisotropy depends on the direction of propagation through the skin due to preferential orientation of filaments [123]. Epidermal and dermal anisotropy in the visible range most likely ranges from $0.7 - 0.9$, increasing with wavelength [120]. Values of g for the *stratum corneum* are expected to be approximately 0.9.

Incorporating surface roughness, Ma *et al.* have measured the anisotropy g of porcine dermis, which can be approximated by the formula [121]:

$$g = 0.653 + 0.219 \left(1 - \exp\left[-\frac{\lambda - 530.2\,\text{nm}}{242.8\,\text{nm}}\right]\right), \qquad \lambda \in [325 - 1557\,\text{nm}] \tag{2.3}$$

Figure 2.2b summarizes the reported values for the anisotropy in human skin. In the following, the experimentally determined values of Ma *et al.* will be used.

2.3.3. Absorption

The absorption coefficient μ_a is defined as $\mu_a = -1/T \partial T/\partial L$, where T is the surviving fraction of the incident light after an incremental pathlength ∂L [117]. Several equivalent definitions

of absorption exist:

$$
\begin{aligned}
T = e^{-\mu_a L} = 10^{-\epsilon C L} = e^{-\frac{4n'' L}{\lambda}} \\
\mu_a : \text{absorption coefficient } \left[\text{cm}^{-1}\right] \\
C : \text{concentration } \left[\frac{\text{mol}}{\text{l}}\right] \text{ or } [\text{M}] \\
\epsilon : \text{extinction coefficient } \left[\text{cm}^{-1}\text{M}^{-1}\right] \\
n'' : \text{imaginary refractive index}
\end{aligned}
\tag{2.4}
$$

Thus, the absorption coefficient is connected to the extinction coefficient via the formula $\mu_a = \epsilon C \ln(10)$. Optical density (OD) or absorbance is defined as $A_\lambda = -\log_{10}(I_1/I_0)$ and relates only in a non-scattering medium to the extinction coefficient via the formula $\text{OD} = \epsilon C L$.

Absorbers in human skin

Although major constituents of the human epidermis and dermis are water, collagen, keratin lipids, and elastin [5, 124], the absorption is governed by different substances. In the UV spectrum from $200 - 320\,\text{nm}$, the major epidermal chromophores are urocanic acid, DNA, tryptophane, tyrosine, melanin, and keratin [125–127]. Main Absorbers of cutaneous tissue in the near-infrared from $900 - 1300\,\text{nm}$ are water, fat, and protein [112,128]. The absorption of visible light by human skin is governed by the natural chromophores eumelanin, pheomelanin, oxyhemoglobin, deoxyhemoglobin, bilirubin, and β-carotene [108, 112, 117, 129, 130]. The yellow pigments bilirubin, and β-carotene absorb in the visible spectrum mostly between $400 - 500\,\text{nm}$ [131, 132].

Measuring the absorption of human skin poses multiple challenges, which result in significant differences in the experimental determination of the absorption coefficient between studies. Whereas *in vitro* measurements allow for transmission measurements of well-defined skin layers, optical properties of these layers are changed during the extraction and preparation of the *in vitro* samples, e.g. blood drains from the samples. *In vivo* measurements do not depend on tissue preparation, however, they rely on reflectance measurements and accurate light fluence models of the skin. Notable differences in the measured values of *in vivo* samples have been observed between different groups [130].

An easier and more robust way of estimating the absorption spectrum of human skin was reviewed by Jacques and is given by the sum over all tissue chromophores [117]:

$$
\begin{aligned}
\mu_a = \ln(10) B \left[S \epsilon_{\text{oxy}} C_{\text{Hb}} + (1 - S) \epsilon_{\text{deoxy}} C_{\text{Hb}}\right] + W \mu_{a,\text{water}} + F \mu_{a,\text{fat}} \\
+ \ln(10) \left[\epsilon_{\text{eum}} C_{\text{eum}} + \epsilon_{\text{pheo}} C_{\text{pheo}}\right] + \ln(10) \left[\epsilon_{\text{bili}} C_{\text{bili}} + \epsilon_{\beta\text{c}} C_{\beta\text{c}}\right]
\end{aligned}
\tag{2.5}
$$

where B, W, M, and F are the volume fraction of blood, water, melanin, and fat, respectively. S stands for the blood oxygen saturation.

In the epidermis the main chromophores are eumelanin and pheomelanin. It has been proposed to approximate the absorption of a melanosome within the epidermis by a power law [117], yet, large variations between different groups are observed. A more accurate approach takes into account measured concentrations of eumelanin and pheomelanin within the epidermis. Both eumelanin and pheomelanin are present in human epidermis [133], however,

	stratum corneum	**living epidermis**	**dermis**	**hypodermis**
B: blood volume fraction	-	-	$0.2-4\%$ [108]	$0.2-0.6\%$ [130]
C_{Hb}: hemoglobin conc. in blood	-	-	$1.7-2.7\,\mathrm{mM}$ [117]	$1.7-2.7\,\mathrm{mM}$ [117]
S: blood oxygenation	-	-	$45-99\%$ [60, 61, 78, 91]	$45-99\%$ [60, 61, 78, 91]
C_{eum}: eumelanin concentration	$0.5-4\,\mathrm{mM}$ (estimated)	$5-40\,\mathrm{mM}$ [133, 136]	-	-
C_{pheo}: pheomelanin concentration	$0.03-0.25\,\mathrm{mM}$ (estimated)	$0.3-2.5\,\mathrm{mM}$ [133, 136]	0%	0%
W: water content	$30-65\%$ [138]	$65-70\%$ [138]	$70-75\%$ [108]	10% [139]
F: fat content	-	-	3% [124]	86% [139]
$C_{\beta-\mathrm{c}}$: β-carotene concentration	$0.2-0.6\,\mu\mathrm{M}$ [108]			
C_{bili}: bilirubin concentration	$< 21\,{}^{\mu\mathrm{mol}}/_{\mathrm{l}}$ in human blood [117]			

Table 2.1.: Concentrations of main absorbers in human skin in the visible range.

pheomelanin represents on average $< 10\%$ of total epidermal melanin [134, 135]. Only in red-haired subjects higher concentrations of pheomelanin were found [133, 136]. Assuming a water content of $\sim 70\%$ [134, 137], concentrations of $0.3-2.5\,\mathrm{mM}$ for pheomelanin and $5-40\,\mathrm{mM}$ for eumelanin have been reported [133, 136].

The main absorbers of human dermis are erythrocytes that contain the chromophore hemoglobin (HGb). Hemoglobin exists in different states. The two most important states are: oxyhemoglobin (HbO_2) with oxygen bound to the heme component and deoxyhemoglobin (Hb) with no oxygen bound to the heme complex. The HGb concentration within blood varies between people. HGb concentration lies between $138-172\,{}^{\mathrm{g}}/_{\mathrm{l}}$ in men, $121-151\,{}^{\mathrm{g}}/_{\mathrm{l}}$ in women, $110-160\,{}^{\mathrm{g}}/_{\mathrm{l}}$ in children, and $110-120\,{}^{\mathrm{g}}/_{\mathrm{l}}$ in pregnant women [117]. Usually, a mean concentration of $150\,{}^{\mathrm{g}}/_{\mathrm{l}} = 2.33\,\mathrm{mM}$ is assumed. The blood volume fraction is typically $0.2-4\%$ within the dermis [108, 130].

The water content of the dermis has been measured by several groups, yielding an average of $70.2 \pm 5.2\%$ [108]. Confocal Raman spectroscopy revealed an increase in water content from $\sim 30\%$ at the surface to $\sim 75\%$ at a depth of $200\,\mu\mathrm{m}$ below the surface. Water content in elderly people is slightly higher [138]. To account for the increase in water content, a water content of 50% in the *stratum corneum*, of $65-70\%$ in the living epidermis, and of $70-75\%$ in the dermis will be assumed in the following. The fat content in human dermis was measured to be relatively stable and independent of age at $28\,{}^{\mathrm{mg}}/_{\mathrm{g}}$, corresponding to $\sim 3\%$ volume fraction [124]. The hypodermis consists mostly of fat, its structure showing a wide variability between people. Mean water content is on the order of $110\,{}^{\mathrm{mg}}/_{\mathrm{g}}$ and fat content lies approximately at $850\,{}^{\mathrm{mg}}/_{\mathrm{g}}$ [139], corresponding to volume fractions of $\sim 10\%$ and $\sim 86\%$ respectively.

β-carotene is found at a concentration of $0.03-0.63\,{}^{\mathrm{nmmol}}/_{\mathrm{g}}$, depending on body site [108,140]. The highest concentration of β-carotene are found in the forehead, back, and palm. Concentrations of bilirubin are expected to lie below $20\,{}^{\mathrm{mg}}/_{\mathrm{dl}} = 342\,\mu\mathrm{M}$, which is the concentration

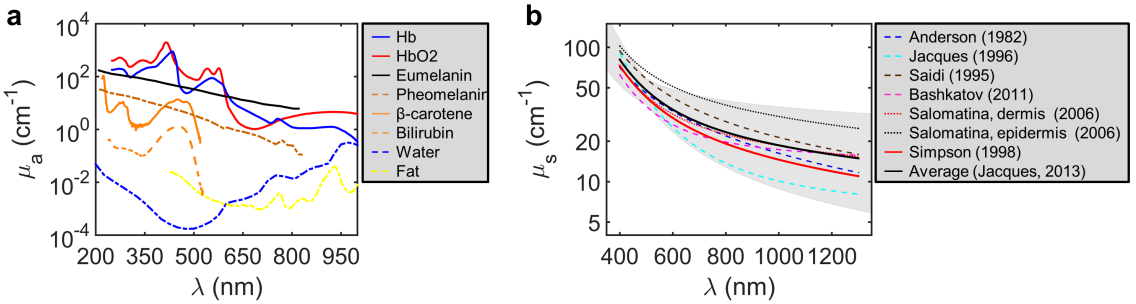

Figure 2.3.: Typical absorption and reduced scattering coefficient in human skin. **a)** Absorption coefficient of human skin, assuming values of 70% water content, 30% fat content, 105 g/l oxyhemoglobin, 45 g/l deoxyhemoglobin, 10 mM eumelanin, 1 mM pheomelanin, 43 μM β-carotene, and 10 μM bilirubin. **b)** Scattering coefficients approximating the experimental data of multiple studies [108, 117, 141–145]. Data was fitted to the model formula in equation (2.6). The average reduced scattering coefficient is very similar to the results from Simpson *et al.* , who have reported minimal tissue processing.

of bilirubin in the blood of a neonate suffering from jaundice [117]. Normal concentrations of bilirubin in blood lie below 21 μM [117].

Table 2.1 summarizes the concentrations and additional parameters needed for the calculation of the absorption coefficient according to equation (2.5). The parameter listing is broken down into different skin layers.

Figure 2.3a shows the spectra of the main absorbers in the visible spectrum at physiological meaningful concentrations (see Table 2.1). The three chromophores melanin, oxyhemoglobin, and deoxyhemoglobin are the dominant absorbers over the entire visible spectral range. That is why only melanin and hemoglobin are considered as intrinsic chromophores in section 2.5 and chapter 7.

2.3.4. Scattering coefficient and reduced scattering coefficient

Human skin is a strongly scattering tissue for light in the visible spectrum due to filamentous proteins, *i.e.* keratin in the epidermis and collagen in the dermis [108, 130]. Additional scattering include structures such as melanosomes, cell nuclei, cell walls, and blood vessels [130]. Scattering in the cutaneous layer is approximately twice as strong compared to the subcutaneous tissue, which in turn is stronger than in the muscle tissue [145].

In theory, scattering in human skin is approximated by an overlay of Mie scattering (large filamentous molecules) and Rayleigh scattering (small scale structures) [117, 146]. Jacques *et al.* fitted the data points of multiple studies to a formula describing Mie and Rayleigh scattering [117]:

$$\mu_s'(\lambda) = a\left[f_{\text{Ray}}\left(\frac{\lambda}{500\,\text{nm}}\right)^{-4} + (1-f_{\text{Ray}})\left(\frac{\lambda}{500\,\text{nm}}\right)^{-b_{\text{Mie}}}\right] \tag{2.6}$$

Figure 2.3b shows the data of several experimental studies fitted to equation (2.6). Since extensive tissue preparation will change the optical properties of the excised tissue samples, special attention should be paid to *in vitro* measurements of studies that reported minimal

tissue preparation, e.g. Simpson *et al.* [145], or mild tissue treatment, e.g. Salomatina *et al.* [144]. The average calculated over several studies is very close to the data of Salomatina *et al.* and Simpson *et al.*. Best fit parameters for the average curve are: $a' = 48.0 \pm 10.6\,\mathrm{cm}^{-1}$, $f_{\mathrm{Ray}} = 0.409 \pm 0.178$, and $b_{\mathrm{Mie}} = 0.702 \pm 0.351$.

Similar studies have been performed on subcutaneous fat layers, which depends significantly on the connective tissue septa and varies with body site [144]. The reduced scattering coefficient of fatty tissue that has been averaged over several studies yields best fit for the parameters $a' = 19.3 \pm 9.1\,\mathrm{cm}^{-1}$, $f_{\mathrm{Ray}} = 0.174 \pm 0.111$, and $b_{\mathrm{Mie}} = 0.447 \pm 0.263$ [117].

2.4. Theory of optoacoustic signal generation

The photoacoustic effect describes the generation of acoustic waves upon absorption of light by a material. This effect was discovered over a century ago by Alexander Graham Bell [85]. It is the most efficient way to generate acoustic waves below the ablation threshold [147].

The fractional volume change dV/V upon tissue excitation depends on the changes in pressure Δp and in temperature ΔT [148]:

$$\frac{\Delta V}{V} = -\kappa \Delta p(\vec{r}) + \beta \Delta T(\vec{r}), \tag{2.7}$$

where $\kappa = -1/V(\partial V/\partial p)_T$ denotes the isothermal compressibility, and $\beta = 1/V(\partial V/\partial T)_p$ is the isobaric coefficient of thermal volume expansion. For biological tissue the isothermal compressibility is given by $\kappa = C_p/\rho v_s^2 C_V \approx \rho^{-1} v_s^{-2}$, where C_V and C_p are the specific heat capacities at constant volume and pressure respectively. Thus, for water and soft tissue with a mass density of $\rho \approx 1000\,\mathrm{kg/m^3}$ and a speed of sound of $1500\,\mathrm{m/s}$, the isothermal compressibility is on the order of $\kappa \approx 4 \cdot 10^{-10}\,\mathrm{Pa}^{-1}$. The thermal expansion coefficient changes with temperature and material and is $\beta \approx 4 \cdot 10^{-4}\,\mathrm{K}^{-1}$ in muscle tissue [148].

The efficiency in the generation of acoustic waves, *i.e.* the change in initial pressure $\Delta p_0(\vec{r})$, depends on the thermal and acoustic relaxation times of the tissue [149, 150]:

Thermal relaxation time: The thermal relaxation time is calculated as [151]:

$$t_{\mathrm{th}} = \frac{d^2}{D}, \tag{2.8}$$

where D is the thermal diffusivity of the material, and d denotes the smallest dimension of a thermally confined volume. Typical values for thermal diffusivity are $D \approx 0.14 - 0.15\,\mathrm{mm^2/s}$ in water [152, 153] and $D < 0.14\,\mathrm{mm^2/s}$ in protein and soft tissue [154]. Thus, for a cube of $(5\,\mu\mathrm{m})^3$, the thermal relaxation time is $t_{\mathrm{th}} > 175\,\mu\mathrm{s}$.

The condition of thermal confinement is met if the heat deposited by the absorption of light within a specific volume stays within the volume during the laser pulse, *i.e.* the heat cannot escape from the volume through thermal conduction. If thermal confinement is fulfilled, the temperature increase after absorption is maximized, and the generation of acoustic waves is most efficient.

Stress relaxation time: The stress relaxation time is given by the formula [151]:

$$t_{\mathrm{s}} = \frac{d}{v_s}, \tag{2.9}$$

where d denotes the smallest dimension of a stress confined volume. Assuming a cube of $(5\,\mu\text{m})^3$ and $v_s = 1500\,\text{m/s}$, the stress relaxation time reads $t_\text{s} = 3.3\,\text{ns}$.

The stress relaxation time, also named acoustic relaxation time, is the time lapse for an acoustic wave to propagate over a distance d. If the heating pulse is much shorter than the typical time of acoustic relaxation within a specific volume, the condition of stress confinement is fulfilled.

If the laser pulse length is much shorter than the thermal relaxation time and the stress relaxation time, the conversion of optical energy into acoustic waves is most efficient. Then, the fractional volume expansion is negligible, and the local pressure rise in equation (2.7) after tissue excitation is given by [147]:

$$\Delta p_0(\vec{r}) = \frac{\beta \Delta T(\vec{r})}{\kappa} \tag{2.10}$$

Inserting typical values ($\kappa = 4 \cdot 10^{-10}\,\text{Pa}^{-1}$ and $\beta = 4 \cdot 10^{-4}\,\text{K}^{-1}$) a temperature rise of $1\,\mu\text{K}$ gives rise to a pressure rise of $1\,\text{Pa}$.

The temperature rise itself depends on the absorbed optical energy. Assuming that all of the absorbed light energy is converted into heat, the temperature rises by:

$$\Delta T(\vec{r}) = \frac{\mu_a(\vec{r})\phi(\vec{r}, \mu_a, \mu_s, g)}{\rho C_V}, \tag{2.11}$$

where μ_a is the absorption coefficient, and ϕ denotes the light fluence. Thus, the initial rise in pressure is given by:

$$\Delta p_0(\vec{r}) = \frac{\beta \mu_a(\vec{r})\phi(\vec{r}, \mu_a, \mu_s, g)}{\kappa \rho C_V} = \frac{\beta v_s^2 \mu_a(\vec{r})\phi(\vec{r}, \mu_a, \mu_s, g)}{C_p} = \Gamma \mu_a(\vec{r})\phi(\vec{r}, \mu_a, \mu_s, g) \tag{2.12}$$

The Grüneisen parameter Γ is a dimensionless thermodynamic constant that describes the tissue-dependent efficiency of converting absorbed light energy to pressure. Usually Γ is considered to vary weakly between different tissue types. However, optoacoustic image contrast is affected by the heterogeneities in the Grüneisen coefficient, which may vary considerably: $\Gamma \approx 0.7 - 0.9$ for fat and $\Gamma \approx 0.25$ for blood [155, 156].

From equation (2.12) and appropriate tissue parameters, the initial pressure change can be estimated. Assuming a blood vessel with an average hemoglobin concentration of $c_\text{Hb} = 150\,\text{g/l}$, an excitation wavelength of $\lambda = 532\,\text{nm}$, a light fluence of $\phi = 100\,\mu\text{J/cm}^2$, molar extinction of $\epsilon_\text{oxy} = 43876\,\text{l/cm·mole}$, and molar mass of $m_\text{Hb} = 64458\,\text{g/mole}$ the initial pressure change is calculated to be:

$$\Delta p_0 = \Gamma \mu_a \phi = 0.25 \cdot 100\,\mu\text{J/cm}^2 \cdot \frac{\ln(10) 43876\,\text{l/cm·mole} 150\,\text{g/l}}{64458\,\text{g/mole}} = 5.9\,\text{kPa}, \tag{2.13}$$

corresponding to a temperature rise of $5.9\,\text{mK}$.

The distribution of local pressure changes $\Delta p_0(\vec{r})$ will initiate an acoustic wave propagating through the elastic tissue. The propagation of the acoustic wave is described by the following conditions [156]:

$$\text{Linear wave operator} := \mathcal{L}_\omega p(\vec{r}, t) = 0 \tag{2.14}$$

$$\text{Initial pressure distribution} := p(\vec{r}, 0) = \Delta p_0(\vec{r}) \tag{2.15}$$

$$\text{Initial particle velocity} := \partial / \partial t p(\vec{r}, t) = 0 \tag{2.16}$$

$\Delta p_0(\vec{r})$ is the initial pressure distribution. The initial particle velocity inside the tissue is zero. The linear wave operator describes the propagation of the acoustic wave inside the tissue. Written in this general form it leaves room to incorporate acoustic absorption, variations in sound speed and density inside a heterogeneous tissue. In most cases, however, an acoustically homogeneous, isotropic, and liquid-like medium is assumed [157, 158]:

$$\frac{\partial^2 p(\vec{r},t)}{\partial t^2} - v_s^2 \nabla^2 p(\vec{r},t) = \Gamma \frac{\partial \mu_a(\vec{r}) \phi(\vec{r},\mu_a,\mu_s,g,t)}{\partial t} = \Gamma \frac{\partial H(\vec{r},t)}{\partial t}, \tag{2.17}$$

where $H(\vec{r},t)$ is the heat energy per unit volume and unit time deposited by the excitation beam.

A powerful tool in solving an inhomogeneous linear differential equation of the form given in equation (2.17) is the Green's function. The Green's function solves the inhomogeneous wave equation in response to a delta impulse:

$$\left(\nabla^2 - \frac{1}{v_s^2}\frac{\partial^2}{\partial t^2}\right) G(\vec{r},t) = \delta(\vec{r})\delta(t) \tag{2.18}$$

The solution to equation (2.18) is given by:

$$G(\vec{r},t) = -\frac{1}{4\pi} \frac{\delta\left(t - \frac{|\vec{r}|}{v_s}\right)}{|\vec{r}|} \tag{2.19}$$

Therefore, the general solution to the inhomogeneous differential equation (2.17) is expressed by a convolution of the Green's function with the inhomogeneity:

$$\begin{aligned} p(\vec{r},t) &= G(\vec{r},t) * \left(-\frac{\Gamma}{v_s^2}\frac{\partial H(\vec{r},t)}{\partial t}\right) \\ &= \frac{\Gamma}{4\pi v_s^2} \iiint d\vec{r'} \int d\tau \frac{\delta\left((t-\tau) - \frac{|\vec{r}-\vec{r'}|}{v_s}\right)}{|\vec{r}-\vec{r'}|} \frac{\partial H(\vec{r'},\tau)}{\partial \tau} \\ &= \frac{\Gamma}{4\pi v_s^2} \iiint \frac{d\vec{r'}}{|\vec{r}-\vec{r'}|} \left.\frac{\partial H(\vec{r'},\tau)}{\partial \tau}\right|_{\tau = t - \frac{|\vec{r}-\vec{r'}|}{v_s}} \end{aligned} \tag{2.20}$$

The heating function is a function of time and space. It is the product of the absorption coefficient and the light fluence:

$$H(\vec{r},t) = \mu_a(\vec{r})\phi(t,\vec{r};\mu_a,\mu_s,g) \tag{2.21}$$

Since propagation of light can be considered instantaneous at the scales encountered in biomedical applications, *i.e.* several micrometers, the heating function is separable and may be approximated by an initial pressure rise initiated by impulse heating:

$$H(\vec{r},t) = H_r(\vec{r})H_t(t) = \frac{\Delta p_0(\vec{r})}{\Gamma}\delta(t) \tag{2.22}$$

Assuming impulse heating, equation (2.20) simplifies to:

$$\begin{aligned} p(\vec{r},t) &= \frac{1}{4\pi v_s^2} \iiint \frac{d\vec{r'}}{|\vec{r}-\vec{r'}|} \Delta p_0(\vec{r'}) \left.\frac{\partial \delta(\tau)}{\partial \tau}\right|_{\tau = t - \frac{|\vec{r}-\vec{r'}|}{v_s}} \\ \Delta p_0(\vec{r}) &= \Gamma \mu_a(\vec{r}) \phi(\vec{r},\mu_a,\mu_s,g) \end{aligned} \tag{2.23}$$

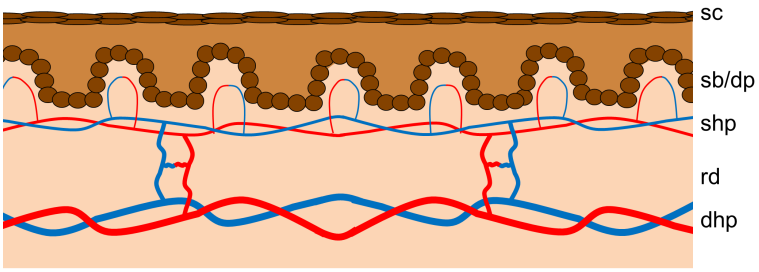

Figure 2.4.: Layers in human skin characterized by high concentrations of melanin and/or hemoglobin. sc: *stratum corneum*, sb: *stratum basale*, dp: dermal papillae, shp: superficial horizontal plexus, rd: reticular dermis, dhp: deep horizontal plexus. Adapted from Schwarz *et al.* [106].

Equation (2.23) provides an illustrative description of the propagation of acoustic waves through the tissue. The term $\Delta p_0(\vec{r'})/|\vec{r}-\vec{r'}|$ represents an acoustic spherical acoustic wave originating from location $\vec{r'}$. The amplitude of the acoustic point wave is proportional to the initial pressure change at this location and decays with $1/\Delta r$, where Δr is the distance between the propagating wave front and the origin of the acoustic point wave. The pressure distribution at an arbitrary point $\vec{r}$ in space and at an arbitrary time point t is given by the superposition of all point like sources that lie on a spherical shell located at a distance $v_s t$ from the point $\vec{r}$.

2.5. Optoacoustic contrast in the human skin

In this section, background information on the anatomy of human skin (see section 2.2), optical absorbers in human skin (see section 2.3.3), and the theory of optoacoustic signal generation (see section 2.4) will be merged to define the required imaging depth and detection bandwidth in optoacoustic dermoscopy.

Human skin is a source of rich contrast in optoacoustic mesoscopy. The absorption spectrum of skin chromophores and the excitation wavelength determine the source of optical contrast (see section 2.3). The anatomy of human skin (see section 2.2) determines the size and depth of absorbing structures that are visible at a specific excitation wavelength. The theory of optoacoustic signal generation in turn (see section 2.4) relates the size of absorbers to ultrasound frequencies that are emitted upon tissue excitation. Merging the knowledge from chromophores, anatomy, and optoacoustic signal generation, a generic skin model emerges, which defines imaging depth and frequency bandwidth required for optoacoustic dermoscopy.

To define the required imaging depth and detection bandwidth of optoacoustic mesoscopy, the optoacoustic frequency response generated by simulated human skin will be modeled in the following. The frequency response of two generic skin types, which are characterized by different epidermal and dermal thicknesses, will be analyzed: thick hairless skin (human palm) and thin hair-bearing skin (lower arm). The model takes into account the major skin chromophores in the visible electromagnetic spectrum between $480 - 650\,\mathrm{nm}$, *i.e.* melanin and hemoglobin, their location and size. Figure 2.4 shows all layers that contain melanin or hemoglobin and, thus, will show up on optoacoustic images. Melanin is contained within the epidermis, mainly in the *stratum basale*. Hemoglobin is contained in the blood vessels of the dermis, from capillary loops in the dermal papillae, to vessels within the superficial

Layer	**Depth z of layer** (μm)	**Diameter d of absorber** (μm)
Stratum corneum	0-20 [5, 111]	20 [5, 111]
Mid-epidermis	20-220 [109, 110, 159]	-
Stratum basale	220-240 (estimated)	20 (estimated)
Dermal papillae	240-370 (estimated)	6.75 [113, 114]
Superficial plexus	370-570 [112]	12.5 [113, 114]
Reticular dermis	570-870 [159–162]	40 [113, 115]
Lower plexus	870-970 [159–162]	50 [113, 115]
Hypodermis	> 970	100 [113, 116]

Table 2.2.: Depth of absorbing skin layer and diameter of absorbers within each layer in the human palm. Values were compiled from [5, 109–116, 159–162].

horizontal plexus, to vessels of the reticular dermis and deep horizontal plexus. The skin model simulated a multi-layered media, containing the *stratum corneum*, *stratum basale*, capillary loops in the dermal papillae, vessels within the superficial horizontal plexus, vessels of the reticular dermis, and the vessels within the deep horizontal plexus. Table 2.2 and 2.3 are a compilation of previous publications [5, 109–116, 159–162], which summarize the depth of each skin layer and the corresponding radius of the absorbers within each layer for both the human palm and the lower arm.

To mimic the broadband optoacoustic signal generated by the different layers in human skin, the signal is calculated by the analytic formula for a circular absorber of radius a [148]:

$$p_{\text{gen}}(t; a) = p_0 \frac{R - v_s t}{2R} \cdot H(a - |R - v_s t|), \tag{2.24}$$

where $H(x)$ is the Heaviside step function, v_s the speed of sound, and R specifies the distance between source and absorber.

The depth-dependent frequency response $f_{\text{oa}}(z, f)$ as a function of depth z is calculated via the Fast Fourier Transform (FFT) of the pressure wave equation:

$$f_{\text{oa}}(z, f) = \frac{[\mathcal{FFT}[p_{\text{gen}}(t; r)](f)]_{r=r(z)}}{\max_f [\mathcal{FFT}[p_{\text{gen}}(t; r)](f)]_{r=r(z)}}, \tag{2.25}$$

where the absorber radius $r(z)$ is a continuous function of depth that was obtained by linear interpolation of the absorber diameters in Table 2.2 and 2.3. For visualization purposes, the frequency response $f_{\text{oa}}(z, f)$ was normalized.

Layer	**Depth z of layer** (μm)	**Diameter d of absorber** (μm)
Stratum corneum	0-10 [5, 111]	10 [5, 111]
Mid-epidermis	10-60 [109, 110, 159]	-
Stratum basale	60-80 (estimated)	20 (estimated)
Dermal papillae	80-210 (estimated)	6.75 [113, 114]
Superficial plexus	210-410 [112]	12.5 [113, 114]
Reticular dermis	410-1060 [159–162]	40 [113, 115]
Lower plexus	1060-1260 [159–162]	50 [113, 115]
Hypodermis	> 1260	100 [113, 116]

Table 2.3.: Depth of absorbing skin layer and diameter of absorbers within each layer in the lower arm. Values were compiled from [5, 109–116, 159–162].

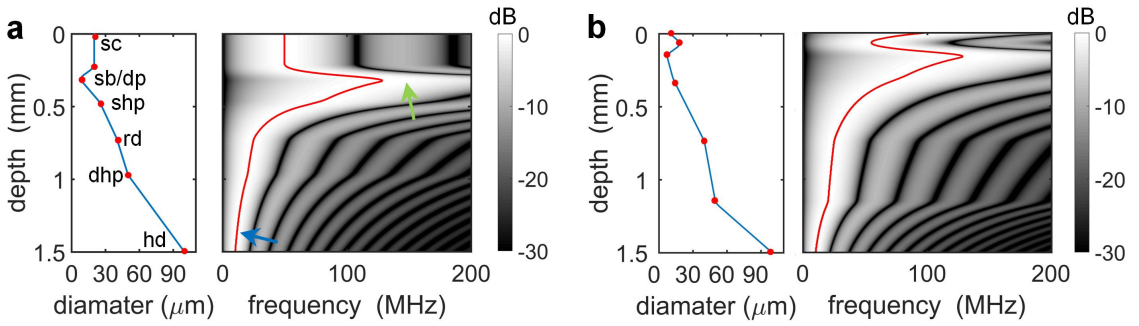

Figure 2.5.: Optoacoustic frequency response as a function of depth generated by human skin. **a)** Diameter size of absorbing structures and simulated optoacoustic frequency response $f_{\mathrm{oa}}(z, f)$ as a function of depth generated by absorbers in the human palm. Frequencies emitted by the capillary loops (green arrow, $240 - 370\,\mu$m below the surface) have a maximum at ~ 150 MHz. The peak frequency in the dermis decreases with depth and is as low as ~ 10 MHz in the hypodermis (blue arrow). **b)** Diameter size of absorbing structures and optoacoustic frequency response as a function of depth generated by absorbers in the lower arm. The dermal papillae and superficial horizontal plexus are much closer to the skin surface compared to (a). sc: *stratum corneum*, sb: *stratum basale*, dp: dermal papillae, shp: superficial horizontal plexus, rd: reticular dermis, dhp: deep horizontal plexus, hd: hypodermis. Adapted from Schwarz *et al.* [106].

The simulated frequency response generated by the human palm and lower arm is shown in Figure 2.5. For both skin regions, a decrease in the peak ultrasound frequency with depth is observed. The highest frequencies are emitted by the capillary loops of the dermal papillae that have a maximum at approximately 150 MHz. Thus, to correctly visualize the dermal papillae, it is necessary to acquire frequencies > 150 MHz. Since the human palm has a much thicker epidermis than the lower arm, optoacoustic signals originating from the dermal papillae and the superficial horizontal plexus have to penetrate through a thicker layer of tissue in the human palm. Peak optoacoustic frequencies of the vessels in the superficial horizontal plexus are located at approximately 90 MHz. The optoacoustic signal emitted by larger vessels of the reticular dermis show peaks at $10 - 20$ MHz.

Thus, concurrent imaging of all human skin layers requires superficial detection (up to $450\,\mu$m) of frequencies > 150 MHz and detection of frequencies < 30 MHz up to a depth of 1.5 mm.

2.6. Summary and conclusion

In this chapter, the reader has been familiarized with the basics of optoacoustic dermoscopy, including skin anatomy, optical properties of skin, the theory of optoacoustics, and optoacoustic contrast in human skin.

In sections 2.2 and 2.3, the anatomy and optical properties of the human skin were presented. Human skin consists of three different layers: the epidermis, the dermis, and the subcutis/hypodermis. Each of these layers fulfills specific functions and provides rich optoacoustic contrast. Main attention was paid to the spatial distribution of intrinsic chromophores, which have a strong absorption in the visible wavelength range: eumelanin, pheomelanin,

oxyhemoglobin, deoxyhemoglobin, bilirubin, and β-carotene. Dominant absorption contrast in the visible electromagnetic spectrum arises from melanin of the epidermis and the vascular network of the dermis. The size of skin vasculature ranges from $\sim 3.5\,\mu$m in the smallest capillaries up to $\sim 100\,\mu$m of larger vessels in the mid- and deep dermis.

The theory of optoacoustic imaging was presented in section 2.4. Optoacoustic imaging relies on the principle of the photoacoustic (thermoelastic) effect that describes the generation of acoustic waves upon absorption of light in absorbing materials and was discovered over one century ago by Alexander Graham Bell. Building upon the photoacoustic effect, a detailed theory on optoacoustic signal generation was developed, relating the pressure signal measured outside of the excited sample to the light fluence, the Grüneisen parameter, and the absorption coefficient within the excited volume. Two important conditions for the excitation source arise from the theory of optoacoustics. First, to obtain optimal conversion of optical energy into acoustic energy and high resolution, the excitation pulse needs to be sufficiently short, satisfying the conditions of thermal and stress confinement. Assuming optoacoustic absorbers in biological tissue of diameter $5\,\mu$m, thermal and stress confinement dictate a pulse width of less than 3 ns. Second, the excitation source must provide sufficient energy to the sample since the optoacoustic signal strength increases with the pulse energy of the laser. To obtain an initial pressure rise in the range of 1 kPa a light fluence of $\sim 20\,\mu\mathrm{J}/\mathrm{cm}^2$ is required.

In section 2.5, the background information on the anatomy of human skin, the optical properties of human skin, and optoacoustic signal generation were merged to formulate the requirements of optoacoustic dermoscopy in terms of imaging depth and detection bandwidth. An optoacoustic atlas of human skin was created, mapping skin anatomy to the ultrasonic frequencies produced as a function of depth. Based on the simulated skin atlas, concurrent imaging of all human skin layers requires superficial detection (up to $450\,\mu$m) of frequencies > 150 MHz and detection of frequencies < 30 MHz up to a depth of 1.5 mm.

At this stage it is interesting to come back to the literature survey of state-of-the-art imaging setups in optoacoustic dermoscopy, which was performed in section 1.4.1. Although the technology of optoacoustic dermoscopy has progressed considerably in the last decade, none of the current imaging platforms allows for concurrent imaging of all human skin layers, as outlined in section 2.5.

3. Raster-scan optoacoustic mesoscopy (RSOM)

3.1. Introduction

In chapter 1, multispectral optoacoustic dermoscopy has been identified as potential biomedical imaging modality that can identify angiogenic vessels on the mesoscopic scale. In chapter 2, the requirements of imaging the entire human skin by optoacoustic mesoscopy have been defined, based on a generic model of optoacoustic absorbers in human skin. The requirements were set in terms of imaging depth and ultrasonic detection bandwidth of the detectors.

In this chapter, several experimental implementations of raster-scan optoacoustic mesoscopy (RSOM) will be introduced, aiming to fulfill the requirements specified in chapter 2 for optimal resolution and imaging depth. The introduced RSOM implementations will be used in different chapters throughout the thesis. All of the presented setups are derived from the original RSOM setup, which has been developed in our group [3, 164, 165].

3.2. Experimental setups

The general RSOM setup is illustrated in Figure 3.1. RSOM is built around a $LiNbO_3$ spherically focused ultrasound transducer, which is raster-scanned on the xy-plane. The incoming signal from the ultrasound detector is amplified by a low noise amplifier (63 dB, AU-1291, Mited Inc., Haupppauge, New York, USA) and digitized by a high-speed data acquisition (DAQ) card (CS122G1, Gage, Lockport, Illinois, USA; EON 121 G20, Gage-applied, Montreal, Canada). According to the ultrasound detector and laser source employed, the sampling frequency is chosen between $450 - 1000\,\mathrm{MS/s}$. The optimal sampling frequency for each setup will be evaluated in section 3.7.2.

To excite the sample, high energy lasers are employed, emitting nanosecond laser pulses. Depending on the specific RSOM implementation, single-wavelength or multi-wavelength lasers are used. The pulsed laser light is delivered through fiber bundles to the RSOM scan head, achieving an elliptical illumination area of approximately $4 - 40\,\mathrm{mm}^2$ at the sample surface. The light delivery system is raster-scanned in-tandem with the ultrasound detector on the xy-plane.

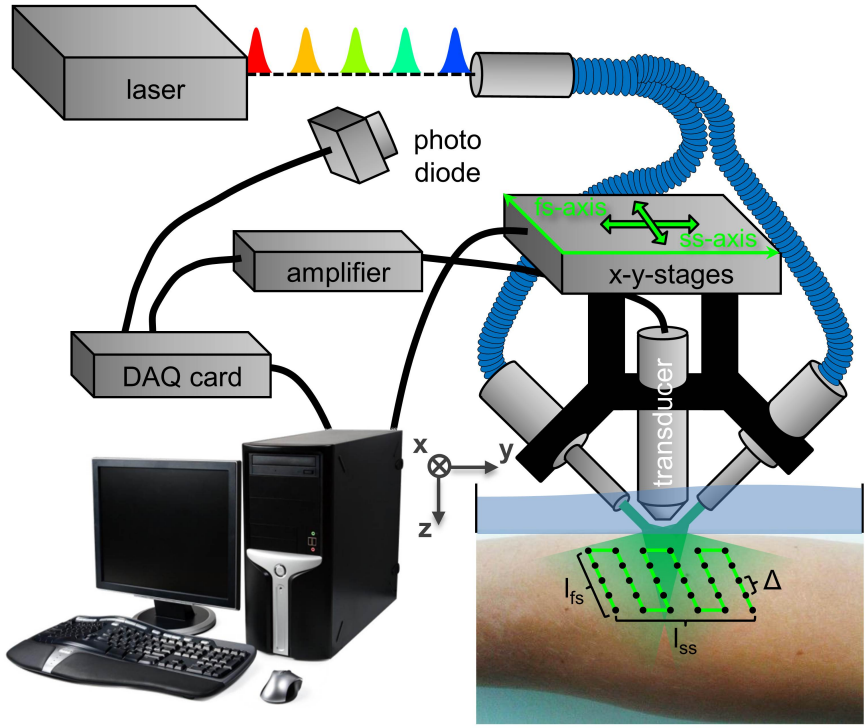

Figure 3.1.: Schematic of RSOM. The light from the laser is coupled into a fiber bundle and directed onto the sample. The illumination fibers and the ultrasound transducer are raster-scanned in-tandem in the xy-plane by two piezoelectric stages along the fast-scanning axis (fs-axis) and the slow-scanning axis (ss-axis). The ROI measures $l_{\mathrm{fs}} \times l_{\mathrm{ss}}$, and the acquisition step size is given by Δ. Reflections of the laser pulse are collected by a photo diode and trigger the acquisition of the DAQ card. The ultrasound signal captured by the transducer are amplified before digitization. The whole acquisition protocol, including navigation of the xy-stages and the digitization, is controlled by a desktop PC. The lab system denoted by the x-, y-, and z-axis will be used throughout the thesis. Adapted from Schwarz *et al.* [91] © 2016 Wiley-VCH Verlag GmbH & Co. KGaA. Reproduced with permission.

An interface unit (IU) has been designed to optimally couple the RSOM scan head to the sample. The IU serves two purposes. First, it enables ultrasonic coupling of pressure waves traveling from the sample to the detector surface. Second, the IU fixes the position of the sample throughout the scan, which is especially important in living subjects. Main component of the IU is a water reservoir with a rectangular hole, measuring approximately 18 mm × 18 mm, in its center. The rectangular hole is either sealed by a thin plastic membrane or by the subject surface itself through applying pressure. If a plastic membrane is used, an additional layer of acoustic gel between membrane and sample surface is applied to improve ultrasound coupling.

In this work, multiple implementations of RSOM will be used according to the problem at hand. In the following all of these implementations shall be introduced and discussed.

RSOM100 and RSOM50: RSOM100 uses a 98 MHz detector with an active aperture of 1.5 mm, an f-number of 1.1, and a −6 dB (−12 dB) bandwidth of 43.9 − 152.1 MHz (25 − 173 MHz). RSOM50 employs a 51.1 MHz detector, which has an active aperture

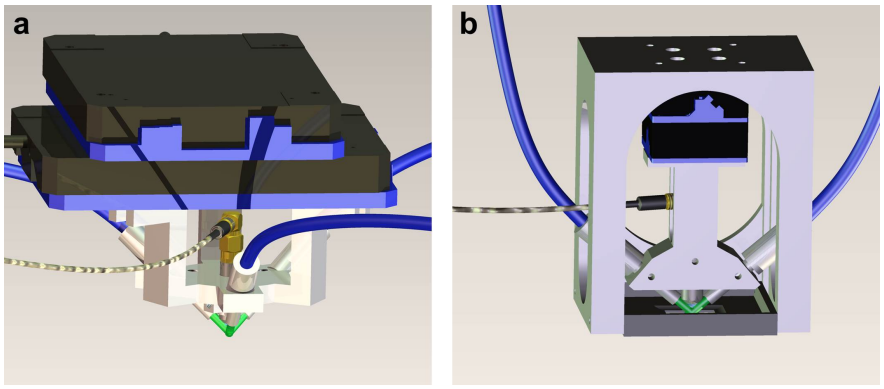

Figure 3.2.: 3D models of RSOM implementations. a) Scan head utilized in RSOM100 and RSOM50. The stationary lab setup uses an optical fiber bundle with three arms. The three fiber arms are held in place by a custom-designed holder, which is attached to two piezoelectric stages. The spherically focused detector is located in the center of the holder. **b)** Miniaturized scan head utilized in clinical RSOM55 and MSOM. To alleviate lateral forces on the small piezoelectric motors only two fibers that are arranged in a symmetric way are used. Thus, the opposing forces of the fiber bundles acting upon the piezoelectric motors cancel each other out. The holder and casing are made out of lightweight PLA.

diameter of 3 mm, an f-number of 0.99, and a −6 dB (−12 dB) bandwidth of 25.5 − 76.8 MHz (15 − 86 MHz). For fast and high-resolution raster-scans a diode-pumped solid state (DPSS) laser is used, providing < 1 ns pulses at up to 2 kHz and an energy of up to 1 mJ per pulse at a wavelength of 532 nm (Wedge HB.532, Bright-solutions, Pavia, Italy). The stationary lab setup uses an optical fiber bundle, which splits up into three arms. The three fiber arms are attached with a custom-designed-holder to two piezoelectric stages (M683,Physik Instrumente GmbH & Co. KG, Karlsruhe, Germany): travel range 50 mm, resolution 0.1 μm, maximum velocity 350 $^{\text{mm}}/_{\text{s}}$.

Clinical RSOM55: RSOM55 employs a 54.2 MHz detector, which has an active aperture diameter of 3 mm, an f number of 1, and a −6 dB (−12 dB) bandwidth of 27.9−80.5 MHz (20 − 114 MHz). The laser source in RSOM55 is the same as in RSOM100, *i.e.* a DPSS laser providing < 1 ns pulses at 532 nm and high repetition rate. To use the system in hand-held mode in the clinic, the RSOM system was miniaturized. The raster-scan is performed by two compact piezoelectric-stages (M663,Physik Instrumente GmbH & Co. KG, Karlsruhe, Germany): travel range 18 mm, resolution 0.1 μm, maximum velocity 250 $^{\text{mm}}/_{\text{s}}$. To alleviate lateral forces on the small piezoelectric motors only two fibers that are arranged in a symmetric way, are used. Thus, the opposing forces of the fiber bundles acting upon the piezoelectric motors cancel each other out. The holder and casing are made out of lightweight polylactide (PLA).

MSOM: Multispectral raster-scan optoacoustic mesoscopy (MSOM) utilizes the same detector as RSOM50, *i.e.* a 51.1 MHz detector, which has an active aperture diameter of 3 mm, an f number of 0.99, and a −6 dB (−12 dB) bandwidth of 25.5 − 76.8 MHz (15 − 86 MHz). For multispectral images the tissue is excited by a flash-lamp pumped yttrium aluminum garnet (YAG) optical parametric oscillator (OPO). An upgraded SpitLight OPO (InnoLas Laser GmbH, Krailling, Germany) emits 4 − 7 ns pulses in the spectral range from 413 − 2300 nm with a repetition rate of up to 100 Hz.

Figure 3.2 shows the scan head of the different implementations of RSOM. The stationary

lab setup depicted in Figure 3.2a utilizes large and robust piezoelectric stages that are built to withstand strong lateral forces. In the clinical setup the scan head is miniaturized to reduce both size and weight (see Figure 3.2b). The holder attached to the small piezoelectric stages and casing are printed by a 3D printer and are made out of lightweight PLA.

3.2.1. Detection bandwidth and noise-equivalent pressure

The main component of the RSOM setup is the spherically focused detector. The two most important features of the detector are bandwidth and sensitivity. The detection bandwidth determines the detectable frequencies. The noise-equivalent pressure (NEP) quantifies the minimal detectable pressure change. In the following, both the detection bandwidth and NEP will be calculated and plotted for all RSOM detectors.

To determine the detection bandwidth, data of pulse echo measurements from the manufacturer were used. The pulse echo was measured by placing acrylic glass at the focal distance of the detector in a water tank. Based on the company specifications, the detection bandwidth was calculated as follows:

$$\mathrm{BW}(f) = \frac{1}{2}\mathrm{PE}_{\mathrm{norm}} + 20\log_{10}\sqrt{\frac{V_{\mathrm{out}}}{V_{\mathrm{in}}\sqrt{R}}} \tag{3.1}$$

$$R = \left(\frac{Z_{\mathrm{ag}} - Z_{\mathrm{w}}}{Z_{\mathrm{ag}} + Z_{\mathrm{w}}}\right)^2, \tag{3.2}$$

where $\mathrm{PE}_{\mathrm{norm}}$ is the normalized detection bandwidth specified by the manufacturer, V_{in} and V_{out} are the maximal voltages of the input (emit) and output (receive) pulse respectively, and R is the reflectivity of the interface between water and acrylic glass. Multiplication of the normalized pulse echo bandwidth $\mathrm{PE}_{\mathrm{norm}}$ with the factor $1/2$ is equivalent to calculating the square root of the pulse echo bandwidth. The second term in equation (3.1) normalizes the received amplitude by the emitted amplitude taking into account the reflectivity of the water-glass interface. The reflectivity is calculated by the mismatch in the impedances of water $Z_{\mathrm{w}} = 1.483\,\mathrm{MRayl}$ and acrylic glass $Z_{\mathrm{ag}} = 3.1\,\mathrm{MRayl}$.

The NEP of a spherically focused detector can be calculated from pulse echo measurements as well. The formula is specified in [166]:

$$\mathrm{NEP}(f) = \sqrt{k_b T\left(1 + {}^{F_n}/_{\eta(f)}\right){}^{Z_w}/_{A}} \tag{3.3}$$

$$\eta(f) = \frac{2V_{\mathrm{out}}(f)}{V_{\mathrm{in}}(f)\sqrt{R}}, \tag{3.4}$$

where k_b is the Boltzmann constant, T is the absolute temperature, F_n is the noise factor of the amplifier, $\eta(f)$ is the transducer efficiency, and A is the detector surface. The transducer efficiency $\eta(f)$ is closely connected to the transducer bandpass and is calculated through pulse echo measurements.

Figure 3.3a shows the bandwidths of the three detectors employed in RSOM100, RSOM50, and RSOM55. The 100 MHz detector has a broader bandwidth but is less sensitive than the 50 MHz and 55 MHz detectors. Figure 3.3b shows the noise-equivalent pressure of all detectors. The NEP varies with frequency and is lowest at the central frequency of the detector. The NEP of the 100 MHz detector is at least two times higher compared to the 50 MHz detector, *i.e.* the 100 MHz detector is two times less sensitive.

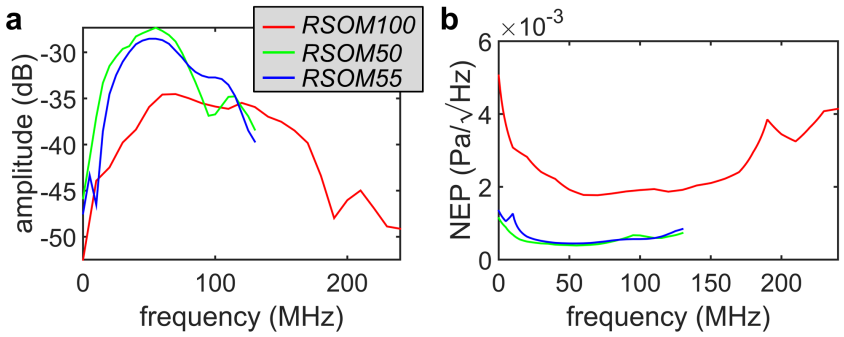

Figure 3.3.: Detection bandwidth and noise-equivalent pressure of RSOM detectors. a) Emit/receive bandwidth of different detectors used in RSOM. The bandwidth plots were calculated from pulse echo measurements (see equation (3.1)). **b)** Noise-equivalent pressure for different RSOM detectors. The 100 MHz detector has a broader bandwidth, but is less sensitive than the 50 MHz and 55 MHz detectors.

3.3. Data acquisition

RSOM uses high precision motorized stages ($< 1\,\mu$m) for the scanning process. Arising from the acquisition process, the detector-illumination unit is scanned along a fast-scanning axis (fs-axis) and a slow-scanning axis (ss-axis) (see Figure 3.1). The movement along the fs-axis is continuous, *i.e.* the stage is moving while one-dimensional (1D) depth resolved time signals are acquired at successive acquisition points. The 1D time-resolved signal acquired at each acquisition point is referred to as A-line. A 2D sinogram, referred to as B-scan, is acquired by 1D scanning of the detector along the fs-axis. After each B-scan the acquired data is transferred from the DAQ card to the PC and the detector is moved along the ss-axis to the position of the successive scan line. Thus, by scanning of the detector along both the fs-axis and the ss-axis, a stack of B-scans, *i.e.* a 3D sinogram, is acquired.

Throughout the thesis the following notation will be used. The transducer is scanned along the horizontal xy-plane, also called lateral direction. The depth is encoded by the z-axis, referred to as axial direction, since it coincides with the acoustic axis of the transducer.

The distance between neighboring acquisition points is given by the acquisition step size Δ, which is adapted according to the bandwidth and, thus, resolution of the transducer (see section 3.7.2). The detector is scanned over a 2D region measuring $l_{\mathrm{fs}} \times l_{\mathrm{ss}}$. The speed of the stage along the fs-axis is determined by the PRR of the laser and the acquisition step size Δ:

$$v_{\mathrm{fs}} = \Delta PRR \tag{3.5}$$

Stage movement and data acquisition are synchronized using MATLAB (MATLAB R2015a, The MathWorks GmbH, Ismaning, Germany) on a desktop PC.

Taking into account the PRR of the laser, the acquisition step size, and the dimension of the ROI, the acquisition time is calculated by the formula:

$$t_{\mathrm{acq}} = \frac{l_{\mathrm{fs}}}{\Delta} \frac{l_{\mathrm{ss}}}{\Delta} \frac{1}{\mathrm{PRR}} \tag{3.6}$$

For more details on hardware and software implementation of the raster-scan, the reader is referred to a previous dissertation [165].

3.4. Pre-processing of acquired data

Before the acquired raw data is reconstructed on a graphics processing unit (GPU), several pre-processing steps are applied. These processing steps are important to improve image quality and to get rid of artifacts in the reconstructed volume. The most important pre-processing steps will be explained and illustrated in the following.

3.4.1. Filtering of reflection lines

When biological tissue is illuminated by a laser source, a fraction of the laser light is reflected back onto the surface of the ultrasound transducer, where it generates a piezoelectric signal. This laser-induced signal is very strong and is reflected back and forth several times within the acoustic lens until the signal is completely attenuated. Since the speed of light is orders of magnitudes faster than the speed of sound, the recorded reflection signals always show up after the same time delay with respect to the laser pulse. Thus, when plotting neighboring A-scans versus time on a 2D image, the laser-induced reflections show up as vertical stripes (see Figure 3.5).

To get rid of these reflection stripes, a frequency filter in the Fourier space was created. The frequency filter suppresses specific frequencies that give rise to vertical stripes. The design of an appropriate Fourier domain filter can be well understood by studying the Fourier Transform of a vertical line. In mathematical terms, a vertical line along the y-axis with a full width at half maximum FWHM $= 2\sqrt{2\ln(2)}\sigma$ transforms as follows:

$$\mathcal{FFT}2\left[e^{\left(-\frac{x^2}{2\sigma^2}\right)}\right](k_x,k_y) \propto e^{\left(-\frac{k_x^2\sigma^2}{2}\right)} \cdot \delta(k_y) \tag{3.7}$$

Thus, a vertical stripe of one pixel along the y-axis shows up as horizontal line in Fourier space at $k_y = 0$. A vertical line of finite dimension transforms into a horizontal curve in Fourier space at $k_y = 0$ with decreasing amplitude towards increasing $|k_x|$. The thinner the dimension of the line along the x-axis, the broader is its spectrum along k_x (see Figure 3.4a,b).

To get rid of all vertical lines oriented along the x-axis, it would be sufficient to create a filter that sets all frequencies at k_y to zero. Such a filter would filter vertical lines of arbitrary size. However, by filtering all frequencies at $k_y = 0$ not only vertical lines are affected, but larger objects, carrying low-frequency components as well. Thus, a more sophisticated Fourier domain filter was created, which leaves the frequencies at low k_x unchanged. In mathematical terms it takes the form:

$$f(k_x,k_y) = \begin{cases} 1 & k_y \neq 0, \\ \exp\left[-\frac{k_x^2\sigma^2}{2}\right] & k_y = 0, \end{cases} \tag{3.8}$$

where σ is a parameter that can be fine-tuned in order to reliably filter out laser-induced reflection lines, while leaving low-frequency objects, e.g. large vessels, unchanged. Figure 3.4 shows the functioning of the filter presented in equation (3.8). As explained above, a thin vertical line along the y-axis contains a broad spectrum in k_x. A thicker vertical line contains mostly low-frequencies in both k_x and k_y. By primarily filtering the high frequencies in k_x at $k_y = 0$, a filter is created that almost completely filters out thin lines and keeps most of the signal from thicker lines (see Figure 3.4c, d).

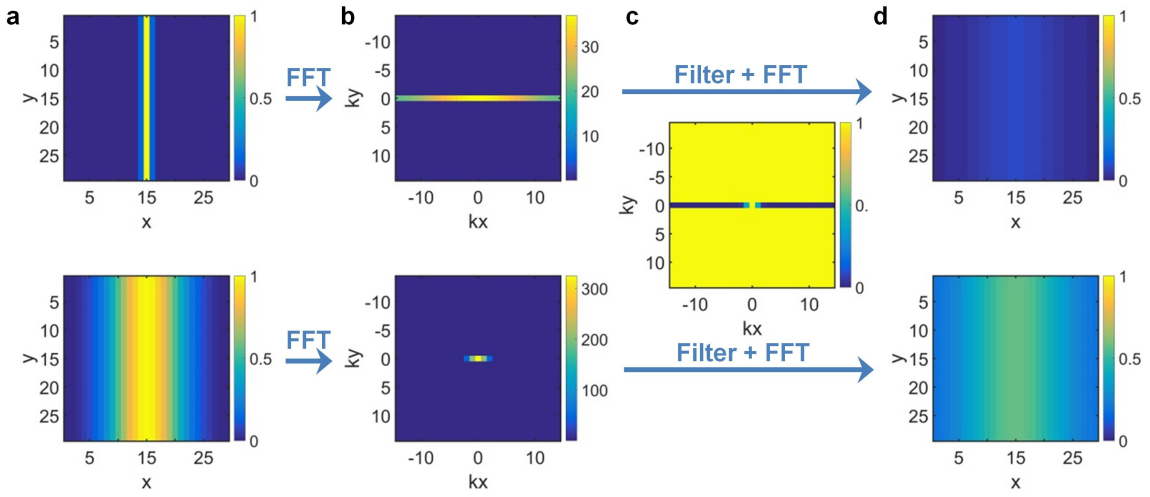

Figure 3.4.: FFT filtering of vertical lines. The upper row presents the results obtained for a thin vertical line, whereas the lower row shows data for a thicker vertical line. **a)** 2D matrix containing vertical lines oriented along the y-axis. **b)** Frequency spectrum of the 2D matrix depicted in (a). The thin vertical line along the y-axis contains a broad spectrum in k_x. The thicker vertical line contains mostly low-frequencies in both k_x and k_y. **c)** Design of FFT filter, which filters primarily the high frequencies in k_x at $k_y = 0$. **d)** 2D matrix from (a) after frequency filtering. The thin line is almost completely filtered out, whereas signal from the thicker line remains at higher amplitude.

Figure 3.5 shows the effect of the Fourier domain filter defined in equation (3.8) applied to two exemplary B-scans that were acquired by scanning the lower arm and the human palm. It is observed that the vertical reflection lines are filtered out reliably, while low-frequency signals are kept.

3.4.2. Bandpass filtering

The focused transducer used in the RSOM system is characterized by a specific detection bandwidth. Nonetheless, the signal digitized by the DAQ card contains strong low-frequency signal as well as high-frequency noise (see Figure 3.5). Thus, a digital bandpass filter is applied to the raw data to dispose of undesired frequencies. An exponential bandpass filter was designed:

$$f_{\mathrm{bp}}(f) = \left(\exp\left[-\left(\frac{f}{f_{\mathrm{high}}}\right)^{\mathcal{O}}\right]\right) \cdot \left(1 - \exp\left[-\left(\frac{f}{f_{\mathrm{low}}}\right)^{\mathcal{O}}\right]\right), \tag{3.9}$$

where f_{low} and f_{high} are the lower and upper cutoff frequencies respectively. $\mathcal{O}$ is an even integer number and represents the order of the filter. In experiments the exponential filter of order 4 was used.

Figure 3.5 shows the effect of the bandpass filter defined in equation (3.9) applied to two exemplary B-scans acquired by scanning the lower arm and the human palm. It is observed that low-frequency bands that lie outside of the transducer bandpass are filtered out. The remaining signal is mostly high-frequency signal generated by vasculature.

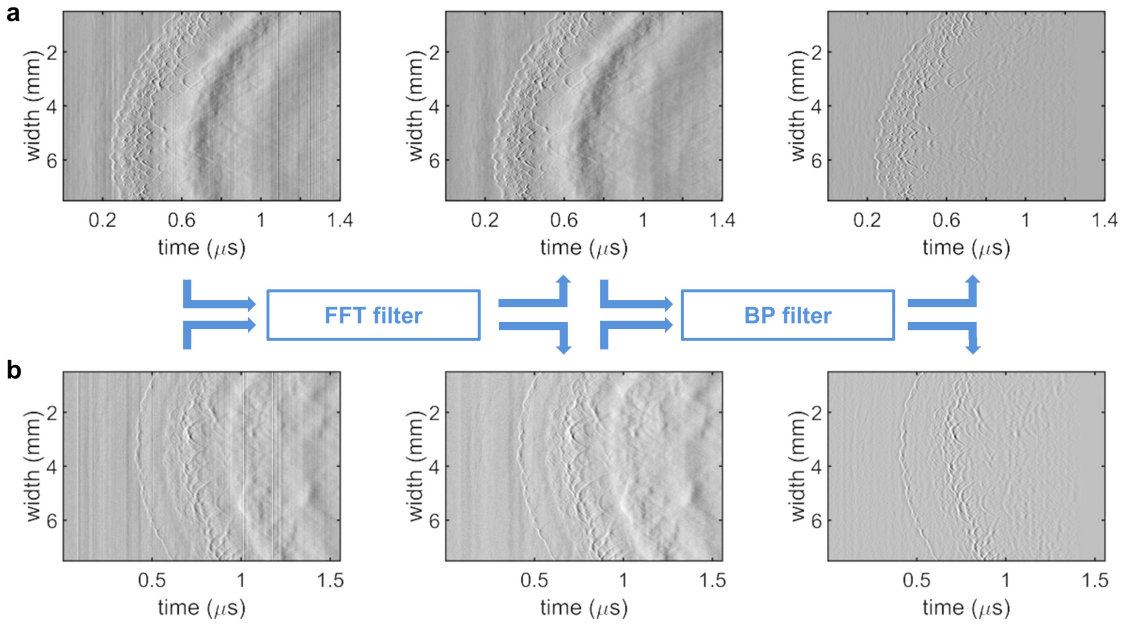

Figure 3.5.: FFT and bandpass filtering of raw data. Effects of FFT filtering and bandpass filtering are visualized for **a)** a single B-scan acquired at the lower arm and for **b)** a single B-scan acquired at the human palm. The first column shows the unprocessed B-scan. Column 2 depicts the B-scan after the vertical reflections lines, caused by the laser, are filtered by the FFT filter presented in equation (3.8). The third column shows the B-scans filtered additionally by a bandpass filter, defined in equation (3.9).

3.4.3. Co-registration of scanning directions

The transducer is scanned along a check board pattern (see Figure 3.1). Subsequent B-scans are acquired in opposing directions. Due to inertia, the micro-positioning stages do not accelerate instantaneously after the turning point. For this reason, the transducer position along the two scanning positions have a small offset (see Figure 3.6a) and must be calibrated for accurate reconstructions. Instead of using a tedious and expensive hardware solution, an automated offset calibration between the two scanning directions has been implemented, using co-registration of subsequent B-scans. This method is based on the assumption that strongly absorbing anatomical landmarks that are visible in one B-scan are expected to be present in close proximity in neighboring B-scan as well. By calculating the maximum of the co-registration map between neighboring B-scans, the offset between the two scanning directions is calculated reliably. Figure 3.6b depicts the overlay of B-scans acquired along the two scanning directions after co-registration. Since both scanning directions are well aligned, the raw signal carries the color yellow, which is the overlay of red and green.

3.5. Three-dimensional reconstruction algorithm

After pre-processing the recorded raw data, the processed data is reconstructed to form a 3D image. The reconstruction algorithm needs to be time efficient and must be adapted to the specific scanning and detector geometry. The algorithm presented herein is based on the universal back-projection algorithm for optoacoustic tomography [167], which will

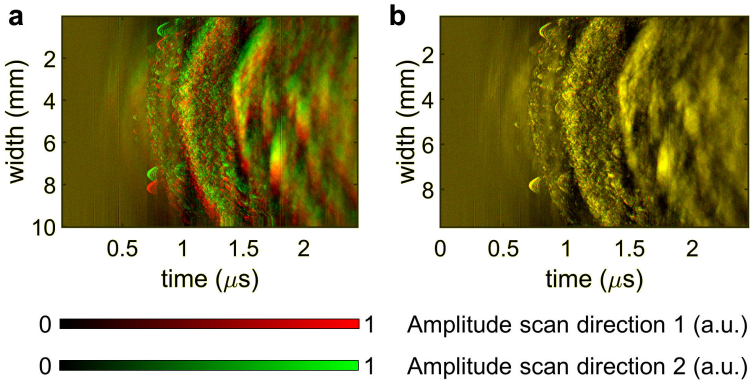

Figure 3.6.: Co-registration of B-scans along the two scanning directions. a) Overlay of a stack of B-scans acquired along scanning direction 1 (red channel) and along scanning direction 2 (green channel). Due to inertia, the scanning head is not accelerated instantaneously and there is a small offset in the position between the two scanning directions. **b)** Overlay of a stack of B-scans acquired along scanning direction 1 (red channel) and along scanning direction 2 (green channel) after the shift has been extracted and corrected for by co-registration. Yellow color signifies perfect overlay since it is the mixing color of red and green.

be introduced in section 3.5.1. Building upon a generalized idea of the back-projection algorithm, a specifically adapted back-projection algorithm will be presented thereafter.

3.5.1. Universal back-projection algorithm

In section 2.4, the theory of optoacoustic signal generation has been introduced to the reader. Based on the assumption of a homogeneous, isotropic, liquid-like medium under the conditions of thermal confinement and stress confinement, the forward solution for the propagation of acoustic waves through tissue was presented (see equation (2.23)). Optoacoustic tomography is faced by the inverse problem: Given a temporal pressure distribution $p(\vec{r}_{\mathrm{us}}, t)$ recorded outside of a ROI at multiple detector positions $\vec{r}_{\mathrm{us}}$, the initial pressure distribution inside the ROI must be tomographically reconstructed. Based on three common geometries, an exact reconstruction formula has been presented [167]. The exact reconstruction formula relies on ideal conditions:

Thermal and stress confinement: The condition of thermal and stress confinement has been explained in detail in section 2.4. Essentially, impulse heating is assumed, which gives rise to a precise initial pressure distribution $\Delta p_0(\vec{r})$.

Homogeneous, isotropic, liquid-like medium: Acoustic absorption and variations in sound speed and density inside a heterogeneous tissue are not accounted for. To the best of our knowledge, an analytic solution for a heterogeneous medium is not known. Typically, the forward solution of sound propagation in a heterogeneous medium is simulated numerically.

Infinite detection aperture: The derivation of the universal back-projection formula is based on three ideal geometries: a full spherical surface, an infinitely long cylinder, and an infinitesimally large plane. It is assumed that the spherical surface and the cylinder

entirely enclose the ROI, covering a solid angle of $\Omega_{\mathrm{us}} = 4\pi$. In the case of the infinitesimal plane the ROI is located on one side of the plane, covering a solid angle of $\Omega_{\mathrm{us}} = 2\pi$. Apart from the angular coverage, an exact reconstruction relies on an infinitesimally dense grid of point detectors, *i.e.* even in the case of the finite spherical surface, an infinite number of detectors is needed.

Point-like detectors: Point-like detectors are infinitesimally small and have omnidirectional sensitivity.

Detectors of infinite bandwidth: An infinite bandwidth allows for the detection of all acoustic frequencies, providing infinite resolution.

Neglecting acoustic attenuation and light fluence distribution: Acoustic and light fluence attenuation in biological tissue limit the imaging depth and resolution. The universal back-projection algorithm does not account for acoustic and light attenuation.

Based on these assumptions, the exact reconstruction of the original pressure distribution $\Delta p_0(\vec{r})$ is given by:

$$\begin{aligned} \Delta p_0(\vec{r}) &= \iint_{\Omega_{\mathrm{us}}} \frac{d\Omega_{\mathrm{us}}}{\Omega_{\mathrm{us}}} b(\vec{r}_{\mathrm{us}}, t_{\mathrm{sp}} = |\vec{r} - \vec{r}_{\mathrm{us}}|) \\ b(\vec{r}_{\mathrm{us}}, t_{\mathrm{sp}}) &= 2p(\vec{r}_{\mathrm{us}}, t_{\mathrm{sp}}) - 2t_{\mathrm{sp}} \frac{\partial p(\vec{r}_{\mathrm{us}}, t_{\mathrm{sp}})}{\partial t_{\mathrm{sp}}} \\ d\Omega_{\mathrm{us}} &= \frac{dS_{\mathrm{us}}}{|\vec{r} - \vec{r}_{\mathrm{us}}|^2} \cdot \left(\vec{n}_{\mathrm{us}} \cdot \frac{\vec{r} - \vec{r}_{\mathrm{us}}}{|\vec{r} - \vec{r}_{\mathrm{us}}|} \right) \end{aligned} \tag{3.10}$$

where $t_{\mathrm{sp}} = v_s t$ is the time coordinate transformed to space coordinates, $\vec{r}_{\mathrm{us}}$ is a vector pointing to the detector surface, and $b(\vec{r}_{\mathrm{us}}, t_{\mathrm{sp}})$ is the back-projection term. It consists of two parts. The first term is the direct pressure term and the second term comprises the derivative term weighted by the distance between the transducer and the source. The derivative in time domain corresponds to a ramp filter in frequency domain. For a source point $\vec{r}$ close to the transducer surface the direct term dominates, for points far from the transducer surface the derivative term dominates. $d\Omega_{\mathrm{us}}/\Omega_{\mathrm{us}}$ is the normalized solid angle of the detection element dS_{us} with respect to the reconstruction point. It can be understood as a weighting factor that takes into account how much of the original wave front could have possibly reached the surface of the detection element. Figure 3.7 schematically illustrates the main elements of equation (3.10).

3.5.2. General discrete back-projection formula

Under realistic conditions, a bandwidth-limited transducer with finite detection aperture is scanned in a discrete manner over a detection surface that is usually smaller than 2π. In general, there is a set of N ultrasound transducer positions $\vec{r}_i$, $i = \{1, 2, 3, ..., N\}$ that record the time varying pressure signal $p(\vec{r}_i, t_j)$ at predefined time points t_j. In this case, a generalized discrete back-projection formula can be formulated as follows:

$$\Delta p_0(\vec{r}) = \sum_{i=1}^{N} W_i(\vec{r}) \cdot b(\vec{r}_i, \mathrm{NN}(t_{\mathrm{sp},j}; |\vec{r} - \vec{r}_i|)) \tag{3.11}$$

where $W_i(\vec{r})$ is a weighting factor and $\mathrm{NN}(t_{\mathrm{sp},j}; |\vec{r} - \vec{r}_i|)$ calculates the nearest time point $t_{\mathrm{sp},j}$ based on the relative position between the source and the detector.

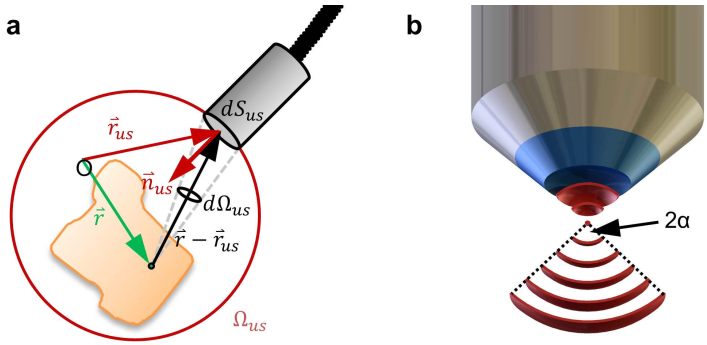

Figure 3.7.: Concept of universal back-projection and virtual point detector. a) Schematic of main elements in the universal back-projection formula (3.10). $\vec{r}$ is the position vector of a point within the absorbing structure. $\vec{r}_{\mathrm{us}}$ is a vector pointing to the detector surface. $d\Omega_{\mathrm{us}}$ is the solid angle of the detection element dS_{us} with respect to $\vec{r}-\vec{r}_{\mathrm{us}}$. $\vec{n}_{\mathrm{us}}$ indicates the vector normal to the detector surface and Ω_{us} indicates the detection aperture covering the full solid angle. **b)** Concept of the virtual point detector. The acoustic lens (blue) of the detector focuses the acoustic waves (red) onto a focal point. The acoustic focus acts as a virtual point detector with detection angle 2α.

In literature, the so called synthetic aperture focusing technique (SAFT) algorithm has been used for reconstruction [168, 169]. In essence, SAFT and back-projection belong to the same class of algorithms that consist of delay-and-sum. The generalized discrete back-projection formula (3.11) is a more generalized form of a SAFT algorithm. In contrast to original SAFT, the generalized equation (3.11) allows for more sophisticated back-projections terms, comprising more than the direct term and improved beam-forming.

The reconstruction algorithm presented in the following builds upon the generalized back-projection formula presented in equation (3.11). To do so, the weighting factor $W_i(\vec{r})$ and the back-projection term will be further specified in sections 3.5.3 and 3.5.4 respectively.

3.5.3. Beam-forming

RSOM uses strongly focused high-frequency transducers. For such detectors the focal point of the detector acts as a virtual finite point detector [168] with a limited detection angle. Figure 3.7b illustrates the concept of virtual point detectors. The acoustic lens of the detector focuses the acoustic wave front originating from the piezoelectric element onto a focal point. The acoustic focus acts as a virtual point detector with a detection angle of 2α.

Virtual detector transformation

Since the focal point of the detector is the symmetry point of the virtual detector, it is useful to perform a transformation in time:

$$\vec{t}_{\mathrm{sp}} = \left(\vec{t} - t_{\mathrm{foc}}\right) v_s \tag{3.12}$$

where $\vec{t}$ is the time vector representing the sampled time points, and t_{foc} is the time delay of the focal point with respect to the laser trigger. Equation (3.12) not only shifts the focal point to zero but transforms the time delay into a spatial delay.

Figure 3.8a illustrates the cone-shaped sensitivity field (SF). The focal point located at the tip of the two opposing cones is infinitesimally small.

Hyperbolic focal zone

Figure 3.7b illustrates the general idea of the virtual point detector. In reality, the focal point is not a perfect point but is well approximated by a hyperbola:

$$\begin{aligned} 1 &= \left(\frac{r}{a}\right)^2 - \left(\frac{z}{b}\right)^2 \\ a &= \frac{1}{2} D_{\text{foc}} \\ b &= \left(\frac{2F_{\text{td}}}{D_{\text{td}}}\right) a \end{aligned} \tag{3.13}$$

where r is the radius of the SF, and z is the vertical distance from the focal point, defining the hyperbola parameters a and b. F_{td} is the focal length of the detector, and D_{td} is the diameter of the active element. The lateral width of the focal zone is approximated by the formula given in [170]:

$$D_{\text{foc}} = 1.02 \frac{v_s}{1/2 (f_{\text{high}} + f_{\text{low}})} \frac{F_{\text{td}}}{D_{\text{td}}} \tag{3.14}$$

where f_{high} and f_{low} are the upper and lower boundary of the detection bandwidth of the transducer respectively. Equation (3.14) shows that the width of the focal zone and, thus, the width of the SF depends on the recorded frequencies of the detector. The higher the frequencies, the smaller the lateral width of the focal zone is. Figure 3.8d illustrates the hyperbolic approximation of the focal zone. As a result, the virtual point detector becomes a virtual point detector of finite size (see Figure 3.8b).

Sensitivity field simulation

To overcome the binary weighting of the sensitivity field, the real sensitivity of the detector is simulated. The detector's sensitivity is strongly related to the spatial impulse response (SIR) of the detector. For an arbitrary point $\vec{r}$ in space the SIR is calculated by integrating delta impulses $\delta(t)$ over the detector surface:

$$\text{SIR}(t_{\text{sp}}, \vec{r}) = \int_S \left(\frac{\delta(t_{\text{sp}} - |\vec{r}_{\text{us}} - \vec{r}|)}{|\vec{r}_{\text{us}} - \vec{r}|} d\vec{S}(\vec{r}_{\text{us}}) \right) \tag{3.15}$$

where $\vec{r}_{\text{us}}$ is the position of the infinitesimally small detector surface element and $d\vec{S}(\vec{r}_{\text{us}})$ the directed surface area.

Optoacoustic signals detected by the ultrasound transducer will be further filtered by the detection bandwidth of the detector. Thus, to calculate the SF of the detector the SIR from equation (3.15) must be convoluted by a generic bandwidth-limited broadband ultrasound signal. As in section 2.5 the analytic formula for a circular absorber of radius a is used [148]:

$$p_{\text{gen}}(t_{\text{sp}}; a) = \frac{R - t_{\text{sp}}}{2R} \cdot H(a - |R - t_{\text{sp}}|), \tag{3.16}$$

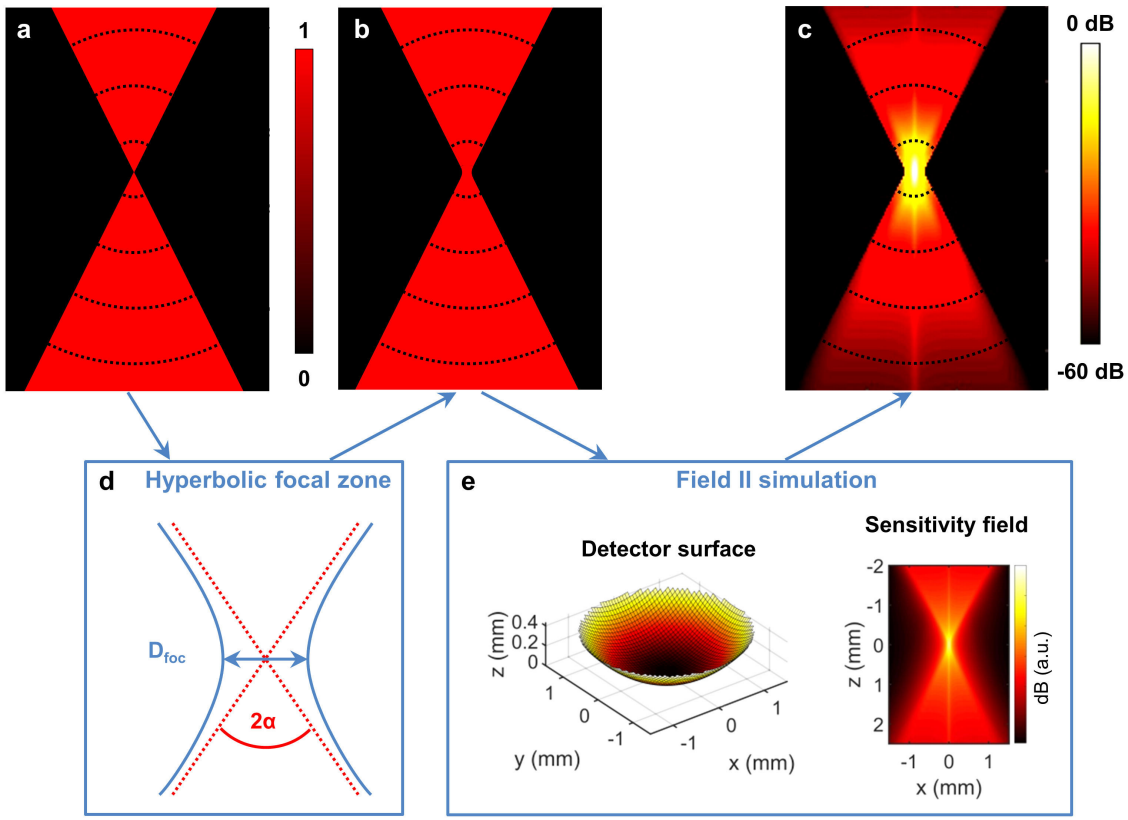

Figure 3.8.: Beam-forming in RSOM. a) Simplified model of a virtual point detector with limited detection angle. The SF is modeled by a binary map, taking the value 1 within the cone-shaped detection angle and 0 outside. **b)** To compensate for the finite focal width of the acoustic focus of the detector, the outline of the SF is modeled by a hyperbola according to equation (3.13). The SF is still binary. **c)** In a second step the binary weighting of the SF is replaced by a 3D weighting function obtained from Field II simulations. All values outside of the hyperbola-shaped area (b) are set to zero ($-\infty$, black area). **d)** Schematic of the hyperbolas mimicking the width of the focal zone. In the focus, the focal diameter takes the value D_{foc}. **e)** To calculate the sensitivity field of the detector, the detector surface is modeled by finite elements on a curved surface with focal distance F_{td}. In Field II simulations, the signal is averaged over the detector surface.

where $H(x)$ is the Heaviside step function, and R specifies the distance between the source and the absorber. According to [171] the frequency peak of the time signal in equation (3.16) is located at $f_{\mathrm{max}} = 0.8\,{}^{v_s}/_{2a}$. Thus, to mimic a realistic broadband optoacoustic source, the radius of the circular absorber is set to $a = 0.8 \cdot v_s/(f_{\mathrm{high}} + f_{\mathrm{low}})$.

Finally the sensitivity field of the detector is estimated by the peak-to-peak amplitude of the convoluted SIR:

$$\mathrm{SF}(\vec{r}) = \max(\mathrm{SIR}(t_{\mathrm{sp}}, \vec{r}) * p_{\mathrm{gen}}(t_{\mathrm{sp}})) - \min(\mathrm{SIR}(t_{\mathrm{sp}}, \vec{r}) * p_{\mathrm{gen}}(t_{\mathrm{sp}})) \tag{3.17}$$

To model the spatially-varying and frequency-dependent sensitivity field of the focused ultrasound detector, Field II simulations were performed [172], based on equation (3.17). The detector surface was modeled by N finite elements, the width of each element measuring ${}^{D_{\mathrm{td}}}/_{50}$. To mimic acoustic focusing of the acoustic lens, a concave detector surface was

simulated with the focal length given by the detector characteristics in section 3.2 (see Figure 3.8e). Figure 3.8c,e show a 2D cut through the sensitivity field $SF(\vec{r})$, which varies both in space and with the frequency content of the ultrasound signal [173]. The angular dependence and amplitude of the SF stems from the finite size of the virtual detector. Ultrasound waves emitted by an optoacoustic absorber will reach different areas of the detector surface at different time. The resulting detector response is an average over the whole detector surface.

Figure 3.8c illustrates a cut through the final weighting factor $W_i(\vec{r})$ in equation (3.11) that is used in the reconstruction.

3.5.4. Back-projection term

As can be seen from equation (3.10) and equation (3.11), the back-projection term consists of two components:

$$b(t_{\mathrm{sp}}) = \left[b \cdot p(t_{\mathrm{sp}}) - t_{\mathrm{sp}} \frac{\partial p(t_{\mathrm{sp}})}{\partial t_{\mathrm{sp}}} \right]_{t_{\mathrm{sp}}=|\vec{r}-\vec{r_i}|}, \tag{3.18}$$

where $p(t_{\mathrm{sp}})$ is the directly recorded time signal multiplied by a ratio parameter b, and the second term is the derivative of the time signal weighted by the distance to the virtual detector. A quick estimation explains, which of the two terms is expected to dominate. Since the model optoacoustic signal has the form of an N-shape (see equation (2.24)), the pressure changes Δp are of the order $\mathcal{O}(p)$. The time it takes for the pressure to change is inversely proportional to the central frequency of the detector $\Delta t \approx 1/f_c$. Hence, the direct term is expected to dominate at the focal zone, for $-b\, v_s/f_c < t_{\mathrm{sp}} < b\, v_s/f_c$. In the universal back-projection formula, the ratio parameter b takes the value $b = 1$. However, the angular coverage of the focused ultrasound detector is smaller than the solid angle 4π of a full sphere. Thus, the energy of the ultrasonic wave outside of the focal zone is restricted to a smaller region, and b is estimated by the ratio of the half solid angle 2π to the solid angle of the opening cone, *i.e.*:

$$b = \frac{\Omega}{2\pi} = \frac{4\pi \sin^2(0.5\alpha)}{2\pi} = \frac{4\pi \sin^2[0.5 \tan^{-1}\left(\frac{D_{\mathrm{td}}}{F_{\mathrm{td}}}\right)]}{2\pi} \tag{3.19}$$

For the 100 MHz detector, equation (3.19) yields $b \approx 11.2$, and for the 50 MHz detector equation (3.19) yields $b \approx 9.5$. Thus, for the 100 MHz detector the derivative term dominates for $|t_{\mathrm{sp}}| > 168\,\mu$m, and in the case of the 50 MHz detector the derivative term dominates for $|t_{\mathrm{sp}}| > 285\,\mu$m.

Experimental measurements in section 3.7.3 confirm that the signal amplitude of the focal zone and outside of the focal zone are nicely balanced by setting an appropriate ratio parameter b.

3.5.5. Implementation of the algorithm on the GPU

The advantage of the back-projection formula introduced in section 3.5.3 is its linearity, *i.e.* each voxel value can be calculated independently and may be calculated in parallel on a GPU. Parallel reconstruction speeds up the reconstruction significantly. To implement the back-projection algorithm presented in section 3.5.3, the resources of the GPU must be taken into account. The most critical part of the GPU implementation is optimized memory usage.

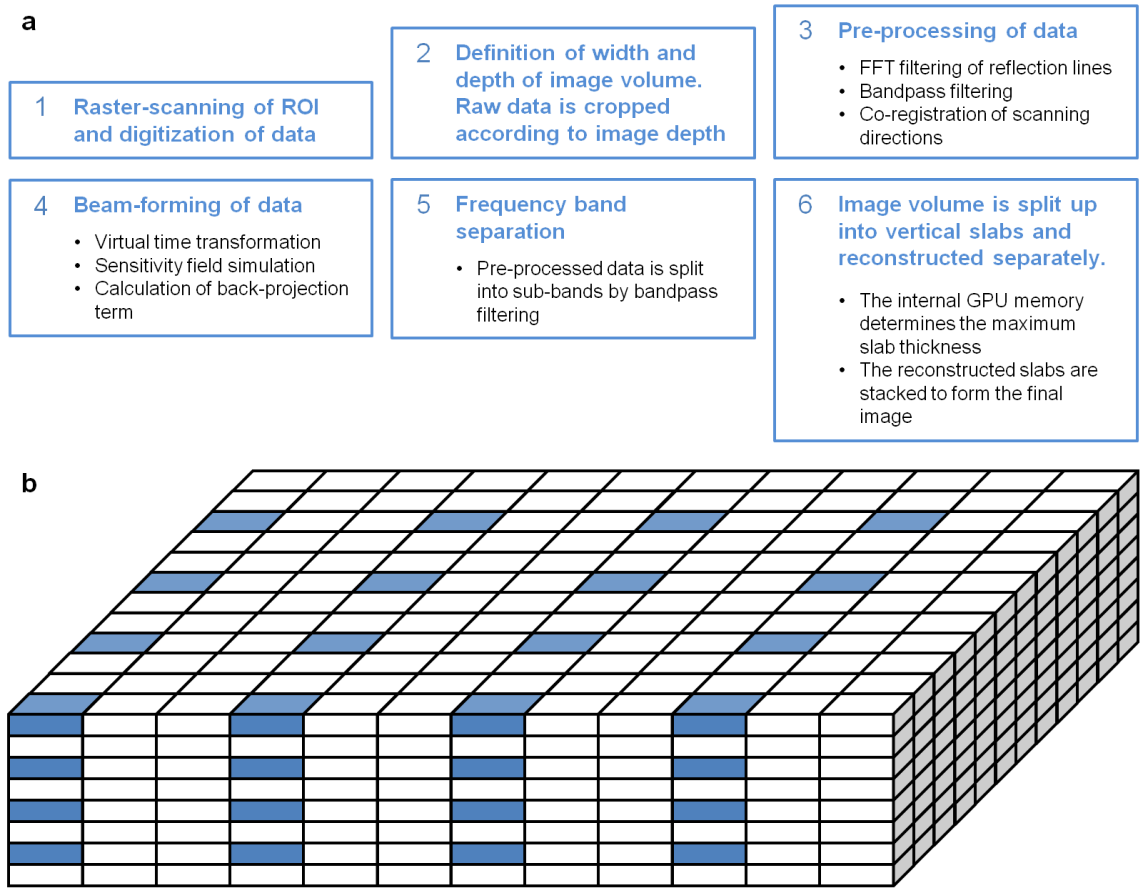

Figure 3.9.: Implementation of the reconstruction algorithm. a) Workflow of data processing, starting from the acquisition of raw data to the reconstruction on the GPU. **b)** Illustration of parallel reconstruction of voxels on the GPU for an exemplary block size of $4 \times 4 \times 4$. The blue voxels correspond to image grid points within a vertical slab that are reconstructed in parallel.

Every upload of data and download of results is restricted by a limited data transfer time. The less data transfer and memory access between PC and GPU, the faster is the algorithm. Since the memory size on the GPU is limited, the reconstruction volume must be split up into thinner slices.

The schematic of the implemented reconstruction algorithm is illustrated in Figure 3.9a. First, the ROI is raster-scanned and the data is digitized. Second, to minimize memory, the time signal is cropped according to the desired image depth. Third, the raw data is filtered and pre-processed according to the steps presented in section 3.4. Fourth, the weighting factor and back-projection term are calculated for the corresponding geometry according to sections 3.5.3 and 3.5.4. Fifth, the filtered raw data is split into sub-bands to improve the visibility of small structures (see section 3.6). Sixth, depending on the internal memory capacity of the GPU, the 3D volume is split into thinner vertical slabs, which are reconstructed successively. The larger the lateral size of the ROI, the thinner the vertical slabs. Each vertical slab is reconstructed independently and only the required raw data is loaded onto the GPU, *i.e.* the time signals are cropped to the required slab thickness. Within the vertical slab a block of $9 \times 9 \times 9$ voxels is reconstructed in parallel on the GPU. Figure 3.9b illustrates the distribution of voxels within a slab that are reconstructed in parallel. The voxels are

distributed in space to minimize readouts of the same memory spaces by multiple kernels in parallel, since conflicting memory readouts slow down the reconstruction time. The block size of $9 \times 9 \times 9$ is optimized for the GeForce GTX 780 graphics card. If a different GPU is used, the block size may be adapted. On the GPU each voxel is reconstructed separately. Only, those voxels lying within the hyperbolic sensitivity field are updated. Finally, after each vertical slab has been reconstructed on the GPU, all of the slabs are stacked together to form the complete 3D reconstruction matrix.

3.6. Bandwidth separation for improved imaging performance

Because of the ultra-wide bandwidth of the employed detectors, the reception bandwidth was divided into several smaller sub-bands [164, 174]. In this way, images are reconstructed using a sequential narrow band inversion (SNBI), which inverts the low frequencies separately from the high frequencies. Throughout the thesis, a 2-band split is used; however, a finer band reconstruction can be implemented. The advantage of SNBI is that each frequency band is reconstructed with parameters better suited to the signal-to-noise characteristics of the band. By also rendering the different reconstructed bands in different colors [164], the resulting image allows for a better representation of the high frequencies (smaller structures) avoiding their masking by the low frequencies on the final reconstruction. To assure that no ringing effects appear from filtering, the frequencies are divided in such a way, that the relative bandwidth is kept constant for all the sub-bands:

$$\frac{\mathrm{BW}_1}{f_{c_1}} = \frac{\mathrm{BW}_2}{f_{c_2}} \tag{3.20}$$

For all RSOM setups described in section 3.2, the reception bandwidth was split into 2 sub-bands with 100% relative bandwidth. After choosing the value of the relative bandwidths and the first cutoff frequency, the successive cutoff frequency is determined by:

$$f_2 = \frac{2 + \mathrm{BW}_{\%}}{2 - \mathrm{BW}_{\%}} f_1, \tag{3.21}$$

where f_1 and f_2 are the first and second cutoff frequencies, and $\mathrm{BW}_{\%}$ characterizes the relative bandwidth of each sub-band.

Throughout this work, the same color-coding is used, where red represents the reconstruction of the low frequencies, and green represents high frequencies:

RSOM100: red: $20 - 60\,\mathrm{MHz}$, green: $60 - 180\,\mathrm{MHz}$.

RSOM50: red: $10 - 30\,\mathrm{MHz}$, green: $30 - 90\,\mathrm{MHz}$.

RSOM55: red: $14 - 42\,\mathrm{MHz}$, green: $42 - 126\,\mathrm{MHz}$.

3.7. Optimization of acquisition and reconstruction parameters

To a large extend, the image quality depends on the characteristics of the experimental setup, *i.e.* excitation wavelength, light delivery system, detector bandwidth, and detector

sensitivity. Given the scan geometry and detector characteristics an estimation of the resolution can be calculated analytically [175]. Apart from system design, the image quality depends on several parameters of the acquisition and reconstruction protocol, most importantly spatial and temporal sampling of the acquisition and the reconstruction grid. From an image quality point of view, dense spatial and temporal sampling of both the acquisition and the reconstruction grids are advantageous. However, oversampling affects acquisition and reconstruction times and results in excessive memory consumption. Thus, for fast and high-quality imaging optimal sampling is beneficial. Apart from optimizing the acquisition and reconstruction grids, appropriate beam-forming and modeling of the synthetic aperture affect image quality. In the following the performance of the reconstruction results with respect to acquisition and reconstruction parameters will be analyzed experimentally.

3.7.1. Experimental evaluation of optimal sampling

To test the optimal settings for acquisition step size, temporal sampling, voxel size, and reconstruction mode an experimental approach has been carried out. For this reason a sample containing two nylon sutures measuring approximately 15 μm in diameter was prepared. The suture was fixed on both sides on 5 mm high platforms located within a water tank. The sutures were slightly tilted with respect to the acoustic axis of the transducer in order to cover a depth range of $-20\,\mu$m to $460\,\mu$m with respect to the focal point of the transducer. The sample was acquired with both RSOM100 and RSOM50. To avoid redundant results, only RSOM50 data will be presented in this section.

To investigate optimal settings for spatial and temporal sampling, a phantom sample was acquired and reconstructed at different sampling parameters. Image quality of the reconstructed volumes was quantified by three parameters, *i.e.* the axial width of the sutures, the lateral width of the sutures, and the contrast-to-noise (CNR) ratio of the sutures on the final images. The original scan was acquired with RSOM50, using a step size of 15 μm and a sampling rate of 500 MHz. The two sutures were scanned over a region of interest of 9 mm $\times$ 5 mm. Undersampling of the data was simulated by omitting recorded data points. More details on the methodology is given in the corresponding subsections of section 3.7.2. The processed raw data was reconstructed with the 3D beam-forming algorithm presented in section 3.5.

To calculate the axial width of the two sutures, the following procedure was followed. First, a maximum amplitude projection (MAP) along the x-axis (fs-axis) was performed, resulting in a 2D projection of the sutures in the yz-plane:

$$R_{yz}(i_y, i_z) = \max_{i_x=1}^{N_x} \left[R(i_x, i_y, i_z)\right] \tag{3.22}$$

where $R(i_x, i_y, i_z)$, $i_x = \{1, 2, 3, \ldots, N_x\}$, $i_y = \{1, 2, 3, \ldots, N_y\}$, $i_z = \{1, 2, 3, \ldots, N_z\}$ is the 3D matrix representing the reconstructed volume, and N_x, N_y, and N_z are the number of voxels along the x-, y-, and z-axis, respectively. For every position i_y the full width at half maximum (FWHM) of the two sutures was evaluated by extracting the two highest peaks by the built-in MATLAB (MATLAB R2015a) function "findpeaks". The FWHM of the two sutures was stored in a 1D vector $\mathrm{FWHM}_{\mathrm{ax}}(i_y)$, which was visualized in boxplots.

To calculate the lateral width of the two sutures, a similar procedure was followed. First, a maximum amplitude projection (MAP) along the z-axis was performed, resulting in a 2D

projection $R_{xy}(i_x, i_y)$ of the sutures in the xy-plane. The lateral width of the two sutures was evaluated by extracting the two highest peaks by the built-in MATLAB function"findpeaks" at every position i_y. The FWHM of the two sutures was stored in a 1D vector $\mathrm{FWHM}_{\mathrm{lat}}(i_y)$.

The contrast-to-noise ratio was calculated from the lateral profiles of the sutures. The maximum amplitude of the lateral profile was calculated for each position i_y and stored in a 1D vector $\mathrm{max}_{\mathrm{peak}}(i_y)$. The noise at every position i_y was calculated by the standard deviation of a neighboring image region containing only background signal and stored in a 1D vector $\mathrm{std}_{\mathrm{bg}}(i_y)$. Consequently, the CNR of the sutures was evaluated by the following formula:

$$\mathrm{CNR}(i_y) = 20\log_{10}\left(\frac{\mathrm{max}_{\mathrm{peak}}(i_y)}{\mathrm{std}_{\mathrm{bg}}(i_y)}\right) \tag{3.23}$$

3.7.2. Spatial and temporal sampling

Image quality is significantly affected by spatial and temporal sampling of both the acquisition grid and the reconstruction grid. In general, to avoid aliasing the spatial sampling period should be less than half of the resolution of the sensing aperture. [176]. "The sensing aperture size of the detector limits the lateral resolution while the temporal-frequency bandwidth affects both axial and lateral resolution." [177].

In this section, optimal sampling criteria will be established for RSOM for both acquisition and reconstruction grid.

Nyquist-Shannon sampling criterion

The theory on optimal sampling is based on the Nyquist-Shannon sampling criterion. It has to be applied to three different parts in the acquisition/reconstruction procedure. First, temporal sampling of the DAQ card. Second, spatial sampling of the acquisition step size. Third, spatial sampling of the reconstruction grid. In theory, the sampling frequency should be larger than twice the largest detectable frequency. Thus, temporal sampling in RSOM50 should be digitized at a frequency larger than $2f_{\mathrm{max}} \approx 172\,\mathrm{MHz}$. However, the theory relies on infinitely many samples with a perfect low pass filter at f_{max}.

In practice, there is a finite number of samples, and there is no perfect analog lowpass filter. That is why a sampling rate of at least $2.2\,\mathrm{f}_{\mathrm{max}}$ is recommended. Oversampling is often used if the effective bandwidth is close to half of the sampling frequency. The larger the bandwidth, the higher has to be the quality of the analog filter (transition steepness). The higher the oversampling, the less requirements are needed for the lowpass. Typically, the data is oversampled by a factor of 2 or 4. Due to the ultra-wide-band characteristics of RSOM detectors (see section 3), oversampling is an important factor in the acquisition and reconstruction process. Thus, taking into account a sampling rate of $2.2\,\mathrm{f}_{\mathrm{max}}$ and an additional oversampling factor of 2, RSOM50 should, in theory, employ a sampling frequency of at least $f_{\mathrm{samp}} = 378\,\mathrm{MHz}$.

Analogously, the acquisition step size and resolution grid size should be chosen such that it is lower or equal to $2-2.5$ times the spatial resolution of the system. Hence, if the resolution of the system is given as $(\mathrm{res}_z, \mathrm{res}_x, \mathrm{res}_y) = (7.5, 25, 25)\,\mu\mathrm{m}$ and a rate of 2.5 is used, the reconstruction voxel size should not exceed $(\Delta_z, \Delta_x, \Delta_y) = (3, 10, 10)\,\mu\mathrm{m}$.

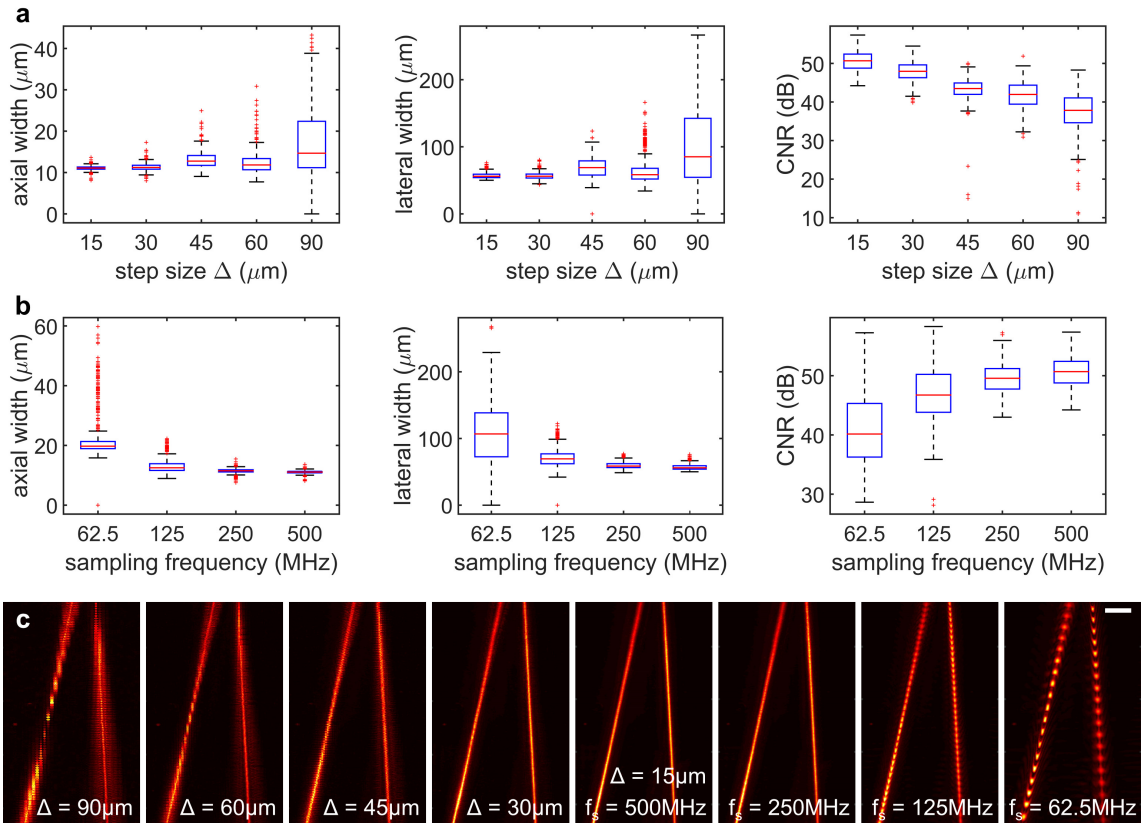

Figure 3.10.: Resolution and contrast as a function of the acquisition step size and the sampling frequency. Data points were obtained from the reconstruction of two 9 mm long sutures according to the processing steps outlined in section 3.7.1 and equation (3.24)-(3.25). The number of data points evaluated in every boxplot is $n = 504$. **a)** Boxplot of axial with, lateral width, and CNR at varying acquisition step size. The mean and standard deviation of axial and lateral width increase with the step size, the CNR decreases. **b)** Boxplot of axial with, lateral width, and CNR at varying sampling frequency. The mean and standard deviation of axial and lateral width decrease with increasing sampling frequency, the CNR increases with higher sampling frequency. **c)** Lateral MAPs (top view) of the two sutures at variable acquisition step size and sampling frequency. Aliasing effects are observed for $\Delta > 30\,\mu$m and $f_s < 250\,$MHz. Scale bar: 1 mm.

Spatial and temporal sampling of acquisition

As outlined above, the original performed scan was acquired with RSOM50, using a step size of 15 μm and a sampling rate of 500 MHz. Larger step sizes were mimicked by extracting every n$^{\text{th}}$ A-line within every B-scan and every n$^{\text{th}}$ B-scan within the 3D sinogram, *i.e.*:

$$\begin{aligned} S_n(i_x, i_y, i_z) = & S(i_x = \{1, n+1, 2n+1, \ldots, N_x\}, \\ & i_y = \{1, n+1, 2n+1, \ldots, N_y\},\ i_z = \{1, 2, 3, \ldots, N_z\}) \end{aligned} \tag{3.24}$$

where $S(i_x, i_y, i_z)$ is the mathematical representation of the acquired 3D sinogram, and N_x, N_y, and N_z are the number of sampling points along the x-, y-, and z-axis.

Analogously, slower sampling frequencies were mimicked by extracting every n$^{\text{th}}$ time point

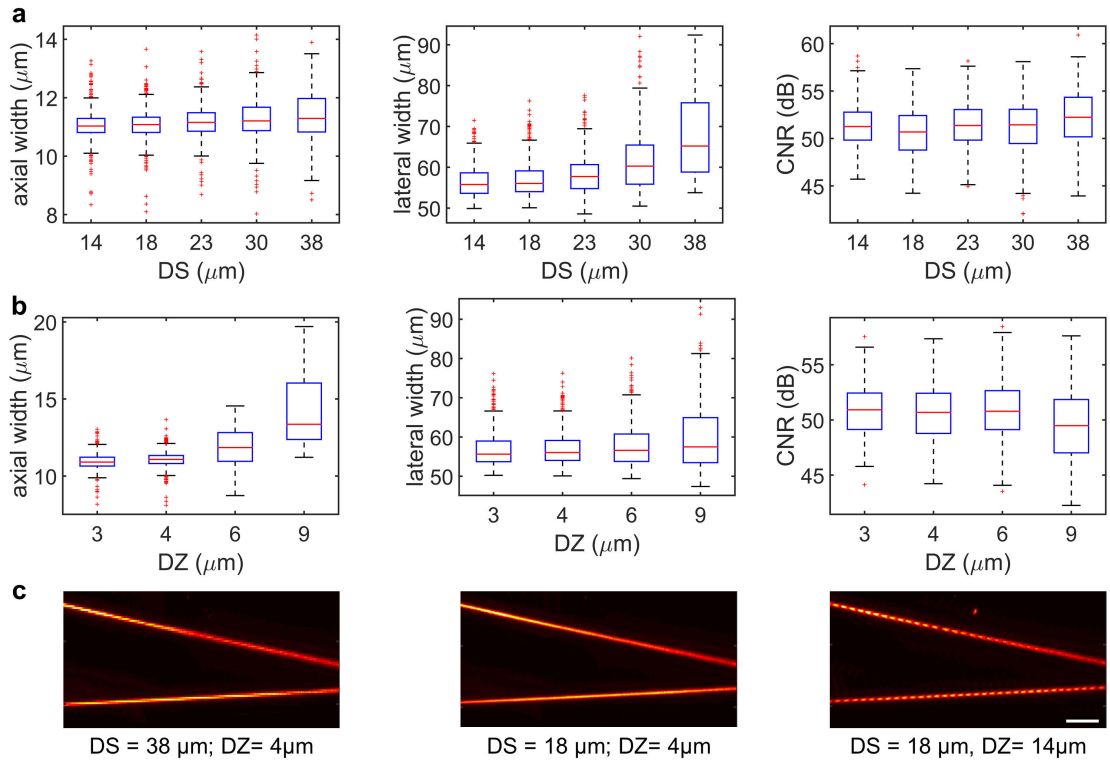

Figure 3.11.: Resolution as a function of the reconstruction grid parameters. Data points were obtained from the reconstruction of two 9 mm long sutures according to the processing steps outlined in section 3.7.1. The number of data points equals $n = \{639, 504, 387, 297, 234\}$ depending on the grid size parameters DZ $= \{14, 18, 23, 30, 38\}$ μm. **a)** Boxplot of lateral with, axial width, and CNR at varying lateral grid step size DS. Axial grid step size was fixed to DZ $= 4\,\mu$m. Lateral width and spread increase with DS. Axial width and SNR are less affected by a change in DS. **b)** Boxplot of lateral with, axial width, and CNR at varying axial grid step size DZ. Lateral grid step size was fixed to DZ $= 18\,\mu$m. Axial width and spread increase with DZ. Lateral width and CNR are less affected by a change in DZ. **c)** Lateral MAPs (top view) of the two sutures at variable reconstruction grid parameters. For $DS = 38\,\mu$m or $DZ = 14\,\mu$m aliasing effects are observed.

within every A-line of the 3D sinogram, *i.e.*:

$$\begin{aligned} S_{f/n}(i_x, i_y, i_z) =& S(i_x = \{1, 2, 3, \ldots, N_x\}, \\ & i_y = \{1, 2, 3, \ldots, N_y\},\ i_z = \{1, n+1, 2n+1, \ldots, N_z\}) \end{aligned} \tag{3.25}$$

Figure 3.10 depicts the changes of axial width, lateral width, and CNR as function of acquisition step size and sampling frequency. Data points were obtained from the reconstruction of two 9 mm long sutures according to the processing steps outlined in section 3.7.1 and equation (3.24)-(3.25). The mean and standard deviation of axial and lateral width increase with the step size. For $\Delta < 30\,\mu$m the effect is minor, but for $\Delta > 30\,\mu$m the resolution increasingly deteriorates. The contrast decreases with increasing step size. The decrease in CNR correlates with the square root of the acquired A-lines. Take for instance $\Delta = 90\,\mu\text{m} = 6 \cdot 15\,\mu$m. 36 times less data points are measured at a step size of $90\,\mu$m compared to a step size of $15\,\mu$m. Hence, a 6-fold (~ 15.6 dB) decrease in CNR is expected. Figure 3.10a shows indeed a decrease of ~ 14 dB. Similar effects are observed when changing

the sampling frequency (see Figure 3.10b). For a sampling frequency of $f_s < 250\,\mathrm{MHz}$, axial and lateral resolution as well as its standard deviation increases, the CNR in turn decreases with decreasing frequencies.

The impact of acquisition step size and sampling frequency, which was quantified by deterioration of axial width, lateral width, and CNR of the sutures, is confirmed by the images plotted in Figure 3.10c. The panel of lateral MAPs, visualizing the two sutures from the top, reveals aliasing effects that are observed for $\Delta > 30\,\mu\mathrm{m}$ and $f_s < 250\,\mathrm{MHz}$. The parameter settings $\Delta = 30\,\mu\mathrm{m}$ and $f_s = 250\,\mathrm{MHz}$ represent the limiting parameter settings that show slightly visible deterioration of image quality.

Reconstruction grid size

The reconstruction grid size has to be chosen carefully to avoid artifacts. To investigate the impact of the reconstruction grid on the image quality, the scanned phantom was reconstructed at different reconstruction voxel sizes. Two grid size parameters are of interest: the lateral voxel size termed DS (xy-plane) and the axial voxel size termed DZ (z-axis).

Figure 3.11 shows how the grid size of the reconstruction grid impacts the image quality. Data points were obtained from the reconstruction of two 9 mm long sutures according to the processing steps outlined in section 3.7.1. The lateral voxel size DS has the strongest impact on the lateral resolution (see Figure 3.11a). Whereas the lateral width of the suture is robust for $\mathrm{DS} \leq 18\,\mu\mathrm{m}$, an increase of the median and upper quartile is observed for $\mathrm{DS} \geq 23\,\mu\mathrm{m}$ (3.11a). The median of the axial width remains constant with increasing DS, however, for $\mathrm{DS} > 23\,\mu\mathrm{m}$, the width of the distribution around the median increases. Analogously, the axial voxel size DZ shows its strongest impact on the axial width of the suture. Axial resolution is robust for $\mathrm{DZ} \leq 4\,\mu\mathrm{m}$ and deteriorates for $\mathrm{DS} \geq 6\,\mu\mathrm{m}$. The median lateral width remains constant with increasing DZ, however, there is an increase in the width of the distribution around the median for $\mathrm{DS} \geq 6\,\mu\mathrm{m}$. The CNR of the reconstructed suture is independent of both DZ and DS.

3.7.3. Quality check for different reconstruction modes

In sections 3.4 and 3.5 a sophisticated model has been introduced for the back-projection algorithm. Here, the effect of the single pre-processing and modeling steps will be analyzed. The following reconstruction modes will be compared:

- rm 0: Without co-registration of scanning directions.
- rm 1: Without spatial filtering of laser-induced reflection lines.
- rm 2: Raw data is not band pass filtered before reconstruction.
- rm 3: Focal region is modeled by a point-like focus.
- rm 4: No weighting factor is employed.
- rm 5: Direct term is used as back-projection term.
- rm 6: Negative derivative term is used as back-projection term.

- rm 7: Negative derivative term multiplied by t_{sp} is used as back-projection term.
- rm 8: Full back-projection term (see equation (3.18)) is used.

Figure 3.12 shows the quantitative and qualitative image quality of all the reconstruction modes. Boxplot data was obtained from the reconstruction of two 9 mm long sutures according to the processing steps outlined in section 3.7.1. Figure 3.12a depicts the axial width, lateral width, and contrast of two 15 μm sutures embedded in water and reconstructed by different reconstruction modes. Reconstruction modes 3, 5, and 7 show deteriorated axial and lateral resolution of the sutures. Reconstruction modes 1, 2, 5, 6, and 7 are characterized by a drop in CNR compared to reconstruction modes 3, 4, and 8. Thus, reconstruction modes 4 and 8 show the best image quality, providing best resolution and contrast.

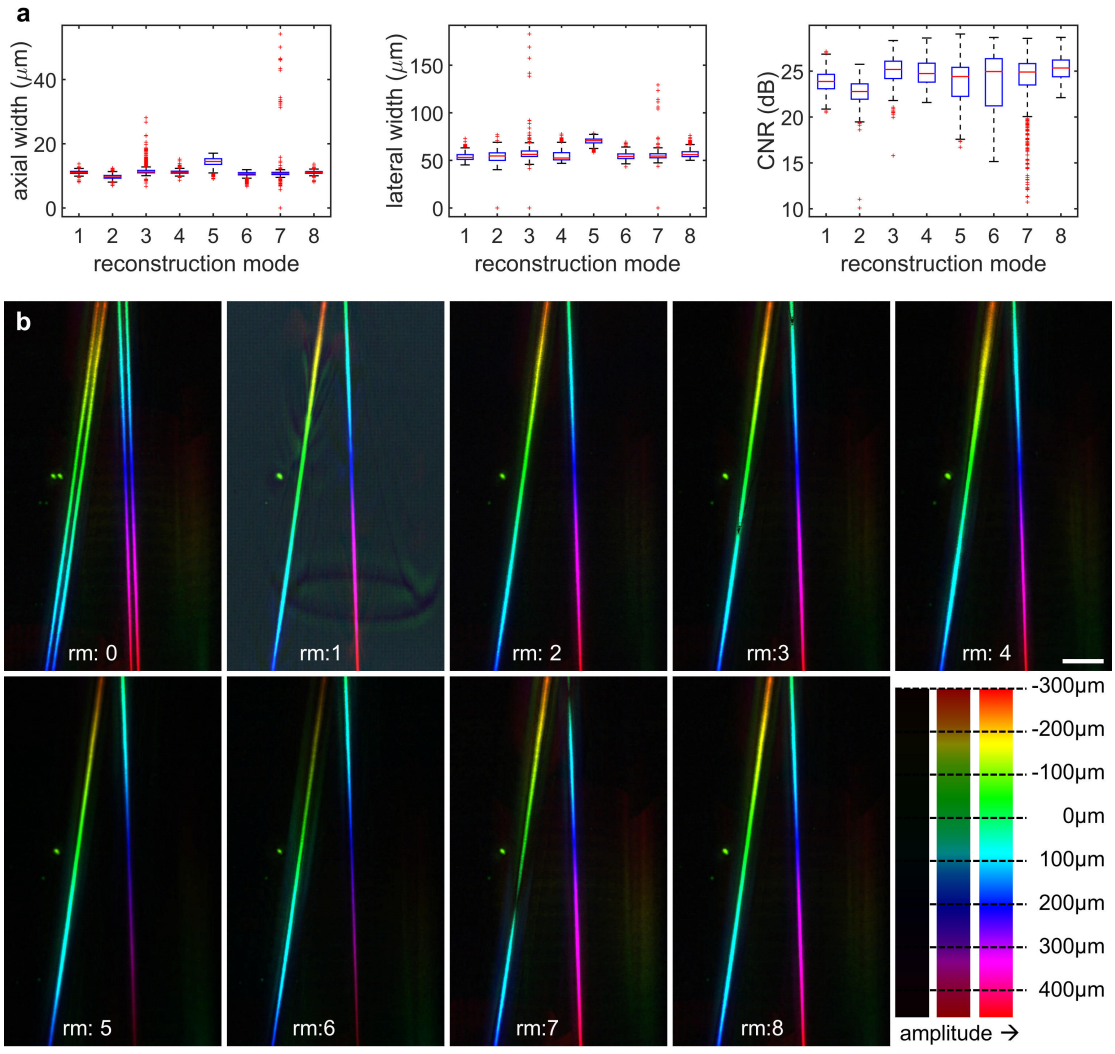

Figure 3.12.: Resolution and contrast as a function of reconstruction mode. Data points were obtained from the reconstruction of two 9 mm long sutures according to the processing steps outlined in section 3.7.1. The number of data points evaluated in every boxplot is $n = 504$. **a)** Boxplot of axial with, lateral width, and CNR at various reconstruction modes. **b)** Depth-encoded lateral MAPs (top view) of the two sutures at various reconstruction modes. The depth is encoded by the color, and the brightness scales proportional to the amplitude of the voxel. Reconstruction modes 4 and 8 show best performances.

3.8. Summary and conclusion

In this chapter, raster-scan optoacoustic mesoscopy (RSOM) has been introduced, which was developed in our group [3,164,165]. Emphasis has been put on different RSOM implementations, fast and improved reconstruction methods, and optimal sampling of both acquisition and reconstruction.

In section 3.2, the experimental setup of RSOM was presented. In RSOM, nanosecond laser pulses are coupled into fiber bundles, and the light is directed onto the tissue surface. A spherically focused $LiNbO_3$ detector records the ultrasound waves emitted by the tissue after excitation. The illumination-detector unit is raster-scanned in-tandem on a 2D surface by two piezoelectric stages. A depth-encoded time signal is recorded on a regularly-spaced acquisition grid. The acquired raw data is digitized and stored on a desktop PC for further reconstruction of 3D images. Several experimental implementations of RSOM were presented in section 3.2, aiming to fulfill the requirements specified in chapter 2 for optimal resolution and imaging depth. The introduced RSOM implementations will be used in different chapters throughout the thesis. RSOM100 is a lab system using a high-frequency $20-180\,\mathrm{MHz}$ detection bandwidth. RSOM50 employs a more sensitive detector of $10-90\,\mathrm{MHz}$ detection bandwidth. For clinical use a miniaturized and portable RSOM system was developed, named clinical RSOM55. RSOM55 uses a detection bandwidth of $14-126\,\mathrm{MHz}$. RSOM100, RSOM50, and clinical RSOM55 employ a high repetition rate single-wavelength excitation source at 532 nm for fast and high-resolution anatomical imaging. To gain spectral information, a multispectral raster-scan optoacoustic mesoscopy (MSOM) system was developed. MSOM uses the same detector as RSOM50. The tissue in MSOM is excited by a tunable laser, which emits nanosecond laser pulses in the range from $413-2300\,\mathrm{nm}$.

The reconstruction in RSOM consists of two main parts, *i.e.* pre-processing of the acquired data, presented in section 3.4, and the 3D beam-forming reconstruction algorithm, presented in section 3.5. To get rid of reconstruction artifacts, three main processing steps are performed before reconstruction (see section 3.4). First, laser reflection lines are filtered by a custom-designed filter in Fourier space. Second, the frequency content of the raw data is bandpass filtered to dispose of recorded frequencies that lie outside of the detection bandwidth of the detector. Third, an offset of the recorded position between the two scanning directions are automatically corrected for by a co-registration algorithm. The offset in acquisition positions arises from the inertia of the micro-positioning stages, which prevents instantaneous acceleration. After pre-processing of the data, a custom-designed 3D reconstruction algorithm reconstructs optoacoustic images. The algorithm was implemented on a GPU. The reconstruction algorithm is based on a generalized idea of the back-projection algorithm [167]. The most important beam-forming steps of the algorithm were presented in section 3.5.3. First, a virtual detector transformation is used, which calibrates the recorded time signal with respect to the focal point of the spherically focused detector, which acts as the symmetry point of the virtual point detector. Second, the sensitivity field of the finite point detector is simulated using Field II finite element simulations. The sensitivity field is implemented as a 3D weighting factor in the reconstruction algorithm. Third, the back-projection term is calculated, which consists of a combination of the direct recorded time signal and the derivative thereof. Fourth, the linear back-projection algorithm is run on a GPU to allow for parallel and fast reconstruction of the 3D images.

For improved visualization, the ultra-wide detection bandwidth is separated into two subbands before reconstruction (see section 3.6). In this way, images are reconstructed using

a sequential narrow band inversion, which inverts the low frequencies separately from the high frequencies. Sequential narrow band inversion allows for improved signal-to-noise characteristics and enables the visualization of low and high frequencies simultaneously. Thus, the resulting image allows for a better representation of the high frequencies (smaller structures), avoiding their masking by the low frequencies on the final reconstruction. The relative bandwidth of the two sub-bands is kept constant at 100% relative bandwidth. Throughout this work, the same color-coding is used, where red represents the reconstruction of the low frequencies and green represents high frequencies.

In section 3.7, optimal parameters for spatial and temporal sampling of acquisition as well as reconstruction grid were evaluated experimentally. From an image quality point of view, dense spatial and temporal sampling of both acquisition and reconstruction grids are advantageous. However, oversampling affects acquisition and reconstruction time and results in excessive memory consumption. To prevent reconstruction artifacts, both acquisition and reconstruction must fulfill the Nyquist-Shannon sampling criterion (see 3.7.2), stating that the recorded or reconstructed frequencies must be sampled at twice the largest detectable frequency. Optimal sampling parameters were evaluated experimentally for RSOM50 by scanning two $\sim 15\,\mu$m thick nylon sutures over a length of 9 mm and a depth range of $-20\,\mu$m to $460\,\mu$m. The image quality of the suture phantom was quantified by the axial width, lateral width, and contrast-to-noise ratio of the sutures in the reconstructed images. Aliasing effects and resolution loss is observed for a step size of $\Delta > 30\,\mu$m and a sampling frequency of $f_s < 250\,$MHz. Thus, time- and memory-efficient sampling will be obtained by setting $\Delta = 20\,\mu$m and $f_s = 500\,$MHz.

The same phantom experiment was used to optimize the reconstruction grid voxel size. For RSOM50 the maximum voxel size without loss of resolution was determined to be DZ $= 4\,\mu$m and DS $= 18\,\mu$m. Since the detector properties of RSOM100, RSOM50, and RSOM55 are very similar, the sampling results of RSOM50 can be transferred to RSOM100 and RSOM55. Spatial and temporal sampling of both acquisition and reconstruction grid scale inversely proportional to the detection bandwidth, *i.e.* optimal parameters for RSOM100 are $\Delta = 10\,\mu$m, $f_s = 1000\,$MHz, DZ $= 2\,\mu$m, and DS $= 9\,\mu$m.

4. Detection bandwidth and imaging depth in RSOM

This section contains adapted text passages and figures from a manuscript submitted for publication by Schwarz *et al.* [106]. More information on the permission to reproduce textual material, illustrations, and tables is found in appendix B.

4.1. Introduction

In chapter 2, a detailed introduction into optoacoustic signal generation, anatomy of human skin, and optical properties of human skin was given. Based on this knowledge of chromophores, skin anatomy, and optoacoustic signal generation, a generic skin model of hair-bearing (lower arm) and hairless skin (palm) was introduced in section 2.5. This model defines imaging depth and frequency bandwidth required for optoacoustic dermoscopy. To briefly summarize: Contrast rich human skin [5, 18, 109, 110, 112, 159–162, 178] produces broadband optoacoustic signals (from a few to hundreds of MHz) owing largely to the wide variability in size of optical absorbers, including diameter of vasculature feeding the skin (3.5 μm to 100 μm) [113].

The detection bandwidth must be chosen according to the target size [179]. Nevertheless, most acoustic resolution optoacoustic dermoscopy studies used a detection bandwidth of less than 40 MHz and central frequency of $\leq$ 50 MHz. At these bandwidths, many skin structures cannot be resolved, including most of the elements within the *stratum corneum*, dermal papillae, and superficial horizontal plexus [96, 99, 102, 103, 105, 180, 181]. Optical resolution optoacoustic microscopy has the capability of resolving in greater detail superficial structures but comes at a limited penetration depth that fails to visualize parts of the reticular dermis or sub-dermal layers [182].

In chapter 3, ultra-broadband raster-scan optoacoustic mesoscopy (UB-RSOM) was introduced. UB-RSOM achieves a bandwidth greater than 100% at central frequencies of 100 MHz and 50 MHz. Initial studies on selective frequency bands by Schwarz *et al.* showed that while the use of ultrasound above 60 MHz is needed for imaging the *stratum corneum* and vascular features of the papillary dermis, frequencies below 25 MHz are required for resolving the vasculature of the lower reticular dermis [174]. These measurements highlight the benefits of using ultra-broadband ultrasound detectors for dermoscopy.

Despite recent advances in optoacoustic dermoscopy, the relation between frequency-dependent signal-to-noise ratio (SNR), excitation energy, and achieved imaging depth is not thoroughly studied. Sensitivity studies in the past have focused on quantifying the minimum number of targets needed to detect optoacoustic signal above the noise [166, 183], neglecting the depth-dependency of the detection bandwidth. Understanding the interplay between delivered energy, depth, and bandwidth is important in the context of selecting appropriate

illumination technology and meeting safety limits for exposure of human skin to light fluence. A majority of earlier reports used high excitation per-pulse energy ($3.5-10\,\mathrm{mJ/cm^2}$) for optoacoustic dermoscopy albeit at slow ($<50\,\mathrm{Hz}$) PRR [96, 98, 103, 105, 180, 181]. Current laser technologies can afford higher imaging speed at a PRR of several kHz [99, 174, 184], which is advantageous for improved imaging quality, accelerating the data acquisition speed and reducing motion artifacts. Conversely, accelerating imaging speed increases the amount of energy per time deposited to tissue, with possible laser safety concerns [98, 100].

In this chapter, the relation between the excitation energy, frequency response, and the imaging depth achieved by UB-RSOM will by investigated in simulations, phantom measurements, and *in vivo* measurements of the human skin. Simulations will outline physical limitations of detection bandwidth and imaging depth due to acoustic and optical attenuation. Phantom experiments will be performed to evaluate the dependence of the detection bandwidth and penetration depth as a function of excitation energy. The experimental results on depth-dependent detection bandwidth will be related to the emitted frequency response of skin (see section 2.5). Finally, skin UB-RSOM images at central frequencies of 100 MHz and 50 MHz will be studied to confirm the simulations and phantom data and to evaluate optimal detection bandwidth and excitation energy for fast and high contrast optoacoustic dermoscopy. Attention will be given to laser safety regulations.

4.2. Optical attenuation limits imaging depth

Optoacoustic signal strength is proportional to the light fluence (see section 2.4) and is the limiting factor in imaging depth. The optical penetration depth of light in a homogeneous diffuse medium can be estimated by the penetration depth δ, which corresponds to the tissue depth at which light fluence has dropped to $1/e \approx 36.7\%$, where e is Euler's constant [112]:

$$\delta = \frac{1}{\sqrt{3\mu_a(\mu_a+\mu_s')}} \overset{\mu_s'\gg\mu_a}{\approx} \frac{1}{\sqrt{3\mu_a\mu_s'}} \tag{4.1}$$

Thus, if $\mu_s' \gg \mu_a$, the penetration depth in human skin is proportional to $\mu_a^{-1/2}$ and increases with decreasing absorption. That is why the penetration depth of light in human skin varies with excitation wavelength.

Due to high absorption of green laser light by hemoglobin, RSOM uses an excitation wavelength of 532 nm (see section 3.2). To gain knowledge on the achievable penetration depth of light at 532 nm, the light fluence was simulated. Simulations were performed with the CUDAMCML Monte Carlo simulation software [185], which models light fluence for multilayered turbid media with an infinitely narrow normally incident photon beam as a light source. Since the light fluence shows rotational invariance with respect to the axis of the infinitely narrow pencil beam, the fluence $\phi_\delta(\rho, z)$ depends only on the depth z and the distance ρ to the axis of the pencil beam.

Based on the light fluence $\phi_\delta(\rho, z)$ originating from the pencil beam, an arbitrarily shaped finite laser beam can be simulated by convolution of $\phi_\delta(\rho, z)$ with the finite beam profile. Herein, a 1 mm spherically shaped flat laser beam was modeled with beam profile:

$$\begin{aligned} \phi_{1\,\mathrm{mm}}(\rho(x,y),z) &= \phi_\delta(\rho(x,y),z) * \mathrm{kernel}(\rho(x,y)) \\ \mathrm{kernel}(\rho(x,y)) &= H\left(1\,\mathrm{mm} - \rho(x,y)\,\mathrm{mm}\right) \end{aligned} \tag{4.2}$$

Table 4.1.: Model of optical properties and layer thickness of the human palm used for light fluence simulations at 532 nm**.** Values were compiled from sections 2.3, 2.2, and 2.5.

Layer	**Refractive index**	**Absorption coefficient μ_a (cm^{-1})**	**Scattering coefficient μ_s (cm^{-1})**	**Anisotropy g**	**Thickness of layer (μm)**
Water	1.33	4e-3	2e-5	0	1000
Stratum corneum	1.52	1.44	605	0.9	20
Mid-epidermis	1.44	0.175	175	0.65	200
Stratum basale	1.44	4.3	175	0.65	20
Papillary dermis	1.38	3.16	123	0.65	330
Reticular dermis	1.38	1.78	123	0.65	400
Subcutis	1.38	1.1	52.5	0.65	10000

where $H(x)$ is the Heaviside step function, which takes the value 1 within a circle of radius 1 mm and the value 0 outside of the circular shaped beam area.

Three different light fluence simulations were performed. Simulation SIM1 modeled the light fluence of the laser light in pure water, which served as baseline simulation. In addition, the light fluence within two generic skin types, which are characterized by a difference in epidermal thickness, were modeled: thick hairless skin (human palm, SIM2) and thin hair-bearing skin (lower arm, SIM3). The intensity of the fluence in simulations SIM2 and SIM3 were calculated with respect to the maximum light fluence of the baseline measurement in pure water, *i.e.*:

$$\phi_{\mathrm{hp}}(\rho, z) = 10 \log_{10} \left(\frac{\phi_2(\rho, z)}{\max_{\rho,z}[\phi_1(\rho, z)]} \right), \tag{4.3}$$

$$\phi_{\mathrm{la}}(\rho, z) = 10 \log_{10} \left(\frac{\phi_3(\rho, z)}{\max_{\rho,z}[\phi_1(\rho, z)]} \right), \tag{4.4}$$

where ϕ_1, ϕ_2, and ϕ_3 are the light fluences simulated in simulations SIM1, SIM2, and SIM3, respectively. Thus, ϕ_{hp} and ϕ_{la} give the light fluence in the human palm and the lower arm respectively with respect to the baseline fluence in pure water.

Table 4.2.: Model of optical properties and layer thickness of the lower arm used for light fluence simulations at 532 nm**.** Values were compiled from sections 2.3, 2.2, and 2.5.

Layer	**Refractive index**	**Absorption coefficient μ_a (cm^{-1})**	**Scattering coefficient μ_s (cm^{-1})**	**Anisotropy g**	**Thickness of layer (μm)**
Water	1.33	4e-3	2e-5	0	1000
Stratum corneum	1.52	14.4	605	0.9	10
Mid-epidermis	1.44	0.175	175	0.65	50
Stratum basale	1.44	43	175	0.65	20
Papillary dermis	1.38	3.16	123	0.65	330
Reticular dermis	1.38	1.78	123	0.65	650
Subcutis	1.38	1.1	52.5	0.65	10000

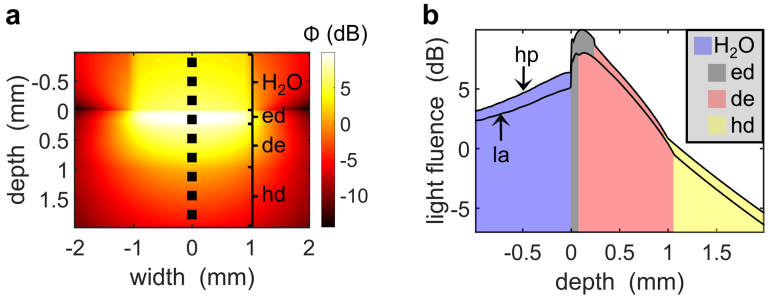

Figure 4.1.: Limited imaging depth due to optical attenuation. **a)** Monte Carlo simulation of light fluence at 532 nm in the human palm. A cross-section through the optical axis of the laser beam (side view) is depicted. **b)** Mean light fluence for both the human palm (hairless skin) and the lower arm (hair-bearing skin). The mean fluence was calculated over the central region (200 μm in diameter) of the laser beam, indicated by the black dashed line in (a). The shaded areas under the light fluence curves indicate the skin layer. hp: human palm, la: lower arm, ed: epidermis, de: dermis, hd: hypodermis.

The required input parameters for the Monte Carlo simulation are refractive index, scattering coefficient, absorption coefficient, anisotropy, and layer thickness for each layer. Optical parameters were derived from section 2.3, skin layer thickness estimations were based on section 2.2 and section 2.5. A set of parameters was defined for both the human palm and the lower arm. In addition to section 2.5, a 1 mm thick layer of water was added above the skin surface, mimicking optoacoustic coupling. Furthermore, a 1 cm thick subcutaneous layer was added below the reticular dermis. A summary of input parameters for the human palm and the lower arm are given in Table 4.1 and Table 4.2 respectively.

Figure 4.1 visualizes the light fluence as a function of depth. In Figure 4.1a, a 2D cut through the center of the 3D light fluence map ϕ_{hp} is visualized using a logarithmic color scale. Above the skin surface, the laser beam passes through water, where it is hardly scattered and absorbed. As soon as the light hits the epidermis, the strong scattering and absorption of human skin govern the light propagation. Figure 4.1b shows the mean light fluence for both the human palm and the lower arm. The mean fluence was calculated by taking the average over the central region (200 μm in diameter) of the laser beam, indicated by the black dashed line in Figure 4.1a. The light fluence increases towards the skin surface and reaches a maximum approximately 150 μm below the surface. In the human palm, the maximum fluence reaches values up to 10 dB. Subsequently, the fluence decays exponentially with depth. Through all skin layers, higher light fluence is observed in the human palm compared to the lower arm.

Several interesting aspects follow from Figure 4.1. First, the light fluence in human cutaneous tissue can reach up to 10 times higher values $100 - 200\,\mu$m below the skin surface compared to the light fluence within a laser beam of the same power passing through pure water. This phenomenon is attributed to the large scattering coefficient in cutaneous tissue compared to the absorption coefficient and the mismatch in refractive index between tissue layers and water [186]. Since the scattering coefficient is approximately two orders of magnitude higher than the absorption coefficient (see Tables 4.1 and 4.2), a single photon undergoes on average dozens of scattering events before it is absorbed. Since photon scattering randomizes the photon path, a single photon may pass through the same tissue depth multiple times before absorption. Thus, the light fluence below the skin surface accumulates due to recurring photons. Only at a depth of approximately 1 mm below the skin surface, the light fluence

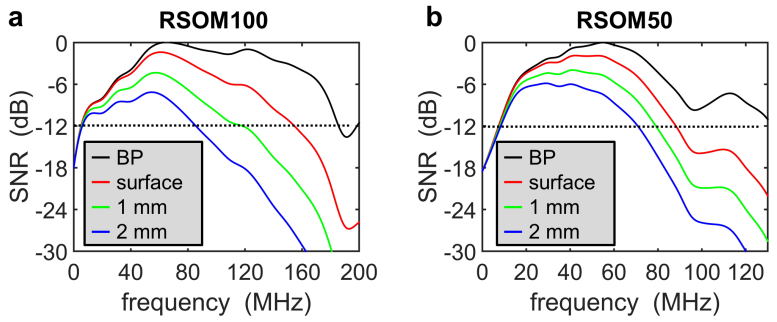

Figure 4.2.: Limited detection bandwidth due to acoustic attenuation. The detection bandwidth at different depth is shown for **a)** the 100 MHz and for **b)** the 50 MHz detector. The black curves depict the detection bandwidth of the two detectors (see section 3.2). The red, green, and blue curves show detectable ultrasound frequencies originating from the tissue surface (situated at the focal distances of the detectors), 1 mm, and 2 mm below the tissue surface, respectively. The detection bandwidth decreases with depth. The higher the frequency, the stronger acoustic attenuation is.

decays to 0 dB, *i.e.* to the maximum light fluence in the baseline measurement of light fluence in pure water. Second, the light fluence in the human palm is higher than the fluence in the lower arm. The cause for this observation is that hairless skin is characterized by less melanin content within the epidermis, *i.e.* lower absorption within the first layer. Third, the light fluence decreases exponentially (linear drop in the logarithmic plot in Figure 4.1b) with depth below the fluence peak. At a depth of 1 mm (2 mm) the light fluence is approximately $7-8$ dB ($12-13$ dB) weaker compared to the light fluence within the epidermis. Since optoacoustic signal amplitude is proportional to the light fluence, the strength of optoacoustic signals drops exponentially with depth, limiting the imaging depth.

4.3. Acoustic attenuation limits detection bandwidth

The resolution of MOD depends on the detectable frequencies on the transducer surface as well as its aperture. The smaller the object, the broader the frequency response is (see section 2.5). The detectable frequencies are primarily determined by the detector bandwidth, which is plotted for all detectors in section 3.2. In addition to the detection bandwidth, ultrasound gets attenuated by biological tissue and water as it propagates through the corresponding media. In the following, the impact of acoustic attenuation on the detectable frequencies will be analyzed.

In a homogeneous medium like water or biological tissue, acoustic attenuation is well approximated by a frequency power law. The acoustic amplitude $A(z)$ at depth z decays exponentially from the initial maximum amplitude A_0, *i.e.*:

$$A(f,z) = A_0 \cdot \exp[-(\alpha|f|^{\gamma}z)], \tag{4.5}$$

where α is the attenuation constant, and γ is the power law exponent. In water, typical parameters are $\gamma = 2$ and $\alpha = 0.00217\,{}^{\mathrm{dB}}/_{\mathrm{MHz}^2\mathrm{cm}}$ [187, 188]. Cutaneous tissue is well approximated by $\gamma \approx 1$ and $\alpha \approx 0.5\,{}^{\mathrm{dB}}/_{\mathrm{MHz\,cm}}$ [187, 188].

In a heterogeneous medium, equation (4.5) needs to be generalized since the parameters α and γ change with the medium. To correctly simulate acoustic attenuation in optoacoustic

imaging, the integrated attenuation between the optoacoustic source and the detector surface along the path of the propagating acoustic wave has to be taken into account:

$$A(f,z) = A_0 \cdot \exp\left[-\int_0^z dz'(\alpha(z')|f|^{\gamma(z')})\right] \tag{4.6}$$

In RSOM the acoustic waves propagate through both cutaneous tissue and water. The surface of the sample that is scanned is typically located slightly below the focal zone of the detector, *i.e.* at a distance of $\mathrm{FD}_{100\,\mathrm{MHz}} = 1.65\,\mathrm{mm}$ for RSOM100 and $\mathrm{FD}_{50\,\mathrm{MHz}} = \mathrm{FD}_{55\,\mathrm{MHz}} = 3\,\mathrm{mm}$ for RSOM50 and RSOM55. Thus, acoustic attenuation in RSOM is well approximated as follows:

$$\begin{aligned} A(f,z) =& A_0 \cdot \exp\left[-\mathrm{FD_{td}} 0.00217\,{}^{\mathrm{dB}}/_{\mathrm{MHz^2 cm}}|f|^2\right] \\ & \cdot \exp\left[-(z-\mathrm{FD_{td}}) 0.5\,{}^{\mathrm{dB}}/_{\mathrm{MHz\,cm}}|f|\right], \end{aligned} \tag{4.7}$$

where $\mathrm{FD_{td}}$ is a placeholder for the focal length of the used detector. The lowpass filtering property of water and tissue $A(f,z)$ adds to the impulse response function of the detector and leads to the reduction of detection bandwidth with depth.

Figure 4.2 shows how acoustic attenuation in water and biological tissue reduces the detection bandwidth of RSOM as a function of depth, based on equation (4.7). The black curves in Figure 4.2 depict the detection bandwidth of RSOM100 and RSOM50. The red, green, and blue curves show detectable ultrasound frequencies originating from the tissue surface (corresponding to the focal distances of the detectors), 1 mm, and 2 mm below the tissue surface. Due to acoustic attenuation, the detection bandwidth gets smaller and smaller with increasing depth. In case of RSOM50, the −12 dB high-cutoff frequency reduces from 88 MHz at the tissue surface to 70 MHz at a depth of 2 mm. For RSOM100, the relative loss in the transducers sensitivity is more significant. The high-cutoff frequency reduces from 155 MHz at the tissue surface to 85 MHz at a depth of 2 mm. Figure 4.2 shows that high frequencies are significantly attenuated with depth and frequencies above 120 MHz are expected to be detectable only superficially.

4.4. Detection bandwidth of RSOM as a function of excitation energy and depth

To evaluate how the experimental detection bandwidth and penetration depth of RSOM100 and RSOM50 depend on the excitation energy, a cylindrically shaped phantom (Figure 4.3a) was designed with optical properties reminiscent to those of human skin. The phantom consisted of 1.3% w/v agar (Sigma, Germany) mixed with distilled water. Black India ink 0.92% v/v was used as an optoacoustic absorber (Pelikan, Tusche A, Black, 17). The optical density of the mixture measured OD = 1.62, which corresponds to an absorption coefficient of $3.7\,\mathrm{cm}^{-1}$. For scattering, 13% v/v of intralipid-20% (Intralipid 20%, emulsion, l141-100ML, Sigma-Aldrich, Germany) was used to mimic a reduced scattering coefficient of $\sim 42\,\mathrm{cm}^{-1}$ [189]. To generate a broadband optoacoustic signal, 10 μm black polystyrene microspheres were added to the phantom (Polybead, Polysciences Inc., Warrington, Pennsylvania) at a final concentration of ~ 270 microspheres per cubic millimeter.

The energy-dependent detection bandwidth and penetration depth were calculated as follows. The phantom was scanned at excitation energies of 35 μJ, 78 μJ, 145 μJ, and 275 μJ per-pulse

with both RSOM100 and RSOM50. At each acquisition point, a 1D depth resolved time signal was acquired, which is referred to as A-line. 801×801 A-lines ($8\,\text{mm} \times 8\,\text{mm}$ area) were acquired in RSOM100 and 501×501 A-lines ($10\,\text{mm} \times 10\,\text{mm}$ area) in RSOM50. Raw data was stored in a 3D signal matrix $S(x_i, y_j, z_k)$, $i = \{1, 2, 3, \ldots, N_x\}$, $j = \{1, 2, 3, \ldots, N_y\}$, $k = \{1, 2, 3, \ldots, N_z\}$, where N_x and N_y are the number of acquisition points along the x- and y-axis. N_z refers to the number of time samples within each A-line.

To eliminate low-frequency artifacts in the raw data an exponential high pass filter of 4^{th} order was designed with a cutoff frequency at $f_{\text{low}} = 10\,\text{MHz}$:

$$f_{\text{hp}}(f) = 1 - \exp\left[-\left(\frac{f}{f_{\text{low}}}\right)^4\right], \tag{4.8}$$

The exponential highpass filter was applied to all the A-lines in the signal matrix S.

To measure the detectable frequencies at a specific depth z_{k_0}, a vertical slab was extracted from the signal matrix:

$$\text{slab}(x_i, y_j, z_{k'}; k_0) = S\left(x_i, y_j, z_{k\in[k_0-25, k_0+25]}\right), \tag{4.9}$$

where $k' = \{1, 2, 3, \ldots, 51\}$. To prevent aliasing of the frequency spectra, each of the A-lines within the extracted slab were apodized by a Hanning window. The depth-dependent detection bandwidth was then determined by calculating the FFT of all A-lines within the slab and taking the mean thereof:

$$f_{\text{bp}}(f_{k'}, z_{k_0}) = \frac{1}{N_x N_y} \sum_{i,j=1}^{N_x, N_y} \left(\mathcal{FFT}_{k'}\left[\text{slab}(x_i, y_j, z_{k'}; k_0)\right]\right), \tag{4.10}$$

where $\mathcal{FFT}_{k'}$ is the Fast Fourier Transform with respect to index k'. The frequency spectrum $f_{\text{bp}}(f_{k'}, z_{k_0})$ was further normalized by the noise spectrum $f_{\text{n}}(f_{k'})$, which was defined by the measured detection bandwidth of a slab above the skin-mimicking phantom, *i.e.* the signal of pure water. Finally, the SNR of the depth-dependent detection bandwidth is given:

$$\text{SNR}_{\text{bp}}(f_{k'}, z_{k_0}) = 20 \log_{10}\left[\frac{f_{\text{bp}}(f_{k'}, z_{k_0})}{f_{\text{n}}(f_{k'})}\right] \tag{4.11}$$

Figure 4.3 summarizes the results from the phantom measurements. Figure 4.3a shows a schematic of the imaging setup and illustrates how the detection bandwidth as a function of depth was extracted from the optoacoustic signal generated by the phantom. Figure 4.3b plots the detection bandwidth as a function of depth for RSOM100 at per-pulse excitation energies of $35\,\mu\text{J}$, $78\,\mu\text{J}$, $145\,\mu\text{J}$, and $275\,\mu\text{J}$, while Figure 4.3c depicts corresponding measurements of the detection bandwidth as a function of depth for RSOM50. Several interesting features emerge from these phantom experiments. Firstly, the maximum SNR of the raw data is twice as high ($> 6\,\text{dB}$) for RSOM50 compared to RSOM100 (Figure 4.3b,c). Secondly, RSOM100 detects higher frequencies than RSOM50. Indeed, at an excitation energy of $275\,\mu\text{J}$ per-pulse, the peak frequency measured by RSOM50 is approximately 140 MHz, whereas RSOM100 captures frequencies up to 180 MHz. Thirdly, RSOM50 detects optoacoustic signals from larger depths than RSOM100. As shown, at an energy of $275\,\mu\text{J}$ per laser pulse, the 6 dB line reaches approximately 1 mm and 1.5 mm depths for RSOM100 and RSOM50 respectively. Fourthly, the maximum frequency and penetration depth of detected ultrasound signal depends on the per-pulse energy. In RSOM50, these characteristics increase

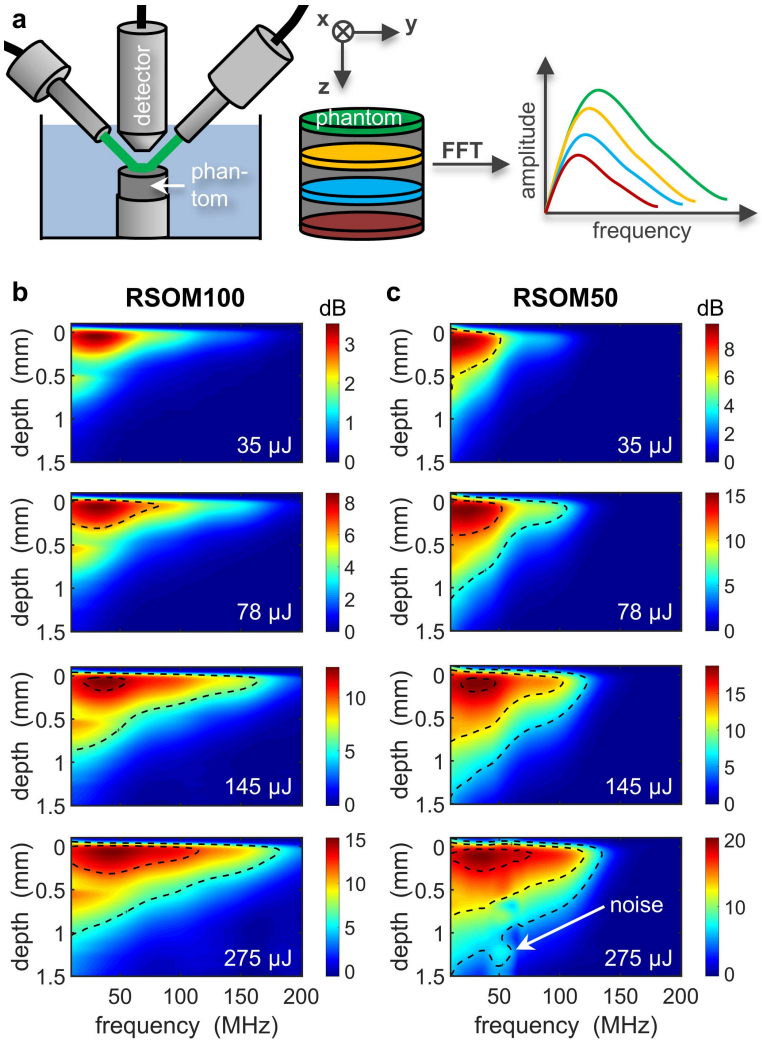

Figure 4.3.: Experimental evaluation of detection bandwidth as a function of excitation energy and penetration depth. a) Schematic of the experiment performed on the phantom containing broadband optoacoustic absorbers. The phantom is characterized by optical properties similar to human skin. To determine the detection bandwidth as a function of depth, the time signal matrix was segmented into vertical slabs, corresponding to different imaging depths, and the frequency response of each slab was calculated via FFT. **b)** SNR of the depth-dependent detection bandwidth of RSOM100 at incrementing energies. **c)** SNR of the detection bandwidth of RSOM50 at different energies. Note that RSOM50 is more sensitive at lower frequencies and penetrates deeper, while RSOM100 is more sensitive to higher frequencies but images superficial layers. The detection bandwidth decreases with depth for both RSOM100 and RSOM50. The 6 dB, 12 dB, and 18 dB contour lines are shown as black-dashed curves. Adapted from Schwarz *et al.* [106].

from $\sim$ 50 MHz and 0.5 mm at an energy of 35 μJ to $\sim$ 140 MHz and 1.5 mm penetration at 275 μJ. In RSOM100, the maximal frequency and penetration depth increase from $\sim$ 80 MHz and 0.3 mm penetration depth at an energy of 78 μJ to 180 MHz and 1.0 mm penetration at 275 μJ. Finally, the highest detectable frequency throughout the skin phantom decreases gradually with imaging depth. For example, at an excitation power of 145 μJ the 6 dB SNR curve in RSOM50 is above 100 MHz for depths $<$ 0.5 mm and decreases to approximately

50 MHz at a depth of 1 mm.

The observations in Figure 4.3 slightly deviate from theoretical considerations. Since the amplitude of the generated optoacoustic signals scales proportionally with the light fluence [190], a 6 dB increase in SNR is expected by doubling the excitation power. Figures 4.3 confirms the 6 dB increase at low energies. At high energies, however, a series of 3 dB attenuators was used after the amplifier in order to match the signal amplitude with the dynamic range of the DAQ card. Although the 3 dB attenuators have a flat attenuation plateau, which should result in a uniform attenuation of both signal and noise strength, it is very likely that the system noise level increases by introducing additional hardware components into the circuit. Thus, SNR increase is slightly lower than theoretical considerations.

4.5. In vivo RSOM100 and RSOM50 measurements

To compare the contrast and imaging performance achieved *in vivo* in human skin, the human palm of a healthy volunteer was measured at a range of per-pulse excitation energies of $35 - 220\,\mu$J with RSOM100 and RSOM50. All measurements were carried out one after the other, and care was taken not to change the position of the ROI. In the following the imaging performance of RSOM100 and RSOM50 will be compared in two ways. First, the resolution capabilities of both setups will be compared. Second, the impact of excitation energy will be studied for both RSOM100 and RSOM50.

4.5.1. Comparison of human skin RSOM100 and RSOM50

Figure 4.4 compares the results obtained from RSOM100 and RSOM50 from the human palm *in vivo*. Figure 4.4a shows cross-sectional images, measuring 7.25 mm × 1.5 mm, of the skin. Notably, the RSOM50 image reveals vessels of the reticular dermis and deep horizontal plexus, not visible on the RSOM100 image (green and white arrows). On the other hand, the higher resolution achieved by RSOM100, compared to RSOM50, is clearly evident on Figure 4.4b,c, which depict lateral MAPs of the *stratum corneum* ($0 - 210\,\mu$m below the surface) and the epidermal-dermal junction ($210 - 350\,\mu$m below the surface). These images reveal fine details of the skin surface and dermal papillae, with single capillary loops clearly resolved with RSOM100 but not with RSOM50. Figure 4.4d shows lateral MAPs $350 - 1200\,\mu$m below the skin surface, visualizing the vascular network of the dermis. RSOM100 images reveal the small vessels of the superficial horizontal plexus, whereas RSOM50 images reveal larger vessels of the deeper reticular dermis.

4.5.2. Human skin RSOM100 and RSOM50 as a function of energy

To elucidate optoacoustic contrast as a function of depth, the CNR and absorber volume fraction (AVF) were calculated.

Initially each reconstructed volume was stored in a 3D matrix $R(x_i, y_j, z_k)$, $i = \{1, 2, 3, \ldots, N_x\}$, $j = \{1, 2, 3, \ldots, N_y\}$, $k = \{1, 2, 3, \ldots, N_z\}$, where N_x, N_y, and N_z are the number of voxels along the x-, y-, and z-axis. To investigate the optoacoustic contrast achieved as a function

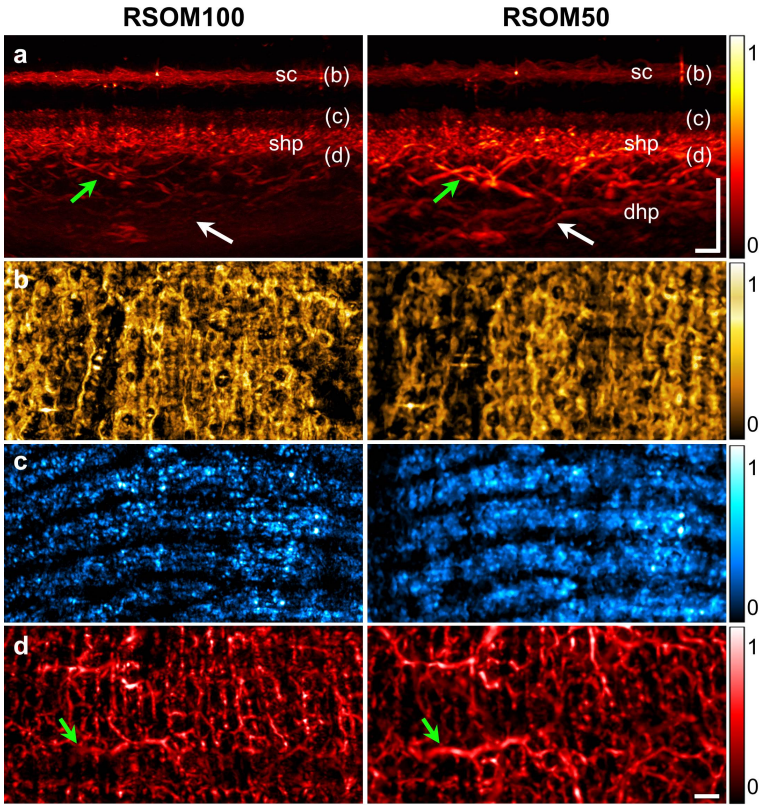

Figure 4.4.: Comparison of *in vivo* contrasts in RSOM100 and RSOM50. The left column shows images acquired with RSOM100, the right column depicts results from RSOM50. **a)** Vertical MAP of the human palm area. The arrows (green and white) indicate vessels of the upper reticular dermis and deep horizontal plexus. Note that the latter are visible only with RSOM50. sc - *stratum corneum*, shp - superficial horizontal plexus, dhp - deep horizontal plexus. **b)** Lateral MAP of the *stratum corneum* depicting a slice located $0-210\,\mu$m below the skin surface. RSOM100 yields higher resolution images with structures visible in greater details. **c)** Lateral MAP of the epidermal-dermal junction $210-350\,\mu$m below the surface. The vascular structures follow the shape of the epidermal ridges. Note that single capillary loops readily discernible on RSOM100 image are barely visible in the RSOM50 image. **d)** Lateral MAP of the dermis below the capillary loops at a depth of $350-1200\,\mu$m. RSOM100 visualizes smaller vessels of the superficial horizontal plexus but fails to reveal vessels of the deep horizontal plexus (see green arrow). Scale bars: $500\,\mu$m. Adapted from Schwarz *et al.* [106].

of depth, the contrast-to-noise ratio was calculated with respect to depth, *i.e.*:

$$\mathrm{CNR}(z_k) = 20\log_{10}\left[\frac{R_{\max}(z_k)}{\mathrm{noise}_{\max}}\right], \tag{4.12}$$

whereby $R_{\max}(z_k) = \max_{i,j} R(x_i, y_j, z_k)$ is the highest amplitude within the imaging plane at a depth z_k, and $\mathrm{noise}_{\max}$ is the background signal calculated by the maximal amplitude of a plane above the skin surface. The CNR calculation determined the contrast of anatomical structures at different energies for both RSOM100 and RSOM50.

To identify skin layers of large blood volume fraction, vertical slabs $R_{\mathrm{slab}}(x_i, y_j, z_{k'}; k_0) = R(x_i, y_j, z_{k\in[k_0-10,k_0+10]})$ were extracted from the 3D image, and the AVF within each slab

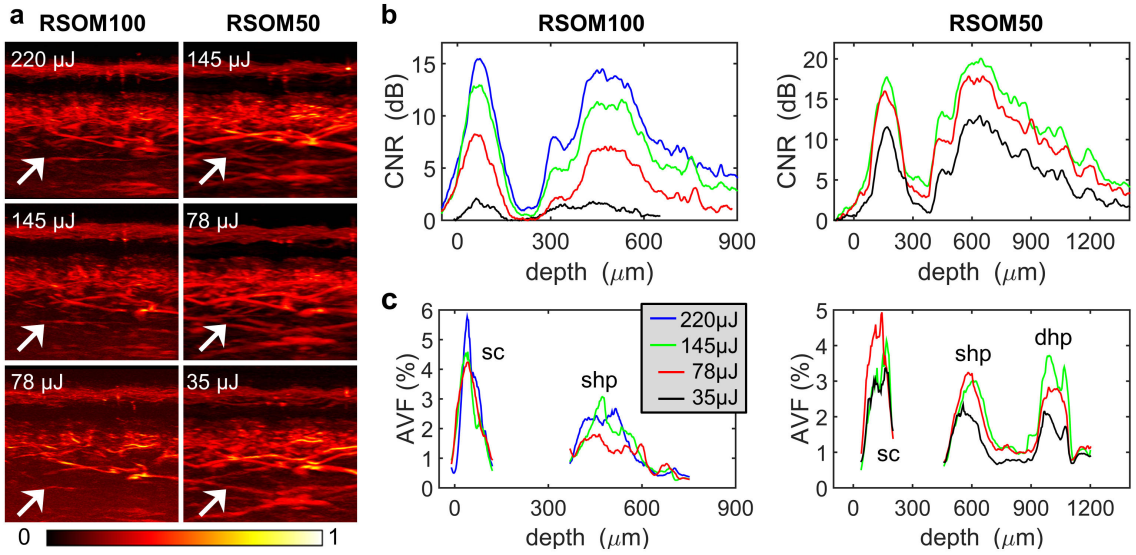

Figure 4.5.: Contrast of RSOM100 and RSOM50 as a function of excitation energy. The palm of a healthy volunteer was imaged at various energies. **a)** Vertical MAPs of a ROI measuring 2.25 mm × 1.4 mm, scanned with RSOM100 and RSOM50. Note that deep-seated vessels are resolved by RSOM50 (white arrows), which turn indiscernible at lower excitation energy. **b)** Contrast-to-noise ratio of anatomical structures as a function of depth at various energies. CNR decreases with excitation energy. RSOM50 provides contrast of deeper structures. **c)** Absorber volume fraction of optoacoustic contrasts at various energies as a function of depth. The superficial and deep horizontal plexus are characterized by a peak in the AVF. The deep horizontal plexus is only observed in RSOM50. With decreasing energy the AVF of the deep horizontal plexus decreases, *i.e.* some of the vascular features are lost. sc - *stratum corneum*, shp - superficial horizontal plexus, dhp - deep horizontal plexus. Adapted from Schwarz *et al.* [106].

was calculated:

$$\mathrm{AVF}(z_{k_0}) = \frac{1}{N_x N_y 21} \sum_{i,j,k'=1}^{N_x,N_y,21} H\left(R_{\mathrm{slab}}(x_i, y_j, z_{k'}; k_0) - 0.25 \max_{i,j,k'} \left[R_{\mathrm{slab}}(x_i, y_j, z_{k'}; k_0)\right]\right), \tag{4.13}$$

where the Heaviside step function $H(x)$ takes the value 1 if the voxel amplitude is greater than 25% of the maximum amplitude within the slab and 0 if the voxel amplitude lies below 25%. Thus, the sum in equation (4.13) counts the number of voxels within the slab, whose amplitude lies above 25%. Since each slab has a vertical size of 21 pixels, the summation over z runs from 1 to 21. The AVF provides information on the concentration of optoacoustic absorbers within the skin at a specific depth. Since the vascular network in human skin is organized in layers of high blood volume, e.g. the superficial and deep horizontal plexus, and layers of low blood volume, e.g. most of the reticular dermis, skin layers are identified with the help of the AVF. The AVF is only meaningful in areas where optoacoustic absorbers are observed, *i.e.* at depths yielding only background signal, the AVF was not calculated.

Figure 4.5 depicts the influence of excitation energy on the image contrast for both RSOM100 and RSOM50. The vertical MAPs shown in Figure 4.5a reveal several interesting features.

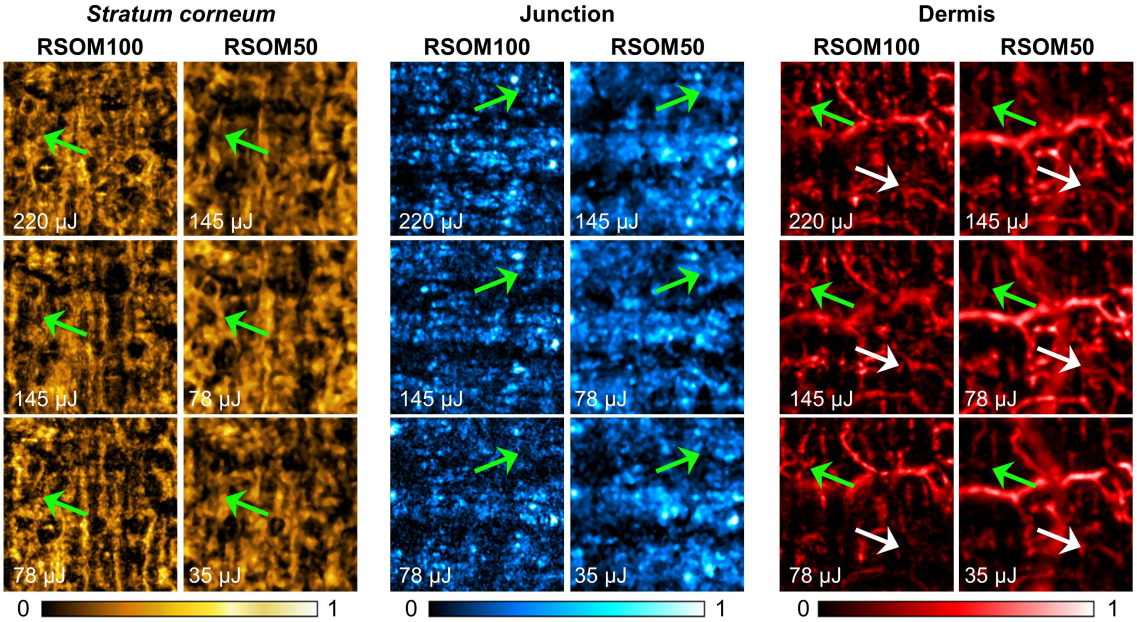

Figure 4.6.: Image quality of RSOM100 and RSOM50 as a function of excitation energy. The palm of a healthy volunteer was imaged at various energies. Comparison of ROIs, measuring 2.25 mm × 2.25 mm, acquired with RSOM100 and RSOM50 at different energies. Golden (left): lateral MAP of the *stratum corneum* ($0 - 210\,\mu$m). Hot cyan (center): epidermal-dermal junction ($210 - 350\,\mu$m). Note superior resolution of RSOM100 as compared to RSOM50 (green arrows). The background signal increases with decreasing excitation energy. Neon-red (right): dermal vasculature ($350 - 1200\,\mu$m). The green arrows pinpoint small vessels resolved better with RSOM100, whereas RSOM50 reveals in more detail larger vessels. The white arrows mark a region where vascular features disappear with decreasing energy. Adapted from Schwarz *et al.* [106].

First, RSOM50 resolves better the vascular network of the deep horizontal plexus compared to RSOM100, even at very low excitation energy (see white arrows). Second, vascular features of the deep horizontal plexus that are resolved at per-pulse excitation energies above 78 μJ disappear on images acquired with RSOM50 at an excitation energy of 35 μJ. Third, with decreasing excitation energy the background increases, *i.e.* the CNR drops. Figure 4.5b quantifies the drop in CNR related to reduction of excitation energy. The CNR decreases from > 15 dB at 220 μJ per-pulse to approximately 2 dB at 78 μJ per-pulse for RSOM100. Similarly, the CNR drops from 20 dB at 145 μJ to 12 dB at 35 μJ in RSOM50. Figure 4.5c depicts the absorber volume fraction, *i.e.* the fraction of volume occupied by optoacoustic absorbers in reconstructed images, as a function of depth. Peaks in the AVF within the dermis correspond to a high density of blood vessels, which is found in the superficial and deep horizontal plexus. Whereas the superficial horizontal plexus is visualized by both RSOM50 and RSOM100, the deep horizontal plexus is only visible in RSOM50 images. Furthermore, the AVF in the superficial and deep horizontal plexus decreases when reducing the excitation energy, *i.e.* blood vessels disappear at very low excitation energy.

The qualitative influence of excitation energy on the contrast was further analyzed in Figure 4.6, which compares the contrast of RSOM100 and RSOM50 images of identical ROIs within three different skin layers. As can be seen within the *stratum corneum*, RSOM100 provides higher resolution and reveals morphological features in greater detail. Decrease in

excitation energy in all instances has been associated with decline of contrast, albeit principal morphological features remained visible. Similar results are obtained from the epidermal-dermal junction, with RSOM100 providing higher resolution, with reconstructed images however appearing noisier at lower energies. Interestingly, the most pronounced differences between various excitation energies have been observed within the vascular structures of the dermal layer. As evident from the green arrows in Figure 4.6, small vessels of the superficial horizontal plexus can be resolved with RSOM100, whereas large vessels of the lower dermis are visible with RSOM50 only. The white arrows in Figure 4.6 present an example where reduction of the energy leads to loss of vascular features.

4.6. Deposited energy and maximum imaging speed of in vivo RSOM

To safely image skin in patients and healthy volunteers with RSOM, it is essential to comply with laser safety guidelines. To our knowledge, laser safety standards endorsed by the American National Standards Institute (ANSI) [100] and by DIN in the European Union (standard 60825-1) define more restrictive safety limits for raster-scanning optoacoustic systems, compared to formulas presented previously [98].

4.6.1. Laser safety regulations

The maximum permissible pulse energy delivered to tissue depends on operational RSOM parameters, *i.e.* wavelength and pulse length of the laser, pulse repetition rate PRR, illumination diameter d, RSOM scanning step Δ, and lateral size l_{fs} of the scanned ROI. Figure 4.7a depicts the acquisition protocol of RSOM and illustrates important operational parameters. Based on the RSOM acuqisition protocol, three safety limits have to be fulfilled according to [100].

First, a single pulse must not exceed the maximum permissible exposure (MPE) of 20 $\mathrm{mJ/cm^2}$:

$$E_{\mathrm{pulse}} \leq \pi \left(\frac{d}{2}\right)^2 20 \frac{\mathrm{mJ}}{\mathrm{cm}^2} \tag{4.14}$$

Following equation (4.14), the maximum pulse energy increases with increasing diameter of the illumination spot.

Second, the MPE of a pulse train of duration shorter than 10 s must not exceed $1100\, t^{1/4}$ $\mathrm{mJ/cm^2}$:

$$E_{\mathrm{pulse}} \leq 275\pi \left(\frac{1}{2}\right)^{3/4} \left(\frac{d}{\mathrm{cm}}\right)^{5/4} \left(\frac{\Delta}{\mathrm{cm}}\right)^{3/4} \left(\frac{\mathrm{PRR}}{\mathrm{Hz}}\right)^{-1/4} \mathrm{mJ} \tag{4.15}$$

The additional factor $(1/2)^{3/4}$ compared to a previous study [98] stems from the fact that some areas close to the turning point of neighboring B-scans are exposed over a distance of $2d$. Following equation (4.15), the maximum pulse energy increases with increasing diameter of the illumination spot, increasing step size, and decreasing pulse repetition rate.

Third, the average MPE incident on the skin surface for more than 10 s must not exceed 200 $\mathrm{mW/cm^2}$:

$$E_{\mathrm{pulse}} \leq \left(\frac{2d}{\Delta}\right)^{-1} \left(\frac{2l_{\mathrm{fs}}}{\Delta \mathrm{PRR}}\right) \pi \left(\frac{d}{2}\right)^2 200 \frac{\mathrm{mW}}{\mathrm{cm}^2} = \frac{\pi d l_{\mathrm{fs}}}{4\mathrm{PRR}} 200 \frac{\mathrm{mW}}{\mathrm{cm}^2}, \tag{4.16}$$

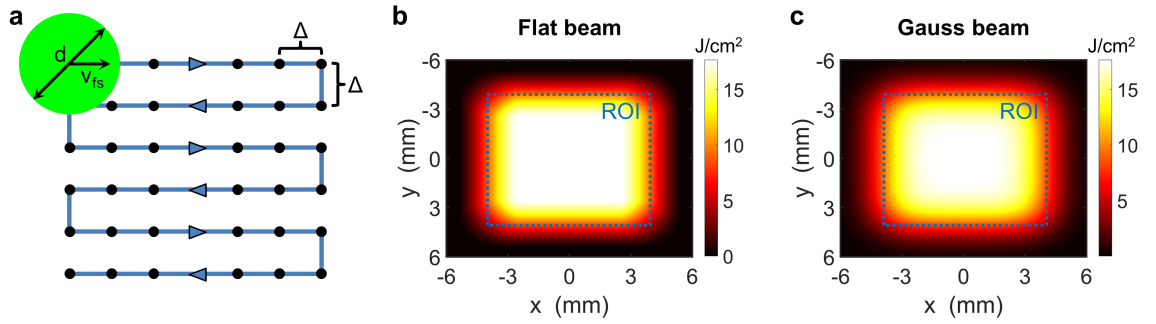

Figure 4.7.: RSOM acquisition protocol and accumulated deposited energy. a) Schematic of the acquisition protocol in RSOM. The pulsed laser beam (green circle) with diameter d is scanned along a raster-pattern over the ROI spanning l_{fs} in width at a speed of $v_{\mathrm{fs}} = \Delta PRR$. The black dots illustrate the center position of subsequent laser pulses. Neighboring scan positions are separated by a distance Δ. **b)** Accumulated light fluence incident on the ROI after one complete raster-scan. The ROI measured 8 mm × 8 mm, the step size was set to $\Delta = 20\,\mu$m, and the diameter of the flat laser beam was set to $d = 3$ mm. The pulse energy was set to $100\,\mu$J. **c)** Accumulated light fluence incident on the ROI after one complete raster-scan, assuming a Gaussian beam of $100\,\mu$J pulse energy. All other parameters are the same as in (b). Note that the peak energy incident on the ROI is slightly lower for the Gaussian beam compared to the flat beam.

where $^{2d}/_{\Delta}$ represent the number of laser pulses incident on a single spot during two B-scans, $^{2l_{\mathrm{fs}}}/_{\Delta PRR}$ the time needed to perform two B-scans, and $\pi(^{d}/_{2})^2$ is the illuminated area. Following equation (4.16), the maximum pulse energy increases with increasing diameter of the illumination spot, increasing size of the ROI, and decreasing pulse repetition rate.

For typical RSOM operational parameters equation (4.16) is the most restrictive laser safety limit (see Table 4.3), the reason being the accumulation of deposited energy within the ROI during the 2D scan.

To illustrate the accumulation of deposited energy within the scanning area, the light accumulated light fluence was simulated for typical RSOM parameters in Figure 4.7b for a flat laser beam. The accumulated light fluence was obtained by convolution of the laser beam profile with every acquisition point on the 2D acquisition grid. The diameter of the flat laser beam was set to $d = 3$ mm, and the pulse energy was set to $100\,\mu$J. The ROI measured 8 mm × 8 mm, and the step size was set to $\Delta = 20\,\mu$m. Figure 4.7b shows that the accumulated light fluence is in the range of several $^{\mathrm{J}}/_{\mathrm{cm}^2}$ despite a relatively low pulse energy of $100\,\mu$J. The light fluence within the ROI is relatively homogeneous, whereas the accumulated energy decreases towards the boundary of the ROI. In equations (4.14)-(4.16) the MPE limits were calculated for a flat circular beam profile. In reality, however, the beam profile has usually a Gaussian beam profile. For this reason the accumulated deposited energy was as well simulated for a Gaussian beam profile assuming a standard deviation of the Gaussian to be equal to the radius of the flat laser beam. Again the pulse energy was assumed to be $100\,\mu$J. All other parameters are the same as in Figure 4.7b. By comparing the light fluence distribution of the flat beam with the Gaussian beam profile, several features are observed. First, the distribution is relatively similar. In the case of the Gaussian beam profile, the energy is slightly more distributed. Second, maximum value of accumulated energy within the ROI is slightly smaller for the Gaussian beam profile. Thus, although equations (4.14)-(4.16) arise from a simplified model of the laser beam profile, the formulas constitute an upper limit

$\mathbf{E_{pulse}}$	$\mathbf{E_{pulse,\,max}}$	$\mathbf{PRR_{max}}$			**IPPS**	
	Eq. (4.14)	Eq. (4.15)		Eq. (4.16)	Eq. (4.17)	
	RSOM100 RSOM50	RSOM100[a]	RSOM50[b]	RSOM100 RSOM50	RSOM100[a]	RSOM50[b]
220 μJ	3.9 mJ	929 Hz	7.43 kHz	286 Hz	71 IPPS	63 IPPS
145 μJ	3.9 mJ	4.92 kHz	39.4 kHz	433 Hz	108 IPPS	95 IPPS
78 μJ	3.9 mJ	58.8 kHz	470 kHz	806 Hz	201 IPPS	178 IPPS
35 μJ	3.9 mJ	1.45 MHz	11.6 MHz	1.80 kHz	449 IPPS	397 IPPS

Table 4.3.: Maximal permissible exposure and maximal imaging speed for RSOM100 and RSOM50 according to equation (4.14)-(4.17). System parameters: illumination diameter $d = 5$ mm, ROI = 8 mm × 8 mm.
[a] RSOM100: $\Delta = 10\,\mu$m, lateral resolution = 20 μm.
[b] RSOM50: $\Delta = 20\,\mu$m, lateral resolution = 42.5 μm.

for laser safety regulations that is applicable to a Gaussian beam profile as well.

4.6.2. Maximal imaging speed of RSOM

Imaging speed is of primary importance in clinical imaging, concerning both image quality and patient comfort (see chapter 5). To compare the imaging speed of UB-RSOM to skin imaging systems used by other groups, a platform-independent measure of imaging speed, which calculates the image pixels acquired per second (IPPS) is given as follows:

$$\text{IPPS} = \frac{\text{Scanned area}}{\text{Lateral resolution}^2 \cdot \text{Acquisition time}}, \tag{4.17}$$

where the scanned area divided by the lateral resolution squared gives the number of pixels in the final image.

Pulse repetition rate and, thus, imaging speed in raster-scan optoacoustic mesoscopy is limited by laser safety regulations and depends on several operational parameters (see section 4.6.1), most importantly on the acquisition step size, the per-pulse excitation energy, the illumination diameter, and the size of the ROI. Table 4.3 summarizes the maximum permissible exposure, resulting from equations (4.14)-(4.16), assuming an illumination diameter of 5 mm and a ROI measuring 8 mm × 8 mm. Equation (4.14) specifies the maximal energy for a single pulse, which takes the same value for RSOM100 and RSOM50. The maximum per-pulse energy is 3.9 mJ independent of PRR and, thus, much larger than 220 μJ, which is the highest *in vivo* per-pulse energy used in this chapter. Equation (4.15) determines limits for the maximal PRR of a pulse train shorter than 10 s, based on the per-pulse energy employed and acquisition step size Δ. In RSOM50 the maximal PRR is greater than 2 kHz (*i.e.* the maximum repetition rate of the laser) for all per-pulse energies. RSOM100, by contrast is limited to a PRR of 929 Hz at a per-pulse energy of 220 μJ. The most restrictive MPE limits arise from equation (4.16), which determines the mean maximal power incident on the skin surface for exposure longer than 10 s. Table 4.3 shows the maximal PRR according to equation (4.16), which is the same for both RSOM100 and RSOM50. Based on the most restrictive laser safety limits, the number of imaged pixels per second were calculated and are visualized in Table 4.3. The number of imaged pixels per second is inversely proportional to the per-pulse energy, ranging between $63 - 449$ IPPS.

4.7. Summary and discussion

This chapter presents the first quantitative account on the relation between the excitation energy, detection bandwidth, and imaging depth achieved with optoacoustic dermoscopy. It combines computer modeling with phantom measurements and *in vivo* imaging of human skin to gain rigorous data on optimal and marginal energy ranges required for concurrent interrogation of all skin layers. Implementation of high-frequency RSOM100 has yielded superb imaging of dermal papillae and superficial horizontal plexus at higher resolutions, while RSOM50 enabled visualization of the architecture and vascularization patterns throughout the entire skin depth, albeit at lower resolution. The results reported herein not only assist in making a valid choice for detector bandwidth but also provide an empirical basis for enhancing the imaging speed and performance to yield high resolution 3D data.

Optical - and acoustic attenuation limit imaging depth and detection bandwidth

In section 4.2 and 4.3, the physical limitations dictated by optical attenuation of the excitation light and acoustic attenuation of ultrasound waves have been studied.

Several interesting aspects follow from the light fluence simulations presented in section 4.2. First, due to the large scattering coefficient of cutaneous skin, the light fluence in human cutaneous tissue can reach up to 10 times higher values $100 - 200\,\mu$m below the skin surface compared to the light fluence above the skin surface in water. Second, the light fluence decreases exponentially with depth. Since optoacoustic signal amplitude is proportional to the light fluence, the strength of optoacoustic signals drops exponentially with depth, limiting imaging depth.

To increase the imaging depth, the excitation wavelength can be tuned, since the optical penetration depth in human skin is proportional to $\mu_a^{-1/2}$ and increases with decreasing absorption. The excitation wavelength of 532 nm, which is used for single-wavelength RSOM, enables an optical penetration depth in the range of $1 - 1.5$ mm in cutaneous tissue [112]. Interestingly, although both ROSM100 and RSOM50 were capable of resolving epidermal structures and dermal vessels of thick human skin, they fall short in visualizing subcutaneous vessels. To achieve a better penetration depth for RSOM, the excitation wavelength could be increased up to ~ 650 nm or even to the near-infrared range, where the optical penetration depth extends to several millimeters [112]. However, due to dramatic decline in hemoglobin absorption by approximately two orders of magnitude from 532 nm to 650 nm [117, 155], the use of far red or near-infrared wavelengths would result in a decline in imaging sensitivity, necessitating imaging at much higher energies (up to $10\,^{\mathrm{mJ}}/_{\mathrm{cm}^2}$) with greatly reduced imaging speed [103, 105].

The study on acoustic attenuation in section 4.6 shows how the detection bandwidth of RSOM decreases as a function of depth. In case of RSOM50, the -12 dB cutoff frequency reduces from 88 MHz at the tissue surface to 70 MHz at a depth of 2 mm. For RSOM100, the relative loss in the transducers sensitivity is more significant. The high-cutoff frequency reduces from 155 MHz at the tissue surface to 85 MHz at a depth of 2 mm. Especially high frequencies are attenuated by biological tissue and water, and frequencies above 120 MHz are expected to be detectable only superficially, within the first few 100 μm.

Relating experimentally determined detection bandwidth as a function of depth to the requirements dictated by skin anatomy

In section 4.4, the depth-dependent detection bandwidth of both RSOM100 and RSOM50 has been evaluated experimentally. At this point it is highly interesting to relate the findings on the experimentally determined detection bandwidth to the requirements dictated by the anatomy of human skin (see section 2.5). In section 2.5, the requirements in terms of imaging depth and frequency bandwidth have been defined for optoacoustic dermoscopy. Simulations have shown that the peak frequencies generated by modeled human skin decrease from $\sim 150\,\mathrm{MHz}$ at the dermal papillae to $\sim 90\,\mathrm{MHz}$ within the superficial horizontal plexus and further down to $\sim 15\,\mathrm{MHz}$ at the deep horizontal plexus. Hence, concurrent imaging of the entire human skin requires detection of ultrasound frequencies above 150 MHz for resolving superficial (up to $450\,\mu\mathrm{m}$) elements while visualizing deeper structures (up to 1.5 mm depth) entails detection of signals below 30 MHz. Indeed, measurements performed on the skin-mimicking phantom (Figure 4.3) have confirmed that RSOM100 detects frequencies up to 180 MHz but at limited 1 mm depth, whereas deeper imaging (up to 1.5 mm) at meaningful resolutions can be achieved with RSOM50 at frequencies lower than 140 MHz. Hence, RSOM100 detects higher frequencies but resolves dermal features more superficially, whereas RSOM50 samples signals with lower frequency but from the entire skin depth.

To conclude, RSOM conforms well to the frequency response generated by simulated skin tissue. Thus, RSOM is well-suited to detect vessels of various sizes through all skin layers.

Optimal range of excitation energy and imaging speed

Following the experimental evaluation of detection bandwidth as a function of excitation energy in section 4.4, the consequences for humans skin RSOM *in vivo* have been studied in section 4.5 and 4.6. Both the impact of excitation energy on the image quality and on the imaging speed have been studied. Finding the best compromise between fast imaging speed and high contrast, while of major importance, is also a daunting task given that several physical processes are involved. Since optoacoustic signals can only be detected above the NEP of the detector [166,183], and signals in UB-RSOM are expected to scale proportionally with the light fluence [190] at constant temperature [191], greater pulse energies favor higher imaging contrast. Conversely, higher per-pulse energies result in lower PRR, *i.e.* lower imaging speed (see equations (4.14)-(4.16)), rendering the imaging with high excitation energy slow and prone to distortion due to motion. Selection of the optimal excitation energy is therefore of great importance in RSOM in order to achieve reproducible data at reasonable pace under clinical settings [155]. As demonstrated herein, reduction of the excitation power below a certain threshold results in deterioration of the imaging quality with complete loss of major structural features acquired with both RSOM100 and RSOM50. Based on *in vivo* measurements and computational studies, a range of excitation pulse energies of $150-200\,\mu\mathrm{J}$ and $80-100\,\mu\mathrm{J}$ present the best compromise between the imaging speed while maintaining high sensitivity (contrast) at sufficient imaging depth for RSOM100 and RSOM50. At a pulse energy of $100\,\mu\mathrm{J}$, RSOM50 enables fast measurements at a maximal PRR of 625 Hz through the entire skin depth, acquiring a ROI of $8\,\mathrm{mm} \times 8\,\mathrm{mm}$ in less than 260 s, corresponding to 138 imaged pixels per second (see equation (4.17)), which is faster compared to other optoacoustic measurements reported elsewhere (up to 85 pixels per second) [99,102,103,105]. For comparison, RSOM100 is limited by a maximal PRR of 314 Hz at $200\,\mu\mathrm{J}$ excitation energy, imaging 78 pixels per second. Note that both RSOM100 and RSOM50 allow for similar

or even higher imaging speed compared to other studies, despite the more restrictive laser safety limit specified in equation (4.16).

5. Motion correction

This chapter contains adapted text passages and figures from a manuscript submitted for publication by Schwarz *et al.* [192]. More information on the permission to reproduce textual material, illustrations, and tables is found in appendix B.

5.1. Introduction

Although, in early RSOM publications by our group, the resolution and image quality of human skin *in vivo* was already impressive [174, 184], patient/volunteer motion prevents to fully exploit the resolution of $< 20\,\mu$m achieved by RSOM [3,164]. In optoacoustic mesoscopy a raster-scanning approach is typically used, where the piezoelectric detector or laser interrogation beam is scanned point-by-point over a 2D ROI. The whole acquisition process takes several minutes [3, 99, 102, 103, 105, 106, 164, 174, 184, 193], whereas motion-inducing physiological processes such as the respiration rate are much faster; *i.e.* 12-18 respiratory cycles per minute in adults [194] and up to 30 cycles per minute in elderly people [195]. Since RSOM is a tomographic imaging modality, the quality and resolution of reconstructed images rely on accurate knowledge of the relative position of the ultrasound detector with respect to the ROI. Patient motion during data acquisition inevitably leads to a deterioration of image quality and motion artifacts in the reconstructed images.

Optoacoustic tomography is based on the acquisition of broadband ultrasonic waves. Thus, the ROI needs to be acoustically coupled to the detector in a way that losses of broadband ultrasonic signals are minimized. Coupling is commonly done with water [174, 180], acoustic gel [181], very thin plastic membranes [102,163,184,196–198], or a combination of the former. None of the aforementioned coupling media are solid and, thus, susceptible to be deformed by the motion of the subject. To reduce breathing motion in small animal imaging, the animals are usually anaesthetized and restrained [98, 163], or the small animal is positioned on top of the detector or mouse bed [199, 200]. The restriction of motion in humans is more challenging compared to small animals since human subjects can neither be anaesthetized nor sufficiently restrained during measurements. Thus, the tiniest movement of the head, limbs, or breathing motion of the abdomen will give rise to micromotion even in distant locations on the human body. Speeding up the acquisition will reduce motion artifacts [99], however, the imaging speed in optoacoustic mesoscopy of human skin is limited by safety regulations (see section 4.6.1). Through parallel acquisition of optoacoustic data, motion artifacts could be evaded, yet, the resolution and SNR of optoacoustic devices using parallel acquisition is not comparable to RSOM technology [180, 181, 198, 200–202].

Only a few software solutions have been proposed in optoacoustic imaging to compensate for motion. In small animal imaging, whole 2D cross-sections have been clustered according to the breathing cycle or cardiac cycle [203,204]. Since the proposed algorithms rely on simultaneous imaging of whole 2D cross-sections and a repetitive cycle of motion, it is not applicable

to RSOM of human skin. According to the authors of reference [205], a surface-alignment algorithm has been used to reduce artifacts at the expense of resolution in optoacoustic endoscopy. Yet, the surface-alignment algorithm was neither described in detail nor tested for accuracy.

In this chapter, a correction algorithm will be presented, which was developed for RSOM. The algorithm enables robust tracking of the skin surface and compensates for motion during the acquisition. The algorithm takes advantage of melanin absorption in the epidermis and is based on the assumption of a continuous and smooth skin surface. Due to the motion correction, unprecedented resolution of single capillary loops and the microvessels of the superficial horizontal plexus will be shown in *in vivo* experiments of human skin. The correction algorithm applied to clinical data not only improves image quality but enables the researcher to distinguish between vascular changes due to disease and motion artifacts. Finally, it will be shown that motion correction is inevitable in multispectral mesoscopy in order to gain accurate readings of blood oxygenation *in vivo*.

Experimental image quality improvement is shown for high resolution RSOM100, clinical RSOM55, and MSOM. The experimental setups are described in section 3.2. All of the reconstructed data in chapters 4, 7, and 8 were processed by the motion correction algorithm presented below.

5.2. Origin of motion in raster-scan optoacoustic mesoscopy

Originating from the raster-scanning approach used in mesoscopic setups, the ultrasound detector is scanned along a fast-scanning axis and a slow-scanning axis (see Figure 3.1 and 5.1a). At each acquisition point, a 1D depth resolved time signal is acquired, referred to as A-line. By 1D scanning of the detector along the fs-axis, a 2D cross-section is acquired, referred to as B-scan. By additional scanning of the detector along the ss-axis, a stack of B-scans, i.e. a 3D sinogram, is acquired. Assuming an acquisition step size of Δ and a ROI spanning l_{fs} along the fs-axis, the acquisition speed takes the values $v_{\mathrm{fs}} = \mathrm{PRR}\Delta$ and $v_{\mathrm{ss}} = v_{\mathrm{fs}}\Delta/l_{\mathrm{fs}}$. Since the step size is much smaller than the dimension of the ROI, it is $v_{\mathrm{fs}} \gg v_{\mathrm{ss}}$. In case of RSOM55 typical values are $v_{\mathrm{fs}} = 15\,\mathrm{mm/s}$ and $v_{\mathrm{ss}} = 0.045\,\mathrm{mm/s}$. Due to motion of the patient, e.g. caused by motion of neighboring body parts or breathing events, the vertical position of the ROI is changed between successive B-scans (see Figure 5.1b). Consequently, cross-sections along the ss-axis appear discontinuous and rippled (see Figure 5.1d), whereas cross-sections along the fs-axis appear continuous and smooth (see Figure 5.1c). Motion arises since the whole acquisition process takes several minutes [3, 99, 102, 103, 105, 106, 164, 174, 184, 193], whereas motion-inducing physiological processes, such as the respiration rate and head or limb movement, are much faster. Furthermore, in a clinical context, the ROI is often located on body sites, such as the elbow, that are difficult to stabilize while scanning.

5.3. The motion correction algorithm

The motion correction algorithm presented in this work is based on one assumption: The skin surface is assumed to be continuous and smooth on a mesoscopic scale, *i.e.* on the scale of several micrometers. Since melanin is a strong absorber at 532 nm, the epidermal layer of

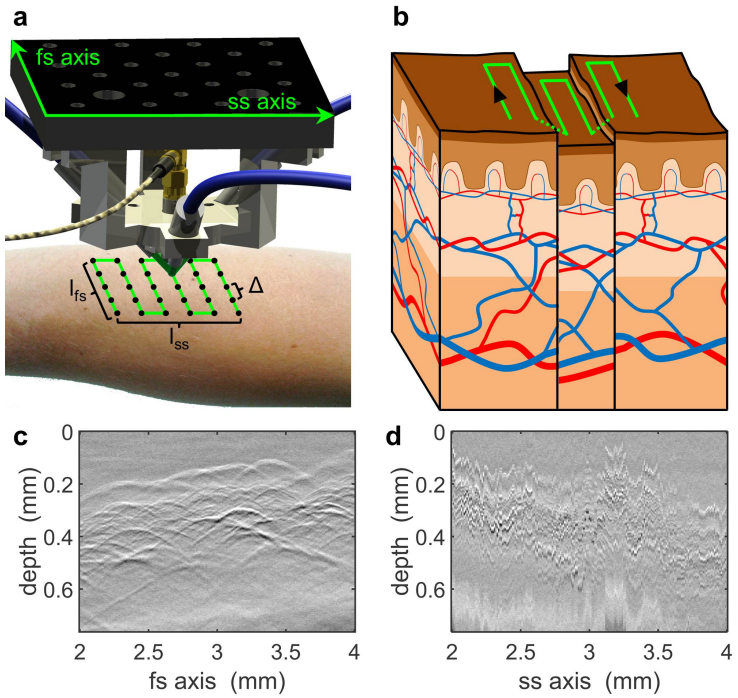

Figure 5.1.: Origin of motion artifacts in RSOM. a) Schematic of the detector-illumination unit, which is scanned over the sample along a raster pattern. The ROI measures $l_{\mathrm{fs}} \times l_{\mathrm{ss}}$, and the acquisition step size is given by Δ. **b)** Schematic of motion occurring during the acquisition. Movement of the sample causes disruption of the skin surface of epidermis and dermal vessels. **c)** B-scan along the fs-axis showing no movement between subsequent scanning positions. **d)** B-scan along the ss-axis showing strong motion between neighboring scanning positions. Adapted from Schwarz *et al.* [192]

human skin generates a strong optoacoustic signal. According to the principle of Huygens-Fresnel, an ultrasonic wave following the shape of the skin surface is emitted toward the ultrasound detector. Movement during the measurement, however, will distort the recorded skin surface, and disruptions in the absorption of the epidermal layer will be visible in the recorded 3D sinogram (see Figure 5.1d). The motion correction algorithm consists of two main steps. First, an algorithm is applied to detect the skin surface. Second, an artificial smooth skin surface is generated from the detected disrupted surface to correct for the motion.

The main challenge lies in detecting the footprint of the skin surface in the 3D sinogram. Depending on body site, two different approaches have been employed. In case of hairless skin, e.g. the human palm, signal from the *stratum corneum* is separated spatially by several 100 μm (see Figure 5.2a). Thus, the *stratum corneum* can be roughly segmented by a 2D parabolic slab (see Figure 5.2b). Within the segmented slab, the surface is found by the maximum value within each A-line.

In case of hair-bearing skin, e.g. the lower arm, a different approach has to be employed since the *stratum corneum* is not sufficiently separated in space from the underlying *stratum basale* and dermal papillae (see Figure 5.3c). Still, the melanin layer of the epidermis leaves a distinctive footprint in the 3D sinogram. Ultrasound signals emitted by the broadly illuminated melanin layer of the skin induce lateral modes in the piezoelectric detector, leaving a

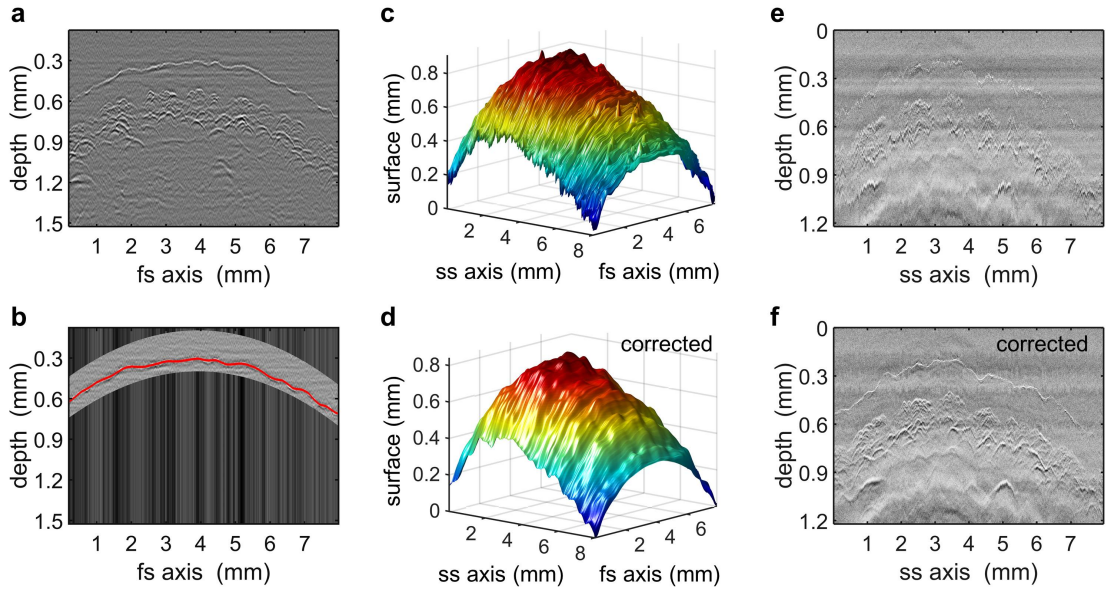

Figure 5.2.: Skin surface recognition in thick hairless skin. a) In hairless skin, such as the human palm, there is a clear separation of the *stratum corneum* from underlying vascular of the dermis. **b)** Performance of skin surface detection algorithm applied to a semi-automatic segmentation of the *stratum corneum* within the B-scan shown in (a). The red line indicates the detected skin surface. **c)** 2D skin surface detected by the algorithm. Motion during data acquisition shows up as small ripples on the surface. **d)** 2D skin surface after motion correction. Motion-induced ripples have disappeared. **e)** Acquired B-scan along the ss-axis before motion correction. **f)** Same B-scan as in (e) after motion correction. ss: slow-scanning; fs: fast-scanning. Adapted from Schwarz *et al.* [192]

characteristic low-frequency footprint in the raw data approximately 600 μm below the skin surface. Intensity profiles show that shape and intensity of the low-frequency band scale with the shape and intensity of the skin surface (see Figure 5.3a). Multispectral images of the lower arm confirm that the low-frequency band carries the spectral signature of melanin (see Figure 5.3b). Normally, the low-frequencies are filtered before reconstruction. The correction algorithm takes advantage of the low-frequency band by applying an exponential bandpass filter from $1-3$ MHz to the acquired raw data and roughly segmenting the time interval that captured the strongest peak (see Figure 5.3d). For each A-line the location of the maximum in the low-frequency band is determined, resulting in a 2D map representing the rippled motion-corrupted surface of the acquired data (see Figure 5.3e).

Assuming that the skin surface follows a continuous and smooth surface, an artificially-smoothed surface is created (see Figure 5.2d and Figure 5.3f) by applying a moving average filter to the rippled surface. The moving average filter showed best performance for a span of 200 (10) with respect to the ss-axis (fs-axis). To correct for the z-position of each detector position in the reconstruction algorithm, the 2D difference map between the motion-corrupted and the artificially-smoothed surface is calculated. The difference map is used to correct for the relative detector position with respect to the skin surface in the reconstruction process.

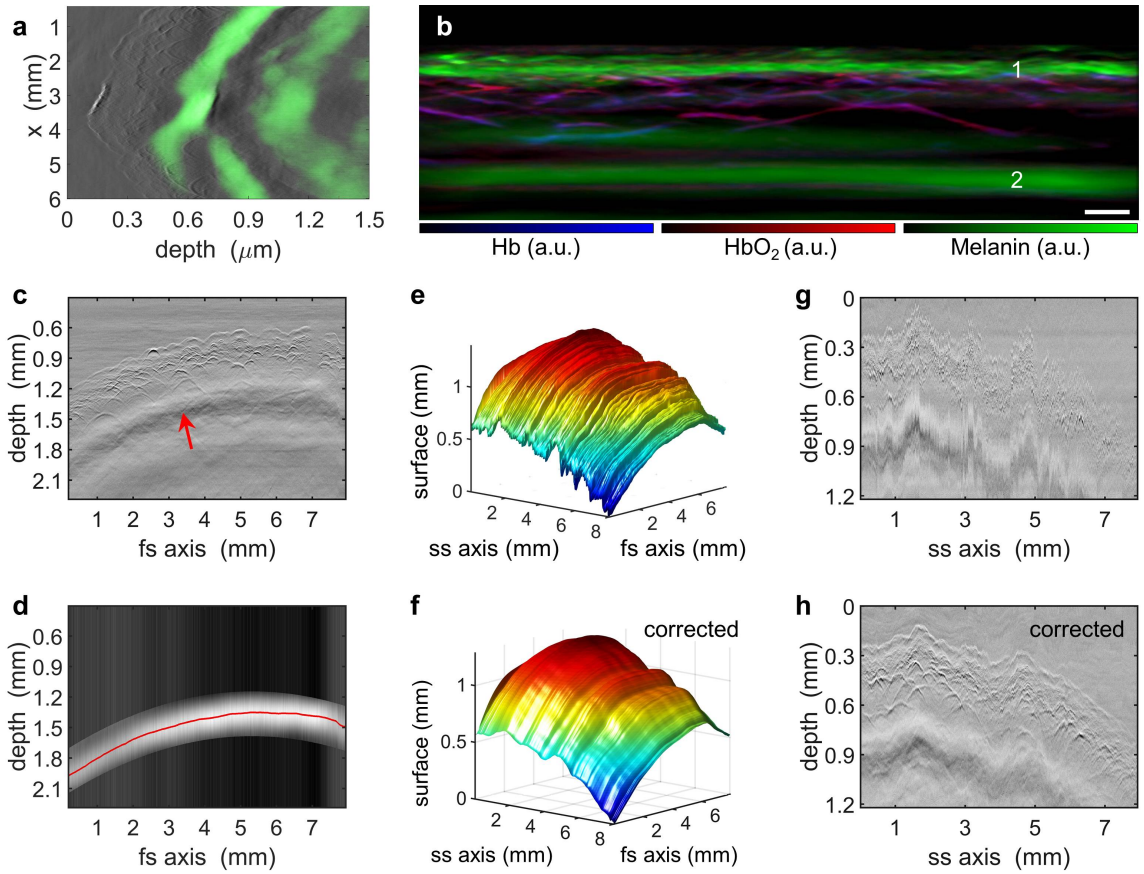

Figure 5.3.: Skin surface recognition in thin hairy skin. a) Gray-scale image of raw data overlain by low-frequency signal (1 – 10 MHz) in green. Shape and intensity of the low-frequency band scale with the shape and intensity of the skin surface. **b)** Vertical MAP of the lower arm reconstructed without bandpass filtering. The reflection signal (2) has the spectral signature of melanin and follows the shape of the epidermal layer (1). Scale bar: 250 μm. **c)** In hairy skin, e.g. the lower arm, there is no clear separation of the *stratum corneum* from underlying vascular structures. Skin surface detection is performed on the low-frequency band indicated by the red arrow. **d)** Performance of skin surface detection algorithm applied to a semi-automatic segmentation of the low-frequency band within the B-scan shown in (c). The red curve indicates the maximum value of the low-frequency band. **e)** 2D skin surface detected by the algorithm. Motion during data acquisition shows up as ripples on the surface. **f)** 2D skin surface after motion correction. Motion-induced ripples have disappeared. **g)** Acquired B-scan along the ss-axis before motion correction. **h)** Same B-scan as in (g) after motion correction. ss: slow-scanning; fs: fast-scanning. Adapted from Schwarz *et al.* [192]

5.4. Performance of the motion correction algorithm

The motion correction algorithm presented in this work has been developed for RSOM technology and was tested on *in vivo* data measured by three different RSOM implementations. High-frequency RSOM100 was applied to image the smallest vessels in healthy human skin. Clinical RSOM55 was used to acquire clinical data of diseased skin. MSOM was applied to measure blood oxygenation in healthy human skin. In the following sections, the results for each of these implementations will be shown and discussed. More detail on the clinical

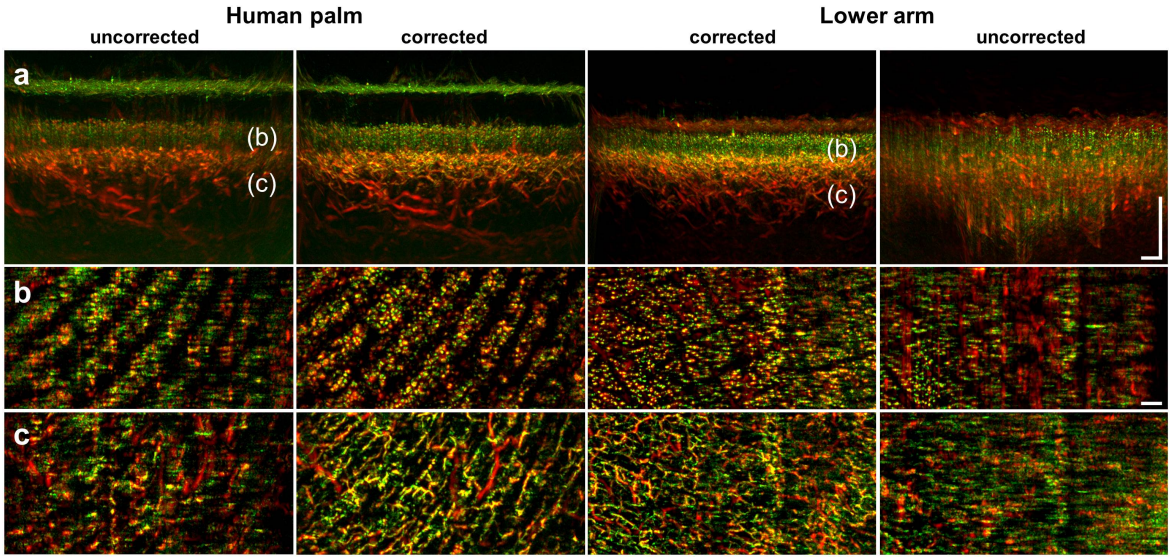

Figure 5.4.: Performance of the motion correction algorithm in the human palm and lower arm. Data was acquired with RSOM100 by scanning the human palm and lower arm of a healthy volunteer. First column: Corrupted data of the human palm. Second column: Motion-corrected data of the human palm. Third column: Motion-corrected data of the lower arm. Fourth column: Motion-affected data of the lower arm. **a)** Vertical MAPs of the reconstructed volumes showing the layered structure of human skin. Especially the high-frequency reconstruction (green channel) show strong blurring due to incoherent summation. **b)** Lateral MAPs of the dermal papillae. The structure of capillary loops is recovered after motion correction. **c)** Lateral MAPs of the superficial horizontal plexus. The small vessels captured by the high-frequency reconstruction (green channel) show a dense vascular network, which is only observed after motion correction. Scale bars: 500 μm.

RSOM55 system is found in chapter 8, more information on multispectral imaging is found in chapter 7.

5.4.1. High resolution RSOM100

To show the importance of motion correction on high resolution images acquired with RSOM100, three different body sites of a healthy male volunteer of skin type II were acquired. The first body site was located on the human palm, illustrating the results of the algorithm applied to hairless skin, characterized by a thick epidermal layer. The raw data and skin surface recognition results of this body site are shown in Figure 5.2. The second body site was located on the lower arm, presenting the results of the correction algorithm applied to hair-bearing skin, characterized by a thin epidermal layer. The raw data and skin surface recognition results of this body site are shown in Figure 5.3. The third body site was a benign nevus located on the lower arm, which was imaged to show the impressive imaging performance after motion correction.

In all RSOM100 images the low- and high-frequency bands were reconstructed separately (see section 3.6). For improved visualization of skin layers the skin surface was flattened, and the contrast of anatomical structures was evaluated as a function of depth, as described in section 4.5.2.

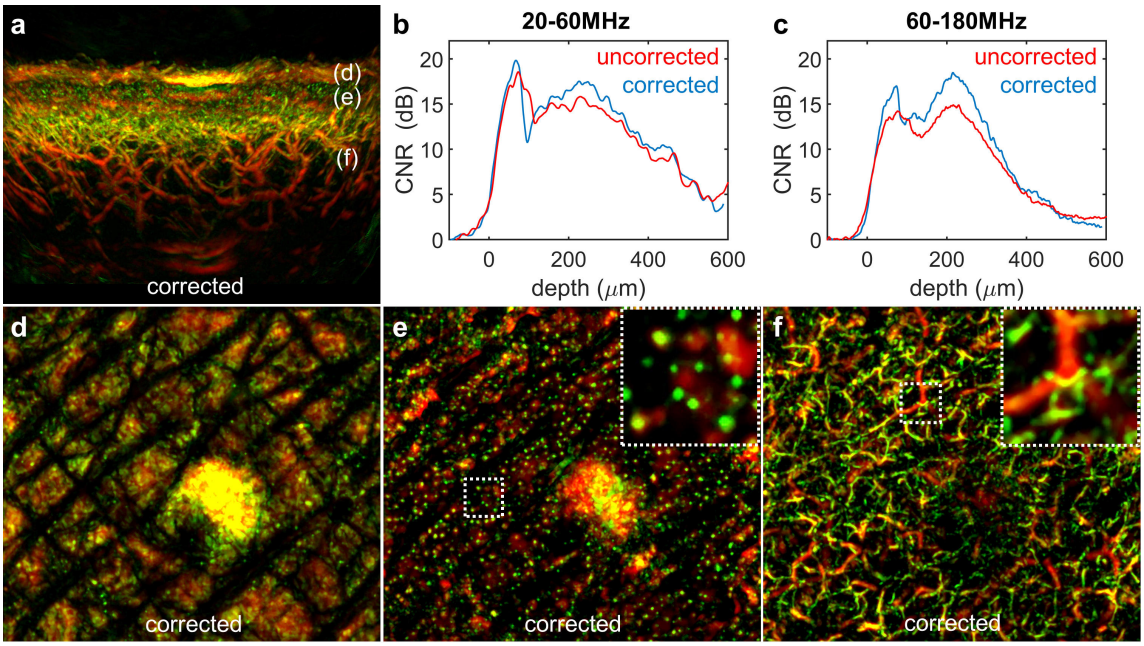

Figure 5.5.: Quantification of performance improvement due to motion correction. a) Vertical MAP of a ROI located on the lower arm surrounding a benign nevus. **b)** Mean CNR of optoacoustic absorbers with respect to depth at $20-60\,\mathrm{MHz}$. **c)** Mean CNR of optoacoustic absorbers with respect to depth at $60-180\,\mathrm{MHz}$. The CNR is calculated from the vertical MAP in (a). The CNR is higher in corrected data, most prominently at high frequencies. **d)** Lateral MAP of the epidermal layer, comprising the benign nevus. **e)** Lateral MAP of the epidermal-dermal junction. Single capillary loops are visible in the corrected image. **f)** Lateral MAP of the vast vascular network of the dermal layer. Both large vessels, depicted in red, and microvessels, depicted in green, are observed after motion correction. Scale bars: $500\,\mu\mathrm{m}$. Adapted from Schwarz *et al.* [192]

The surface recognition algorithm applied to the raw data for both hairless and hair-bearing skin shows a rippled surface, indicating micromotion on the order of several micrometers between successive B-scans (see Figure 5.2c and Figure 5.3e). The discontinuity of the skin surface is only visible along the ss-axis, but not along the fs-axis. The motion-corrected skin surface shows a continuous and smooth surface with no offset between neighboring B-scans (see Figure 5.2d and Figure 5.3f). Figure 5.4 presents the results for the reconstructed images of the human palm and lower arm before and after motion correction in direct comparison. Vertical MAPs of both body sites show strong artifacts and blurring especially of high-frequency structures before motion correction (see Figure 5.4a). The capillary loops of the epidermal-dermal junction are not resolved (see Figure 5.4b), and the dermal vasculature is not forming a network of connected vessels (see Figure 5.4c). The resolution is significantly increased after applying the motion correction algorithm for both body sites. The layered structure of human skin catches the eye in the corrected plots of Figure 5.4a. The thicker epidermal layer in hairless skin compared to thick skin is nicely seen. Single capillary loops are resolved in the epidermal-dermal junction after correction (see Figure 5.4b). In the case of the human palm, the structure of the capillary loops follows the pattern of the epidermal ridges that are observed as curved stripes of absorption. After motion correction, the dermal vasculature is organized in a dense network of larger vessels (red) and smaller vessels (green) in Figure 5.4c. The improvement in resolution in high-frequency RSOM100 is striking.

In Figure 5.5 the performance of the motion compensation algorithm is shown for the benign nevus located on the lower arm. Impressive imaging performance and quantitative improvement due to motion-compensation is shown in Figure 5.5. The vertical MAP of the corrected imaging volume is displayed in Figure 5.5a, revealing the size of the benign nevus and the underlying vascular network. Based on the vertical MAPs of both corrected and uncorrected data, the mean CNR with respect to depth was calculated and is depicted in Figure 5.5b,c. An increase in CNR of corrected data is observed in the *stratum corneum* as well as the superficial horizontal plexus. The increase in CNR is stronger at high frequencies (up to 5 dB) than in low frequencies (up to 2.5 dB). The high resolution imaging performance after motion correction is shown in lateral MAPs of the epidermis, epidermal-dermal junction, and the dermis (see Figures 5.5d-f). The boundary of the benign nevus and the epidermal ridges are sharp and clear (see Figure 5.5d). In the epidermal-dermal junction the increase in resolution becomes most apparent (see Figure 5.5e). In the epidermal-dermal junction a structured pattern of capillary loops is observed after correction. The inlay in Figure 5.5e shows a zoom-in on a region measuring $500\,\mu\text{m} \times 500\,\mu\text{m}$. A dozen distinct capillary loops are observed. Similarly, the microvessels of the papillary dermis are well resolved after motion correction. The inlay in Figure 5.5f reveals that both large (red) and small (green) vessels are resolved after correction.

5.4.2. Clinical RSOM55

To show the importance of motion correction to reliably detect vascular changes in skin disease, three patients were scanned with RSOM55. The study was approved by the ethics committee of the Technical University of Munich, and all measurements were performed in compliance with laser safety standards [100]. Patients were recruited and diagnosed by expert dermatologists. Patient 1 suffered from eczema. Patient 2 and patient 3 were both affected by psoriasis.

In all RSOM55 images the low- and high-frequency bands were reconstructed separately (see section 3.6). For improved visualization of skin layers, the skin surface was flattened, and the contrast of anatomical structures was evaluated as a function of depth, as described in section 4.5.2.

The analysis performed on the three different patient datasets, served three different purposes. First, it will be shown in a comparative study that the presented motion correction algorithm is able to fully restore the original skin surface. Second, motion correction will be applied to a dataset strongly affected by breathing motion. Third, the skin surface detection will be introduced as a measure of accuracy and reliability in clinical imaging.

Comparative study

Data from patient 1 was used in a comparative study. The original raw data acquired from patient 1 (P1orig) showed hardly any motion during acquisition and was used as quality control. A corrupted dataset (P1motion) was created by artificially introducing motion to P1orig. To create P1motion, every 700^{th} A-line of P1orig was moved randomly in time by ± 20 time points, corresponding to $\pm 30\,\mu\text{m}$ of vertical motion. The relocation of all intermediate scanning positions was calculated by spline interpolation. The motion correction algorithm was then applied to P1motion to recover a corrected dataset (P1corrected).

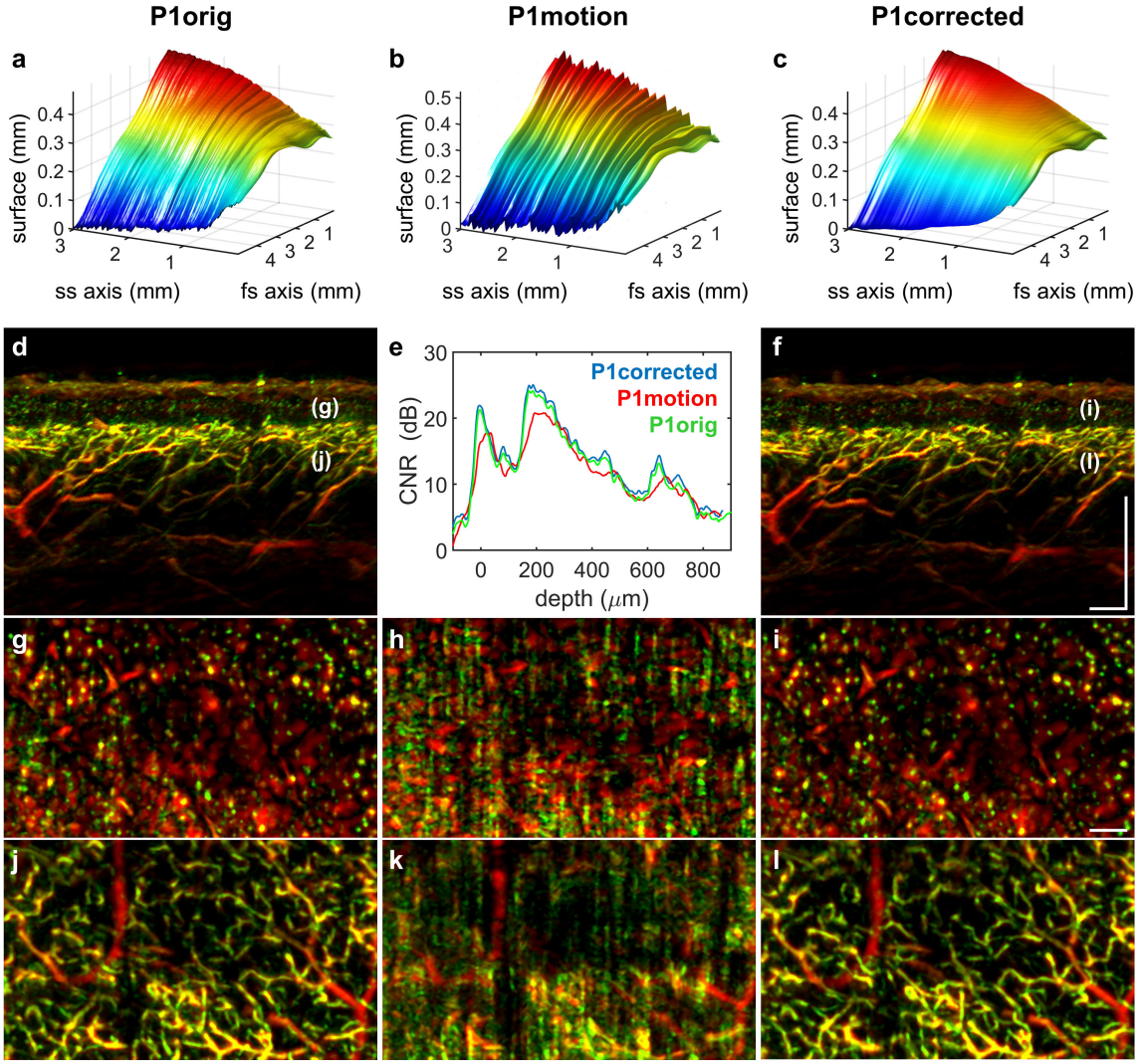

Figure 5.6.: Performance test of the motion correction algorithm applied to artificially corrupted data. Data was acquired with RSOM55 by scanning patient 1, who suffered from eczema. Left column: original data (P1orig). Center column: data with artificially introduced motion (P1motion). Right column: data obtained by correcting P1motion (P1corrected). **a-c)** Surface recognition of original, corrupted, and corrected raw data. The original skin surface shows minor discontinuities. P1motion shows large ripples similar to breathing motion. The corrected skin surface fully recovers the original shape. **d,f)** Cross-sectional MAP (side view) of the reconstructed ROI showing the layered structure of human skin. **e)** Mean CNR of optoacoustic absorbers with respect to depth. The CNR of motion-corrected images outperforms the CNR in motion-corrupted and original images. **g-i)** Lateral MAP of the epidermal-dermal junction. The capillary loops are not resolved in P1motion. **j-l)** Lateral MAP of the dermal vasculature. Scale bars: 500 μm.

The results of the comparative study are shown in Figure 5.6. Very little motion was observed in the original acquired dataset P1orig (see Figure 5.6a), which served as control for the performance of the motion correction algorithm applied to the motion corrupted dataset P1motion (see Figure 5.6b). In Figure 5.6b ripples are observed in the motion-corrupted skin surface, which are similar to patient movement. The motion correction algorithm applied to

P1motion manages to fully recover the original skin surface (see Figure 5.6c). The epidermal layer is thickened in eczema skin, measuring $\sim 140\,\mu$m. The layered structure of human skin and the exact epidermal thickness are well discernible in the original image (see Figure 5.6d). In the epidermal-dermal junction, enlarged capillary loops are observed, showing a median diameter of $48.5\,\mu$m in the high-frequency image depicted in Figure 5.6g. The vascular network of the dermis showed small vessels within the papillary dermis and larger vessels deeper inside the skin (see Figure 5.6d,j). Most of the vascular features relevant for the skin condition were not resolved in P1motion. The boundaries between skin layers are less obvious in the motion-corrupted image, and the information on capillary loops is completely lost (see Figure 5.6h). Furthermore, the small vessels of the papillary dermis are not resolved in Figure 5.6k. The image corrected for motion not only outperforms the quality of P1motion, but shows a slight improvement with respect to P1orig as well. The original shape of the skin surface was fully recovered (see Figure 5.6c). The correction algorithm filtered out even the tiniest motion in the skin surface compared to the original shape. Thus, the layered structure of the human skin and the whole vascular network of the capillary loops, papillary dermis, and the reticular dermis were resolved at higher CNR than the original data and the motion-induced data (see Figure 5.6e).

Correction of breathing motion

The measured psoriasis plaque of patient 2 was located on the long head of triceps brachii, approximately 5 cm above the olecranon. For comparison, a healthy skin region was imaged, which was located as well on the long head of triceps brachii, approximately 4 cm proximal of the psoriasis plaque. Surface detection in healthy and diseased skin showed a sinusoidal modulation of the skin surface at ~ 15 cycles per minute, *i.e.* 17-18 cycles per measurement (see Figure 5.7a).

Figure 3 shows the effect of breathing motion on reconstructions of both healthy and psoriatic skin. After motion correction, the periodic movement of the surface has disappeared for both healthy and diseased skin (see Figure 5.7a). In the motion-corrected images of psoriatic skin, typical biomarkers of inflammation are observed, e.g. thickening of the epidermis, broadening of capillary loops within the dermal papillae, and an increase in blood volume fraction of dermal vasculature (see Figure 5.7b-d). The image quality in motion-corrupted data is significantly lower compared to motion-corrected data. Whereas broadened capillary loops are well distinguished in the psoriasis plaque after correction, the same structures appear blurred before motion correction (see Figure 5.7c). The strongest discrepancy in image quality is observed in the microvessels of the superficial horizontal plexus, depicted in Figure 5.7d. In both healthy and diseased skin a structured network of smaller (green) and larger (red) vessels runs through the dermis. The smaller vessels depicted in green on Figure 5.7d appear completely blurred without motion correction.

Motion correction as a measure of reliability

To show the importance of robust and motion-free imaging in a clinical environment, healthy and diseased skin of patient 3 suffering from psoriasis was scanned. Figure 5.8 shows anatomical changes in psoriatic skin compared to nearby healthy skin. Optical absorption of the *stratum corneum* is reduced, and the epidermal thickness in psoriatic skin measures $\sim 330\,\mu$m

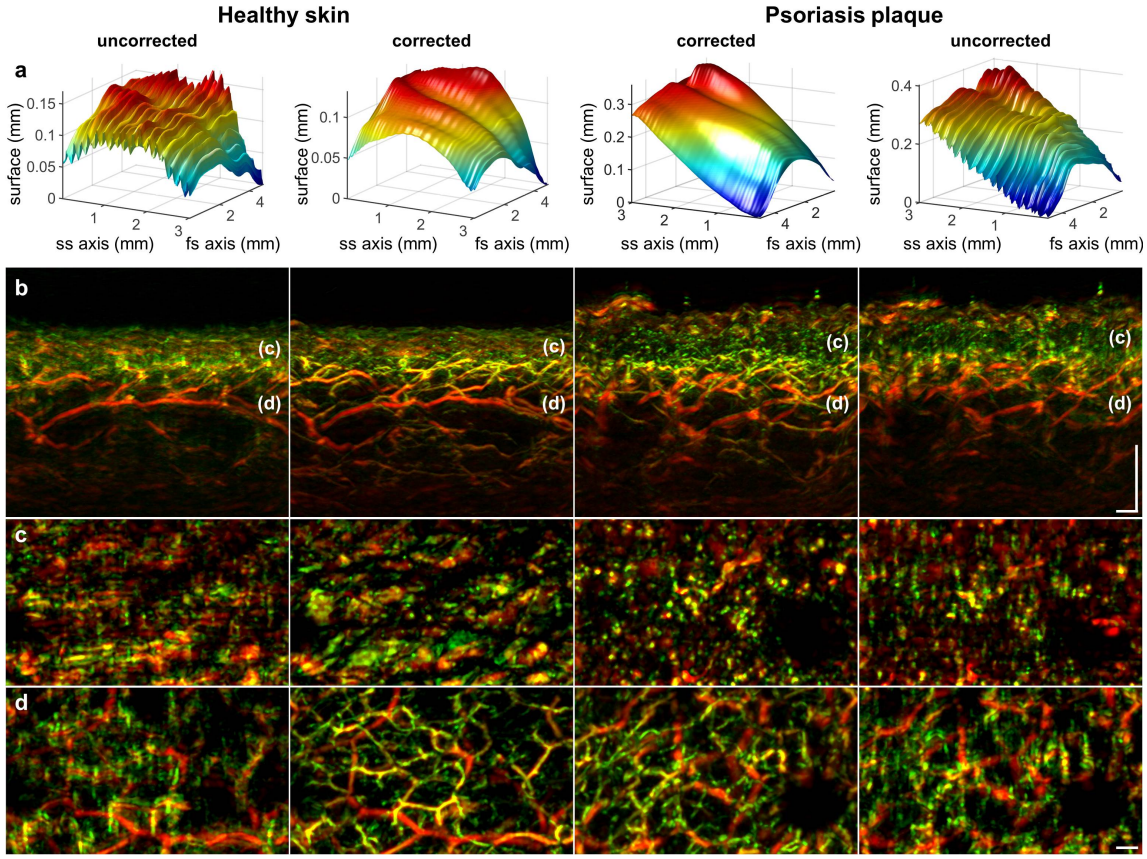

Figure 5.7.: Motion correction in clinical RSOM55. Data was acquired with clinical RSOM55 by scanning a psoriasis plaque and close-by healthy skin approximately 5 cm above the elbow of patient 1. First column: healthy skin without motion correction. Second column: healthy skin after motion correction. Third column: motion-corrected data of a psoriasis plaque. Fourth column: psoriasis plaque before correction. **a)** Detected skin surface in the raw data before and after motion correction. A periodic motion pattern due to breathing is shown on uncorrected data. **b)** Vertical MAP of healthy and psoriatic skin before and after motion correction. Psoriatic skin shows typical biomarkers: thickening of epidermis, broadening of capillary loops, and increase of blood volume fraction. **c)** Lateral MAP of the epidermal-dermal junction. Broadening of capillary loops in psoriatic skin is observed in corrected data. Capillaries in healthy skin are too small to be captured by RSOM55. **d)** Lateral MAP of the vast vascular network of the dermal layer. The microvessels, depicted in green, are not seen in motion-corrupted data for both healthy and psoriatic skin. Scale bars: 250 μm. Adapted from Schwarz *et al.* [192]

compared to $\sim 125\,\mu$m in healthy skin (see Figure 5.8a,b). Apart from epidermal thickening, the dermal vasculature is inflamed. RSOM55 is not able to resolve the small capillary loops in the epidermal-dermal junction in healthy skin (see Figure 5.8f). In diseased skin of patient 3, however, enlarged papillae are observed measuring $\sim 60\,\mu$m in diameter (see Figure 5.8d). The dermal vasculature in healthy skin is intact and forms a continuous network in the dermal layer (see Figure 5.8i). By contrast the dermal vasculature in psoriatic skin shows discontinuities and a larger volume fraction (see Figure 5.8a,g). The importance of the motion correction algorithm becomes obvious, by comparing Figure 5.8g and Figure 5.4c. Whereas in patient 3 the discontinuity in dermal vasculature results from the disease phe-

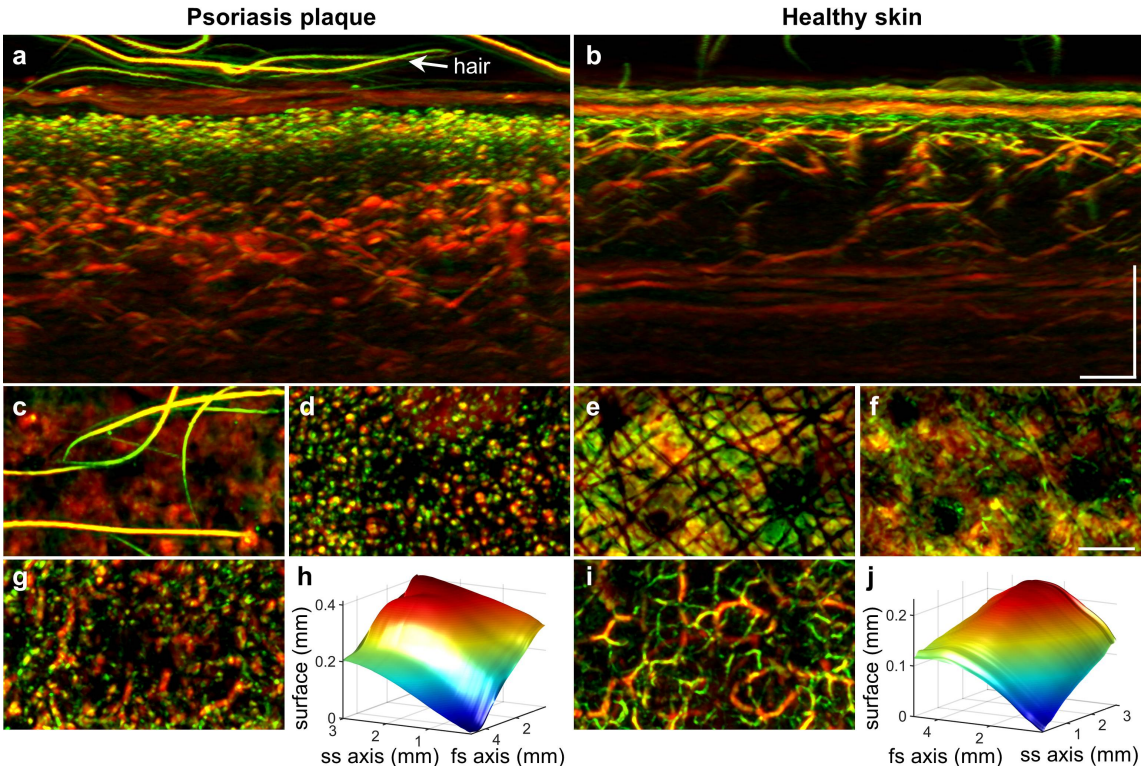

Figure 5.8.: Comparison of psoriatic and healthy skin acquired with motion-corrected RSOM55. Comparison of psoriatic and healthy skin acquired with motion-corrected RSOM55. Images were acquired by scanning a psoriasis plaque and a nearby healthy skin region on the lower arm of patient 3. **a,b)** Cross-sectional MAP (side view) of the reconstructed ROI showing the difference in the skin layers of psoriatic skin (a) compared to healthy skin (b). In psoriatic skin the signal from the *stratum corneum* is weaker, the epidermal layer is thickened, and the vascular network is distorted. **c,e)** Lateral MAP of the epidermis. Epidermal ridges are only observed in healthy skin. **d,f)** Lateral MAP of the epidermal-dermal junction. The capillary loops are enlarged in psoriatic skin. The capillary loops in healthy skin are too small to be resolved by RSOM55. **g,i)** Lateral MAP of the dermal vasculature. The vasculature of psoriatic skin shows discontinuities, which could be confused with motion artifacts. **h,j)** The corrected skin surfaces of diseased (h) and healthy (j) skin verify that the vascular changes in psoriasis do not stem from motion artifacts but are specific to the disease. Scale bars: 500 μm.

notype of psoriasis, similar effects arise due to motion. The surface detection algorithm provides a measure of reliability in the observed abnormalities in the vascular features. Since the skin surface is smooth and continuous after motion compensation (see Figure 5.8h), it follows that the vascular discontinuities arise from the disease and do not stem from motion artifacts.

5.4.3. Multispectral RSOM

By measuring 3D absorption maps at multiple wavelengths, MSOM provides functional information based on the spectral signature of intrinsic chromophores. Multispectral images were performed on the lower arm of a healthy male volunteer of skin type III with MSOM.

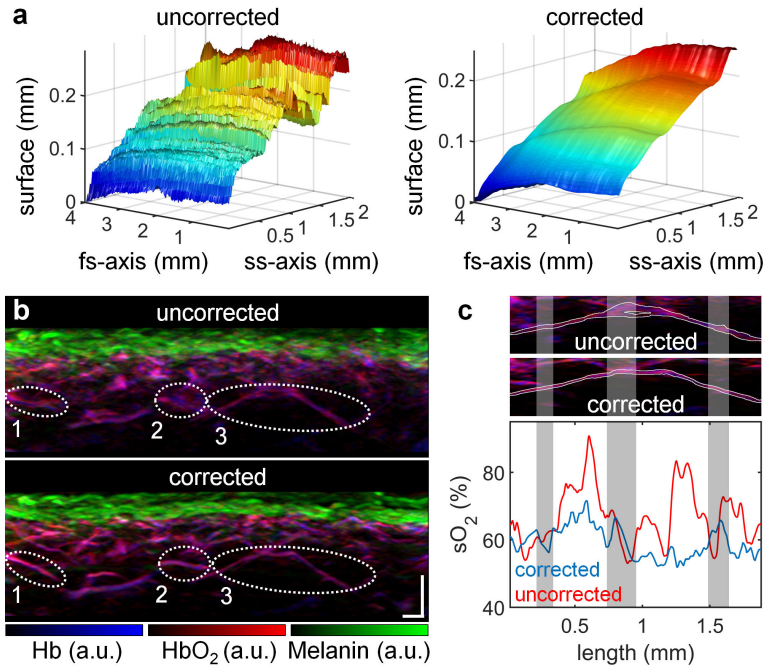

Figure 5.9.: Impact of motion on readings of blood oxygenation. Data was acquired with MSOM by measuring a volunteer of skin type III. **a)** Skin surface of the lower arm area before (left) and after (right) motion correction. Long measurement times in multispectral acquisitions lead to strong motion even along the fs-axis. The corrected surface is smooth and continuous. **b)** Vertical MAP of unmixed chromophores in the lower arm. Two exemplary vessels marked by ellipses 1 and 2 are not resolved if motion is not corrected for. **c)** Course of blood oxygenation along the vessel marked by ellipse 3 in (b). The white contour line in the top and middle panel shows the outline of the segmented vessel. Blood oxygenation was calculated across the diameter of the blood vessel within the segmented area following its path from left to right. The blood oxygenation along the vessel in the motion-corrected image is relatively stable at approximately 60%, whereas readings of blood oxygenation fluctuate significantly in the uncorrected image (bottom). The gray background indicates regions of vessel bifurcation, which are characterized by a drop or increase in blood oxygenation in the corrected image. Scale bars: 250 μm. Adapted from Schwarz *et al.* [192]

Unmixing was performed before and after motion correction. The following method was used to assess the performance of the algorithm.

To compare the unmixing results the same vessel was segmented in the motion-corrupted and corrected 3D reconstruction. The blood oxygenation along the segmented vessel was traced and compared. The vessel was segmented by thresholding the reconstructed images at 20% of the maximal value:

$$\mathrm{Seg}(x_i, y_j, z_k) = H\left(R(x_i, y_j, z_k) - 0.2 \max_{i,j,k}[R(x_i, y_j, z_k)]\right), \tag{5.1}$$

where $H(x)$ is the Heaviside step function, and $R(x_i, y_j, z_k)$ represents a cuboid section of the reconstructed volume, which encompasses the vessel of interest. $\mathrm{Seg}(x_i, y_j, z_k)$ takes the value 1 if the voxel amplitude is greater than 20% of the maximum amplitude within the cuboid and 0 if the amplitude lies below 20%.

The segmented vessel in Figure 5.9 was primarily oriented along the y-axis, and blood oxygenation at a location y_j was averaged across the diameter of the vessel:

$$\mathrm{sO_2}(y_j) = \frac{\sum_{i,k} [\mathrm{Seg}(x_i, y_j, z_k) \cdot \mathrm{sO_2}(x_i, y_j, z_k)]}{\sum_{i,k} [\mathrm{Seg}(x_i, y_j, z_k)]}, \tag{5.2}$$

where $\mathrm{sO_2}(x_i, y_j, z_k)$ represents the voxel-to-voxel ratio of oxygenated hemoglobin to total amount of hemoglobin.

The oxygenation level within blood vessels changes smoothly along its length and in the absence of vessel bifurcation. By comparing the trace of blood oxygenation $\mathrm{sO_2}(y_j)$ of motion-corrupted and corrected data, the influence of motion is shown. Abrupt changes or large fluctuations in $\mathrm{sO_2}$ are an indication of motion.

Figure 5.9 shows the impact of motion on the quantification of blood oxygenation. The long measurement time leads to strong motion during data acquisition even along the fs-axis, resulting in a rippled skin surface (see Figure 5.9a). The corrected surface is smooth and continuous along both the fs-axis and the ss-axis. Two main errors arise due to the motion during the acquisition: unresolved anatomical structures and inaccurate readings of blood oxygenation. The ellipses 1 and 2 in Figure 5.9b indicate two areas, where blood vessels are not resolved in the uncorrected image. Single vessels appear as a cloud of absorption without clear boundary. In the motion-corrected image single vessels are clearly resolved. To show the impact of motion on readings of blood oxygenation, the vessel marked by ellipse 3 in Figure 5.9b was segmented, and the mean blood oxygenation was traced along the vessel. The white contour line in the top and middle panel of Figure 5.9c shows the outline of the segmented vessel. In the uncorrected image the blood vessel appeared as a double structure. After motion correction the shadow structure disappeared. In the uncorrected image the blood oxygenation level fluctuates between 55% and 90%. To study whether the change in blood oxygenation along the vessel could stem from vessel bifurcations, regions of vessel bifurcation were marked by the grayed areas in Figure 5.9c. In the uncorrected image local changes in blood oxygenation and sites of vessel bifurcation are not correlated. The level of blood oxygenation along the vessel in the motion-corrected image is more stable and takes values between 55% and 70%. In the corrected image regions of vessel bifurcation are characterized by a drop or increase in blood oxygenation.

5.5. Summary

In this chapter, a powerful motion correction algorithm has been presented, which was designed for raster-scan optoacoustic mesoscopy.

In section 5.2, the origin of motion was introduced. Originating from the raster-scanning approach used in mesoscopic setups, the whole acquisition process takes several minutes [3, 99,102,103,105,106,164,174,184,193], whereas motion-inducing physiological processes, such as respiration [194] and head or limb movement, are much faster. Furthermore, in a clinical context, the ROI is often located on a body site that is difficult to stabilize while scanning. Since RSOM is a tomographic imaging modality, the quality and resolution of reconstructed images rely on accurate knowledge of the relative positioning of the ultrasound detector with respect to the ROI. In humans, motion cannot be reduced by anesthetizing or restraining the volunteer, as in animal imaging [98, 163].

Section 5.3 introduces a powerful algorithm to correct for motion after data acquisition. The motion correction algorithm presented in this work is based on one assumption: The skin surface is assumed to be continuous and smooth on a mesoscopic scale, *i.e.* on the scale of several micrometers. The strongly absorbing melanin layer in the epidermis is used to detect the skin surface. Depending on the body site, two different approaches have been employed. In case of hairless skin, e.g. the human palm, the location of the *stratum corneum* is used for surface detection. In case of hair-bearing skin, e.g. the lower arm, a low-frequency band carrying the signature of melanin is used to detect the skin surface. A representation of the detected skin surface reveals the motion artifacts as disruptions in the surface. Assuming that the skin surface follows a continuous and smooth surface, an artificially-smoothed surface is created by applying a moving average filter to the disrupted surface. To correct for the z-position of each detector position in the reconstruction algorithm, the 2D difference map between the motion-corrupted and the artificially-smoothed surface is calculated.

Section 5.4 presents the improvement in image quality after motion correction for multiple RSOM implementations. Experimental image quality improvement is shown for high resolution RSOM100, clinical RSOM55, and MSOM. The experimental setups are described in section 3.2.

Due to its high-resolution capability and limited sensitivity (see chapter 4), RSOM100 is particularly affected by motion artifacts. In section 5.4.1, it has been shown that motion correction can restore motion-corrupted data to reach unprecedented imaging performance of the epidermal-dermal junction as well as the superficial horizontal plexus. Significant improvement in resolution was shown for both hairless skin of the human palm, characterized by a thick epidermis, and hair-bearing skin of the lower arm, characterized by a thin epidermal layer. A high-resolution absorption map was acquired by imaging a benign nevus on the lower arm, visualizing in detail the boundary of the nevus and the surrounding vasculature.

Section 5.4.2 presents the impact of motion correction in clinical data. To show the importance of motion correction to reliably detect vascular changes in skin disease, three patients were scanned with RSOM55, suffering from eczema and psoriasis. The analysis performed on the three different patient datasets, served three different purposes. First, it was shown in a comparative study that the presented motion correction algorithm is able to fully restore the original skin surface. Second, motion correction was applied to a dataset strongly affected by breathing motion. Surface detection in healthy and diseased skin showed a sinusoidal modulation of the skin surface at ~ 15 cycles per minute, *i.e.* $17 - 18$ cycles per measurement. After motion correction, the periodic movement of the surface disappeared for both healthy and diseased skin. Third, the skin surface detection was introduced as a measure of accuracy and reliability in clinical imaging. Only in motion-corrected data it becomes obvious if vascular distortion arises from the disease phenotype or motion artifacts. Likewise, corrected data is required for meaningful quantification of disease biomarkers (see chapter 8).

In MSOM, precise co-registration of multispectral datasets is necessary to accurately unmix intrinsic chromophores. Since a scan of $4\,\text{mm} \times 2\,\text{mm}$ takes up to 14 minutes (see chapter 7), MSOM is affected more intensely by motion compared to RSOM55. In section 5.4.3 it has been shown that uncorrected data does not only fail to resolve anatomical structures but corrupts readings of blood oxygenation as well. To gain reliable unmixing results in MSOM motion correction is indispensable.

The algorithm presented herein relies on an absorbing layer close to the skin surface. Human skin is a perfect sample for the detection algorithm, since it contains an absorbing layer of

melanin within the epidermis. Nonetheless, the same low-frequency layer has been observed in the skin of nude mice devoid of melanin. In this case, the horizontal plexus of microvessels acts as an absorbing layer. Even without an absorbing layer close to the skin surface it is easy to artificially create such an absorbing layer on the surface; for example by dissolving ink in the coupling layer of acoustic gel, by coloring the surface slightly with a marker, or by introducing absorbing molecules in the coupling membrane. A similar approach has been employed in OCT, where a fiducial marker is used to mark the skin surface [206]. Thus, the approach presented in this chapter is not limited to human skin but can easily be extended to a large range of samples.

6. Imaging tumor growth and angiogenesis in melanoma mouse model

6.1. Introduction

In chapter 1, an overview of common skin disorders was given. The most fatal skin disorder is the malignant melanoma [7, 12] with an increasing incidence in the last decades [6, 8]. To increase the overall survival rate of melanoma patients, early detection of melanoma is essential.

The clinical tools for melanoma screening are limited (see chapter 1) and primarily based on superficial features according to the ABCDE-rule (A: asymmetry, B: boundary, C: coloring, D: diameter, and E: evolution). However, essential information on the melanoma is encoded in the infiltration thickness. Melanoma thickness, for instance, is an important factor in the prognosis of recurrence and metastasis [19, 20], as well as the vascular network surrounding the melanoma. The vascular network feeds the tumor with nutrients and oxygen. Growing tumors will induce new vessels, *i.e.* angiogenesis, because no living cell can exist at a distance further than $\sim 100\,\mu$m away from the vascular network [207]. The vasculature is further involved in tumor spreading through metastasis since vessels carry the tumor cells to distant locations [1]. Imaging of tumor growth, tumor dynamics, and tumor angiogenesis is important in elucidating tumor biology and physiology [207, 208] and understanding the tumor microenvironment [209, 210].

The vascular network of tumors has been imaged in the past by optoacoustic tomography. Depending on the detection bandwidth of the detector, different vessel sizes are targeted (see section 2.5). Optoacoustic imaging at frequencies on the order of $20 - 30\,$MHz have achieved resolutions of $70 - 100\,\mu$m [199]. In these images, only large vessels of minimum apparent diameter of $81\,\mu$m have been observed [199].

In this chapter the rich potential of RSOM100 and RSOM50 in imaging angiogenesis of microcirculation around B16F10 melanoma tumors will be shown. The use of broadband ultrasound detectors leads to new, previously not reported, performance in resolving tumor vasculature reaching better than $5\,\mu$m axial resolution and better than $20\,\mu$m lateral resolution through at least 2 mm of tissue depth.

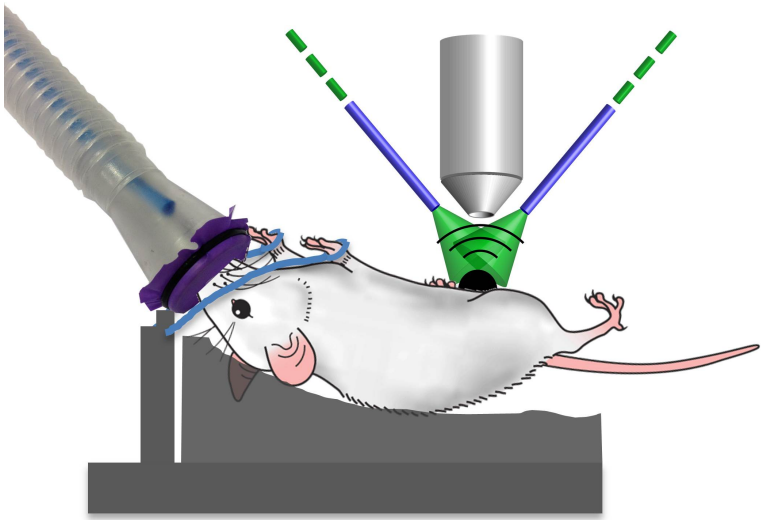

Figure 6.1.: Experimental scanning setup for mouse models. Depiction of the raster-scan system, showing the position of the mouse, the mouse bed, the anesthesia unit, the detector, and the illumination.

6.2. Preclinical melanoma model and experimental procedure

Selected from the pool of transgenic mouse models of melanoma and melanoma cell line xenografts, the established B16F10 cell line was chosen as a model to proof the ability of RSOM to characterize angiogenesis in skin tumors. B16F10 melanoma cells ($0.5 \cdot 10^6$ cells solved in 25 μl PBS solution) were injected subcutaneously into the mammary fat pad of eight week old female Hsd:Athymic Nude-Foxn1nu mice. Melanoma tumor growth and vascular changes were monitored over a time course of nine days. Both RSOM100 and RSOM50 (see section 3.2) were used to image angiogenesis. The mouse was scanned three times, with an additional final scan directly before euthanasia.

Figure 6.1 illustrates the scanning setup and the positioning of the mouse on a custom made bed, which was designed for the *in vivo* experiments in order to keep the head of the mouse above water while covering the tumor area by several millimeters of water. The bed was slightly curved, increasing in height towards the headpiece, to keep the animal's head above water. During the experiment, the mouse lay on its back with a boundary on the sides of the bed to hold it in position. The ROI around the tumor side was covered by a thin plate, made of acrylic glass, with a 2 cm $\times$ 2 cm opening in the center. The opening was sealed with a thin plastic membrane and coupled to the mouse skin above the ROI with ultrasound gel. The mouse bed was immersed in warm water, covering the ROI by several millimeters to maintain body temperature. The mice were imaged under 1.8% isoflurane anesthesia. All procedures were approved by the District Government of Upper Bavaria.

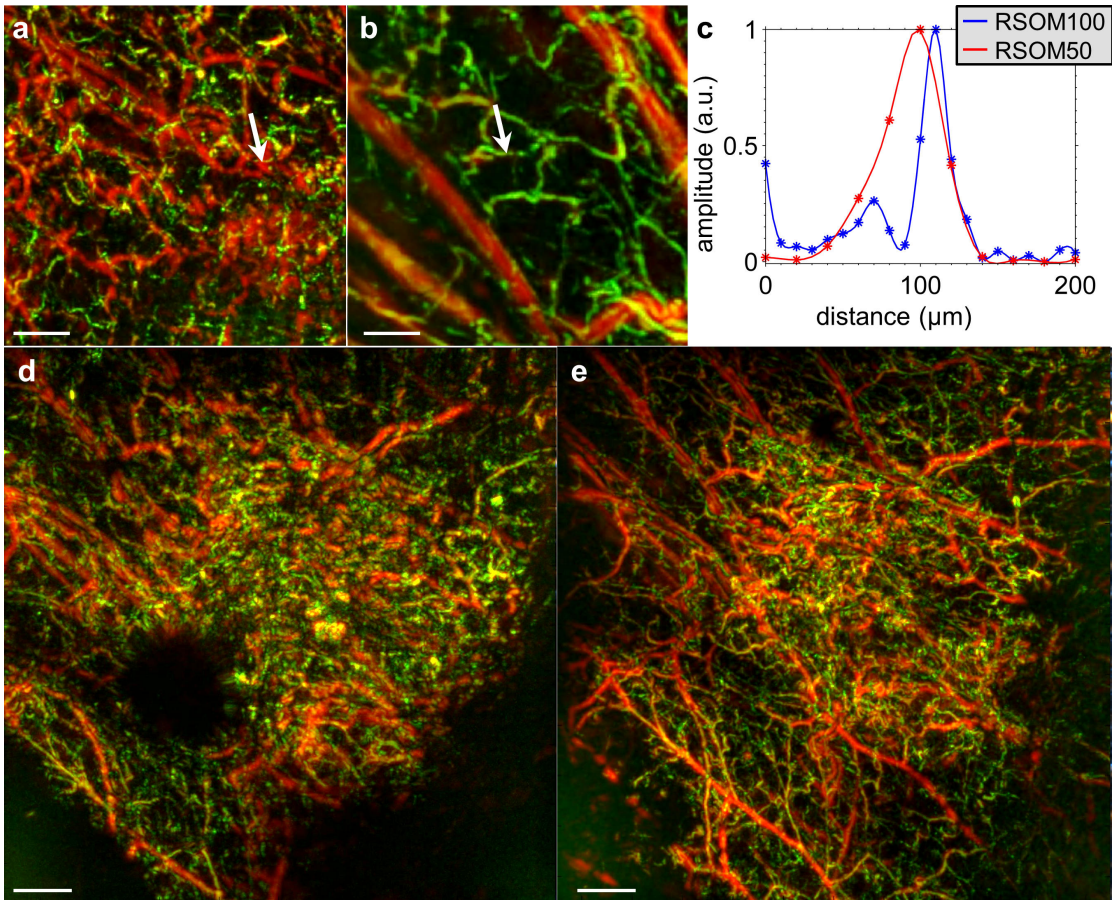

Figure 6.2.: Comparison of the imaging performance achieved by RSOM100 and RSOM50 by imaging the vasculature of a melanoma tumor. A ROI of 3 mm × 3 mm was acquired with **a)** RSOM100 and **b)** RSOM50. **c)** Lateral profile through the vessels marked by the white arrows in (a, b). The FWHM of the vessel acquired with RSOM100 is 20 μm, in RSOM50 it measures 42.5 μm. **d,e)** Lateral MAPs of the same ROI around the tumor at day 4 after tumor cell injection. In RSOM100 (d), the center of the tumor shows up as a black hole. In RSOM50 (e), the vasculature appears as a continuous network. Scale bars in (a,b): 500 μm, Scale bars in (d,e): 1 mm. Adapted from Omar and Schwarz *et al.* [163] © 2015 Neoplasia Press, Inc. Published by Elsevier Inc. Reproduced with permission.

6.3. Applications

6.3.1. Comparison of RSOM100 and RSOM50 imaging performance

Figure 6.2a,b shows a zoom into a vascular network recorded with the two systems. Both large vessels (red) and small vessels (green) are visualized. The apparent vessel diameters in the RSOM100 image are smaller than the vessels in the RSOM50 image. In Figure 6.2c, profiles of the vessels marked by the arrows in Figure 6.2a,b are shown. The profiles served to calculate the FWHM of the vessels and, thus, the lateral resolution of the imaging system. A lateral resolutions of 42.5 μm and 20 μm was calculated for RSOM50 and RSOM100 respectively.

For direct comparison of the two different detectors, the same ROI was acquired at day 4 after melanoma cell injection with both the 100 MHz and the 50 MHz detectors. The

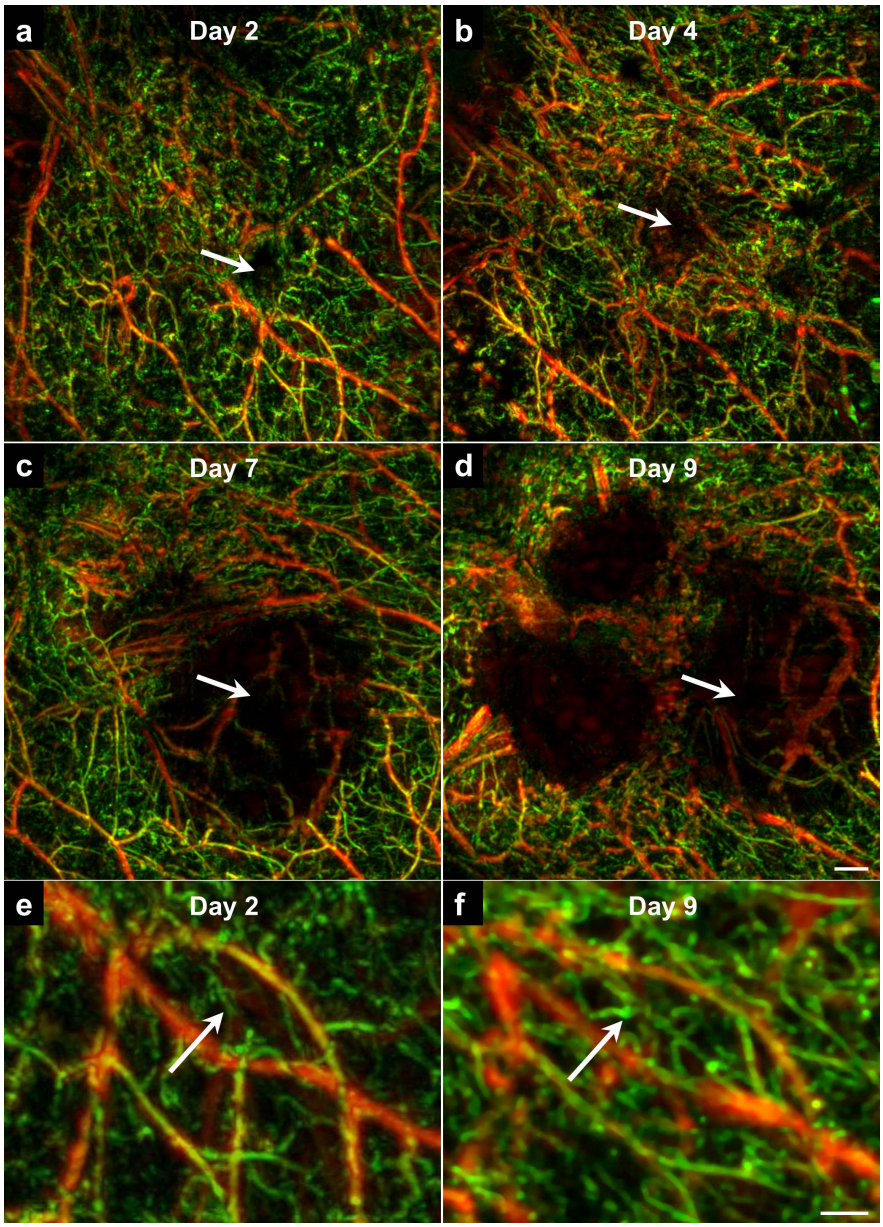

Figure 6.3.: Imaging tumor growth and angiogenesis over time with RSOM50. **a-d)** Progression of tumor size over time. Images of the tumor area were acquired at day 2, day 4, day 7, and day 9 after injection of the melanoma cells. The white arrows point to the center of the tumor mass. The images are generated by taking lateral MAPs of the tumor area from a depth of $440 - 2000\,\mu$m. Scale bar: 1 mm. **e, f)** Vascular changes observed within the same ROI imaged at day 2 and day 9 after tumor cell injection. The ROI is located on the boundary of the tumor area at day 9 after injection. The white arrows indicate an increase in small vessels over time. Scale bar: $500\,\mu$m.

results are depicted in Figure 6.2d,e. Figure 6.2d shows a black hole where the tumor is located. The vasculature around the tumor can be clearly identified, however, showing some discontinuities. Hence, tilted structures, such as vessels, which generate an optoacoustic wave normal to them, *i.e.* oblique to the axis of the detector will not be detected. In Figure 6.2e, an improved image quality is clearly observed, where vessels appear as continuous structures,

the appearance of additional vasculature in Figure 6.2e compared to Figure 6.2d is attributed to the higher angle of acceptance, of the 50 MHz detector. With a larger acceptance angle, RSOM50 enables the observation of some tilted vessels.

6.3.2. Imaging tumor growth and angiogenesis over time

In Figure 6.3a-d, tumor growth over time is followed, the images were measured using RSOM50. For better visualization, a partial MAP of the reconstruction is taken, where instead of taking the MAP of the whole volume only a partial MAP at a depth of $440-2000\,\mu$m below the surface of the skin is shown. This way the tumor growth, the re-arrangement of the vessels around the tumor, and the growth of new vessels due to angiogenesis are observed on the same image. The growth of the tumor, represented by the growth of the black non-vascularized spot, is observed over time (see white arrows in Figure 6.3a-d). Figure 6.3e,f shows a zoom-in on the same area, at day 2 and day 9, from a location in the proximity of the tumor. In the zoomed-in ROI, it is observed that upon interaction with the tumor the two big vessels start rearranging, while at the same time smaller vessels start growing in that region (see white arrows in Figure 6.3e,f). Due to tumor growth, the flexibility of skin and differences in fixing the tumor location through the different days, it is not possible to show the exact same ROI in all the subfigures of Figure 6.3.

6.3.3. Three-dimensional tumor representation and comparison to cryo-slices

Figure 6.4 shows a volumetric representation of a tumor imaged at day 9, which was validated by cryo-slices. For validation purposes a prototype imaging cryo-microtome was used [211, 212]. Reflection (RGB) and Fluorescence (740/780 exc/emm wavelengths) imaging were acquired resulting in a multispectral volume with voxel dimensions of $25\,\mu\text{m} \times 25\,\mu\text{m} \times 50\,\mu$m. In Figure 6.4a, a lateral MAP of the ROI from within the depth range $930 - 2115\,\mu$m is shown. The tumor itself shows up as a dark area, because the melanin-rich tumor strongly absorbs visible laser light already in the upper layers, and high-frequency detectors cannot detect the extremely low frequencies (on the order of $0.1-1$ MHz) generated from the tumor bulk. Figure 6.4a correlates well with the cryo-slice taken at a depth of $930\,\mu$m, as shown in Figure 6.4e. In Figure 6.4b-d, a MAP of the ROI from $615\,\mu$m, $390\,\mu$m, and $0\,\mu$m to a depth of $2115\,\mu$m are shown, visualizing the feeding vessels of the tumor. Figure 6.4b,c correlate well to the corresponding cryo-slices shown in Figure 6.4f,g.

6.4. Summary

In this chapter, tumor growth, the corresponding rearrangement of the surrounding vascular network, and the growth of new microvessels in the vicinity of the tumor has been imaged with UB-RSOM. To the best of our knowledge, this is the first time that tumor vasculature has been imaged at such depths with such resolution *in vivo*. Longitudinal growth studies and growth-related changes of the tumor were shown with RSOM.

In section 6.3.1, the performance of RSOM100 and RSOM50 was compared. The images obtained show that imaging using the 100 MHz detector resolves smaller structures, such as

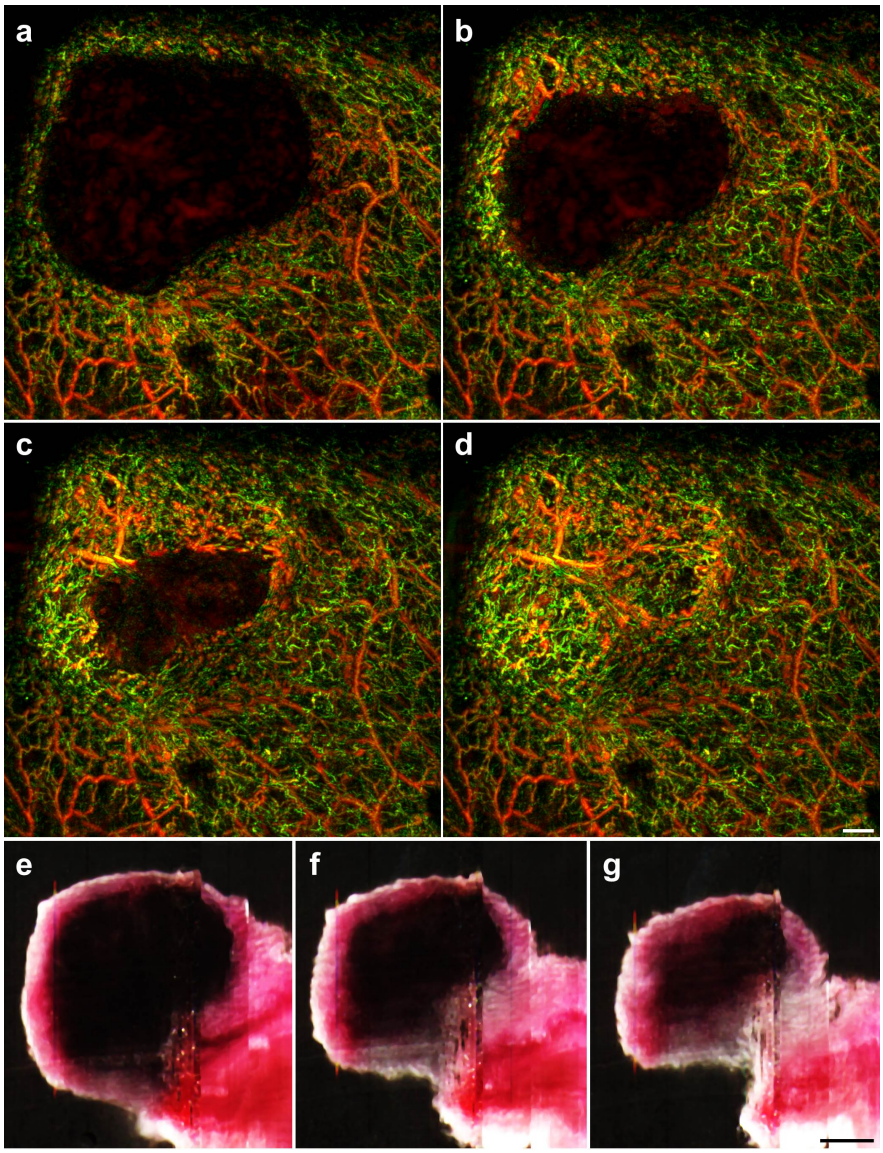

Figure 6.4.: Three-dimensional representation of tumor area correlated with cryo-slices. The RSOM50 image was taken at day 9 post injection. MAP of the 3D RSOM data from a depth of **a)** 930 μm, **b)** 615 μm, **c)** 390 μm, and **d)** 0 μm to a depth of 2115 μm. **e-g)** correspondingly show cryo-slices taken at a depth of **e)** 930 μm, **f)** 615 μm, and **g)** 390 μm. Scale bars in (a-d): 1 mm. Scale bars in (e-g): 2 mm. Adapted from Omar and Schwarz *et al.* [163] © 2015 Neoplasia Press, Inc. Published by Elsevier Inc. Reproduced with permission.

the newly sprouting vessels, especially when implemented with multi-frequency reconstruction. On the other hand, as expected, the 50 MHz detector performs better in imaging larger structures generating lower frequencies, such as large blood vessels (larger than 50 μm in diameter). Consequently, most of the vasculature were better seen with the 50 MHz detector. Additionally, the smaller f-number (*i.e.* higher numerical aperture) of the 50 MHz detector performed better in imaging oblique vessels, making the vasculature appear more continuous in RSOM50 images compared to RSOM100 images. A hybrid implementation of RSOM100 together with RSOM50 might offer a more complete picture of the tumor microvasculature.

RSOM100 could be used to image the tumor in the first days of development or image the small sprouting microvessels, and RSOM50 could provide complementary information especially as tumor structures and vessels become larger as a function of tumor growth.

In section 6.3.2, tumor growth and angiogenesis within the tumor environment was studied. The tumor showed up as a black mass, which increases in size. Close to the tumor boundary small newly sprouting vessels were observed, confirming the visualization of angiogenesis. In section 6.3.3, the tumor size and shape were compared to cryo-slices. The size and shape of the tumor as seen in RSOM confirmed well to the features observed in cryo-slices. Thus, RSOM enables non-invasive monitoring of 3D tumor volumes with additional information on the vascular network surrounding the melanoma tumor.

Applying multi-frequency reconstruction (see section 3.6) improves the visibility of the small structures, *i.e.* structures corresponding to high frequencies, such as the newly sprouting vessels during angiogenesis. Because the amplitude of the signals is proportional to the size of the object generating those signals, the high-frequencies generally have a lower SNR compared to the low frequencies. Additionally high frequencies are more strongly attenuated than low frequencies, thus, if all the frequencies are simultaneously reconstructed, the high-frequencies will be masked by the low frequencies.

The obtained capabilities should enable a better understanding of tumor growth and tumor angiogenesis, which is important in understanding tumor physiology, mechanisms of metastasis, and planning of therapy, where RSOM is capable of imaging tumor growth, tumor angiogenesis, and theoretically tumor response to various kinds of therapy. This specifically applies to those kinds of therapies that affect tumor vasculature, target tumor angiogenesis, and which are based on enhanced permeability and retention (EPR) [209, 210].

7. Multispectral raster-scan optoacoustic mesoscopy

7.1. Introduction

As summarized in section 2.3 human skin contains numerous intrinsic chromophores that exhibit unique absorption spectra. In the ultraviolet spectrum ($200 - 320\,\mathrm{nm}$) the major epidermal chromophores are urocanic acid, DNA, tryptophane, tyrosine, melanin, and the fibrous protein keratin [125–127]. Main absorbers of cutaneous tissue in the infrared ($900 - 1300\,\mathrm{nm}$) are water, fat, and protein [112, 128]. The absorption of visible and near-infrared light ($320 - 900\,\mathrm{nm}$) by human skin is governed by the natural chromophores eumelanin, pheomelanin, oxyhemoglobin, deoxyhemoglobin, bilirubin, and β-carotene [108,112,117,129–134].

The quantification of tissue chromophores has great potential in the diagnosis and therapy of skin diseases. There are whole books on the impact of changes in oxygen saturation in the microenvironment of tumors and new opportunities for cancer therapy arising thereof [214, 215]. It was shown that two hypoxia-inducible factors play a critical role in the progression of melanoma [216]. The amount of eumelanin compared to pheomelanin has been shown to vary between melanomas and nonmalignant nevi [217]. Furthermore, dysplastic melanocytic nevi contain significantly higher amount of pheomelanin and are, according to the National Cancer Institute, more likely to develop into melanoma [218]. But hypoxia is not only found in skin cancer. For instance, hypoxia was observed in systemic sclerosis [219], and oxygen levels in ischemic wounds play an important role in the healing process [220].

Optical diffusion spectroscopy or imaging have been considered for 3D sensing of oxygenated and deoxygenated hemoglobin in tissues but offer low resolution and lack accurate quantification due to the diffusive nature of photon propagation in tissues [59, 62, 63]. OCT offers only poor spectral capability [79]. All other optical imaging modalities as well as US imaging lack the capability to record optical absorption spectra (see section 1.3). In contrast to other methods employed in dermatology, optoacoustic mesoscopy offers unique imaging potential by resolving in high resolution tissue chromophores and photoabsorbing moieties, including melanin, hemoglobin, fluorochromes, and metal nanoparticles [88,198,221]. This contrast has

been engaged in many applications spanning from cancer imaging and tumor hypoxia [222], to kidney perfusion [198], or vascular morphology [4]. Detection of chromophores relies on illuminating tissue at multiple wavelengths and then using spectral unmixing techniques to resolve the spectra of the different chromophores present in tissue.

Despite the suitability of optoacoustic mesoscopy for human skin imaging, there has been limited progress in resolving spectral signatures of skin chromophores such as oxyhemoglobin, deoxyhemoglobin, or melanin *in vivo*. An important technological limitation has been the lack of fast tunable lasers [96,99] and improved algorithms to correct for motion and improved co-registration of spectral datasets (see chapter 5). So far, MOD has been demonstrated with dye lasers which cannot rapidly switch between wavelengths. MOD implementations with dye lasers require a wavelength switch after completing a B-scan (10 s) or even after a whole raster-scan (several minutes). However, at timescales on the order of several seconds, motion is inevitable when imaging human skin *in vivo*. Quantification of chromophores without precise co-registration of multispectral data will be prone to motion artifacts and is therefore not meaningful (see chapter 5). Furthermore, the dye lasers employed in previous studies show a narrow tuning range of approximately 30 nm only, preventing the acquisition of broadband spectra. For example, Favazza *et al.* have shown qualitative changes in oxygen saturation in the human palm within a single B-scan during a forearm occlusion release experiment [223]. Imaging was performed at only two narrowly-spaced wavelengths (561 nm and 570 nm) impeding robust and quantitative measurements of oxygen saturation. Moreover, a 20 MHz transducer has been employed, providing resolutions not suited for imaging the vasculature of the dermal papillae and the superficial horizontal plexus [174, 184].

In this chapter, multispectral optoacoustic dermoscopy of the skin will be demonstrated, employing the MSOM system described in section 3.2. Compared to previous studies, MSOM offers significantly higher resolution and interleaved laser pulses that allow for inherent co-registration of spectral measurements. This technique enables for the first time, to the best of our knowledge, 3D spectral mesoscopy of human skin *in vivo*, providing 3D absorption maps of melanin, oxygenated hemoglobin, deoxygenated hemoglobin, and blood oxygenation levels of the dermal vasculature. Furthermore, MSOM shows previously undisclosed *in vivo* absorption spectra over a broad wavelength range from 460−650 nm of specific skin structures such as the *stratum corneum*, epidermis, and upper as well as lower dermal vasculature. Experimental results will be compared to bulk tissue oxygenation levels obtained by optical spectroscopy techniques.

7.2. Methods and feasibility considerations

7.2.1. Spatial undersampling of data

The experimental setup is described in section 3.2. A multi-wavelength OPO laser is used at a repetition rate of 50 Hz or 100 Hz respectively. Compared to the single wavelength RSOM system, the acquisition time is much slower. Furthermore, multiple wavelengths have to be acquired, reducing the effective repetition rate further. For instance, by using 4 different wavelengths the 50 Hz (100 Hz) PRR is reduced to an effective PRR of 12.5 Hz (25 Hz). Thus, the acquisition time for a relatively small ROI, measuring 4 mm × 2 mm, takes 26.7 min (13.3 min) at a recommended step size of $\Delta = 20\,\mu$m (see equation (3.6)). Especially for a PRR of 50 Hz it is very challenging for the volunteer to keep still for such a long time.

One possibility to decrease the acquisition time is to increase the step size Δ. In section 3.7.2 it was shown that aliasing affects appear, and axial as well as lateral resolution deteriorate for step sizes larger than $\Delta = 30\,\mu$m. To reduce acquisition time and simultaneously prevent aliasing effects the following procedure can be followed. First, the data is recorded on an undersampled grid with a step size of $40\,\mu$m, resulting in a decrease of acquisition time by a factor of 4. Second an artificial acquisition grid of $20\,\mu$m step size is created. The missing A-lines are calculated by interpolation of neighboring A-lines, employing the built-in MATLAB function "interp2" for every time point.

The method of undersampling and interpolating missing data was used for a PRR of 50 Hz (see section 7.2.3).

7.2.2. Laser pulse width and detection bandwidth considerations

In section 2.4, the notion of stress confinement was introduced, *i.e.* the condition where the heating pulse is much shorter than the typical time of acoustic relaxation time within a resolved voxel. If the length of the heating pulse is on the order of the acoustic relaxation within a resolved voxel, the finite pulse width of the laser acts as a lowpass filter [151]. The larger the pulse width, the lower is the cutoff frequency of the lowpass filter. In single-wavelength implementation of the RSOM system (see section 3.2) a laser with a pulse width of < 1 ns has been used, whereas the wavelength-tunable MSOM system uses a pulse with of $4 - 7$ ns. The question arises if the laser source of the MSOM system is appropriate for the bandwidth of the 50 MHz transducer. To justify the appropriateness of the laser source, the signal distortion due to the finite laser pulse width was studied. The signal distortion was studied theoretically for a $15\,\mu$m thick solid suture made of nylon. The theoretical optoacoustic signal of the nylon suture is similar to the typical N-shape arising from a fluid sphere (see equation (2.24)). Accurate modeling of the optoacoustic response of a solid cylinder takes a slightly more complicated form and was modeled by a combination of Bessel functions [224].

To model the finite detection bandwidth of the detector, the theoretical time signal was filtered by the transducer bandpass, specified in section 3.2.1. The laser pulse was modeled by a Gaussian curve with a FWHM of 7 ns and the time signal was convoluted with the kernel function:

$$\text{kernel}(t) = \exp\left(-\frac{4\ln(2)t^2}{\text{FWHM}^2}\right) \tag{7.1}$$

The Fourier Transform of the pulse width kernel function (see equation (7.1)) transforms into a lowpass filter in frequency domain:

$$\mathcal{F}_t\left[\text{kernel}(t)\right](f) = \exp\left(-\frac{\pi^2\text{FWHM}^2 f^2}{4\ln(2)}\right) \tag{7.2}$$

The results of the analysis are shown in Figure 7.1, which shows the distortion of the analytical optoacoustic time signal and the frequency spectrum, originating from a $15\,\mu$m thick nylon suture surrounded by water. The black curve in Figure 7.1a corresponds to the original optoacoustic time signal. When imaged with a bandwidth limited detector, the original signal broadens in time, as can be seen by the blue-dashed line in Figure 7.1a. The influence of the laser pulse width on the bandpass filtered signal is shown by the red-dotted line in Figure 7.1a. A pulse width of 7 ns causes an additional broadening of the time signal and,

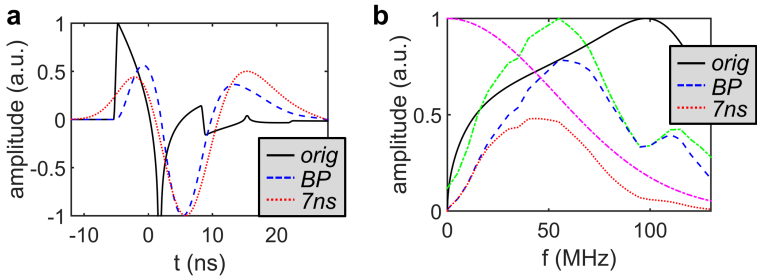

Figure 7.1.: Impact of the transducer bandpass and the laser pulse width on a theoretical optoacoustic signal. a) Effect of bandpass and pulse width on a time signal originating from a 15 μm thick nylon suture surrounded by water. Solid black curve: analytic optoacoustic signal. Dashed blue curve: Bandpass filtered optoacoustic signal. Dotted red curve: Optoacoustic time signal that was bandpass filtered and convolved with a Gaussian curve corresponding to the laser pulse width of 7 ns (see equation (7.1)). **b)** Frequency content of the optoacoustic signal. Solid black, dashed blue, and dotted red curve: Frequency content corresponding to the optoacoustic signals shown in (a). Dot-dashed green curve: Transducer bandpass as specified in section 3.2.1. Dot-dashed magenta curve: Lowpass filter due to a 7 ns long laser pulse width. Adapted from Schwarz *et al.* [213]

thus, a loss of resolution. The effect of temporal broadening can be understood by looking at the frequency spectrum of the distorted signals, as shown in Figure 7.1b. The transducers bandwidth, depicted by the green dot-dashed curve, filters out the detectable frequencies, in this case by shifting the maximum of the original frequency spectrum to lower frequencies. The laser pulse width, depicted by the magenta dot-dashed curve, acts as a lowpass filter and further reduces the original frequency content. From equation (7.2) it follows that a laser pulse width of 7 ns (FWHM) translates into a lowpass filter with cutoff frequency at 63 MHz (−6 dB). Thus, despite the lowpass filtering properties of the laser pulse width, broadband optoacoustic detection of acoustic frequencies above 50 MHz is possible with the used OPO laser.

7.2.3. Characterization of MSOM system

A phantom containing two sutures $\sim$ 15 μm in diameter (NYL03DS, vetsuture, France) was used for the characterization of the system. The sutures were attached between two posts glued to a Petridish and immersed in water. The phantom was imaged by the same acquisition, data processing, and reconstruction protocol as for *in vivo* tissue. To evaluate the lateral and axial width of the sutures, a cuboid surrounding each suture was extracted from the reconstructed dataset. Thereafter, a lateral and vertical MAP of the cuboid was performed, as depicted in Figure 7.2a,b. For every x-position, *i.e.* every position along the length of the sutures, a lateral and axial profile was extracted from the lateral and vertical MAP respectively. Figure 7.2c,d depicts exemplary profiles of the sutures. The FWHM of the sutures was calculated from the lateral and axial profiles. Since in the lateral MAP suture 1 was at an angle of 6.1° and suture 2 was at an angle of 12.7° with respect to the x-axis, the FWHM was calculated by multiplying the FWHM of the profile along the y-axis with $\cos(\alpha_1)$ and $\cos(\alpha_2)$ respectively. The average FWHM and its standard deviation was evaluated for every x-position and is summarized in Table 7.1. The width of the sutures

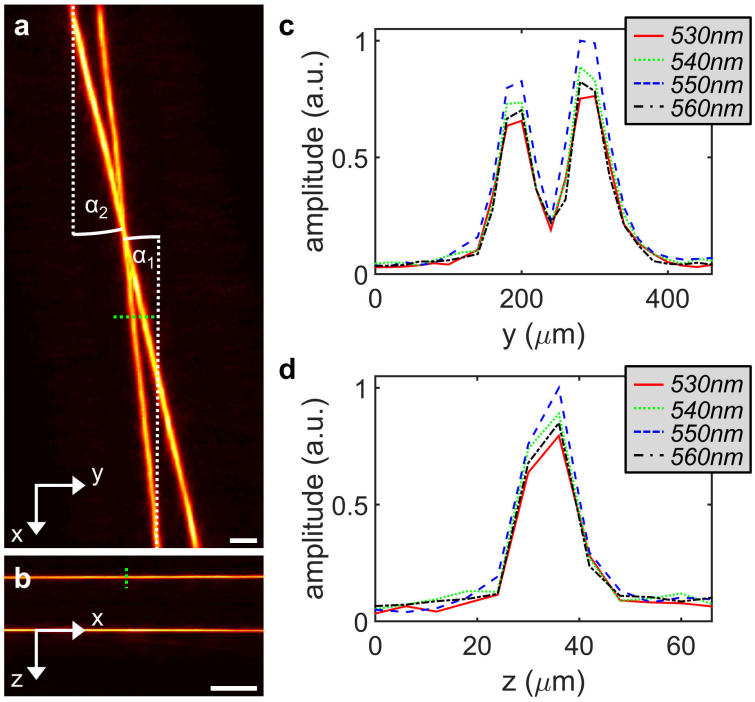

Figure 7.2.: Lateral and axial resolution achieved in MSOM. Lateral and axial resolution of MSOM was evaluated by plotting the profile of $\sim 15\,\mu$m thick sutures. **a)** Top-view of the suture phantom (lateral MAP). The green dashed line corresponds to the location of the lateral profile shown in (c). Suture 1 encloses an angle of 6.1° and suture 2 is at an angle of 12.7° with respect to the x-axis. **b)** Side-view of the suture phantom (vertical MAP). The green dashed line corresponds to the location of the axial profile shown in (d). **c)** Lateral profile of the two sutures at different wavelengths. **d)** Axial profile of the upper suture at different wavelengths. All scale bars: $250\,\mu$m. Adapted from Schwarz *et al.* [213] © 2016 SPIE. Reproduced with permission.

varies only slightly with wavelength.

The lateral resolution was calculated from the mean lateral FWHM of the reconstructed sutures while taking into account the diameter d of the suture itself:

$$\text{lateral resolution} = \sqrt{(\text{FWHM}^2 - d^2)} \tag{7.3}$$

Table 7.1.: Mean axial and lateral width of $15\,\mu$m sutures acquired and reconstructed with the MSOM system. The FWHM of the sutures is independent of wavelength.

wavelength (nm)	Upper suture		Lower suture	
	axial FWHM (nm)	lateral FWHM (nm)	axial FWHM (nm)	lateral FWHM (nm)
530	12.4 ± 0.9	59.8 ± 4.0	13.2 ± 0.9	63.1 ± 5.5
540	12.2 ± 1.1	52.3 ± 5.1	13.1 ± 1.2	56.3 ± 6.1
550	12.4 ± 0.9	59.2 ± 3.8	13.1 ± 1.0	62.7 ± 5.3
560	12.2 ± 1.1	52.3 ± 5.1	13.1 ± 1.4	56.0 ± 6.0

From the mean width of the reconstructed sutures and equation (7.3), the lateral resolution is calculated to be $50-60\,\mu$m for all wavelengths under consideration. Since the theoretically calculated axial resolution is expected to be $\sim 15\,\mu$m [175] and, thus, of the same size as the dimension of the suture itself, it is hard to derive the axial resolution of the MSOM system from the values in Table 7.1. Still, the axial resolution is smaller than the measured axial FWHM of the sutures, *i.e.* smaller than $13\,\mu$m.

7.3. Applications

7.3.1. Absorption spectra of skin compartments

Broadband absorption spectra of skin compartments were recorded. To do so, two distinct skin areas of a 28 year old healthy male volunteer were imaged. Skin color was classified as skin type II according to the Fitzpatrick scale. The first area was located on the skin covering the thenar eminence (palm of hand), representing hairless skin with a thick epidermal layer. The second area was located on the lower arm, representing hairy skin, which is characterized by a thin melanin-rich epidermal layer.

To show the spectroscopic ability of the MSOT system, cross-sectional planes (B-scans) of human skin were acquired by sweeping over 20 equidistant wavelengths in the range from $460-650\,$nm. B-scans were acquired with a step size of $0.4\,\mu$m. After acquisition each of the 20 multispectral datasets was interpolated to an identical grid of $10\,\mu$m step size. The absorption spectra of four different skin compartments were evaluated, comprising the *stratum corneum*, epidermis, and upper as well as lower dermal vasculature. First, a 2D cross-section of each skin compartment was selected by manually choosing the corresponding depth range within the full 2D cross-section. Second, the pixels of highest amplitude within each of the four selected compartments were manually segmented by applying a threshold to the 2D datasets. Based on the segmented pixels the mean absorption spectra and their standard deviation were calculated. Blood oxygenation levels sO_2 were calculated by nonlinear least-squares fitting of the theoretical absorption spectra of oxy- and deoxyhemoglobin to the experimentally measured absorption spectrum.

Figure 7.3 shows the broadband absorption spectra recorded by MSOM. Figure 7.3a shows that within the broad spectral range, covering almost 200 nm, oxygenated and deoxygenated hemoglobin exhibit distinct absorption peaks, in comparison to the monotonically decreasing spectrum of eumelanin. Figure 7.3b shows an unmixed cross-sectional plane of the lower arm. Two compartments are depicted: The epidermal layer characterized by strong melanin signal and the dermal layer exhibiting absorption of hemoglobin. Figure 7.3c depicts a cross-section of the human palm. The two marked compartments comprise the *stratum corneum* and the upper dermal vessels. Figure 7.3d shows the spectrum of the epidermal layer on the lower arm area, which follows closely the absorption spectrum of eumelanin. Figure 7.3e displays the spectrum of the *stratum corneum* of the human palm, which resembles the absorption spectrum of eumelanin. In the spectrum of the *stratum corneum*, total absorption is weaker, and inter-voxel variations are much higher compared to the spectrum of epidermal hairy skin. Figure 7.3f shows the absorption spectrum of the lower dermal vessels, which fits best to an oxygenation level of $sO_2 = 58\%$. A higher blood oxygenation level is found in the more superficial upper dermal vessels. Figure 7.3g displays the experimentally determined spectrum in comparison to the theoretical value of 89% oxygenated blood, which yields the best fit.

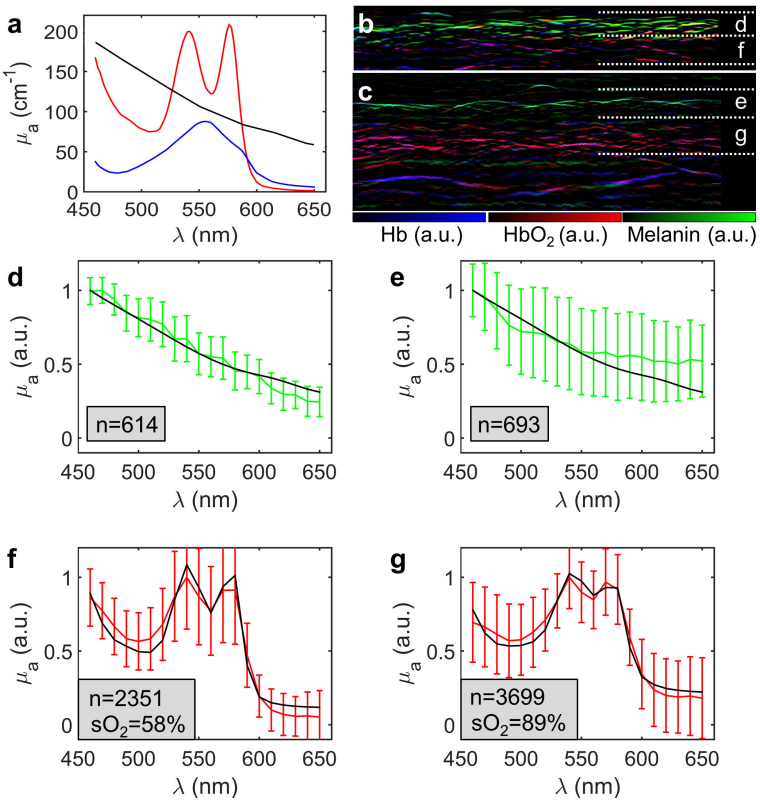

Figure 7.3.: Absorption spectra of anatomical structures in human skin. a) Absorption spectra of oxyhemoglobin at 105 g/l (red curve), deoxyhemoglobin at 45 g/l (blue curve), and eumelanin at 45 mM (black curve). **b)** Cross-sectional view of the lower arm indicating the compartments of the epidermal layer and the lower blood vessels. Corresponding absorption spectra are plotted in (d) and (f) respectively. **c)** Cross-sectional view of the thenar area indicating the compartments of the *stratum corneum*and the upper dermal blood vessels. Corresponding absorption spectra are plotted in (e) and (g) respectively. **d)** Experimentally determined absorption spectrum of the epidermal layer in hairy skin (green) in comparison to the theoretical absorption spectrum of eumelanin (black). **e)** Measured absorption spectrum of the *stratum corneum* in hairless skin (green) in comparison to the theoretical absorption spectrum of eumelanin (black). **f)** Experimentally determined absorption spectrum of lower dermal blood vessels (red) in comparison to the theoretical absorption spectrum of 58% oxygenated blood (black). **g)** Measured absorption spectrum of upper dermal blood vessels (red) in comparison to the theoretical absorption spectrum of 89% oxygenated blood (black). In (d-g) the error bars mark the standard deviation between segmented pixels of the same compartment. n specifies the number of segmented voxels that have been used to calculate the mean and standard deviation of the experimental spectra. Adapted from Schwarz *et al.* [91] © 2016 Wiley-VCH Verlag GmbH & Co. KGaA. Reproduced with permission.

7.3.2. Three-dimensional unmixing of intrinsic chromophores

With the MSOT system not only 2D cross-sections but whole 3D multispectral absorption maps can be acquired. In volumetric imaging mode the four distinct wavelengths 520 nm, 540 nm, 560 nm, and 650 nm were chosen. The step size was set to 5 μm and 20 μm along the fast- and slow-scanning axis respectively, in order to span an equidistant mesh of 20 μm step

size for each wavelength. Each single-wavelength image was reconstructed separately using the beam-forming algorithm presented in 3.5. Due to the operation of the laser in wavelength-sweep mode and motion correction (see chapter 5), the reconstructed multispectral data was inherently co-registered.

A scan of 4 mm × 2 mm took approximately 13 minutes. The volumetric multispectral reconstructions were unmixed by a linear regression algorithm with non-negative constraint [88, 173], considering the spectra of melanin, oxyhemoglobin, and deoxyhemoglobin [117].

In short, optoacoustic images are proportional to the absorbed optical energy, which is a product of the light fluence and the combined absorption coefficient of all absorbing moieties:

$$H(\vec{r},\lambda_i) = \phi(\vec{r},\lambda_i)\sum_{j=1}^{n}\mu_{a,j}(\vec{r},\lambda_i) = \phi(\vec{r},\lambda_i)\sum_{j=1}^{n}\epsilon_j(\lambda_i)c_j(\vec{r}) \tag{7.4}$$

where $\mu_{a,j}(\vec{r},\lambda_i)$ is the absorption coefficient of the j^{th} absorber, $\epsilon_j(\lambda_i)$ its molar extinction coefficient at the wavelength λ_i, and $c_j(\vec{r})$ its concentration. By knowing the absorbed optical energy $H(\vec{r},\lambda_i)$, the light fluence $\phi(\vec{r},\lambda_i)$, and the absorption spectrum $\epsilon_j(\lambda_i)$, the concentration of the different absorbers can be calculated via linear inversion or by non-negative least-squares fitting (in-built MATLAB function "lsqnonneq").

Again two distinct skin areas of two healthy male volunteers were imaged. The first area was located on the skin covering the thenar eminence (palm of hand), representing glabrous skin with a thick epidermal layer. The second area was located on the lower arm, representing hairy skin, which is characterized by a thin melanin-rich epidermal layer. Skin color for area 1 and 2 was classified as skin type II and type III according to the Fitzpatrick scale respectively.

Figure 7.4 depicts the results of the lower arm. Figures 7.4a-c show 3D absorption maps of melanin, oxyhemoglobin, and deoxyhemoglobin that were calculated from the volumetric multispectral datasets. Figure 7.4a displays the superficial epidermal layer, which is characterized by strong absorption of melanin. No noticeable hemoglobin signal is observed in the epidermis. The dermal layer, depicted in Figure 7.4b, features a vascular network characterized by absorption of oxy- and deoxyhemoglobin. The separation of melanin absorption in the epidermis and (de)oxyhemoglobin in the dermis is better seen in a vertical MAP (side view). Figure 7.4c reveals the absorption of melanin on the surface, whereas the vascular network is situated below the melanin layer. From the absorption maps of both oxy- and deoxyhemoglobin, the oxygenation level of the vascular network was calculated. Figure 7.4d shows a blood oxygenation map over the whole skin depth. Extracted oxygen saturation values range between $85 \pm 4\%$ close to the skin surface and $54 \pm 7\%$ of a draining vein deeper inside the dermis.

To our knowledge, there is no other imaging technique that allows for the measurement of blood oxygenation levels in single vessels. Thus, the results of this section cannot be validated by parallel measurements. However, our findings are consistent with bulk blood oxygen saturation measurements recorded by optical reflectance spectroscopy (ORS) of the forearm, which were reported to be $72.9 \pm 12.2\%$ [59], $65 \pm 11.9\%$ [60], and $45 \pm 10\%$ [61]. Near-infrared spectroscopy (NIRS) penetrates deeper into the cutaneous tissue and is widely used for measurements of blood oxygenation. With NIRS, oxygenation levels in human forearms have been reported to be $\sim 70\%$ with relatively large variations between patients [62] and $< 60\%$ [63].

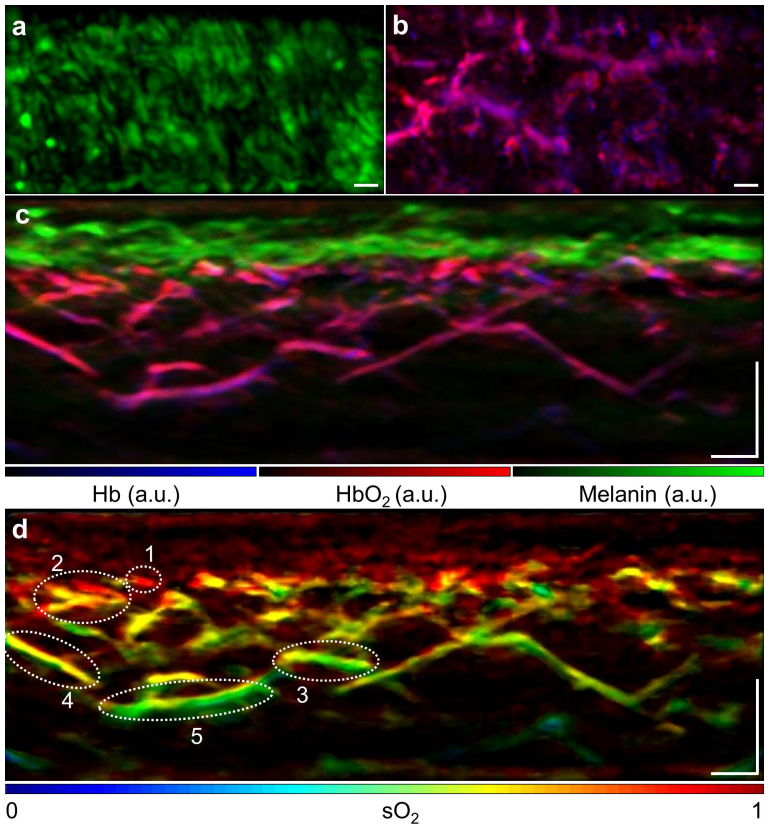

Figure 7.4.: Unmixing intrinsic chromophores of the lower arm in 3D. a) MAP along the z-axis (top view) of the epidermal layer. **b)** MAP along the z-axis (top view) of the dermal layer. **c)** MAP along the x-axis (side view). **d)** MAP of the sO_2 map along the x-axis (side view). The brightness of the anatomical features scales proportional to the amplitude of absorption. The vessels marked by the dotted ellipses exhibit oxygen saturation of 1) $85 \pm 4\%$, 2) $67 \pm 7\%$, 3) $58 \pm 5\%$, 4) $65 \pm 7\%$, and 5) $54 \pm 7\%$. Subfigures (a-d) show a ROI spanning 4 mm in width. All scale bars: 250 μm. Adapted from Schwarz *et al.* [91] © 2016 Wiley-VCH Verlag GmbH & Co. KGaA. Reproduced with permission.

Apart from the lower arm area, MSOM was performed on the thenar area of healthy skin. The location of the ROI is shown in Figure 7.5b. The unmixed absorption maps of melanin, oxyhemoglobin, and deoxyhemoglobin are visualized in Figure 7.5 by the green, red, and blue RGB channel, respectively. Figure 7.5a shows a side view of the ROI that marks the skin layers visualized in Figure 7.5c-e. Figure 7.5c shows the layer where the epidermal-dermal junction is located. In this layer clusters of oxy- and deoxyhemoglobin are seen following the shape of the epidermal ridges. The superficial horizontal plexus, depicted in Figure 7.5d, shows the microvascular network, which is characterized by high blood oxygenation values. The deep horizontal plexus, visualized in Figure 7.5e, is characterized by large vessels that contain mostly deoxyhemoglobin as well as oxyhemoglobin.

7.4. Summary and outlook

In this chapter, the spectral ability of optoacoustic dermoscopy has been shown. For the first time, 3D imaging of blood-oxygenation in human skin *in vivo* has been demonstrated.

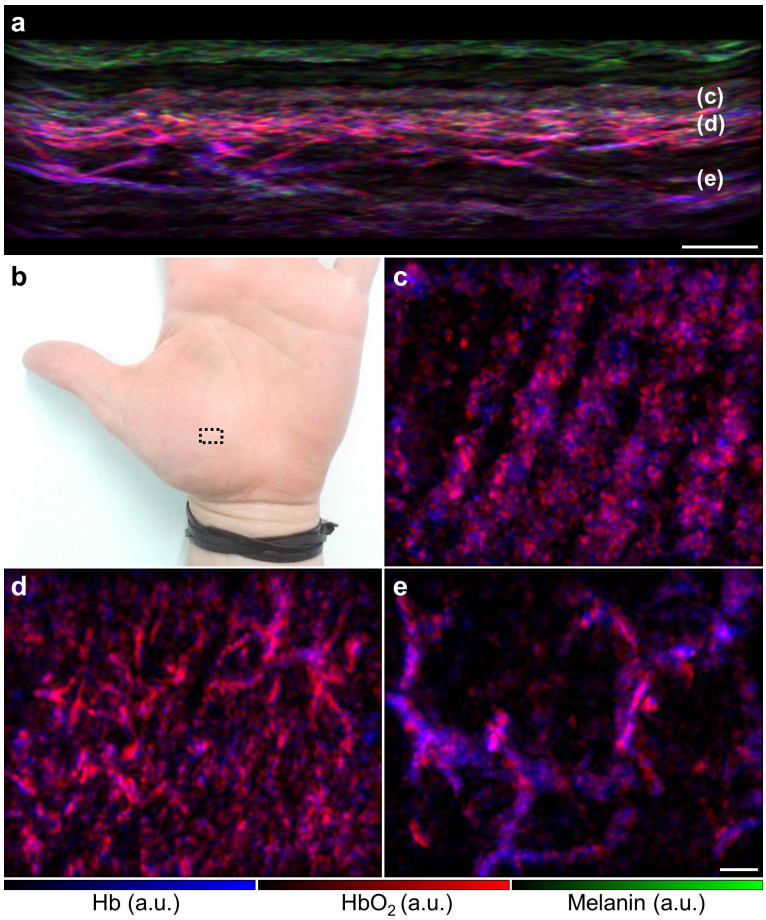

Figure 7.5.: Unmixing intrinsic chromophores of the human palm in 3D. In green, red, and blue the unmixing results for melanin, oxyhemoglobin, and deoxyhemoglobin, are shown, respectively. **a)** Side-view (vertical MAP) of the ROI shown in (b). **b)** Region of interest located on the human palm marked by the black dashed box. **c)** Lateral MAP of the dermal papillae layer. **d)** Lateral MAP of the superficial horizontal plexus. **e)** Lateral MAP of the deep horizontal plexus. All scale bars: 500 μm. Adapted from Schwarz *et al.* [213] © 2016 SPIE. Reproduced with permission.

In section 7.1, the unique spectral capability of MSOM was introduced. No other imaging modality enables high resolution quantification of intrinsic chromophores in 3D. Human skin contains numerous intrinsic chromophores that exhibit unique absorption spectra. The absorption of visible and near-infrared light ($320-900$ nm) by human skin is governed by the natural chromophores eumelanin, pheomelanin, oxyhemoglobin, deoxyhemoglobin, bilirubin, and β-carotene [108, 112, 117, 129–134]. The quantification of tissue chromophores has great potential in the diagnosis and therapy of skin diseases, since metabolic changes are observed in many diseases, e.g. tumors [214, 215], systemic sclerosis [219], and ischemic wounds [220].

The experimental setup of MSOM was described in section 3.2. Due to the low repetition rate of the laser and the necessity to excite the tissue at several wavelengths, the acquisition time in MSOM is very long, limiting image quality and patient/volunteer comfort. To reduce the acquisition time by a factor of 4, an adapted acquisition protocol was presented in section 7.2.1. The data is recorded on an undersampled grid with a step size of 40 μm and subsequently interpolated to an artificial acquisition grid of 20 μm step size. To overcome

the motion artifacts in low speed MSOM, the operation of the laser in wavelength-sweep mode and the motion correction algorithm presented in chapter 5 are inevitable.

Section 7.2.2 and 7.2.3 shed light on the available detection bandwidth and resolution of MSOM. Both detection bandwidth and resolution are limited by the finite pulse width of the laser. The multi-wavelength OPO laser emits laser pulses of width $4-7\,\mathrm{ns}$, violating the condition of stress confinement (see section 2.4). Consequently, the finite pulse width acts as a lowpass filter of the recorded data in frequency domain. From the calculation presented in section 7.2.2 it follows that a laser pulse width of 7 ns (FWHM) translates into a lowpass filter with cutoff frequency at 63 MHz (−6 dB). Thus, the finite pulse width of the OPO laser limits the detection bandwidth but does allow for the detection of acoustic frequencies above 50 MHz. Experimental measurements of the axial and lateral resolution, performed in section 7.2.3, revealed a lateral resolution of $50-60\,\mu\mathrm{m}$ and an axial resolution of $<13\,\mu\mathrm{m}$ independent of the excitation wavelengths.

Section 7.3.1 showed previously undisclosed broadband optoacoustic absorption spectra of skin compartments *in vivo*. The broadband spectra were recorded by sweeping over 20 equidistant wavelengths in the range from $460-650\,\mathrm{nm}$. Measurements showed that the spectrum of the epidermal layer carries the absorption spectrum of eumelanin for both the lower arm and the human palm. An absorption spectrum of the lower dermal vessels yielded the best fit to an oxygenation level of $\mathrm{sO}_2 = 58\%$, whereas higher blood oxygenation levels were found in the more superficial upper dermal vessels.

Finally, section 7.3.2 presents for the first time 3D imaging of blood oxygenation in human skin *in vivo*. In volumetric imaging mode the four distinct wavelengths 520 nm, 540 nm, 560 nm, and 650 nm were recorded, and the volumetric multispectral reconstructions were unmixed by a linear regression algorithm [88]. As a result, 3D absorption maps of melanin, oxyhemoglobin, and deoxyhemoglobin were calculated. From the absorption maps of both oxy- and deoxyhemoglobin, the oxygenation level of the vascular network was calculated, showing oxygen saturation levels between $85\pm4\%$ close to the skin surface and $54\pm7\%$ of a draining vein deeper inside the dermis. To our knowledge, there is no other imaging technique that allows for the measurement of blood oxygenation levels in single vessels. Nonetheless, bulk blood oxygen saturation measurements performed with ORS and NIRS confirm the reported physiological range of blood oxygenation determined by MSOM.

To improve the quantification accuracy of MOD, light fluence correction models should be introduced in the future. As an initial model, wavelength-dependent changes in light fluence could be estimated by iteratively fitting a one-dimensional model of diffuse light transport to the absorbed energy distribution, similar to [225], assuming a reduced scattering coefficient of $\mu_s' = 36\,\mathrm{cm}^{-1}$ and an initial mean absorption coefficient of $\mu_a = 1.5\,\mathrm{cm}^{-1}$. Preliminary results showed that light fluence corrections lead to slightly increased oxygenation values.

MOD brings new sensing ability to dermatology that can impact detection and diagnosis. MOD could enable for the first time three-dimensional mapping throughout the skin, allowing information on lesion penetration and quantitative readings on oxygenation. The spectral capacity demonstrated by MOD relates to lesion pathophysiology, potentially linking to biochemical or metabolic alterations of skin due to disease [226, 227]. Hypoxic conditions have not only been found in cancer but also in tissue inflammation [228, 229], ischemic wounds [220], and systemic sclerosis [219].

8. Clinical applications

8.1. Introduction

As outlined in chapter 1, human skin is affected by skin conditions of different kind: skin cancer, inflammatory diseases, and autoimmune diseases. In chapter 6 tumor progression and angiogenesis in melanoma tumors has been imaged in a preclinical mouse model. In this chapter clinical results of inflammatory and autoimmune diseases will be presented.

Inflammatory skin diseases such as psoriasis and atopic eczema arise from a complex interaction of genetic predisposition, a hyper-responsive immune system, and environmental factors [13, 14]. Herein, the main focus will be put on psoriasis, which is a skin disorder that can severely affect life quality of the person suffering from it [94]. The affected group shows decreased employment rates and less income [230]. Approximately 2% of the whole population are affected by psoriasis [231]. The psoriatic skin is characterized by red, itchy patches with white scales. The scales are due to hyper-proliferation in the epidermis, known as acanthosis. Further characteristics of psoriasis are typically dilated capillaries in the dermal papillae [94] and alterations in dermal vasculature. The self-immune response associated with psoriasis results in a strong inflammatory infiltration [94].

In the dermatology clinic, the psoriasis area severity index (PASI) is used to assess the severity of psoriasis. The local PASI score is the sum of three different parameters ranging from $0-4$: erythema (redness), induration (hardening), and scaling. The global PASI score takes additionally into account the percentage of the body affected. Classification of psoriasis by its appearance into PASI scores is a subjective measure and needs well-trained dermatologists. For this reason an objective severity score would help in clinical practice.

So far the vascular bed has received little attention in the pathogenesis of psoriasis [232]. Furthermore, objective biomarkers of the disease are needed to evaluate disease severity and treatment response [232]. Herein, the strength of optoacoustic dermoscopy in visualizing vascular features and changes due to disease will be shown, aiming for the establishment of an objective set of disease biomarkers. Note that this chapter will be only a short introduction to the topic. The interested reader is referred to our recently submitted publication [233].

8.2. Clinical imaging system and acquisition protocol

The clinical RSOM55 setup was already introduced in chapter 3. Figure 8.1 illustrates the scanning unit of the clinical RSOM system and its usage in clinical measurements. The scan head is attached to an articulated arm, which allows for positioning of the scanning unit on the ROI. The patient rests on a patient bench, while the scanning head is positioned in its correct location. For fast imaging, a ROI measuring $5\,\mathrm{mm} \times 3\,\mathrm{mm}$ is scanned, resulting in imaging times of less than 2 minutes. All studies were approved by the ethics committee of

Figure 8.1.: Scanning unit of clinical RSOM system. **a)** 3D model of scan head utilized in clinical RSOM. **b)** The scanning unit is attached to an articulated arm, which allows for positioning of the scan head on the skin area of interest.

the Technical University of Munich, and all measurements were performed in compliance with laser safety standards [100]. Patients were recruited and diagnosed by expert dermatologists. The results of four psoriasis patients, one lichen ruber patient, and one atopic eczema patient will be shown. In addition a progression study of induced psoriasis was performed and monitored in a healthy volunteer. In every patient two RSOM images were acquired: one image of a ROI covering diseased skin and another image of adjacent healthy skin.

8.3. Clinical applications

8.3.1. Disease biomarkers of psoriasis

To visualize morphological changes in psoriatic skin, a psoriasis plaque was imaged and compared to adjacent healthy skin. The results are shown in Figure 8.2. Expert dermatologists assessed a local PASI score of 6 for the psoriasis plaque. The inlay in Figure 8.2a,d shows the imaged plaque and adjacent healthy skin for comparison. The RSOM images show prominent differences between psoriatic and healthy skin. Quantification of these changes give rise to disease biomarkers. Figure 8.2a,d shows cross-sectional images of the diseased skin. The white arrow indicates that the thickness of both epidermis and epidermal-dermal junction is significantly larger in psoriatic skin compared to healthy skin. Epidermal thickening, more specifically thickening of the *stratum basale*, is a known disease biomarker, which is called acanthosis. The cyan arrow in Figure 8.2a indicates a region of increased blood volume, which is another biomarker of the disease. Lateral MAPs of the epidermal-dermal junction, depicted in 8.2b,e, reveal an additional disease marker, *i.e.* an increase in the diameter of capillary loops. Whereas large circular absorbers are observed in the junction of psoriatic skin, no circular absorption pattern is observed in healthy skin. In healthy skin no capillary loops are seen because the diameter of the capillary loops is too small, *i.e.* the emitted ultrasound frequencies are too high to be detected with RSOM55 (see section 2.5 and 3.2). The fourth biomarker of psoriasis is illustrated by the lateral MAP of the dermal vasculature in Figure 8.2c. The light purple arrow indicates a distortion of the dermal vasculature, most likely due to increased tortuosity. The list of disease biomarkers introduced in this section is meant to give an idea of how RSOM technology can quantify disease. A more sophisticated set of biomarkers has recently been submitted for publication by our group [233].

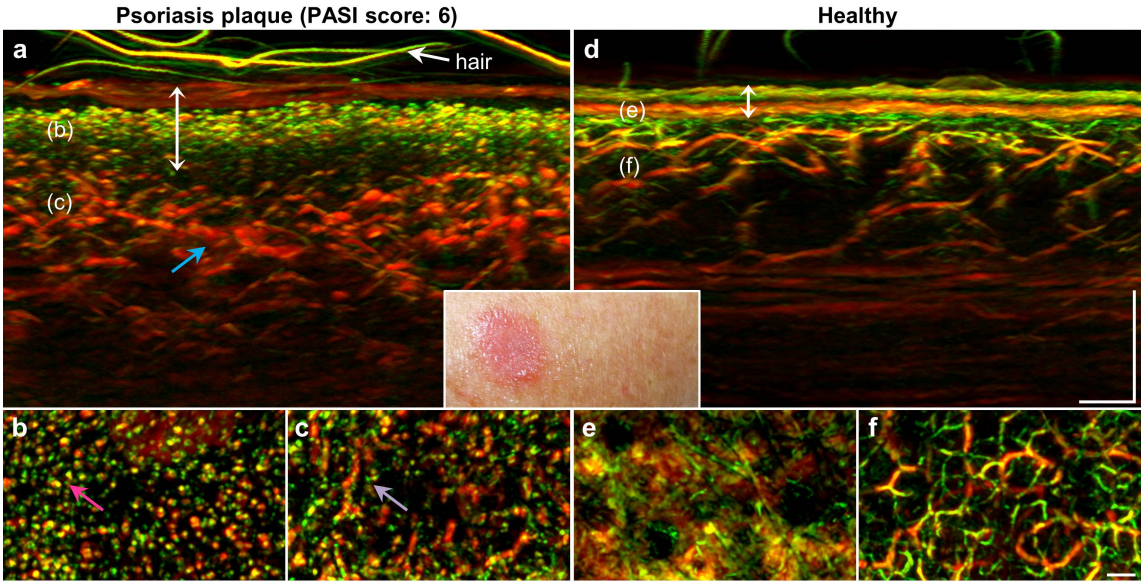

Figure 8.2.: Disease biomarkers in psoriatic skin. a) Vertical MAP of psoriatic human skin of local PASI score 6. The inlay shows the imaged psoriasis plaque. The white arrow indicates epidermal thickening. The cyan arrow indicates blood volume increase. **b)** Lateral MAP of the epidermal-dermal junction. The magenta arrow indicates enlarged capillary loops. **c)** Lateral MAP of the dermal vasculature. The light purple arrow indicates a distortion of the dermal vasculature due to increased tortuosity. **d)** Vertical MAP of close-by healthy skin. The inlay shows the imaged healthy skin area close to the psoriasis plaque. The white arrow indicates the thickness of the epidermis. **e)** Lateral MAP of the epidermal-dermal junction. The diameter of the capillary loops is too small to be seen with RSOM55. **f)** Lateral MAP of healthy human vasculature. Scale bars: 500 μm

8.3.2. Layer thickening and blood volume increase in psoriasis

As discussed in the previous section, several disease biomarkers are present in psoriasis: acanthosis, blood volume increase, increase in diameter of capillary loops, and distortion of the dermal blood network. To quantify layer thickening and blood volume increase, the contrast-to-noise ratio and absorber volume fraction were calculated for the cross-sectional data presented in Figure 8.2a,d. The formulas for CNR and AVF are given in section 4.5. Briefly, the CNR calculation determines the contrast of anatomical structures as a function of depth. The AVF provides information on the concentration of optoacoustic absorbers within the skin at a specific depth. Since the vascular network in human skin is organized in layers of high blood volume, e.g. the superficial and deep horizontal plexus, and layers of low blood volume, e.g. most of the reticular dermis, skin layers are identified with the help of the AVF.

Figure 8.3 quantifies skin thickening and blood volume increase in psoriatic skin. Three different layers are marked by the numbers 1-3 in Figure 8.3: 1) *stratum corneum*, 2) *stratum basale* and dermal papillae, 3) superficial horizontal plexus. Figure 8.3a shows that the *stratum corneum*, *stratum basale*, and horizontal plexus are visible as distinctive contrast peaks. The *stratum basale* and horizontal plexus are located markedly deeper in psoriatic skin compared to healthy skin. Peaks of the *stratum basale*/dermal papillae are separated by $\sim$ 100 μm, whereas the contrast peak of the superficial horizontal plexus is separated

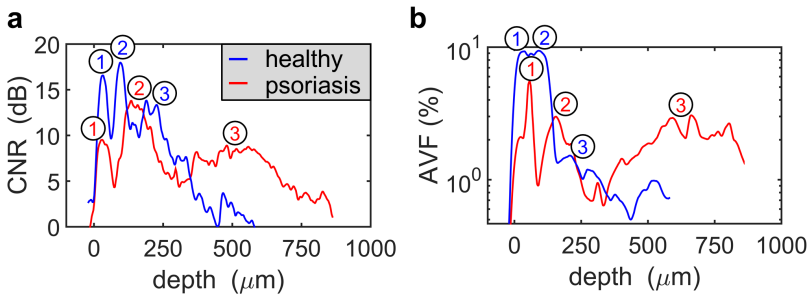

Figure 8.3.: Skin thickening and blood volume increase in psoriatic skin. **a)** Contrast-to-noise ratio of anatomical structures as a function of depth for healthy and psoriatic skin. Different layers show up as local maxima in the CNR. 1) *stratum corneum*, 2) *stratum basale* and dermal papillae, and 3) superficial horizontal plexus. The *stratum basale* and horizontal plexus are located deeper in psoriatic skin. **b)** Absorber volume fraction of optoacoustic absorbers as a function of depth for healthy and psoriatic skin. The AVF of the *stratum corneum*, and *stratum basale* is less pronounced in diseased skin. The superficial horizontal plexus shows increased blood volume fraction in psoriasis.

by $\sim 250\,\mu$m between healthy and diseased skin. Figure 8.3b shows the absorber volume fraction, and prominent structures are marked by the numbers 1-3, analogous to Figure 8.3a. The AVF of the *stratum corneum* and *stratum basale* is less pronounced in diseased skin. The superficial horizontal plexus shows increased blood volume fraction in psoriasis.

8.3.3. Epidermal thickening in psoriasis

Figure 8.4 quantifies epidermal thickening in psoriatic skin. Four different psoriasis plaques were imaged, and cross-sectional images are shown in Figure 8.4a-d. Expert dermatologists diagnosed the plaques with a PASI index of $4-9$. The white brackets in Figure 8.4a-d indicate the thickness of the epidermis and epidermal-dermal junction. In all cases, the epidermis is significantly thicker in diseased skin. Interestingly, epidermal thickening is most prominent in Figure 8.4d, although the PASI index is higher in Figure 8.4c. The epidermal thickness of both healthy and diseased skin has been measured and is plotted in Figure 8.4e in a boxplot. The boxplot shows the distinctive difference in epidermal thickness between healthy and psoriatic skin. Whereas healthy epidermis measures slightly more than $100\,\mu$m, the mean thickness of psoriatic epidermis measures more than $300\,\mu$m. Note that there are large variations in epidermal thickness between different psoriasis plaques, while the thickness measurements of healthy skin show much less variance.

8.3.4. Progression measurements of psoriasis

To study disease development and to provide disease monitoring in the clinic, it is of high importance to provide non-invasive imaging methods. Figure 8.5 shows a time course measurement performed on induced psoriasis. The psoriasis model is based on the epicutaneous application of imiquimod (Aldara 5% cream), which induces psoriasis-like skin reactions in mice [234]. Furthermore, there are several case reports of impaired psoriasis in humans after using Aldara 5% cream [235, 236]. In the healthy volunteer taking part in this study,

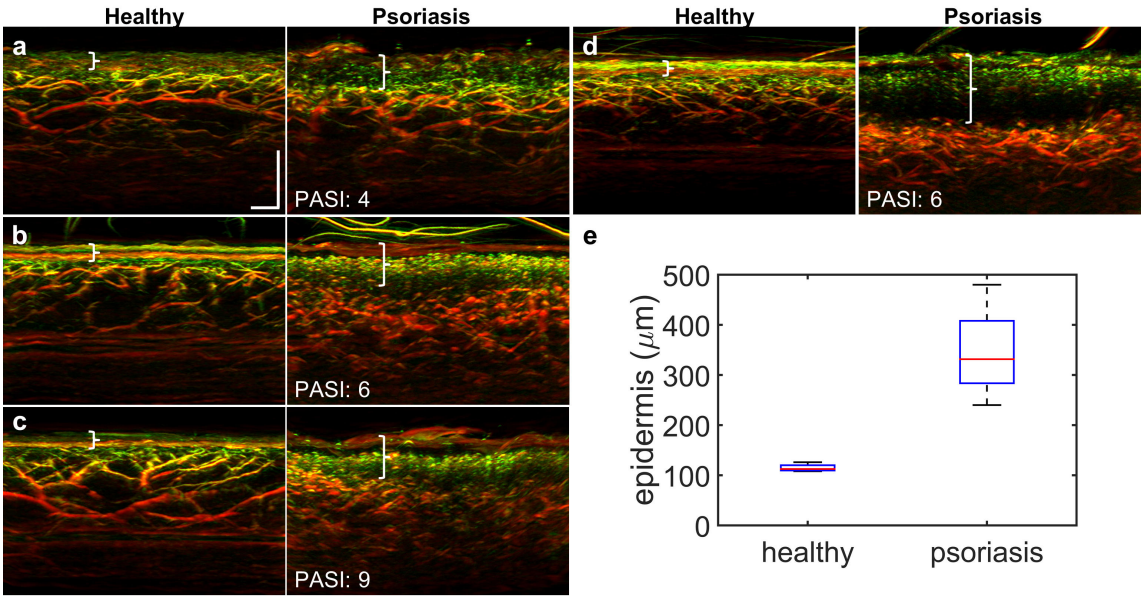

Figure 8.4.: Acanthosis in psoriatic skin. a-d) Vertical MAP of healthy and psoriatic human skin in four different patients. The local PASI index of the psoriasis plaque is depicted in each subfigure. The white brackets indicate the thickness of the epidermis and epidermal-dermal junction. Note that epidermal thickening is most prominent in (d), although the PASI index in (c) is higher. **e)** Boxplot of epidermal thickness in healthy and psoriatic skin. The thicknesses were extracted from (a-d). Note the strong epidermal thickening in diseased skin.

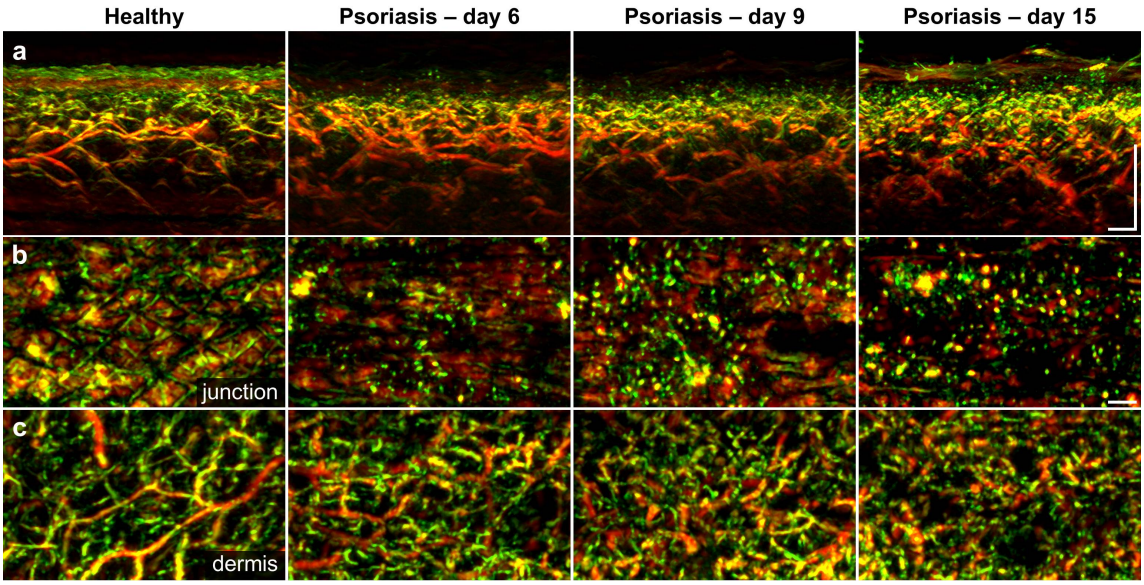

Figure 8.5.: Time course measurements of psoriasis progression. Images were taken before induction (column 1), at day 6 (column 2), day 9 (column 3), and day 15 (column 4) after psoriasis induction. **a)** Vertical MAP of the progressing psoriasis plaque. The *stratum corneum* disappears after induction. **a)** Lateral MAPs of the epidermal-dermal junction. The diameter of capillary loops increases over time. **c)** Lateral MAP of the vascular network of the dermis. The vessels get denser and distorted over time.

imiquimod was repeatedly applied to a ROI measuring $\sim 2\,\mathrm{cm}$ in diameter on the right shoulder. The progression of the induced psoriasis plaque was monitored over time. Figure 8.5a plots vertical MAPs of the affected skin area over time. After psoriasis induction the optoacoustic signal from the *stratum corneum* drops significantly, and the *stratum corneum* seems to disappear. Only at day 15 a low-frequency layer appears again in the area, where the *stratum corneum* should be located. Since the skin of the volunteer was exposed to sunlight between day 9 and day 15, the emerging low-frequency layer could stem from melanin that has migrated from adjacent healthy skin into the psoriasis plaque. Figure 8.5b plots lateral MAPs of the epidermal-dermal junction over time. Before induction no capillary loops are seen because they are too small to be detected with RSOM55 (see section 8.3.1). At day 6 some capillary loops are visible since they have increased in diameter. At day 9 and day 15 more and larger capillary loops are observed. Vascular alterations are not only located in the epidermal-dermal junction but comprise the entire dermal vasculature, as depicted in Figure 8.3.1c. Over time the vessel network gets denser and increasingly distorted.

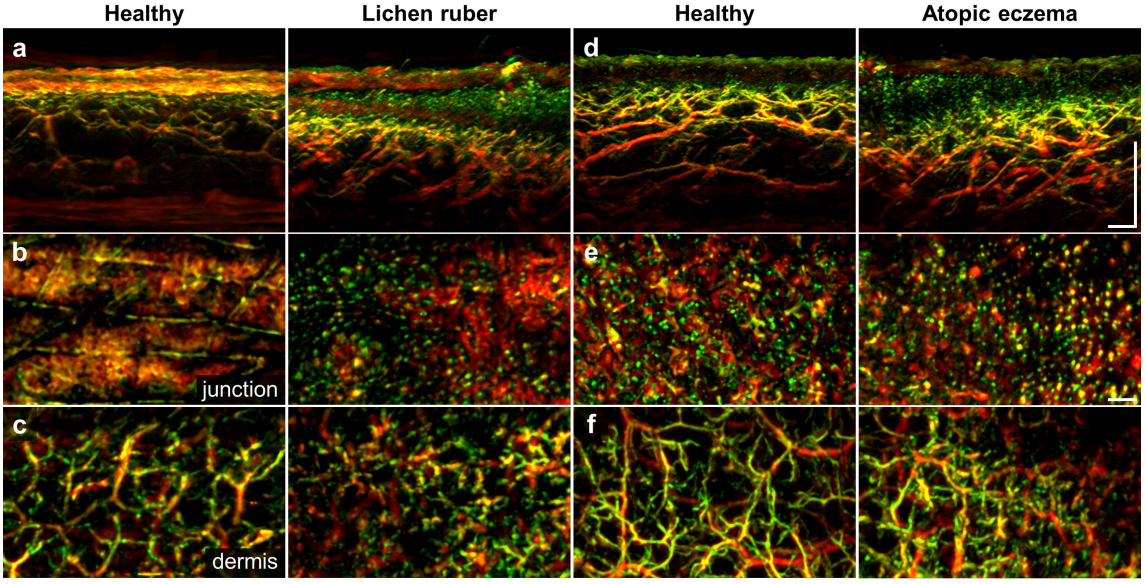

Figure 8.6.: Disease biomarkers of lichen ruber and atopic eczema. Images were taken of both diseased skin and close-by healthy skin. **a)** Vertical MAP of healthy skin and lichen ruber. The epidermis and the junction are thickened. **b)** Lateral MAPs of the epidermal-dermal junction. The diameter of capillary loops is larger in skin affected by lichen ruber. **c)** Lateral MAP of the vascular network of the dermis. The vascular network is distorted in diseased skin. **d)** Vertical MAP of healthy skin and atopic eczema. The junction in diseased skin is thickened. **e)** Lateral MAPs of the epidermal-dermal junction. The diameter of capillary loops is larger in skin affected by atopic eczema. Note that the capillaries of healthy skin are enlarged as well. **f)** Lateral MAP of the vascular network of the dermis. The vascular network is denser in diseased skin.

8.4. Imaging other inflammatory and autoimmune diseases

So far, the main focus was put on imaging psoriasis. Morphological and vascular changes are, however, not limited to psoriasis but are present in a large number of skin disorders. Figure 8.6 shows exemplary results for two other skin disorders, *i.e.* lichen ruber and atopic

eczema. Figure 8.6a-c compares lichen ruber to adjacent healthy skin in cross-sectional and lateral MAPs. Epidermal thickening is observed in lichen ruber, where the thickness of the epidermis increases from left to right in Figure 8.6a. Furthermore, Figure 8.6b shows that the diameter of capillary loops is increased in lichen ruber. Figure 8.6c depicts the dermal vasculature that seems to be denser in diseased skin. Interesting features are seen in the data for atopic eczema as well. Figure 8.6d-f shows epidermal thickening, increased size of capillary loops, and a denser vasculature, similar to psoriasis. Interestingly, adjacent healthy skin shows an increase in capillary loop size as well, indicating that even close-by seemingly healthy skin displays signs of inflammation.

8.5. Summary and Conclusion

In this chapter, the first account on *in vivo* non-invasive clinical optoacoustic imaging of the dermal vascular has been presented. The strength of optoacoustic dermoscopy in visualizing vascular features and changes due to disease have been shown, and a set of objective disease biomarkers has been established for both inflammatory and autoimmune diseases. The classification of psoriasis by objective disease biomarkers through optoacoustic dermoscopy could establish a new age of diagnostics and monitoring, extending the state-of-the-art severity index classifications by the unaided eye.

In section 8.2, the clinical acquisition protocol using RSOM55 was presented. The RSOM scan head is attached to an articulated arm, which allows for positioning of the scanning unit on the ROI of the patient, who rests on a patient bench. The imaging times are less than 2 minutes for a ROI of $5\,\text{mm} \times 3\,\text{mm}$. All studies were approved by the ethics committee of the Technical University of Munich, and all measurements were performed in compliance with laser safety standards [100].

In section 8.3.1, the morphological changes in psoriatic skin were visualized and compared to adjacent healthy skin. A set of disease biomarkers was established that can be quantified accurately with clinical RSOM55. Prominent markers in psoriasis are epidermal thickening (caused by acanthosis), an increase in diameter of capillary loops of the epidermal-dermal junction, increased blood volume in the dermis, and a distortion of the dermal vasculature, which appears denser and with increased tortuosity. In section 8.3.2, the increase in blood volume of the superficial horizontal plexus was quantified. In an exemplary psoriasis plaque a large vertical thickening of the superficial plexus and an up to 2-fold blood volume increase was observed. The quantification of blood volume increase through the entire dermis cannot be accessed with the classical optical skin imaging portfolio. In section 8.3.3, the degree of acanthosis was quantified in RSOM images for four different psoriasis plaques with a PASI index of $4 - 9$. Healthy epidermis measured slightly more than $100\,\mu\text{m}$, and the mean thickness of psoriatic epidermis measured more than $300\,\mu\text{m}$. There were large variations in epidermal thickness between different psoriasis plaques, whereas the thickness measurements of healthy skin showed much less variance.

Section 8.3.4 presented a time course measurement performed on induced psoriasis. The psoriasis model was based on the epicutaneous application of imiquimod (Aldara 5% cream), which induces psoriasis-like skin reactions in mice and humans. The time course measurements revealed the progression of psoriasis through the entire skin. Whereas the *stratum corneum* was affected directly after induction and seemed to recover slightly on day 15, an increase in inflammation of both capillary loops and the dermal vasculature was observed.

In the epidermal-dermal junction more and larger capillary loops were observed, and the dermal vessel network got denser and increasingly distorted.

Finally, in section 8.4, morphological and vascular changes of skin disorders other than psoriasis were presented. The two exemplary skin diseases were lichen ruber and atopic eczema. Again, striking morphological changes of epidermis and dermal vasculature were observed. In the atopic eczema patient, adjacent healthy skin showed an increase in capillary loop size, indicating that even close-by seemingly healthy skin was inflamed.

A clear strength of the presented biomarkers is their objectivity. The proposed biomarkers go beyond the state-of-the-art characterization indexes, such as PASI for psoriasis. Classical severity index scores are based on the subjective impression by observing the lesions with the unaided eye. Clinical RSOM55, implemented in a fast and easy to use format, opens up new possibilities for the structured evaluation of disease biomarkers for a large set of skin disorders in the clinic. The non-invasive monitoring of disease progression or therapy monitoring provides new opportunities inaccessible to traditional diagnostic methods, such as dermatoscopy in combination with biopsies.

9. Summary and Outlook

The skin is the largest organ in humans, constitutes the boundary to our environment, and plays an important role in the human immune defense. Healthy skin is indispensable to provide the proper functionality. Yet, a large number of people are affected by skin conditions that can be classified into skin cancer, inflammatory diseases, and autoimmune diseases. Recent statistics show that the incidence rates of skin diseases, especially skin cancer, are rising. As of today, typical assessment of skin disease in dermatology includes the visual examination of the skin under magnification with a dermatoscope, complemented by histological diagnosis of biopsies. The visual inspection and photographic imaging requires well-trained personnel and only allows for the two-dimensional visualization of a three-dimensional disease. Complementary biopsies cause pain and scars in the patient, and the diagnosis process takes several days. The procedural and invasive nature also comes with some risk for the patient and cost to the health care system. A diagnostic device giving specific information on various skin diseases in 3D could direct the appropriate treatment and help to decrease the cost. However, the current limitations of biomedical imaging techniques in the scope of visualizing angiogenesis in cancer, chronic inflammatory diseases, and other diseases are well known in the biomedical community and have been summarized by Donald M. McDonald and Peter L. Choyke: "An ongoing dilemma is, however, that [optical] microscopic methods provide their highest resolution on preserved tissue specimens, whereas clinical methods give images of living tissues deep within the body but at much lower resolution and specificity and generally cannot resolve vessels of the microcirculation. Future challenges include developing new imaging methods that can bridge this resolution gap and specifically identify angiogenic vessels." [2]

The ambitious goal of this thesis was to develop a new imaging method for dermatology, termed multispectral optoacoustic dermoscopy, that bridges the mesoscopic resolution gap, identifies microvessels, and in addition provides functional information of the vasculature. Optoacoustic (photoacoustic) imaging is based on the photoacoustic effect, which describes the process of sound generation upon excitation of tissue with light. MOD offers three major advantages not available in other methods. First, MOD offers optical contrast at ultrasound-diffraction limited resolution, rendering resolution and imaging depth highly scalable. Second, the contrast in MOD is generated on absorption. Consequently, all natural chromophores, e.g. melanin and hemoglobin, yield direct and strong contrast. Third, multispectral excitation can be used to distinguish the characteristic absorption spectra of deoxyhemoglobin, oxyhemoglobin, and melanin, providing functional and metabolic information. Optoacoustic dermoscopy has the ability to impact screening in dermatology beyond the abilities of current imaging techniques. This thesis was dedicated to the development and application of optoacoustic dermoscopy, which was presented to the reader in eight chapters.

In chapter 2, the reader was familiarized to the basics of optoacoustic dermoscopy, including the theory of optoacoustics, skin anatomy, and optical properties of skin. The background information of optoacoustic signal generation, the anatomy of human skin, and the optical properties of human skin were merged to formulate the requirements of optoacoustic

dermoscopy in terms of imaging depth and detection bandwidth. An optoacoustic atlas of human skin was created, mapping skin anatomy to the ultrasonic frequencies produced as a function of depth. Based on the simulated skin atlas, concurrent imaging of all human skin layers requires superficial detection (up to 450 μm) of frequencies > 150 MHz and detection of frequencies < 30 MHz up to a depth of 1.5 mm. Knowing the requirements of optoacoustic dermoscopy in terms of imaging depth and detection bandwidth, a literature survey of state-of-the-art imaging setups in optoacoustic dermoscopy was performed. The technology of optoacoustic dermoscopy has progressed considerably in the last decade, however, none of the current imaging platforms allowed for concurrent imaging of all human skin layers.

The remainder of the thesis was dedicated to the development and applications of MOD, aiming to overcome the limitations of state-of-the-art optoacoustic dermoscopy setups. In chapter 3, raster-scan optoacoustic mesoscopy (RSOM) was introduced, which was developed in our group [3, 164, 165]. Emphasis was put on different RSOM implementations, improved reconstruction methods, and optimal sampling of both acquisition and reconstruction parameters. In RSOM, nanosecond laser pulses are used to excite the tissue. A spherically focused piezoelectric detector records the ultrasound waves emitted by the tissue after excitation. The illumination-detector unit is raster-scanned in-tandem on a 2D surface by two piezoelectric stages. A depth-encoded time signal is recorded and images are reconstructed tomographically. Four different RSOM implementations were introduced: high-frequency RSOM100 ($20 - 180$ MHz), fast and sensitive RSOM50 ($10 - 90$ MHz), a miniaturized and portable RSOM55 ($14 - 126$ MHz.), developed for clinical applications, and a multispectral raster-scan optoacoustic mesoscopy (MSOM) system, which provides functional information.

The reconstruction in RSOM consists of two main parts, *i.e.* pre-processing of the acquired data and the 3D beam-forming reconstruction algorithm. Both pre-processing and reconstruction steps were explained in detail in this thesis. The main pre-processing steps include the filtering of reflection lines in the Fourier space, bandpass-filtering of the raw data, and automatic co-registration of the raw data. A custom-designed 3D reconstruction algorithm was implemented on a GPU to allow for parallel and fast reconstruction of 3D images. The reconstruction algorithm is based on a generalized idea of the back-projection algorithm, taking into account the geometry of the detector. For improved visualization, the ultra-wide detection bandwidth is separated into two sub-bands before reconstruction. The two sub-bands can be visualized simultaneously by a red and green channel in one image. In this way, the masking of high frequencies by low frequencies was overcome and improved visualization of smaller structures was observed. To improve the image quality further, optimal parameters for spatial and temporal sampling of acquisition as well as reconstruction grid were evaluated.

In chapter 4, the first quantitative account was given on the relation between the excitation energy, detection bandwidth, and imaging depth achieved with optoacoustic dermoscopy. Computer modeling was combined with phantom measurements and *in vivo* imaging of human skin to specify optimal and marginal energy ranges required for concurrent visualization of all skin layers. The findings on the experimentally determined detection bandwidth of RSOM were related to the requirements dictated by the anatomy of human skin (see section 2.5). Measurements have confirmed that RSOM100 detects frequencies up to 180 MHz but at limited 1 mm depth, whereas deeper imaging (up to 1.5 mm) at meaningful resolutions can be achieved with RSOM50 at frequencies lower than 140 MHz. Hence, RSOM100 detects higher frequencies but resolves dermal features more superficially, whereas RSOM50 samples signals with lower frequency but from the entire skin depth. To conclude, RSOM is well-suited to detect vessels of various sizes through all skin layers. Both the impact of

excitation energy on the image quality and on the imaging speed were studied. Finding the best compromise between fast imaging speed and high contrast is of major importance since greater per-pulse energies favor higher imaging contrast, but higher per-pulse energies result in lower imaging speed. Based on *in vivo* measurements, optimal per-pulse excitation energies lie in the range of $150 - 200\,\mu$J and $80 - 100\,\mu$J for RSOM100 and RSOM50 respectively.

In chapter 5, a powerful motion correction algorithm was presented, which was designed for raster-scan optoacoustic mesoscopy. Since RSOM is a tomographic imaging modality, the quality and resolution of reconstructed images deteriorates significantly due to motion, e.g. breathing motion, of the patient/volunteer during the acquisition. In humans, motion cannot be reduced by anesthetizing or restraining the volunteer, as in animal imaging. The motion correction algorithm presented in this work is a mere software algorithm that can be applied after acquisition and is based on one simple assumption: The skin surface is assumed to be continuous and smooth on a mesoscopic scale, *i.e.* on the scale of several micrometers. The strongly absorbing melanin layer in the epidermis is used to detect the skin surface, and an artificially smoothed surface is generated to correct for motion. The improvement in image quality after motion correction was demonstrated for RSOM100, clinical RSOM55, and MSOM. Due to motion correction, unprecedented imaging performance was obtained with RSOM100, visualizing the epidermal-dermal junction as well as the superficial horizontal plexus. In clinical data the algorithm was able to correct strong breathing motion in a patient. Furthermore, in clinical data motion correction is required for reliable quantification of biomarkers. Multispectral images are due to a lack of fast per-pulse tunable lasers slow and time consuming. Thus, spectral data is strongly affected by motion. In this work it was shown that for reliable unmixing results in MSOM motion correction is indispensable.

The last chapters of the thesis dealt primarily with applications of MOD. In chapter 6, melanoma tumor growth, the corresponding arrangement of the surrounding vascular network, and the growth of new microvessels in the vicinity of the B16F10 tumor were imaged with RSOM. This was the first time that tumor vasculature was imaged at such depths with such resolution *in vivo*. Longitudinal growth studies and growth-related changes of the tumor as well as angiogenesis were shown with RSOM. Correct visualization of the 3D tumor with surrounding vessels was confirmed by cryo-slices. In chapter 7, an elaborate multispectral acquisition and data processing protocol was presented and the unique spectral ability of optoacoustic dermoscopy was shown. Human skin contains numerous intrinsic chromophores that exhibit unique absorption spectra. No other imaging modality enables high resolution quantification of intrinsic chromophores in 3D. Previously undisclosed broadband $(460 - 650\,\text{nm})$ optoacoustic absorption spectra of skin compartments *in vivo* were recorded. For the first time, 3D imaging of blood-oxygenation in human skin was demonstrated. In chapter 8, the first account on *in vivo* clinical optoacoustic imaging of the dermal vasculature was presented. The strength of optoacoustic dermoscopy in visualizing vascular features and changes due to disease was shown, and a set of objective disease biomarkers has been established for both inflammatory and autoimmune diseases. Prominent disease biomarkers in psoriasis were epidermal thickening (acanthosis), an increase in the diameter of capillary loops of the epidermal-dermal junction, increased blood volume in the dermis, and a distortion of the dermal vasculature, which appears denser and with increased tortuosity. Time course measurements revealed the progression of psoriasis through the entire skin.

Future work

This work paves the way for effective applications of MOD in basic and translational dermatology and dermoscopy. The classification of psoriasis by objective disease biomarkers through optoacoustic dermoscopy could establish a new age of diagnostics and monitoring, extending the state-of-the-art severity index classifications by the unaided eye. A clear strength of the presented biomarkers is their objectivity. The proposed biomarkers go beyond the state-of-the-art characterization indexes, such as PASI for psoriasis. Classical severity index scores are based on the subjective impression by observing the lesions with the unaided eye. Clinical RSOM55, implemented in a fast and easy to use format, opens up new possibilities for the structured evaluation of disease biomarkers for a large set of skin disorders in the clinic. The non-invasive monitoring of disease progression or therapy monitoring provides new opportunities inaccessible to traditional diagnostic methods, such as dermatoscopy in combination with biopsies. Implementation of clinical RSOM100 could further enable improved visualization of small skin structures and quantification of the microvasculature. Its potential applications in optoacoustic capillaroscopy could improve differential diagnosis of a range of skin disorders, including systemic sclerosis [92, 93], psoriasis [47, 94], and eczemas [13, 14].

Multispectral optoacoustic dermoscopy brings new sensing ability to dermatology that can impact detection and diagnosis. MOD could enable for the first time the three-dimensional mapping throughout the skin, allowing information on lesion penetration and quantitative readings of oxygenation. The spectral capacity demonstrated by MOD relates to lesion pathophysiology, potentially linking to biochemical or metabolic alterations of skin due to disease [226, 227]. Hypoxic conditions have not only been found in cancer, but also in tissue inflammation [228, 229], ischemic wounds [220], and systemic sclerosis [219]. Based on the study of imaging angiogenesis in tumors in combination with 3D quantification of blood oxygenation *in vivo*, it is expected that in the near future MSOM will enable metabolic measurements of a wide range of skin disorders including inflammation [228, 229], skin cancer [226, 227], and wound healing [220]. Exogenous contrast agents could extend the scope of MSOM further towards monitoring the bio-distribution and dynamics of marked biomolecules in a wide range of cutaneous processes [201, 237].

From a technological stand point, MOD technology could be developed in multiple aspects. To increase the imaging depth, the excitation wavelength could be tuned, since the optical penetration depth in human skin is proportional to $\mu_a^{-1/2}$ and increases with decreasing absorption. Changing the wavelength from 532 nm, which is used for single-wavelength RSOM, to a wavelength lying in the spectral range from $610 - 660$ nm could increase imaging depth at still sufficient absorption contrast of hemoglobin and melanin.

To improve the quantification accuracy of MOD, light fluence correction models should be introduced in the future. As an initial model, wavelength-dependent changes in light fluence could be estimated by iteratively fitting a one-dimensional model of diffuse light transport to the absorbed energy distribution, similar to [225], assuming a reduced scattering coefficient of $\mu_s' = 36\,\mathrm{cm}^{-1}$ and an initial mean absorption coefficient of $\mu_a = 1.5\,\mathrm{cm}^{-1}$. Preliminary results showed that light fluence corrections lead to slightly increased oxygenation values.

An everlasting field of improvement is the development of new instrumentation, most importantly adapted laser sources and ultrasound detectors. In the case of light sources, cheap fast-tunable laser sources emitting nanosecond pulses are required. The development of cheap and miniaturized pulsed laser diodes could be of interest. Further development of

sensitive ultrasound detectors with a large detection bandwidth is crucial for the success of optoacoustic imaging. Currently, optoacoustic dermoscopy has to be performed in raster-scan mode since the detector sensitivity scales with the size of the detection element, and the small single elements of detector arrays lack in sensitivity. To increase image quality and patient comfort, it would be desirable to speed up the acquisition process, which is, however, only possible with more sensitive ultrasound detectors and/or parallel acquisition. Alternative detection schemes to piezoelectric detectors are capacitive micromachined ultrasonic transducers (CMUTs), which detect acoustic waves through changes of capacitance. The advantage of CMUTs is that dense 2D arrays can be constructed. CMUTs provide a large angular acceptance angle, which is favorable in tomography. However, current CMUT technology is limited to ultrasound frequencies up to $\sim 10\,\mathrm{MHz}$ [238]. Still, CMUT technology might become an interesting alternative for ultrasound detection in skin imaging. Another alternative for ultrasound detectors are an all-optical optoacoustic pi-phase-shifted fiber Bragg grating with coherence-restored pulsed interferometry used as the interrogation method. A broad detection bandwidth up to hundreds of MHz and high sensitivity is achieved [239]. The technique is expected to advance within the next years.

Acknowledgements

In conclusion of this thesis, I want to thank every person, who has contributed to this work in one way or another. First of all, I would like to thank Prof. Vasilis Ntziachristos for giving me the opportunity to work in the exciting field of optoacoustic dermoscopy. His visionary and inspiring personality opened up great collaborations with clinical partners, interesting clinical studies, and a seemingly endless potential of new applications. His guidance in scientific writing was very precious for me. All of my scientific work was only possible through the strong financial support by his grants. I was given freedom in my work, which I appreciated a lot.

I want to thank the members of my HELENA thesis committee Prof. Norbert Hanik, and Dr. Tanja von Braunmühl, who sacrificed their time to come to my committee meetings and who provided valuable input to my thesis. I am very grateful that Prof. Hanik agreed to be an additional reviewer of my thesis. Thank you to Prof. Friedrich Simmel for the time he will spend reviewing my Ph.D. thesis and participating at my Ph.D. defense. Thank you to Prof. Werner Hemmert, who will be the chair at my Ph.D. defense.

I want to thank Andreas Bühler, who was my first group leader at the IBMI. Especially in the early phase of my thesis, he taught me a lot about optoacoustic imaging and provided me with important MATLAB code for reconstruction and unmixing. He always took time for me, when I had questions both technical and beyond.

A special thanks goes to Juan Aguirre, who became my group leader in the final year of my thesis. Together we worked on the project of clinical optoacoustic dermoscopy and spent many hours measuring patients and ourselves. His humor and openness made work more fun. His mind is full of exciting new ideas and applications, and we spent a lot of time in fruitful discussions. His guidance in improving the story line in my publications, oral presentations, and poster presentations was very valuable, and I learned a lot from him.

I want to thank Murad Omar, who has developed the laboratory system of raster-scan optoacoustic mesoscopy (RSOM). His deep knowledge in electrical engineering was indispensable for the success of this work. We worked together in many projects, especially in preclinical imaging of mice. He always had an open door and always took time for me. He was always helpful and contributed valuable feedback to my publications. Especially, I want to thank Murad for reading through this thesis and helping me to improve it.

A great thank you goes to our clinical collaboration partners at the dermatology at Biederstein (TUM). Kilian Eyerich was a wonderful person to work with, always helpful with great scientific ideas. Through his commitment in writing an ethical protocol, interesting clinical studies became possible. Working with him was always productive, and we were given a lot of freedom and trust. I want to thank Natalie Garzorz and Felix Lauffer, who undertook a great deal of recruiting the patients and were our clinical persons of contact. Natalie Garzorz performed and analyzed all of our biopsies, which was a lot of work.

I would like to thank our collaboration partners at the dermatology of the LMU. We collaborated with Elke Sattler and Tanja von Braunmühl especially in writing book chapters. Thank you to Tanja von Braunmühl for her effort in writing an ethical protocol, which was unfortunately not accepted. More collaboration partners, who I want to thank, are Stefan Haak and Stephanie Musiol. They worked with us on imaging mice with induced psoriasis. The collaboration with them was very promising and I hope that it can be continued in the future.

A great thank you goes to my office mates. Dominik Soliman is a fellow sufferer, who started and ended his Ph.D. at the same time as myself. Together we learned a lot, and he helped me out in all sorts of scientific and administrative issues. Working at IBMI became much easier through the mutual exchange of ideas with him. He contributed and helped out in projects with his time, code, and ideas. Hailong He is my longest room mate. With him, I spent most of my lunch times, and we shared good times, outside of work as well. He is a funny guy, his openness was always inspiring, and I was able to learn a lot about China through him. Ludwig Prade is the person to talk to, when you need hardware components, experimental expertise or want to discuss new concepts. He is always helpful and has great scientific ideas. He is engaged as laser safety officer and sacrificed many hours to keep the 3D printer working. Thank you for all of your commitment. Thank you to Andrei Berezhnoi, who joined our office recently and made our success in the Helmholtz soccer cup possible.

A great thank you goes to Johannes Rebling, who was always motivated to help, especially with the 3D printer and by his GIT tutorial. With him I found as well a motivated climbing partner for the leisure time. Thank you to Benno Koberstein-Schwarz, Paul Vetschera, Luis Den-Ben, and Ara Ghazaryan, who have helped me many times in working with the tunable Innolas laser. Thank you to Nicolas Bézière, especially for our collaboration in imaging psoriasis mice. Andrei Chekkoury helped me at the beginning of my work at IBMI with the linear array. Thanks to Thomas Fehm for his tutorial on CUDA programming. Thank you to Gael Diot for installing the 3D printer. I want to thank Josefine Reber and Saak Ovsepyan for helping me structure and improve my Ph.D. thesis and publications. Thank you to Panagiotis Symvoulidis for his help in working with Amira and cryo-slicing.

I want to thank all the technical personnel Sarah Glasl, Florian Jürgeleit, and Uwe Klemm for precious support in animal handling and cryo-slicing. Also thanks to the administrative personnel Susanne Stern, Silvia Weinzierl, Zsuszanna Öszi, Doris Bengel, Ines Baumgartner, Julia Niefnecker, Andreas Brandstätter, Martina Riedl, Barbara Schroeder, Christiane Ogorek, Christoph Hinzen, and Prof. Karl-Hans Englmeier for their help in administrative matters.

I want to thank all people at IBMI for the last 3.5 years. I much appreciated working with all of you.

My thanks goes also to my family, who supported me all my life, as well during my studies. I want to thank my father for his everlasting support, Ruach for inspiring ideas, and JC for making me alive and his never-ending companionship. Through them I became who I am. Furthermore, I want to thank Manuel Böhme, my flat mates, my smallgroup, and friends for their friendship and good times outside of work.

Last but not least I want to thank my beloved wife Sonja Schwarz, who makes life more beautiful. I cannot think of anyone, who is so precious to me and makes me develop into a better man and husband. Her interest in my work and loving nature are a great source of strength for me.

A. List of publications

Publications in peer-reviewed journals

1. L. Vionnet, J. Gateau, **M. Schwarz**, A. Buehler, V. Ermolayev, and V. Ntziachristos. "24 MHz scanner for optoacoustic imaging of skin and burn." *IEEE Transactions on Medical Imaging*, 33(2):535-545, 2013.

2. **M. Schwarz**, A. Buehler, and V. Ntziachristos. "Isotropic high resolution optoacoustic imaging with linear detector arrays in bi-directional scanning." *Journal of Biophotonics*, 8(1-2):60-70, 2015.

3. J. Aguirre, **M. Schwarz**, D. Soliman, A. Buehler, M. Omar, and V. Ntziachristos. "Broadband mesoscopic optoacoustic tomography reveals skin layers." *Optics Letters*, 39(21):6297, 2014.

4. **M. Schwarz**, M. Omar, A. Buehler, J. Aguirre, and V. Ntziachristos. "Implications of ultrasound frequency in optoacoustic mesoscopy of the skin." *IEEE Transactions on Medical Imaging*, 34(2):672-677, 2014.

5. M. Omar^{+}, **M. Schwarz**$^{+}$, D. Soliman, P. Symvoulidis, and V. Ntziachristos. "Pushing the optical imaging limits of cancer with multi-frequency-band raster-scan optoacoustic mesoscopy (RSOM)." *Neoplasia*, 17(2):208-14, 2015.

6. **M. Schwarz**, A. Buehler, J. Aguirre, and V. Ntziachristos. "Three-dimensional multispectral optoacoustic mesoscopy reveals melanin and blood oxygenation in human skin in vivo." *Journal of Biophotonics*, 9(1-2):55-60, 2016.

7. M. Omar^{+}, J. Rebling^{+}, K. Wicker^{+}, T. Schmitt-Manderbach, **M. Schwarz**, J. Gateau, H. Lopez-Schier, T. Mappes, and V. Ntziachristos. "Optical imaging of post-embryonic zebrafish using multi orientation raster scan optoacoustic mesoscopy." *Light Science & Applications*, 2016.

8. **M. Schwarz**, D. Soliman, M. Omar, A. Buehler, S. V. Ovsepian, A. Aguirre, and V. Ntziachristos. "Optoacoustic Dermoscopy of the Human Skin: Tuning Excitation Energy for Optimal Detection Bandwidth With Fast and Deep Imaging in vivo" *IEEE Transactions on Medical Imaging*, 36(6):1287-1296, 2017.

9. J. Aguirre, **M. Schwarz**, N. Garzorz, M. Omar, D. Soliman, A. Buehler, K. Eyerich, and V. Ntziachristos. "Precision assessment of label-free psoriasis biomarkers with ultra-broadband optoacoustic mesoscopy." *Nature Biomedical Engineering* 1,0068, 2017.

10. **M. Schwarz**, N. Garzorz-Stark, K. Eyerich, J. Aguirre, and V. Ntziachristos. "Motion correction in optoacoustic mesoscopy." *Scientific reports*, 7(1),10386, 2017.

$^{+}$equal contribution

Book chapters

1. **M. Schwarz**[+], J. Aguirre[+], M. Omar, and V. Ntziachristos. Book chapter on "Optoacoustic imaging of skin" in M.R. Hamblin, P. Avci, and G.K. Gupta. "Imaging in dermatology." *Elsevier Science*, 2016.

2. E. Sattler, **M. Schwarz**. Book chapter on "Optoakustische Bildgebung" in Stolz, Hänssle, Sattler, and Welzel. "Bildgebende Diagnostik in der Dermatologie." *Thieme*, 2017.

[+]equal contribution

International conference contributions and proceedings

1. **M. Schwarz**, J. Aguirre, A. Buehler, M. Omar, and V. Ntziachristos. "Visualization of the microcirculatory network in skin by high frequency optoacoustic mesoscopy."
   Published in *Proceedings of SPIE* Opto-Acoustic Methods and Applications in Biophotonics II, vol. 9539, page 95390J, 2015.
   Oral presentation given at the European Conference on Biomedical Optics (ECBO) in Munich, Germany, June 21-25, 2015.

2. J. Aguirre, **M. Schwarz**, H. He, and V. Ntziachristos. "A handheld raster scan optoacoustic mesoscopy system for skin imaging."
   Oral presentation given at the European Conference on Biomedical Optics (ECBO) in Munich, Germany, June 21-25, 2015.

3. **M. Schwarz**, J. Aguirre, D. Soliman, A. Buehler, and V. Ntziachristos. "Unmixing chromophores in human skin with a 3D multispectral optoacoustic mesoscopy system."
   Published in *Proceedings of SPIE* Photons Plus Ultrasound: Imaging and Sensing 2016, vol. 9708, page 970855, 2016.
   Poster presentation given at the SPIE Biomedical Optics, and Imaging Conference (BiOS), Photonics West 2016, in San Francisco (CA), USA, Feb. 13-18, 2016.

4. M. Omar, **M. Schwarz**, D. Soliman, P. Symvoulidis, and V. Ntziachristos. "Imaging melanin cancer growth in-vivo using raster-scan optoacoustic mesoscopy (RSOM) at 50 MHz and 100 MHz."
   Published in *Proceedings of SPIE* Photons Plus Ultrasound: Imaging and Sensing 2016, vol. 9708, page 97080S, 2016.
   Oral presentation given at the SPIE Biomedical Optics, and Imaging Conference (BiOS), Photonics West 2016, in San Francisco (CA), USA, Feb. 13-18, 2016.

5. J. Aguirre, **M. Schwarz**, and V. Ntziachristos. "A broadband handheld raster scan optoacoustic mesoscopy system for skin imaging compatible with the clinic."
   Published in *Proceedings of OSA* In Vivo Human Optical Imaging, pages TTh1B.3, 2016.
   Oral presentation given at the Clinical and Translational Biophotonics (CTB) conference in Fort Lauderdale, Fl, USA, April 2528, 2016

B. Permission to reuse content from publications

Section 1.4.1 and chapter 6 contain excerpts of a book chapter, which was written by Schwarz *et al.* and published in the work of Hamblin *et al.* [1] © 2016 Elsevier.

Section 2.5 and chapter 4 contain adapted text passages and figures from a manuscript submitted for publication by Schwarz *et al.* [106].

Chapter 5 contains adapted text passages and figures from a manuscript to be submitted for publication by Schwarz *et al.* [192].

Chapter 6 contains adapted text passages and figures from the publication by Omar and Schwarz *et al.* [163] © 2015 Neoplasia Press, Inc. Published by Elsevier Inc.

Chapter 7 contains adapted text passages and figures from the publication by Schwarz *et al.* [91] © 2016 Wiley-VCH Verlag GmbH & Co. KGaA.

Chapter 7 contains adapted text passages and figures from the proceedings publications by Schwarz *et al.* [213] © 2016 SPIE.

Written permission to reproduce textual material, illustrations, and tables have been obtained for all of the above mentioned publications in written form through the Copyright Clearance Center RightsLink® or through direct email contact to the editor. The written copyright and/or permission forms are available upon request.

Bibliography

[1] M.R. Hamblin, P. Avci, and G.K. Gupta. *Imaging in Dermatology*. Elsevier Science, 2016.

[2] D. M. McDonald and P. L. Choyke. Imaging of angiogenesis: from microscope to clinic. *Nature Medicine*, 9(6):713–725, 2003.

[3] M. Omar, J. Gateau, and V. Ntziachristos. Raster-scan optoacoustic mesoscopy in the 25-125 mhz range. *Opt Lett*, 38(14):2472–4, 2013.

[4] A. Taruttis and V. Ntziachristos. Advances in real-time multispectral optoacoustic imaging and its applications. *Nature Photonics*, 9(4):219–227, 2015.

[5] Ingrid Moll. *Duale Reihe Dermatologie*. Georg Thieme Verlag, 2010.

[6] N Howlader, AM Noone, M Krapcho, N Neyman, R Aminou, SF Altekruse, CL Kosary, J Ruhl, Z Tatalovich, and H Cho. Seer cancer statistics review, 1975-2009 (vintage 2009 populations), national cancer institute. bethesda, md, 2012.

[7] American Cancer Society. Cancer facts and figures 2013. Technical report, American Cancer Society, 2013.

[8] Cancer Research U. K. Uk and Research Cancer. Skin cancer incidence statistics, 04/09/2013 16:13 2013. Cancer Research UK.

[9] Skin Cancer Facts. Skin cancer facts - skincancer.org, 2014.

[10] Robert Koch-Institut (Hrsg) und die Gesellschaft der epidemiologischen Krebsregister in Deutschland e.V. (Hrsg). Krebs in deutschland 2011/2012, 2015.

[11] J. K. Robinson. Sun exposure, sun protection, and vitamin d. *JAMA*, 294(12):1541–3, 2005.

[12] D. U. Ekwueme, Jr. Guy, G. P., C. Li, S. H. Rim, P. Parelkar, and S. C. Chen. The health burden and economic costs of cutaneous melanoma mortality by race/ethnicity-united states, 2000 to 2006. *J Am Acad Dermatol*, 65(5 Suppl 1):S133–43, 2011.

[13] K. Eyerich and N. Novak. Immunology of atopic eczema: overcoming the th1/th2 paradigm. *Allergy*, 68(8):974–82, 2013.

[14] S. Eyerich, A. T. Onken, S. Weidinger, A. Franke, F. Nasorri, D. Pennino, M. Grosber, F. Pfab, C. B. Schmidt-Weber, M. Mempel, R. Hein, J. Ring, A. Cavani, and K. Eyerich. Mutual antagonism of t cells causing psoriasis and atopic eczema. *N Engl J Med*, 365(3):231–8, 2011.

[15] M Claussen, G Riemekasten, and MM Hoeper. [pulmonary arterial hypertension in collagenoses]. *Zeitschrift fr Rheumatologie*, 68(8):630–638, 2009.

[16] F. Fichel, N. Baudot, J. P. Gaitz, S. Trad, C. Barbe, C. Frances, and P. Senet. Systemic sclerosis with normal or nonspecific nailfold capillaroscopy. *Dermatology*, 228(4):360–7, 2014.

[17] L. Castelo-Soccio. Diagnosis and management of alopecia in children. *Pediatric Clinics of North America*, 61(2):427–+, 2014.

[18] Luiz Carlos Junqueira, Jos Carneiro, Robert O. Kelley, and Manfred Gratzl. Histologie, 2004. 10.1007/978-3-662-07778-8 [Elektronische Ressource] von Luiz Carlos Junqueira, Jos Carneiro, Robert O. Kelley; herausgegeben von Manfred Gratzl Online edition.

[19] Jr. Clark, W. H., L. From, E. A. Bernardino, and M. C. Mihm. The histogenesis and biologic behavior of primary human malignant melanomas of the skin. *Cancer Res*, 29(3):705–27, 1969.

[20] A. Breslow. Thickness, cross-sectional areas and depth of invasion in the prognosis of cutaneous melanoma. *Ann Surg*, 172(5):902–8, 1970.

[21] Hiroshi Shimizu. *Shimizu's Textbook of Dermatology*. Hokkaido University, 2007.

[22] The National Cancer Institute. The cost of cancer, 2011.

[23] Inc The Lewen Group, The Society for Investigative Dermatology Association, and The American Academy of Dermatology. The burden of skin diseases 2005. 2005.

[24] X. Wortsman. Common applications of dermatologic sonography. *J Ultrasound Med*, 31(1):97–111, 2012.

[25] E. Szymanska, A. Nowicki, K. Mlosek, J. Litniewski, M. Lewandowski, W. Secomski, and R. Tymkiewicz. Skin imaging with high frequency ultrasound - preliminary results. *Eur J Ultrasound*, 12(1):9–16, 2000.

[26] Ben Cox and Paul Beard. Imaging techniques: Super-resolution ultrasound. *Nature*, 527(7579):451–452, 2015.

[27] N. Lassau, S. Mercier, S. Koscielny, M. F. Avril, A. Margulis, G. Mamelle, P. Duvillard, and J. Leclere. Prognostic value of high-frequency sonography and color doppler sonography for the preoperative assessment of melanomas. *American Journal of Roentgenology*, 172(2):457–461, 1999.

[28] X. Wortsman. Sonography of the primary cutaneous melanoma: a review. *Radiol Res Pract*, 2012:814396, 2012.

[29] K. Hoffmann, J. Jung, S. el Gammal, and P. Altmeyer. Malignant melanoma in 20-mhz b scan sonography. *Dermatology*, 185(1):49–55, 1992.

[30] P. Guitera, L. X. Li, K. Crotty, P. Fitzgerald, R. Mellenbergh, G. Pellacani, and S. W. Menzies. Melanoma histological breslow thickness predicted by 75-mhz ultrasonography. *Br J Dermatol*, 159(2):364–9, 2008.

[31] T. Gambichler, G. Moussa, K. Bahrenberg, M. Vogt, H. Ermert, D. Weyhe, P. Altmeyer, and K. Hoffmann. Preoperative ultrasonic assessment of thin melanocytic skin lesions using a 100-mhz ultrasound transducer: A comparative study. *Dermatologic Surgery*, 33(7):818–824, 2007.

[32] D. Jasaitiene, S. Valiukeviciene, G. Linkeviciute, R. Raisutis, E. Jasiuniene, and R. Kazys. Principles of high-frequency ultrasonography for investigation of skin pathology. *J Eur Acad Dermatol Venereol*, 25(4):375–82, 2011.

[33] M. M. Music, K. Hertl, M. Kadivec, M. D. Pavlovic, and M. Hocevar. Pre-operative ultrasound with a 12-15 mhz linear probe reliably differentiates between melanoma thicker and thinner than 1 mm. *J Eur Acad Dermatol Venereol*, 24(9):1105–8, 2010.

[34] R. Vilana, S. Puig, M. Sanchez, M. Squarcia, A. Lopez, T. Castel, and J. Malvehy. Preoperative assessment of cutaneous melanoma thickness using 10-mhz sonography. *American Journal of Roentgenology*, 193(3):639–643, 2009.

[35] V. Kaikaris, D. Samsanavicius, Maslauskas Kestutis, R. Rimdeika, S. Valiukeviciene, J. Makstiene, and J. Pundzius. Measurement of melanoma thickness–comparison of two methods: ultrasound versus morphology. *J Plast Reconstr Aesthet Surg*, 64(6):796–802, 2011.

[36] T. D. Desai, A. D. Desai, D. C. Horowitz, F. Kartono, and T. Wahl. The use of high-frequency ultrasound in the evaluation of superficial and nodular basal cell carcinomas. *Dermatologic Surgery*, 33(10):1220–1226, 2007.

[37] M. B. M. El-Zawahry, H. M. A. E. H. El-Cheweikh, S. E. R. Ramadan, D. A. Bassiouny, and M. M. Fawzy. Ultrasound biomicroscopy in the diagnosis of skin diseases. *European Journal of Dermatology*, 17(6):469–475, 2007.

[38] J. Tacke, G. Haagen, O. P. Hornstein, G. Huettinger, F. Kiesewetter, H. Schell, and T. L. Diepgen. Clinical relevance of sonometry-derived tumour thickness in malignant melanoma–a statistical analysis. *Br J Dermatol*, 132(2):209–14, 1995.

[39] G. Krahn, P. Gottlober, C. Sander, and R. U. Peter. Dermatoscopy and high frequency sonography: two useful non-invasive methods to increase preoperative diagnostic accuracy in pigmented skin lesions. *Pigment Cell Res*, 11(3):151–4, 1998.

[40] M. H. Schmid-Wendtner and W. Burgdorf. Ultrasound scanning in dermatology. *Arch Dermatol*, 141(2):217–24, 2005.

[41] S. Gonzalez and Y. Gilaberte-Calzada. In vivo reflectance-mode confocal microscopy in clinical dermatology and cosmetology. *Int J Cosmet Sci*, 30(1):1–17, 2008.

[42] M. Rajadhyaksha, M. Grossman, D. Esterowitz, R. H. Webb, and R. R. Anderson. In vivo confocal scanning laser microscopy of human skin: melanin provides strong contrast. *J Invest Dermatol*, 104(6):946–52, 1995.

[43] M. Rajadhyaksha, S. Gonzalez, J. M. Zavislan, R. R. Anderson, and R. H. Webb. In vivo confocal scanning laser microscopy of human skin ii: advances in instrumentation and comparison with histology. *J Invest Dermatol*, 113(3):293–303, 1999.

[44] N. Kollias and G. N. Stamatas. Optical non-invasive approaches to diagnosis of skin diseases. *Journal of Investigative Dermatology Symposium Proceedings*, 7(1):64–75, 2002.

[45] G. Pellacani, A. M. Cesinaro, and S. Seidenari. Reflectance-mode confocal microscopy of pigmented skin lesions–improvement in melanoma diagnostic specificity. *J Am Acad Dermatol*, 53(6):979–85, 2005.

[46] P. Guitera, S. W. Menzies, C. Longo, A. M. Cesinaro, R. A. Scolyer, and G. Pellacani. In vivo confocal microscopy for diagnosis of melanoma and basal cell carcinoma using a two-step method: analysis of 710 consecutive clinically equivocal cases. *J Invest Dermatol*, 132(10):2386–94, 2012.

[47] R. Archid, A. Patzelt, B. Lange-Asschenfeldt, S. S. Ahmad, M. Ulrich, E. Stockfleth, S. Philipp, W. Sterry, and J. Lademann. Confocal laser-scanning microscopy of capillaries in normal and psoriatic skin. *J Biomed Opt*, 17(10):101511, 2012.

[48] C. L. Evans, E. O. Potma, M. Puoris'haag, D. Cote, C. P. Lin, and X. S. Xie. Chemical imaging of tissue in vivo with video-rate coherent anti-stokes raman scattering microscopy. *Proc Natl Acad Sci U S A*, 102(46):16807–12, 2005.

[49] Y. Ozeki, W. Umemura, Y. Otsuka, S. Satoh, H. Hashimoto, K. Sumimura, N. Nishizawa, K. Fukui, and K. Itoh. High-speed molecular spectral imaging of tissue with stimulated raman scattering. *Nature Photonics*, 6(12):844–850, 2012.

[50] K. Konig, H. G. Breunig, R. Buckle, M. Kellner-Hofer, M. Weinigel, E. Buttner, W. Sterry, and J. Lademann. Optical skin biopsies by clinical cars and multiphoton fluorescence/shg tomography. *Laser Physics Letters*, 8(6):465–468, 2011.

[51] H. G. Breunig, M. Weinigel, R. Buckle, M. Kellner-Hofer, J. Lademann, M. E. Darvin, W. Sterry, and K. Konig. Clinical coherent anti-stokes raman scattering and multiphoton tomography of human skin with a femtosecond laser and photonic crystal fiber. *Laser Physics Letters*, 10(2), 2013.

[52] K. Konig. Clinical multiphoton tomography. *Journal of Biophotonics*, 1(1):13–23, 2008.

[53] D. Soliman, G. J. Tserevelakis, M. Omar, and V. Ntziachristos. Combining microscopy with mesoscopy using optical and optoacoustic label-free modes. *Sci Rep*, 5:12902, 2015.

[54] K. Koenig, E. Dimitrow, and M. Kaatz. Clinical multiphoton tomography of malignant melanoma. *Journal of the American Academy of Dermatology*, 66(4):Ab142–Ab142, 2012.

[55] E. Dimitrow, M. Ziemer, M. J. Koehler, J. Norgauer, K. Konig, P. Elsner, and M. Kaatz. Sensitivity and specificity of multiphoton laser tomography for in vivo and ex vivo diagnosis of malignant melanoma. *J Invest Dermatol*, 129(7):1752–8, 2009.

[56] M. J. Koehler, M. Speicher, S. Lange-Asschenfeldt, E. Stockfleth, S. Metz, P. Elsner, M. Kaatz, and K. Konig. Clinical application of multiphoton tomography in combination with confocal laser scanning microscopy for in vivo evaluation of skin diseases. *Experimental Dermatology*, 20(7):589–594, 2011.

[57] Jozien Goense, Hellmut Merkle, and Nikos K Logothetis. High-resolution fmri reveals laminar differences in neurovascular coupling between positive and negative bold responses. *Neuron*, 76(3):629–639, 2012.

[58] S Ogawa, T M Lee, A R Kay, and D W Tank. Brain magnetic resonance imaging with contrast dependent on blood oxygenation. *Proceedings of the National Academy of Sciences*, 87(24):9868–9872, 1990.

[59] U. Merschbrock, J. Hoffmann, L. Caspary, J. Huber, U. Schmickaly, and D. W. Lubbers. Fast wavelength scanning reflectance spectrophotometer for noninvasive determination of hemoglobin oxygenation in human skin. *Int J Microcirc Clin Exp*, 14(5):274–81, 1994.

[60] L. Caspary, J. Thum, A. Creutzig, D. W. Lubbers, and K. Alexander. Quantitative reflection spectrophotometry: spatial and temporal variation of hb oxygenation in human skin. *Int J Microcirc Clin Exp*, 15(3):131–6, 1995.

[61] C. E. Thorn, S. J. Matcher, I. V. Meglinski, and A. C. Shore. Is mean blood saturation a useful marker of tissue oxygenation? *American Journal of Physiology-Heart and Circulatory Physiology*, 296(5):H1289–H1295, 2009.

[62] C. W. Yoxall and A. M. Weindling. Measurement of venous oxyhaemoglobin saturation in the adult human forearm by near infrared spectroscopy with venous occlusion. *Medical & Biological Engineering & Computing*, 35(4):331–336, 1997.

[63] A. Vogel, V. V. Chernomordik, J. D. Riley, M. Hassan, F. Amyot, B. Dasgeb, S. G. Demos, R. Pursley, R. F. Little, R. Yarchoan, Y. Tao, and A. H. Gandjbakhche. Using noninvasive multispectral imaging to quantitatively assess tissue vasculature. *Journal of Biomedical Optics*, 12(5):051604–051604, 2007.

[64] AF Fercher. *Inverse scattering, dispersion, and speckle in optical coherence tomography*, pages 119–146. Springer, 2008.

[65] J. Welzel, E. Lankenau, R. Birngruber, and R. Engelhardt. Optical coherence tomography of the human skin. *J Am Acad Dermatol*, 37(6):958–63, 1997.

[66] A. Alex, B. Povazay, B. Hofer, S. Popov, C. Glittenberg, S. Binder, and W. Drexler. Multispectral in vivo three-dimensional optical coherence tomography of human skin. *J Biomed Opt*, 15(2):026025, 2010.

[67] Z. P. Chen, T. E. Milner, S. Srinivas, X. J. Wang, A. Malekafzali, M. J. C. vanGemert, and J. S. Nelson. Noninvasive imaging of in vivo blood flow velocity using optical doppler tomography. *Optics Letters*, 22(14):1119–1121, 1997.

[68] Y. H. Zhao, Z. P. Chen, Z. H. Ding, H. W. Ren, and J. S. Nelson. Real-time phase-resolved functional optical coherence tomography by use of optical hilbert transformation. *Optics Letters*, 27(2):98–100, 2002.

[69] B. J. Vakoc, R. M. Lanning, J. A. Tyrrell, T. P. Padera, L. A. Bartlett, T. Stylianopoulos, L. L. Munn, G. J. Tearney, D. Fukumura, R. K. Jain, and B. E. Bouma. Three-dimensional microscopy of the tumor microenvironment in vivo using optical frequency domain imaging. *Nat Med*, 15(10):1219–23, 2009.

[70] G. Liu, W. Jia, V. Sun, B. Choi, and Z. Chen. High-resolution imaging of microvasculature in human skin in-vivo with optical coherence tomography. *Opt Express*, 20(7):7694–705, 2012.

[71] G. J. Liu and Z. P. Chen. Capturing the vital vascular fingerprint with optical coherence tomography. *Applied Optics*, 52(22):5473–5477, 2013.

[72] T. Gambichler, V. Jaedicke, and S. Terras. Optical coherence tomography in dermatology: technical and clinical aspects. *Arch Dermatol Res*, 303(7):457–73, 2011.

[73] J. Enfield, E. Jonathan, and M. Leahy. In vivo imaging of the microcirculation of the volar forearm using correlation mapping optical coherence tomography (cmoct). *Biomed Opt Express*, 2(5):1184–93, 2011.

[74] Ruikang K Wang, Utku Baran, and Woo J Choi. Optical coherence tomography based microangiography: A tool good for dermatology applications (conference presentation). In *SPIE BiOS*, pages 96890L–96890L–1. International Society for Optics and Photonics.

[75] R. K. Wang and L. An. Doppler optical micro-angiography for volumetric imaging of vascular perfusion in vivo. *Optics Express*, 17(11):8926–8940, 2009.

[76] R. K. Wang, S. L. Jacques, Z. Ma, S. Hurst, S. R. Hanson, and A. Gruber. Three dimensional optical angiography. *Opt Express*, 15(7):4083–97, 2007.

[77] L. An, J. Qin, and R. K. Wang. Ultrahigh sensitive optical microangiography for in vivo imaging of microcirculations within human skin tissue beds. *Optics Express*, 18(8):8220–8228, 2010.

[78] Shau Poh Chong, Conrad W. Merkle, Conor Leahy, Harsha Radhakrishnan, and Vivek J. Srinivasan. Quantitative microvascular hemoglobin mapping using visible light spectroscopic optical coherence tomography. *Biomedical Optics Express*, 6(4):1429, 2015.

[79] F. E. Robles, C. Wilson, G. Grant, and A. Wax. Molecular imaging true-colour spectroscopic optical coherence tomography. *Nat Photonics*, 5(12):744–747, 2011.

[80] L. Schmitz, U. Reinhold, E. Bierhoff, and T. Dirschka. Optical coherence tomography: its role in daily dermatological practice. *J Dtsch Dermatol Ges*, 11(6):499–507, 2013.

[81] T. Gambichler, P. Regeniter, F. G. Bechara, A. Orlikov, R. Vasa, G. Moussa, M. Stucker, P. Altmeyer, and K. Hoffmann. Characterization of benign and malignant melanocytic skin lesions using optical coherence tomography in vivo. *Journal of the American Academy of Dermatology*, 57(4):629–637, 2007.

[82] C. Blatter, J. Weingast, A. Alex, B. Grajciar, W. Wieser, W. Drexler, R. Huber, and R. A. Leitgeb. In situ structural and microangiographic assessment of human skin lesions with high-speed oct. *Biomedical Optics Express*, 3(10):2636–2646, 2012.

[83] J. Qin, J. Jiang, L. An, D. Gareau, and R. K. Wang. In vivo volumetric imaging of microcirculation within human skin under psoriatic conditions using optical microangiography. *Lasers Surg Med*, 43(2):122–9, 2011.

[84] W. J. Choi, R. Reif, S. Yousefi, and R. K. Wang. Improved microcirculation imaging of human skin in vivo using optical microangiography with a correlation mapping mask. *J Biomed Opt*, 19(3):36010, 2014.

[85] Alexander Graham Bell. On the production and reproduction of sound by light. *American Journal of Science*, (118):305–324, 1880.

[86] ML Viengerov. New method of gas analysis based on tyndall-roentgen optoacoustic effect. *Doklady Akademii Nauk SSSR*, 19(687):8, 1938.

[87] Alexander A Oraevsky, Steven L Jacques, and Rinat O Esenaliev. Optoacoustic imaging for medical diagnosis, 1998.

[88] V. Ntziachristos and D. Razansky. Molecular imaging by means of multispectral optoacoustic tomography (msot). *Chem Rev*, 110(5):2783–94, 2010.

[89] L. V. Wang and S. Hu. Photoacoustic tomography: in vivo imaging from organelles to organs. *Science*, 335(6075):1458–62, 2012.

[90] V. Ntziachristos. Going deeper than microscopy: the optical imaging frontier in biology. *Nat Methods*, 7(8):603–14, 2010.

[91] M. Schwarz, A. Buehler, J. Aguirre, and V. Ntziachristos. Three-dimensional multispectral optoacoustic mesoscopy reveals melanin and blood oxygenation in human skin in vivo. *J Biophotonics*, 9(1-2):55–60, 2016.

[92] F. M. Wigley. Vascular disease in scleroderma. *Clinical Reviews in Allergy & Immunology*, 36(2-3):150–175, 2009.

[93] A. L. Herrick. Vascular function in systemic sclerosis. *Curr Opin Rheumatol*, 12(6):527–33, 2000.

[94] Frank O. Nestle, Daniel H. Kaplan, and Jonathan Barker. Psoriasis. *New England Journal of Medicine*, 361(5):496–509, 2009.

[95] Alexander A Karabutov, Elena V Savateeva, and Alexander A Oraevsky. Imaging of layered structures in biological tissues with optoacoustic front surface transducer. In *BiOS'99 International Biomedical Optics Symposium*, pages 284–295. International Society for Optics and Photonics.

[96] H. F. Zhang, K. Maslov, G. Stoica, and L. V. Wang. Functional photoacoustic microscopy for high-resolution and noninvasive in vivo imaging. *Nat Biotechnol*, 24(7):848–51, 2006.

[97] H. F. Zhang, K. Maslov, M. L. Li, G. Stoica, and L. V. Wang. In vivo volumetric imaging of subcutaneous microvasculature by photoacoustic microscopy. *Opt Express*, 14(20):9317–23, 2006.

[98] H. F. Zhang, K. Maslov, and L. V. Wang. In vivo imaging of subcutaneous structures using functional photoacoustic microscopy. *Nat Protoc*, 2(4):797–804, 2007.

[99] C. P. Favazza, O. Jassim, L. A. Cornelius, and L. V. Wang. In vivo photoacoustic microscopy of human cutaneous microvasculature and a nevus. *J Biomed Opt*, 16(1):016015, 2011.

[100] American National Standards Institute and The Laser Institute of America. *American National Standard for safe use of lasers : approved March 16, 2007*. The Laser Institute of America, Orlando, FLa., 2007.

[101] Y. Zhou, W. X. Xing, K. I. Maslov, L. A. Cornelius, and L. H. V. Wang. Handheld photoacoustic microscopy to detect melanoma depth in vivo. *Optics Letters*, 39(16):4731–4734, 2014.

[102] W. Bost, R. Lemor, and M. Fournelle. Optoacoustic imaging of subcutaneous microvasculature with a class one laser. *IEEE Trans Med Imaging*, 33(9):1900–4, 2014.

[103] E. Z. Zhang, J. G. Laufer, R. B. Pedley, and P. C. Beard. In vivo high-resolution 3d photoacoustic imaging of superficial vascular anatomy. *Phys Med Biol*, 54(4):1035–46, 2009.

[104] E. Z. Zhang, B. Povazay, J. Laufer, A. Alex, B. Hofer, B. Pedley, C. Glittenberg, B. Treeby, B. Cox, P. Beard, and W. Drexler. Multimodal photoacoustic and optical coherence tomography scanner using an all optical detection scheme for 3d morphological skin imaging. *Biomed Opt Express*, 2(8):2202–15, 2011.

[105] Behrooz Zabihian, Jessika Weingast, Mengyang Liu, Edward Zhang, Paul Beard, Hubert Pehamberger, Wolfgang Drexler, and Boris Hermann. In vivo dual-modality photoacoustic and optical coherence tomography imaging of human dermatological pathologies. *Biomedical Optics Express*, 6(9):3163, 2015.

[106] Mathias Schwarz, Dominik Soliman, Murad Omar, Andreas Buehler, Saak V Ovsepian, Juan Aguirre, and Vasilis Ntziachristos. Optoacoustic dermoscopy of the human skin: Tuning excitation energy for optimal detection bandwidth with fast and deep imaging in vivo. *IEEE Transactions on Medical Imaging*, 36(6):1287–1296, 2017.

[107] A. R. Young. Chromophores in human skin. *Phys Med Biol*, 42(5):789–802, 1997.

[108] A. N. Bashkatov, E. A. Genina, and V. V. Tuchin. Optical properties of skin, subcutaneous, and muscle tissues: A review. *Journal of Innovative Optical Health Sciences*, 4(1):9–38, 2011.

[109] J. T. Whitton and J. D. Everall. The thickness of the epidermis. *Br J Dermatol*, 89(5):467–76, 1973.

[110] T. Gambichler, R. Matip, G. Moussa, P. Altmeyer, and K. Hoffmann. In vivo data of epidermal thickness evaluated by optical coherence tomography: Effects of age, gender, skin type, and anatomic site. *Journal of Dermatological Science*, 44(3):145–152, 2006.

[111] T. L. Troy and S. N. Thennadil. Optical properties of human skin in the near infrared wavelength range of 1000 to 2200 nm. *Journal of Biomedical Optics*, 6(2):167–176, 2001.

[112] A. N. Bashkatov, E. A. Genina, V. I. Kochubey, and V. V. Tuchin. Optical properties of human skin, subcutaneous and mucous tissues in the wavelength range from 400 to 2000 nm. *Journal of Physics D-Applied Physics*, 38(15):2543–2555, 2005.

[113] I. M. Braverman. The cutaneous microcirculation: ultrastructure and microanatomical organization. *Microcirculation*, 4(3):329–40, 1997.

[114] I. M. Braverman and A. Yen. Ultrastructure of the human dermal microcirculation. ii. the capillary loops of the dermal papillae. *J Invest Dermatol*, 68(1):44–52, 1977.

[115] I. M. Braverman and A. Keh-Yen. Ultrastructure of the human dermal microcirculation. iii. the vessels in the mid- and lower dermis and subcutaneous fat. *J Invest Dermatol*, 77(3):297–304, 1981.

[116] I. M. Braverman and A. Keh-Yen. Ultrastructure of the human dermal microcirculation. iv. valve-containing collecting veins at the dermal-subcutaneous junction. *J Invest Dermatol*, 81(5):438–42, 1983.

[117] S. L. Jacques. Optical properties of biological tissues: a review. *Phys Med Biol*, 58(11):R37–61, 2013.

[118] George M Hale and Marvin R Querry. Optical constants of water in the 200-nm to 200-m wavelength region. *Applied optics*, 12(3):555–563, 1973.

[119] G. J. Tearney, M. E. Brezinski, J. F. Southern, B. E. Bouma, M. R. Hee, and J. G. Fujimoto. Determination of the refractive index of highly scattering human tissue by optical coherence tomography. *Opt Lett*, 20(21):2258, 1995.

[120] M. J. van Gemert, S. L. Jacques, H. J. Sterenborg, and W. M. Star. Skin optics. *IEEE Trans Biomed Eng*, 36(12):1146–54, 1989.

[121] X. Y. Ma, J. Q. Lu, H. F. Ding, and X. H. Hu. Bulk optical parameters of porcine skin dermis at eight wavelengths from 325 to 1557 nm. *Optics Letters*, 30(4):412–414, 2005.

[122] H. Ding, J. Q. Lu, W. A. Wooden, P. J. Kragel, and X. H. Hu. Refractive indices of human skin tissues at eight wavelengths and estimated dispersion relations between 300 and 1600 nm. *Phys Med Biol*, 51(6):1479–89, 2006.

[123] S. Nickell, M. Hermann, M. Essenpreis, T. J. Farrell, U. Kramer, and M. S. Patterson. Anisotropy of light propagation in human skin. *Phys Med Biol*, 45(10):2873–86, 2000.

[124] R. H. Pearce and B. J. Grimmer. Age and the chemical constitution of normal human dermis. *J Invest Dermatol*, 58(6):347–61, 1972.

[125] R. R. Anderson and J. A. Parrish. The optics of human skin. *J Invest Dermatol*, 77(1):13–9, 1981.

[126] A. Pena, M. Strupler, T. Boulesteix, and M. Schanne-Klein. Spectroscopic analysis of keratin endogenous signal for skin multiphoton microscopy. *Opt Express*, 13(16):6268–74, 2005.

[127] Kristian P Nielsen, Lu Zhao, Jakob J Stamnes, Knut Stamnes, and Johan Moan. The optics of human skin: aspects important for human health. In *Proceedings from the symposium Solar Radiation and Human Health*.

[128] Cheng-Lun Tsai, Ji-Chung Chen, and Wen-Jwu Wang. Near-infrared absorption property of biological soft tissue constituents. *Journal of Medical and Biological Engineering*, 21(1):7–14, 2001.

[129] Aravind Krishnaswamy and Gladimir VG Baranoski. A study on skin optics. Technical report, Tech. Rep. CS-2004-01, School of Computer Science, University of Waterloo, Canada, 2004.

[130] T. Lister, P. A. Wright, and P. H. Chappell. Optical properties of human skin. *J Biomed Opt*, 17(9):90901–1, 2012.

[131] H. Du, R. C. A. Fuh, J. Z. Li, L. A. Corkan, and J. S. Lindsey. Photochemcad: A computer-aided design and research tool in photochemistry. *Photochemistry and Photobiology*, 68(2):141–142, 1998.

[132] J. M. Dixon, M. Taniguchi, and J. S. Lindsey. Photochemcad 2: A refined program with accompanying spectral databases for photochemical calculations. *Photochemistry and Photobiology*, 81(1):212–213, 2005.

[133] Anthony J Thody, Elisabeth M Higgins, Kazumasa Wakamatsu, Shosuke Ito, Susan A Burchill, and Janet M Marks. Pheomelanin as well as eumelanin is present in human epidermis. *Journal of Investigative Dermatology*, 97(2):340–344, 1991.

[134] S. Alaluf, D. Atkins, K. Barrett, M. Blount, N. Carter, and A. Heath. Ethnic variation in melanin content and composition in photoexposed and photoprotected human skin. *Pigment Cell Res*, 15(2):112–8, 2002.

[135] D. Parsad, K. Wakamatsu, A. J. Kanwar, B. Kumar, and S. Ito. Eumelanin and phaeomelanin contents of depigmented and repigmented skin in vitiligo patients. *Br J Dermatol*, 149(3):624–6, 2003.

[136] G. Hunt, S. Kyne, S. Ito, K. Wakamatsu, C. Todd, and A. Thody. Eumelanin and phaeomelanin contents of human epidermis and cultured melanocytes. *Pigment Cell Res*, 8(4):202–8, 1995.

[137] A. Hennessy, C. Oh, B. Diffey, K. Wakamatsu, S. Ito, and J. Rees. Eumelanin and pheomelanin concentrations in human epidermis before and after uvb irradiation. *Pigment Cell Research*, 18(3):220–223, 2005.

[138] N. Nakagawa, M. Matsumoto, and S. Sakai. In vivo measurement of the water content in the dermis by confocal raman spectroscopy. *Skin Res Technol*, 16(2):137–41, 2010.

[139] Lorette W Thomas. The chemical composition of adipose tissue of man and mice. *Quarterly journal of experimental physiology and cognate medical sciences*, 47(2):179–188, 1962.

[140] W. Stahl, U. Heinrich, H. Jungmann, J. von Laar, M. Schietzel, H. Sies, and H. Tronnier. Increased dermal carotenoid levels assessed by noninvasive reflection spectrophotometry correlate with serum levels in women ingesting betatene. *J Nutr*, 128(5):903–7, 1998.

[141] RR Anderson and JA Parrish. *Optical properties of human skin*, pages 147–194. Springer, 1982.

[142] Steven L Jacques. Origins of tissue optical properties in the uva, visible, and nir regions. *OSA TOPS on advances in optical imaging and photon migration*, 2:364–369, 1996.

[143] I. S. Saidi, S. L. Jacques, and F. K. Tittel. Mie and rayleigh modeling of visible-light scattering in neonatal skin. *Appl Opt*, 34(31):7410–8, 1995.

[144] E. Salomatina, B. Jiang, J. Novak, and A. N. Yaroslavsky. Optical properties of normal and cancerous human skin in the visible and near-infrared spectral range. *J Biomed Opt*, 11(6):064026, 2006.

[145] C. R. Simpson, M. Kohl, M. Essenpreis, and M. Cope. Near-infrared optical properties of ex vivo human skin and subcutaneous tissues measured using the monte carlo inversion technique. *Physics in Medicine and Biology*, 43(9):2465–2478, 1998.

[146] G. Salerud and S. L. Jacques. Skin optics. *Oregon Medical Laser Center News. Jan 1998*, 2007.

[147] V.. Gusev and A.A. Karabutov. *Laser Optoacoustics*. American Institute of Physics, 1993.

[148] L. V. Wang. Tutorial on photoacoustic microscopy and computed tomography. *Ieee Journal of Selected Topics in Quantum Electronics*, 14(1):171–179, 2008.

[149] Markus W Sigrist. Laser generation of acoustic waves in liquids and gases. *Journal of applied physics*, 60(7):R83–R122, 1986.

[150] G. Paltauf and P. E. Dyer. Photomechanical processes and effects in ablation. *Chemical Reviews*, 103(2):487–518, 2003.

[151] Lihong V. Wang and Hsin-i Wu. *Biomedical optics : principles and imaging*. Wiley-Interscience, Hoboken, NJ, 2007.

[152] William M Haynes. *CRC handbook of chemistry and physics*. CRC press, 2013.

[153] Yeram Sarkis Touloukian, PE Liley, and SC Saxena. Thermophysical properties of matter-the tprc data series. volume 3. thermal conductivity-nonmetallic liquids and gases. Technical report, DTIC Document, 1970.

[154] Gavin Hamilton. *Investigations of the thermal properties of human and animal tissues*. PhD thesis, 1998.

[155] P. Beard. Biomedical photoacoustic imaging. *Interface Focus*, 1(4):602–31, 2011.

[156] BT Cox, JG Laufer, and PC Beard. The challenges for quantitative photoacoustic imaging. In *SPIE BiOS: Biomedical Optics*, pages 717713–717713–9. International Society for Optics and Photonics.

[157] G. J. Diebold, T. Sun, and M. I. Khan. Photoacoustic monopole radiation in one, two, and three dimensions. *Phys Rev Lett*, 67(24):3384–3387, 1991.

[158] B. T. Cox and P. C. Beard. Fast calculation of pulsed photoacoustic fields in fluids using k-space methods. *Journal of the Acoustical Society of America*, 117(6):3616–3627, 2005.

[159] Y. Lee and K. Hwang. Skin thickness of korean adults. *Surg Radiol Anat*, 24(3-4):183–9, 2002.

[160] S Seidenari, A Pagnoni, AD di Nardo, and A Giannetti. Echographic evaluation with image analysis of normal skin: variations according to age and sex. *Skin Pharmacology and Physiology*, 7(4):201–209, 1994.

[161] Jean de Rigal, Catherine Escoffier, Bernard Querleux, Brigitte Faivre, Pierre Agache, and Jean-Luc Lvque. Assessment of aging of the human skin by in vivo ultrasonic imaging. *Journal of investigative dermatology*, 93(5):621–625, 1989.

[162] Nicolas Sans, Marie Faruch, Hlne Chiavassa-Gandois, Catherine Lalande Champetier de Ribes, Carle Paul, and Jean-Jacques Railhac. High-resolution magnetic resonance imaging in study of the skin: Normal patterns. *European journal of radiology*, 80(2):e176–e181, 2011.

[163] M. Omar, M. Schwarz, D. Soliman, P. Symvoulidis, and V. Ntziachristos. Pushing the optical imaging limits of cancer with multi-frequency-band raster-scan optoacoustic mesoscopy (rsom). *Neoplasia*, 17(2):208–14, 2015.

[164] M. Omar, D. Soliman, J. Gateau, and V. Ntziachristos. Ultrawideband reflection-mode optoacoustic mesoscopy. *Opt Lett*, 39(13):3911–4, 2014.

[165] M. Omar. *Multi-scale thermoacoustic imaging methods of biological tissues*. PhD thesis, 2014.

[166] A. M. Winkler, K. Maslov, and L. V. Wang. Noise-equivalent sensitivity of photoacoustics. *Journal of Biomedical Optics*, 18(9), 2013.

[167] M. Xu and L. V. Wang. Universal back-projection algorithm for photoacoustic computed tomography. *Phys Rev E Stat Nonlin Soft Matter Phys*, 71(1 Pt 2):016706, 2005.

[168] M. L. Li, W. J. Guan, and P. C. Li. Improved synthetic aperture focusing technique with applications in high-frequency ultrasound imaging. *Ieee Transactions on Ultrasonics Ferroelectrics and Frequency Control*, 51(1):63–70, 2004.

[169] C. K. Liao, M. L. Li, and P. C. Li. Optoacoustic imaging with synthetic aperture focusing and coherence weighting. *Opt Lett*, 29(21):2506–8, 2004.

[170] Olympus. Ultrasnoic transducers technical notes, 2006.

[171] M. J. Caballero Aceituno and V. Ntziachristos. Incorporating sensor properties in optoacoustic imaging. 2013.

[172] J. A. Jensen and N. B. Svendsen. Calculation of pressure fields from arbitrarily shaped, apodized, and excited ultrasound transducers. *IEEE Trans Ultrason Ferroelectr Freq Control*, 39(2):262–7, 1992.

[173] Andreas Bhler. *Multi-Spectral Optoacoustic Tomography: Methods and Applications*. PhD thesis, 2014.

[174] M. Schwarz, M. Omar, A. Buehler, J. Aguirre, and V. Ntziachristos. Implications of ultrasound frequency in optoacoustic mesoscopy of the skin. *IEEE Trans Med Imaging*, 34(2):672–677, 2014.

[175] M. Xu and L. V. Wang. Analytic explanation of spatial resolution related to bandwidth and detector aperture size in thermoacoustic or photoacoustic reconstruction. *Phys Rev E Stat Nonlin Soft Matter Phys*, 67(5 Pt 2):056605, 2003.

[176] Minghua Xu. *Photoacoustic computed tomography in biological tissues: algorithms and breast imaging*. PhD thesis, 2004.

[177] M. H. Xu and L. H. V. Wang. Photoacoustic imaging in biomedicine. *Review of Scientific Instruments*, 77(4), 2006.

[178] D. Yudovsky and L. Pilon. Rapid and accurate estimation of blood saturation, melanin content, and epidermis thickness from spectral diffuse reflectance. *Applied Optics*, 49(10):1707–1719, 2010.

[179] E. M. Strohm, E. S. Berndl, and M. C. Kolios. High frequency label-free photoacoustic microscopy of single cells. *Photoacoustics*, 1(3-4):49–53, 2013.

[180] M. Schwarz, A. Buehler, and V. Ntziachristos. Isotropic high resolution optoacoustic imaging with linear detector arrays in bi-directional scanning. *J Biophotonics*, 8(1-2):60–70, 2015.

[181] L. Vionnet, J. Gateau, M. Schwarz, A. Buehler, V. Ermolayev, and V. Ntziachristos. 24mhz scanner for optoacoustic imaging of skin and burn. *IEEE Trans Med Imaging*, 33(2):535–545, 2013.

[182] Christopher P Favazza, Song Hu, Victor Huang, Omar Jassim, Lynn A Cornelius, and Lihong V Wang. In vivo multiscale photoacoustic microscopy of human skin. In *SPIE BiOS*, pages 789946–789946–6. International Society for Optics and Photonics.

[183] J. Yao and L. V. Wang. Sensitivity of photoacoustic microscopy. *Photoacoustics*, 2(2):87–101, 2014.

[184] Juan Aguirre, Mathias Schwarz, Dominik Soliman, Andreas Buehler, Murad Omar, and Vasilis Ntziachristos. Broadband mesoscopic optoacoustic tomography reveals skin layers. *Optics Letters*, 39(21):6297, 2014.

[185] E. Alerstam, T. Svensson, and S. Andersson-Engels. Parallel computing with graphics processing units for high-speed monte carlo simulation of photon migration. *J Biomed Opt*, 13(6):060504, 2008.

[186] L. Wang, S. L. Jacques, and L. Zheng. *Monte Carlo modeling of light transport in multi-layered tissues in Standard C*. PhD thesis, 1992. Wang, L Jacques, S L Zheng, L.

[187] X. L. Dean-Ben, D. Razansky, and V. Ntziachristos. The effects of acoustic attenuation in optoacoustic signals. *Phys Med Biol*, 56(18):6129–48, 2011.

[188] Thomas L. Szabo. *Diagnostic ultrasound imaging : inside out*. Academic Press series in biomedical engineering. Elsevier Academic Press, Amsterdam ; Boston, 2004.

[189] P. D. Ninni, F. Martelli, and G. Zaccanti. Intralipid: towards a diffusive reference standard for optical tissue phantoms. *Phys Med Biol*, 56(2):N21–8, 2011.

[190] A. Danielli, C. P. Favazza, K. Maslov, and L. V. Wang. Picosecond absorption relaxation measured with nanosecond laser photoacoustics. *Appl Phys Lett*, 97(16):163701, 2010.

[191] O. Simandoux, A. Prost, J. Gateau, and E. Bossy. Influence of nanoscale temperature rises on photoacoustic generation: Discrimination between optical absorbers based on thermal nonlinearity at high frequency. *Photoacoustics*, 3(1):20–5, 2015.

[192] M Schwarz, N Garzorz-Stark, K Eyerich, J Aguirre, and V Ntziachristos. Motion correction in optoacoustic mesoscopy. *Scientific reports*, 7(1):10386, 2017.

[193] M. Schwarz, A. Buehler, J. Aguirre, and V. Ntziachristos. Three-dimensional multispectral optoacoustic mesoscopy reveals melanin and blood oxygenation in human skin in vivo. *J Biophotonics*, 2015.

[194] K.E. Barrett, S.M. Barman, S. Boitano, and H. Brooks. *Ganong's Review of Medical Physiology, 24th Edition*. Mcgraw-hill, 2012.

[195] A. Rodriguez-Molinero, L. Narvaiza, J. Ruiz, and C. Galvez-Barron. Normal respiratory rate and peripheral blood oxygen saturation in the elderly population. *J Am Geriatr Soc*, 61(12):2238–40, 2013.

[196] A. Buehler, X. L. Dean-Ben, J. Claussen, V. Ntziachristos, and D. Razansky. Three-dimensional optoacoustic tomography at video rate. *Optics Express*, 20(20):22712–22719, 2012.

[197] A. Buehler, E. Herzog, D. Razansky, and V. Ntziachristos. Video rate optoacoustic tomography of mouse kidney perfusion. *Opt Lett*, 35(14):2475–7, 2010.

[198] A. Buehler, M. Kacprowicz, A. Taruttis, and V. Ntziachristos. Real-time handheld multispectral optoacoustic imaging. *Opt Lett*, 38(9):1404–6, 2013.

[199] J. Laufer, P. Johnson, E. Zhang, B. Treeby, B. Cox, B. Pedley, and P. Beard. In vivo preclinical photoacoustic imaging of tumor vasculature development and therapy. *J Biomed Opt*, 17(5):056016, 2012.

[200] X. L. Dean-Ben and D. Razansky. Adding fifth dimension to optoacoustic imaging: volumetric time-resolved spectrally enriched tomography. *Light-Science & Applications*, 3, 2014.

[201] I. Stoffels, S. Morscher, I. Helfrich, U. Hillen, J. Lehy, N. C. Burton, T. C. Sardella, J. Claussen, T. D. Poeppel, H. S. Bachmann, A. Roesch, K. Griewank, D. Schadendorf, M. Gunzer, and J. Klode. Metastatic status of sentinel lymph nodes in melanoma determined noninvasively with multispectral optoacoustic imaging. *Sci Transl Med*, 7(317):317ra199, 2015.

[202] X. L. Dean-Ben, E. Bay, and D. Razansky. Functional optoacoustic imaging of moving objects using microsecond-delay acquisition of multispectral three-dimensional tomographic data. *Scientific Reports*, 4, 2014.

[203] J. Xia, W. Chen, K. Maslov, M. A. Anastasio, and L. V. Wang. Retrospective respiration-gated whole-body photoacoustic computed tomography of mice. *J Biomed Opt*, 19(1):16003, 2014.

[204] A. Taruttis, J. Claussen, D. Razansky, and V. Ntziachristos. Motion clustering for deblurring multispectral optoacoustic tomography images of the mouse heart. *Journal of Biomedical Optics*, 17(1), 2012.

[205] J. M. Yang, C. Favazza, R. Chen, J. Yao, X. Cai, K. Maslov, Q. Zhou, K. K. Shung, and L. V. Wang. Simultaneous functional photoacoustic and ultrasonic endoscopy of internal organs in vivo. *Nat Med*, 18(8):1297–1302, 2012.

[206] Y. M. Liew, R. A. McLaughlin, F. M. Wood, and D. D. Sampson. Motion correction of in vivo three-dimensional optical coherence tomography of human skin using a fiducial marker. *Biomed Opt Express*, 3(8):1774–86, 2012.

[207] Douglas Hanahan and Robert A Weinberg. Hallmarks of cancer: the next generation. *Cell*, 144(5):646–674, 2011.

[208] Peter Carmeliet and Rakesh K Jain. Angiogenesis in cancer and other diseases. *nature*, 407(6801):249–257, 2000.

[209] Twan Lammers, Fabian Kiessling, Wim E Hennink, and Gert Storm. Drug targeting to tumors: principles, pitfalls and (pre-) clinical progress. *Journal of controlled release*, 161(2):175–187, 2012.

[210] Hiroshi Maeda. Macromolecular therapeutics in cancer treatment: the epr effect and beyond. *Journal of Controlled Release*, 164(2):138–144, 2012.

[211] Athanasios Sarantopoulos, George Themelis, and Vasilis Ntziachristos. Imaging the bio-distribution of fluorescent probes using multispectral epi-illumination cryoslicing imaging. *Molecular imaging and biology*, 13(5):874–885, 2011.

[212] P Symvoulidis, C Cruz Perez, M Schwaiger, V Ntziachristos, and GG Westmeyer. Serial sectioning and multispectral imaging system for versatile biomedical applications. In *Biomedical Imaging (ISBI), 2014 IEEE 11th International Symposium on*, pages 890–893. IEEE.

[213] Mathias Schwarz, Juan Aguirre, Dominik Soliman, Andreas Buehler, and Vasilis Ntziachristos. Unmixing chromophores in human skin with a 3d multispectral optoacoustic mesoscopy system. 9708:970855, 2016.

[214] Giovanni Melillo. *Hypoxia and Cancer: Biological Implications and Therapeutic Opportunities*. Springer Science & Business Media, 2013.

[215] J. M. Brown. Tumor hypoxia in cancer therapy. *Methods Enzymol*, 435:297–321, 2007.

[216] A. L. Steunou, M. Ducoux-Petit, I. Lazar, B. Monsarrat, M. Erard, C. Muller, E. Clottes, O. Burlet-Schiltz, and L. Nieto. Identification of the hypoxia-inducible factor 2alpha nuclear interactome in melanoma cells reveals master proteins involved in melanoma development. *Mol Cell Proteomics*, 12(3):736–48, 2013.

[217] T. E. Matthews, I. R. Piletic, M. A. Selim, M. J. Simpson, and W. S. Warren. Pump-probe imaging differentiates melanoma from melanocytic nevi. *Science Translational Medicine*, 3(71), 2011.

[218] Thomas G Salopek, Koji Yamada, Shosuke Ito, and Kowichi Jimbow. Dysplastic melanocytic nevi contain high levels of pheomelanin: quantitative comparison of pheomelanin/eumelanin levels between normal skin, common nevi, and dysplastic nevi. *Pigment cell research*, 4(4):172–179, 1991.

[219] Judith L Silverstein, Virginia D Steen, Thomas A Medsger, and Vincent Falanga. Cutaneous hypoxia in patients with systemic sclerosis (scleroderma). *Archives of dermatology*, 124(9):1379–1382, 1988.

[220] A. Modarressi, G. Pietramaggiori, C. Godbout, E. Vigato, B. Pittet, and B. Hinz. Hypoxia impairs skin myofibroblast differentiation and function. *J Invest Dermatol*, 130(12):2818–27, 2010.

[221] Srivalleesha Mallidi, Seungsoo Kim, Andrei Karpiouk, Pratixa P. Joshi, Konstantin Sokolov, and Stanislav Emelianov. Visualization of molecular composition and functionality of cancer cells using nanoparticle-augmented ultrasound-guided photoacoustics. *Photoacoustics*, 3(1):26–34, 2015.

[222] E. Herzog, A. Taruttis, N. Beziere, A. A. Lutich, D. Razansky, and V. Ntziachristos. Optical imaging of cancer heterogeneity with multispectral optoacoustic tomography. *Radiology*, 263(2):461–8, 2012.

[223] C. P. Favazza, L. A. Cornelius, and L. V. Wang. In vivo functional photoacoustic microscopy of cutaneous microvasculature in human skin. *J Biomed Opt*, 16(2):026004, 2011.

[224] M. I. Khan and G. J. Diebold. The photoacoustic effect generated by laser irradiation of an isotropic solid cylinder. *Ultrasonics*, 34(1):19–24, 1996.

[225] B. T. Cox, S. R. Arridge, K. P. Kostli, and P. C. Beard. Two-dimensional quantitative photoacoustic image reconstruction of absorption distributions in scattering media by use of a simple iterative method. *Applied Optics*, 45(8):1866–1875, 2006.

[226] T. N. Seyfried, R. E. Flores, A. M. Poff, and D. P. D'Agostino. Cancer as a metabolic disease: implications for novel therapeutics. *Carcinogenesis*, 35(3):515–527, 2014.

[227] T. N. Seyfried and L. M. Shelton. Cancer as a metabolic disease. *Nutrition & Metabolism*, 7(7):269–270, 2010.

[228] N. Olson and A. van der Vliet. Interactions between nitric oxide and hypoxia-inducible factor signaling pathways in inflammatory disease. *Nitric Oxide-Biology and Chemistry*, 25(2):125–137, 2011.

[229] C. Rosenberger, C. Solovan, A. D. Rosenberger, J. P. Li, R. Treudler, U. Frei, K. U. Eckardt, and L. F. Brown. Upregulation of hypoxia-inducible factors in normal and psoriatic skin. *Journal of Investigative Dermatology*, 127(10):2445–2452, 2007.

[230] E. J. Horn, K. M. Fox, V. Patel, C. F. Chiou, F. Dann, and M. Lebwohl. Association of patient-reported psoriasis severity with income and employment. *J Am Acad Dermatol*, 57(6):963–71, 2007.

[231] E. Christophers. Psoriasis–epidemiology and clinical spectrum. *Clin Exp Dermatol*, 26(4):314–20, 2001.

[232] C. Ryan, N. J. Korman, J. M. Gelfand, H. W. Lim, C. A. Elmets, S. R. Feldman, A. B. Gottlieb, J. Y. Koo, M. Lebwohl, C. L. Leonardi, A. S. Van Voorhees, R. Bhushan, and A. Menter. Research gaps in psoriasis: opportunities for future studies. *J Am Acad Dermatol*, 70(1):146–67, 2014.

[233] Juan Aguirre, Mathias Schwarz, Natalie Garzorz, Murad Omar, Andreas Buehler, Kilian Eyerich, and Vasilis Ntziachristos. Precision assessment of label-free psoriasis biomarkers with ultra-broadband optoacoustic mesoscopy. *Nature Biomedical Engineering*, 1:0068, 2017.

[234] Leslie van der Fits, Sabine Mourits, Jane SA Voerman, Marius Kant, Louis Boon, Jon D Laman, Ferry Cornelissen, Anne-Marie Mus, Edwin Florencia, and Errol P Prens. Imiquimod-induced psoriasis-like skin inflammation in mice is mediated via the il-23/il-17 axis. *The Journal of Immunology*, 182(9):5836–5845, 2009.

[235] Jason K Wu, Greg Siller, and Geoff Strutton. Psoriasis induced by topical imiquimod. *Australasian journal of dermatology*, 45(1):47–50, 2004.

[236] U Patel, NM Mark, BC Machler, and VJ Levine. Imiquimod 5literature and mechanism. *British Journal of Dermatology*, 164(3):670–672, 2011.

[237] N. Beziere, C. von Schacky, Y. Kosanke, M. Kimm, A. Nunes, K. Licha, M. Aichler, A. Walch, E. J. Rummeny, V. Ntziachristos, and R. Meier. Optoacoustic imaging and staging of inflammation in a murine model of arthritis. *Arthritis Rheumatol*, 66(8):2071–8, 2014.

[238] O Warshavski, C Meynier, N Sngond, P Chatain, N Felix, and A Nguyen-Dinh. Experimental evaluation of cmut and pzt transducers in receive only mode for photoacoustic imaging. In *SPIE BiOS*, pages 970830–970830–7. International Society for Optics and Photonics.

[239] Georg Wissmeyer, Dominik Soliman, Rami Shnaiderman, Amir Rosenthal, and Vasilis Ntziachristos. All-optical optoacoustic microscope based on wideband pulse interferometry. *Optics Letters*, 41(9):1953, 2016.